UNIVERSITY OF SOUTHAMPTON

FACULTY OF ENGINEERING AND THE ENVIRONMENT
Aerodynamics and Flight Mechanics

Investigation of Numerical Resolution Requirements of the Eulerian Stochastic Fields and the Thickened Stochastic Field Approach

by

Mark Anthony Picciani

Thesis for the degree of Doctor of Philosophy

July 2018

UNIVERSITY OF SOUTHAMPTON

ABSTRACT

FACULTY OF ENGINEERING AND THE ENVIRONMENT
Aerodynamics and Flight Mechanics

Doctor of Philosophy

INVESTIGATION OF NUMERICAL RESOLUTION REQUIREMENTS OF THE EULERIAN STOCHASTIC FIELDS AND THE THICKENED STOCHASTIC FIELD APPROACH

by Mark Anthony Picciani

The stochastic fields approach is an effective way to implement transported Probability Density Function modelling into Large Eddy Simulation of turbulent combustion. In premixed turbulent combustion however, thin flame-like structures arise in the solution of the stochastic fields equations that require grid spacing much finer than the filter scale used for the Large Eddy Simulation. An investigation into numerical resolution requirements is conducted through simulation of a series of one-dimensional stochastic fields simulations of freely-propagating turbulent premixed flames. The investigation involved various stochastic field simulations at different combustion regimes and numerical resolutions. It was concluded that the conventional approach of using a numerical grid spacing equal to the filter scale can yield substantial numerical error; specifically towards the flamelet regime. However, using a numerical grid spacing much finer than the filter length scale is computationally-unaffordable for most industrially-relevant combustion systems. A Thickened Stochastic Fields approach is developed in this thesis in order to provide physically and numerically-accurate solutions of the stochastic fields equations with reduced compute time compared to a fully resolved simulations. The Thickened Stochastic Fields formulation bridges between the conventional stochastic fields and conventional Thickened-Flame approaches depending on the sub-filter combustion regime and numerical grid spacing utilised. One-dimensional stochastic fields simulations of freely-propagating turbulent premixed flames are used in order to obtain a criteria for the thickening factor required as a function of relevant physical and numerical parameters, and to obtain a model for an efficiency function that accounts for the loss of resolved flame surface area caused by applying the thickening transformation to the stochastic fields equations. The Thickened Stochastic Fields formulation is tested by performing LES of a laboratory premixed Bunsen flame. The results demonstrate that the Thickened Stochastic Fields method produces accurate predictions even when using a grid spacing equal to the filter scale.

Contents

List of Figures

List of Tables

Declaration of Authorship

I, Mark Anthony Picciani, declare that this thesis entitled Investigation of Numerical Resolution Requirements of the Eulerian Stochastic Fields and the Thickened Stochastic Field Approach and the work presented in it are my own and has been generated by me as the result of my own original research.

I confirm that:

1. This work was done wholly or mainly while in candidature for a research degree at this University;
2. Where any part of this thesis has previously been submitted for a degree or any other qualification at this University or any other institution, this has been clearly stated;
3. Where I have consulted the published work of others, this is always clearly attributed;
4. Where I have quoted from the work of others, the source is always given. With the exception of such quotations, this thesis is entirely my own work;
5. I have acknowledged all main sources of help;
6. Where the thesis is based on work done by myself jointly with others, I have made clear exactly what was done by others and what I have contributed myself;
7. Either none of this work has been published before submission, or parts of this work have been published as:

   M. Picciani, E. S. Richardson, and S. Navarro-Martinez, "Resolution Requirements in Stochastic Field Simulation of Turbulent Premixed Flames." *Flow, Turbulence and Combustion*, vol. 101, pp. 1103-1118, 2018

   M. Picciani, E. S. Richardson, and S. Navarro-Martinez, "A Thickened Stochastic Fields Approach For Turbulent Combustion Simulation." *Flow, Turbulence and Combustion*, vol. 101, pp. 1119-1136, 2018.

Signed:

Date:

Acknowledgements

The person that deserves the most of my thanks and praise is my supervisor. His knowledge and insight is inspiring and I want to thank him wholeheartedly for providing me the opportunity to learn from him and for his continuous support throughout our time together.

To my Southampton housemate Jacques VDK, I couldn't have asked for a better housemate. You were one of the few people that kept me sane through all of this and have provided me with amazing (and hilarious!) memories. To my Didcotian housemate from SA that graciously facilitated my continued work after leaving Southampton - you're an angel in disguise. Tomas and Kirsten you were (and are still) my second family. I know my family back home loves you for the support you both provided me in their absence. To the original occupants of the unofficial combustion office - Bruno, Nabil and Tomas - it was a blast sharing that little office with you for the time that we did. When we were all together, it was a great working environment filled with (mainly) productive discussions. Andy and Charles, even though you weren't always present, thank you for the insightful discussions. To all the other (unmentioned) friends I have made during my stay in Southampton, you have all contributed to the lasting memories I will have of this experience.

Most importantly I want to thank my family. These past four years have not been the easiest for us, but through everything, you consistently provided me with motivation and support when I needed it. I couldn't have done this without all of you.

Chapter 1

Introduction

Fossil fuel combustion currently provides more than 85% of the worlds primary energy needs [1]. Even with the current research effort into low carbon energy technology and fuels, it is anticipated that combustion systems will continue to be the primary source of energy globally [2]. Additionally, regulations imposed by governments (such as the Euro 6 legislation [3]) are placing increasingly stringent restrictions on air quality emissions (CO, NOx, UHC, etc) and greenhouse gases (CO_2), while also requiring increased efficiency and energy output from these systems. In order for combustion technology to support the global energy and transport demand and meet emission regulations, overall process improvements need to be made. The most promising way for combustion design to achieve these concurrent objectives is through: (1) novel fuel blends, including low net-CO_2 bio-fuel derived components; and (2) new combustion technology that increases the thermal efficiency of an engine by allowing the engine to operate at higher pressure. Higher pressure combustion intensifies reaction and thus a similar thermal output can be obtained under fuel-lean conditions. This increases fuel efficiency and can reduce the quantity of combustion generated air quality emissions.

Optimisation of power generation devices for increased efficiency and to reduce emissions to within the established regulations is driving combustor design towards increasingly extreme operating conditions. Being able to fine tune combustor geometry and combustion conditions requires fundamental knowledge into the processes and physical behaviour of these systems. Historically, experimentation has been the primary method to obtain understandings of combustion systems. Experiments are beneficial for their lack

of assumptions on physical flow processes and for their relative ease in obtaining high level information. However, uncertainties are often introduced when more detailed measurement techniques are employed. For example, in Particle Image Velocimetry (PIV), errors can be introduced due to random noise and the correlation algorithms used to reconstruct the velocity vectors [4]. Assumptions are often made in regards to the seed particles namely that, 1) the seed density is sufficient for the PIV correlation algorithm, and 2) that the seed particles follow the flow without slip. Therefore, obtaining accurate and detailed information about specific physical flow processes can be challenging and requires careful configuration of the experiment. With the increasing complexity of flow systems, repeated testing of large scale combustors can quickly become extremely expensive and time consuming especially when conducting parametric investigations of combustors.

With the increase in computational power, many industries have adopted Computational Fluid Dynamics (CFD) as a tool in their design process. CFD is relatively easy to implement and is cost effective compared to detailed experimental investigations. It can provide a multi-scale level of detail and flow visualization that experiment is unable to provide. However, it can be limited in its predictive capability due to the use of numerical models often derived for case specific conditions. Additionally, for reacting flows, simplified assumptions are often made to model species diffusion and chemical reactions. The use of simplified chemical mechanisms to describe reaction pathways that may include thousands of elementary chemical reactions may not always be suitable. Due to this drawback of CFD, industry tends to combine use of both experiment and CFD in the design process.

CFD involves solving fluid flow equations though established numerical algorithms and procedures. There are three main approaches for simulation of turbulent reacting flow: Reynolds Averaged Navier Stokes (RANS), Large Eddy Simulation (LES) and Direct Numerical Simulation (DNS). DNS is the most accurate of the approaches used to solve turbulent reacting flows and involves the solution of the equations of fluid flow using enough resolution to accurately capture all the length and time scales of turbulence and the flame. DNS therefore avoids the need for turbulence models and only requires physical models for transport, thermodynamic, and chemical kinetic properties of the fluid. As a consequence of the spatio-temporal resolution required, DNS simulations are plagued by their sometimes prohibitive computational cost. The resulting data

from these simulations, are invaluable since they provide fundamental information on physical processes necessary to identify, derive, and test models for use in lower fidelity modelling approaches. However, full resolution simulations are not yet feasible for most engineering and industrial applications. Thus, lower fidelity modelling approaches are typically used.

The more computationally feasible options are RANS and LES. In RANS a solution is sought by temporally averaging the governing equations of DNS. The nature of this time-averaging process means that turbulent fluctuations are not resolved and require modelling. In LES, the governing equations are spatially filtered. Any turbulent structures larger than the characteristic filter width are resolved by the simulation and only the small scale turbulent structures (below the filter width) are modelled. In many combustion applications, LES predictions are superior to RANS. However, for both methods, two key challenges in the modelling of turbulent combustion are: 1) Important processes and diffusion effects in flames occur at scales which are not resolved in either method; 2) Flame interaction with the turbulent flow needs to be modelled. The reduction in computational overhead allows RANS and LES methods to be applied to engineering scale applications, but comes with the penalty of greater reliance on modelling. Specifically, modelling is required for the unresolved turbulent transport and the filtered/ensemble-averaged chemical source term.

1.1 Combustion

Combustion can be considered a temperature-dependant, exothermic process between a fuel and oxidant, that releases the bond energy within molecules to produce heat and light. There are two classifications of combustion:

- **Non-premixed Combustion or diffusion flames**: In Non-premixed Combustion, combustion is dependant on the mixing between the fuel and oxidiser which are introduced separately. Deep in the respective components the mixture is either too rich or too lean for chemical reaction to occur. The flame is present in regions around stoichiometry where the mixture composition and temperature are sufficient to sustain chemical reaction. Removal of either stream terminates the combustion process. This property makes non-premixed combustion a very safe

combustion mechanism. It has been studied extensively and can be seen in many everyday applications such as furnaces and diesel engines. The principle drawback of this combustion is that it typically produces high temperatures. When coupled with air as the oxidiser, it can lead to increased levels of pollutants such as NOx.

- **Premixed Combustion**: In premixed combustion, the fuel and oxidiser are thoroughly mixed to form a flammable mixture prior to combustion. As such, a flame can develop anywhere in the mixture where there is an ignition source. Practically, this is a much more dangerous mechanism than non-premixed combustion. Many everyday applications exist for premixed combustion such as port fuel injection spark ignition engines, and gas turbine engines. The benefit of this regime of combustion over non-premixed combustion is that the stoichiometry of the flame can be controlled to generate the appropriate post flame conditions. More attractively, premixed flames can operate in fuel lean conditions leading to lower flame temperatures that reduce the formation of NOx. Lean Premixed combustion is a promising approach for many industrial applications such as large scale gas turbines and aero engines. While premixed combustion can provide benefits for combustion systems, there remain some challenges in its safe implementation into future designs due to the inherent instability caused by the strong coupling between molecular diffusion and chemical reaction.

1.1.1 Premixed Combustion Overview

The nature of premixed flames having both oxidiser and fuel mixed prior to ignition gives rise to a different flame structure and combustion mechanisms compared to non-premixed combustion. In non-premixed flames, combustion is sustained by the active and continuous mixing of oxidiser and fuel. Comparatively, in a premixed flame, due to the premixed nature of the reactants, combustion can be self-sustaining.

When ignition occurs in a premixed flame, chemical reaction causes the release of heat and the rapid conversion of reactants to products. This generates (and steepens) thermal and scalar gradients. As a consequence of these sharp gradients, premixed flames are characterised by an interface of finite (measurable) thickness that separates reactants and products (or unburnt and burnt states). The thickness of this interface is known as the flame thickness.

1.1.1.1 Laminar Flame Structure and Thickness

The structure of premixed laminar flames is shown in Figure 1.1. It can be divided into four principle zones. In the *Inert zone*, the fuel and oxidiser are homogeneously mixed at a relatively cool temperatures and no chemical reaction occur. In the *Preheat zone*, thermal diffusion from the reaction zone causes the fresh unburnt reactants to be heated while remaining chemically inert. Additionally, combustion products and radicals from the post flame region diffuse towards the *Inert zone*. The third zone is a very thin layer called the *Reaction Zone*. This zone is dominated by low activation energy chemical reactions and production of intermediate chemical species (such as CO, CH_3, etc.). The result is large temperature and species concentration gradients through this region. The thickness is often denoted δ_r and is termed the reaction zone thickness. In the final region, the *Post Flame zone* (or the *Oxidation zone*), slow recombination of radicals occurs to form the final combustion products (such as H_2O and CO_2 atoms). The oxidation zone thickness is typically much larger than the reaction zone thickness as the chain terminating reactions are typical quite slow [5].

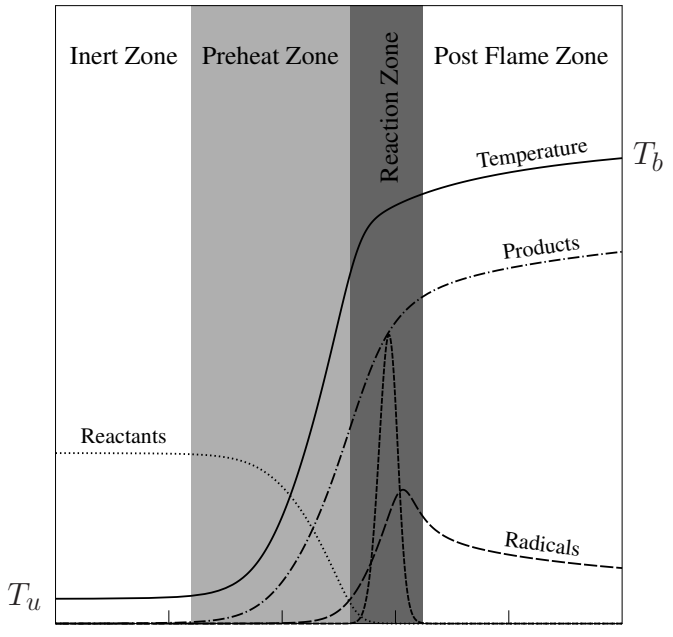

FIGURE 1.1: Schematic of premixed laminar flame structure.

Flame Thickness

There are various definitions of flame thickness (see [6] for a review). The total flame thickness $\left(\delta^t\right)$ is measured by the distance which the temperature varies from $1.01T_u$ to $0.99T_b$ where the subscripts u and b denote unburnt and burnt mixtures respectively. Due to the slow recombination reactions taking place in the oxidation zone (and the resultant long temperature tails), this measure of flame thickness tends to produce a very large estimations of flame thickness.

A second definition is known as the diffusion thickness and is defined as

$$\delta = \frac{D_{th}}{s_L}, \tag{1.1}$$

where D_{th} is the thermal diffusivity, and s_L is the laminar flame speed. Although quite simple to compute once the flame speed is known, it may be too approximate and depends highly on the value of thermal diffusivity which changes through the flame.

A more appropriate (and widely used) measure of thickness is based on the temperature profile and is known as the thermal thickness (δ_L) and is given by

$$\delta_L = \frac{T_b - T_u}{|\nabla T|_{max}}, \tag{1.2}$$

where $|\nabla T|_{max}$ is the maximum temperature gradient through the flame.

Under certain assumptions (i.e adiabatic, simple chemistry, and equal molecular diffusivities), a premixed flame can also be characterised though a progress variable, c. It is constructed through

$$c = \frac{T - T_u}{T_b - T_u} \text{ or } \frac{Y - Y_u}{Y_b - Y_u}, \tag{1.3}$$

where Y is a mass fraction or sum of mass fractions of major reactants and/or product species. The most restrictive condition placed on the choice scalars defining a progress variable is that the resultant progress variable must vary monotonically between the burnt and unburnt states. As such, radicals present within the reaction zone are often not used to define it. With the correct choice scalar(s), the progress variable describes the unique thermo-physical state of any point through the flame.

Under the aforementioned assumptions, the progress variable can also be used to define a flame thickness in a similar form to temperature.

$$\delta_c = \frac{1}{|\nabla c|_{max}}. \tag{1.4}$$

In DNS simulations, accurate simulation of premixed flames requires resolution of the chemical processes that occur within (and through) the thin flame structure. When a combustion model is used, the laminar flame thickness is often used as an input for turbulent combustion models. Therefore, accurate predictions of the flame thickness is essential as it can be used as an *a priori* tool to establish initial numerical grid requirements that may be required within the simulation or provide accurate closure for turbulent combustion models. Poor resolution of chemical processes through the flame can lead to substantial errors in the simulations as will be discussed in Chapter 4.

Flame Speed

The steep thermal and scalar gradients generated by chemical reaction shown above drives diffusion of these quantities to the deficient side of the interface. For example, thermal diffusion from the hot side of the interface towards the cooler, unburnt reactants side, gradually increases the temperature of the unburnt reactants in the vicinity of the reaction zone leading to the generation the Pre-heat zone. At the same time, the higher temperature of the fresh reactive mixture leads to the initiation of chemical reaction. This feedback of chemical reaction and scalar diffusion is continuous, and eventually balances. This continuous process results in the incremental displacement, or propagation, of the interface towards the fresh reactant mixture. The speed at which this interface propagates is known as the laminar flame speed (s_L).

Through asymptotic analysis, analytical expressions have been developed (see for example [7]) for calculating the laminar flame speed. These analytical expressions rely on simplifications of physical processes such as simplified single step irreversible chemistry, and a unity Lewis number ($Le = \alpha/D$) i.e equal thermal diffusivity α and molecular diffusivity D. However, these analytical expressions generally exhibit a dependency on

thermal diffusion and chemical reactions and follows that

$$s_L \propto \sqrt{D_{th} K_r} \tag{1.5}$$

where D_{th} is the thermal diffusivity and K_r is the reaction rate coefficient of a simplified chemical reaction. The reaction rate coefficient is most often represented by the Arrhenius Law.

$$K_r = A_p T^n \exp\left(\frac{-E_a}{R_u T}\right), \tag{1.6}$$

where E_a is the activation energy, R_u is the universal gas constant, T is the temperature, n is the temperature exponent, and A_p is the pre-exponential factor.

The laminar flame speed is known to depend on the unburnt mixture composition, temperature, and pressure. The mixture composition is usually expressed as an equivalence ratio which represents the deviation from stoichiometric conditions

$$\phi = s\frac{Y_F}{Y_O}, \tag{1.7}$$

where s is the stoichiometric ratio, Y_F is the fuel mass fraction, and Y_O is the oxidiser mass fraction. When the equivalence ratio is $\phi < 1$ the mixture is said to be lean (excess oxidiser) and when $\phi > 1$ the mixture is said to be rich. An example of the dependency of the laminar flame speed on these properties is shown in Figure 1.2.

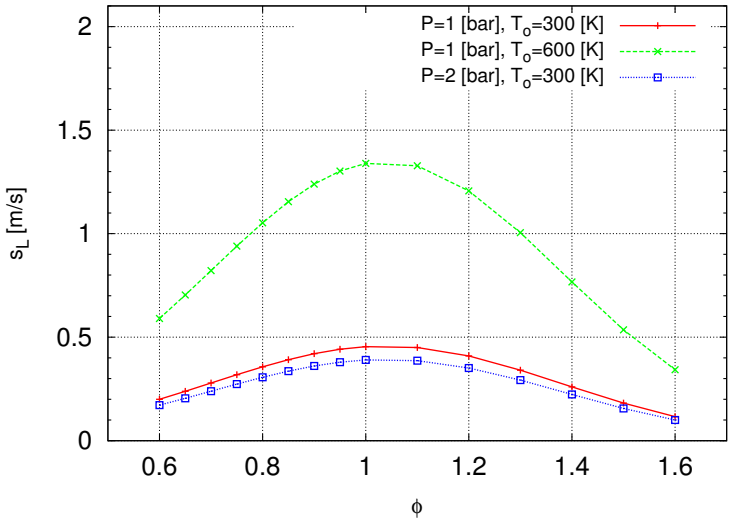

FIGURE 1.2: Variation of laminar flame speed of iso-Octane as a function of equivalence ratio, temperature, and pressure as obtained from analytical functions of [8]

The decrease of laminar flame speed with increasing pressure shown in Figure 1.2 arises from the increased diffusion resistance at elevated pressures. The much stronger dependence of the flame speed on initial temperature arises from the highly non-linear dependence of reaction rate on temperature shown in Equation 1.6.

1.2 Turbulence Overview

In most practical applications of combustion, the presence of turbulence is very common. Turbulent flows are characterised by vortical motions of varying scales. The majority of the energy is contained in the larger scales and is transferred to the smallest scales where it is eventually dissipated into heat. This transfer of energy is known as the energy cascade and is illustrated in Figure 1.3.

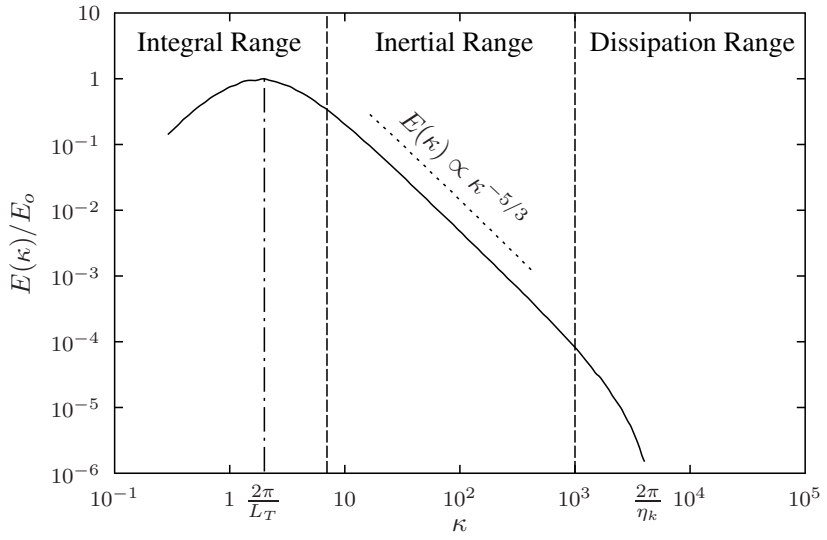

FIGURE 1.3: Representative turbulent kinetic energy spectrum for homogeneous turbulence

The majority of the turbulent kinetic energy (TKE) is contained in the *Integral Range* which has a characteristic length-scale (the integral length scale, L_T) which is normally problem dependant. These large turbulent structures contain the majority of turbulent kinetic energy which is on the order of $u'(L_T)^2$ (where u' is characteristic velocity of the turbulent scale). In general, the largest turbulent structures may be anisotropic, and are influenced by boundary conditions of the flow. The velocity and length scales in this

range are often used to define a turbulent Reynolds number

$$Re_T = \frac{u'(L_T)L_T}{\nu}, \tag{1.8}$$

where ν the kinematic viscosity. This quantity indicates the ratio between turbulent inertial and laminar viscous forces, and gives an indication to the range of scales in the turbulent field under investigation.

The *Inertial Range* is where the energy transfer between scales takes place, independent of viscous effects. Large unstable eddies break up into smaller structures and transfer their kinetic energy. If an equilibrium between local input of kinetic energy from the large scales and dissipation (ϵ) from the small scales is assumed, the kinetic energy at any scale within this range is given by the Kolmogorov Law [9]

$$E(\kappa) \propto C\epsilon^{\frac{2}{3}}\kappa^{\frac{-5}{3}}. \tag{1.9}$$

The dissipation rate (ϵ) of an eddy characterises the rate at which the energy is transferred from the large to the small scales. It is estimated by the ratio of the eddy's kinetic energy and turnover time. With the dependency of the integral scale dropped ($u'(L_T) = u'$), ϵ can be expressed by

$$\epsilon = \frac{u'^2}{\tau_T} = \frac{u'^3}{L_T}. \tag{1.10}$$

The behaviour in the Inertial Range has not been proven analytically, however, it has been demonstrated experimentally and numerically in a wide range of flow conditions as seen in Figure 1.4. This assumption of constant dissipation in the inertial range provides a useful method to relate turbulent characteristics at different scales and is used as a base assumption in the derivation of turbulence models. For example, within the inertial sub-range, the velocity at some arbitrary scale, L_s, can be related to the integral scale quantities through

$$u_s = u_T \left(\frac{L_s}{L_T}\right)^{(1/3)} \tag{1.11}$$

Finally, the *Dissipation Range* is where the majority of the TKE of the flow is dissipated by the smallest scales due to viscous effects. Kolmogorov argued that all anisotropy of the large scales is lost during the cascade process, and that after certain threshold

the turbulent scales are locally isotropic, uniquely determined by ϵ and the kinematic viscosity, ν. Using dimensional analysis, Kolmogorov [10] defined expressions for the scales at which inertial and viscous forces balanced. Known as the Kolmogorov scales, they characterise the smallest turbulent motions in a flow. The Kolmogorov length-scale (η), velocity (u_η), and turnover times (τ_η) can be defined as

$$\eta = \left(\frac{\nu^3}{\epsilon}\right)^{\frac{1}{4}}, \tag{1.12}$$

$$u_\eta = (\nu\epsilon)^{\frac{1}{4}}, \tag{1.13}$$

$$\tau_\eta = \left(\frac{\nu}{\epsilon}\right)^{\frac{1}{2}}, \tag{1.14}$$

respectively.

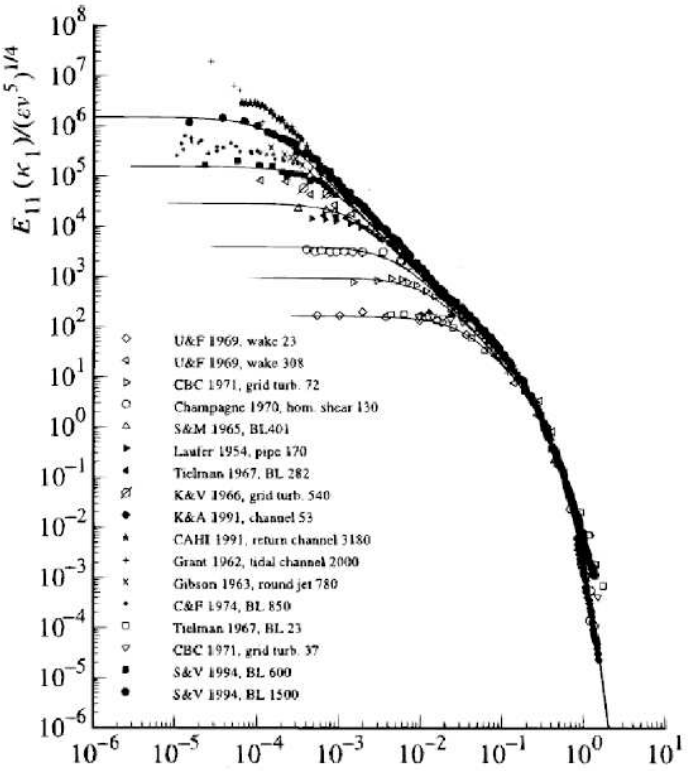

FIGURE 1.4: Turbulent kinetic spectrum depicting the energy dissipation trends proposed by Kolmogorov [11].

1.2.1 Turbulent Premixed Flames

When considering practical combustion configurations such as gas turbine combustors or internal combustion engines, turbulence is nearly always present and it interacts with

the flame by wrinkling and stretching it. Turbulence of different length and velocity scales (and consequently time-scales) in a field will interact uniquely with a flame of a given thermo-physical configuration leading to deviations from the characterising laminar relationships given above.

To aid in describing the influence of turbulence on a laminar flame, a regime diagram (shown in Figure 1.5) was developed by [12, 13]. This diagram provides a rough *a priori* characterisation of the turbulent flame and can indicate whether the turbulent flame exhibits thin, "sheets-like" or distributed reactions zones. Knowledge of the combustion regime provides useful information for the selection of combustion models to be used in simulations as combustion models are usually developed for specific combustion regimes and may not be applicable to others.

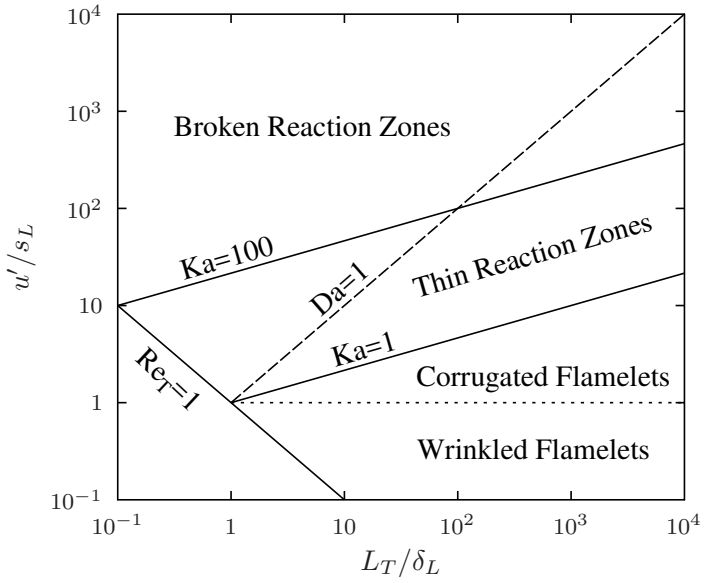

FIGURE 1.5: Premixed combustion regime diagram

This diagram is assembled and navigated through comparison of the relative magnitude of the various chemical and turbulent scales (time, length, and velocity) and non-dimensional numbers:

- The **Damköhler** number is the ratio of turbulent and chemical time-scales given by

$$Da = \frac{\tau_T}{\tau_c} = \frac{L_T}{\delta_L}\frac{s_L}{u'}, \tag{1.15}$$

where τ_T is the characteristic turbulent time-scale and τ_c is the chemical time-scale defined as

$$\tau_c = \frac{\delta_L}{s_L}. \tag{1.16}$$

Very small values of (Da) indicate that turbulent mixing is faster than chemical processes; combustion in the small Da regime is thus reaction rate limited. Conversely, for very large Da, the reaction rate timescale is much smaller (faster reaction rates) than the mixing, and therefore the rate of reaction is limited by turbulent mixing and the subsequent diffusion of scalars; the high Da regime is mixing limited.

- The **Karlovitz** number (Ka) is the ratio of the Kolmogorov and chemical time scale

$$Ka = \frac{\tau_c}{\tau_\eta} = \frac{\delta_L^2}{\eta^2}, \tag{1.17}$$

where τ_η and η are the Kolmogorov time-scale and length-scale respectively. This non-dimensional quantity compares the influence of chemistry to the smallest (Kolmogorov) turbulent scale. With the assumption that $s_L\delta_L/\nu = \mathcal{O}(1)$ [14], the Karlovitz number can be recast in terms of the integral scale quantities as

$$Ka = \left(\frac{u'}{s_L}\right)^{3/2}\left(\frac{\delta_L}{L_T}\right)^{1/2}. \tag{1.18}$$

- With the expressions for Karlovitz number and Damköhler, an alternative expression for the turbulent Reynolds number can be developed as

$$Re_T = \left(\frac{u'}{s_L}\right)\left(\frac{L_T}{\delta_L}\right) = Ka^2Da^2. \tag{1.19}$$

Within the regime diagram, four distinctive combustion regimes can be identified. Each combustion regime can be summarised as follows:

- **Laminar Regime:** Indicated by the lower left hand corner, this regime is characterised by the turbulent Reynolds number being less than unity and represents where the flame is completely laminar in nature.

- **Flamelet Regime:**

  - **Wrinkeled Flamelet:** Combustion in this regime is characterised by the turbulent scales being smaller than the Gibson length-scale, or where $u' < s_L$. Consequently, the turbulence lacks sufficient energy to significantly deform the flame. Laminar flame propagation is dominant.
  - **Corrugated Flamelet:** This regime is characterised by a higher turbulence intensity than the wrinkled flamelet regime. Any structures possessing turnover velocities greater than the laminar flame speed ($u' > s_L$) will be able to deform and wrinkle the flame.

- **Thin reaction zones:** In this reaction regime, the majority of the turbulence scales wrinkle the flame. The largest turbulent scales possessing a turnover time of $\tau_t < \tau_c$ ($Da < 1$) will act to increase transport and thicken the thermal layer (or preheat zone) to a scale on the order of their size, transporting heat and mass ahead of the flame. Smaller turbulent scales will be small enough to penetrate the thickened thermal layer. Additionally, the smaller turbulent structures may begin to strain and deform the inner layer (reaction zone). As Ka is increased, mass transfer begins to be governed more by turbulent diffusion than molecular diffusion.

- **Broken reaction zones:** In this reaction regime, turbulent motions may enter the inner layer increasing the distribution of heat and radicals to the preheat zone.

Turbulent Flame Speed

As a result of the wrinkling of the flame, its total surface area increases. This results in an increase in the volumetric consumption rate of reactants through the flame, and thus, an increase its propagation speed from a laminar to a turbulent speed (s_T). Attempts at deriving analytical expression for the change in flame speed due to turbulence have generally resulted in expressions of the form [6]:

$$\frac{s_T}{s_L} \approx 1 + \frac{u'}{s_L}, \tag{1.20}$$

which simply highlight the general principle that premixed flame propagation is enhanced by turbulent motions. However, the increase in turbulent flame speed with

turbulent fluctuation is not indefinite. It has been shown (example in [15]) that for progressively increasing turbulence intensities, an upper limit on attainable turbulent flame speed exists. At very large turbulent intensities, the turbulent flame speed becomes a function of the turbulent length-scales only. This is known as the "bending" effect.

For a turbulent flame in the flamelet regime (or for small u' and where $L_T \gg \delta_L$), only the larger scale turbulent structures influence the flame structure. These larger structures convolute the turbulent flame increasing its total surface area, but leave the inner (laminar-like) structure of the flame unaffected. As a consequence, the local flame surface elements of the flame roughly propagate at the laminar flame speed. This behaviour is illustrated in Figure 1.6. Damköhler [16] was the first to propose this behaviour and suggested that in this regime, the turbulent flame speed was dictated by turbulent fluctuations $s_T \sim u'$. This is known as Damköhler hypothesis. As such, it can then be stated that in this particular combustion regime, the turbulent flame speed is proportional to the total flame surface area as

$$\frac{s_T}{s_L} \propto \frac{A_T}{A}, \tag{1.21}$$

where A_T is the turbulent flame surface area and A is the projected frontal (or mean) area of the flame brush. This ratio of areas is known as the flame wrinkling factor. Development of analytical expression for this ratio still remains an active area of research. The derived expressions are normally a function of characteristic turbulence or flame describing parameters such as u', L_T, Le, s_L etc.

1.3 Thesis Motivation

The choice of combustion model used in a particular numerical simulation of turbulent reacting flow generally requires *a priori* knowledge of the combustion regime i.e. non-premixed or premixed and the various regimes therein described in Section 1.2.1. This is simply due to fundamental assumptions and inherent limitations in their derivations. For example, flamelet based models [18, 19] (for $\mathrm{Ka} \lesssim 1$) take advantage of the fact that the reaction zones are substantially thinner than turbulent scales. It is therefore assumed that the relatively undisturbed inner structure of the turbulent flame can be represented by an ensemble of many "flamelets" whose properties can be represented by laminar flames. Moving away from this regime towards the broken reaction zones ($\mathrm{Ka} > 1$),

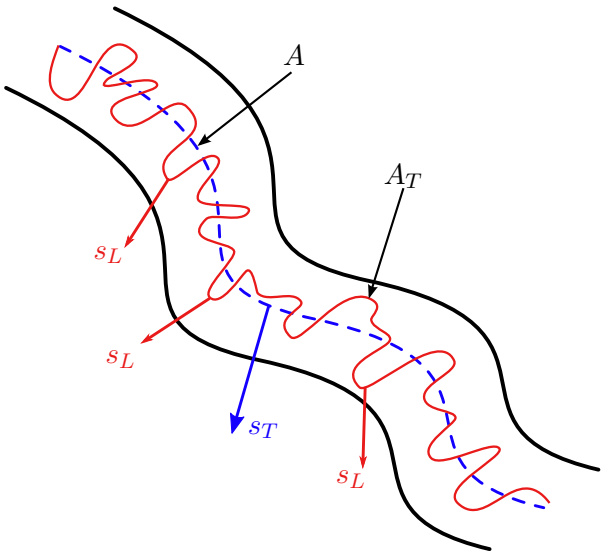

FIGURE 1.6: Turbulent flame speed definition in the flamelet regime - The total turbulent flame surface A_T and mean area A are shown along with the laminar (s_L) and turbulent (s_T) flame speeds. Image modified with permission from [17].

the increasing aerodynamic strain and interaction of turbulence with the reaction zone relaxes the assumption of laminar-like inner flame structure resulting in flamelet methods becoming less applicable and thus requiring a different modelling approach.

Aside from the study of fundamental flame physics, an objective of numerical combustion research is the advancement of modelling potential though relaxation of current modelling limitations and by broadening the regimes of applicability of the existing models. This direction is primarily being driven by the desire to have increasingly complex combustion systems that may exhibit a variety of combustion conditions. In fact, most practical combustion systems do not fall within a specific, well defined premixed or non-premixed combustion regime that the models were designed for, adding to the complexity of numerical modelling. For example, depending on their operating mode, Gasoline Direct Injection (GDI) engines have operating conditions that vary between non-premixed and premixed combustion, and across varying combustion regimes within premixed combustion itself [20]. Gas turbine combustors often exhibit flamelet-like combustion, but with the drive for increased operating pressures, reduced emissions, and increased power output, their operating point can oscillate between flames that exhibit flamelet and distributed flame behaviour. The need to capture such a vast range of potential operating points encroaches on the limits of current modelling capability and cannot be accurately captured by any single model. Simulation at any specific condition may require different modelling approaches.

There are very few models that have the potential to cope with the complex conditions of modern and future combustors, and even within these models, drawbacks and limitations still exist. Models that use one point statistical descriptions of the turbulent flow, such as the probability density function (PDF) framework of Pope [21], are often better suited for the modelling of complex combustion environments primarily due to their general, regime independent formulation. A major attraction of PDF methods is that through their derivation, they are free from supposed flame structure. The method inherently provides a model-free closure for the chemical reaction rates regardless of combustion regime, and thus, the chemical reaction rates are computed directly. As such, reaction rate dependant phenomena such as quenching and pollutant production are inherently captured within the methodology.

Despite the apparent generality of PDF methods, the trade-off of using this methodology is that they can be much more computationally expensive compared to regime specific models such as flamelet methods [19] or Artificially Thickened Flame (ATF) [14, 22]. Additionally, a particular challenge in the use of PDF methods is simulation of premixed flamelet combustion. In practical premixed reactive flow simulation, the flame normally resides entirely below the numerical grid and many of the physical processes that drive flame propagation (namely scalar mixing, molecular diffusion, and chemical reaction) are unresolved. Even if chemical reaction is solved directly, it remains necessary to model the molecular mixing or *micro-mixing* process within PDF methods. Although reasonably well established, the modelling of the micro-mixing process remains the primary focus of PDF modelling research.

To address the issue of computational expense of PDF methods, simplified solution strategies have been developed. Historically, Lagrangian Monte Carlo methods have been used as a solution strategy for the PDF framework (for example [21]). Recently an Eulerian solution methodology known as the stochastic fields method has emerged having first been introduced by Valiño [23, 24] and then by Sabl'nikov [25]. Some of the benefits of the Eulerian methodology over the Lagrangian particle methodology is the ease of numerical implementation, and ability to use conventional numerical techniques in their solution.

In the context of premixed combustion, stochastic fields has been applied to a variety of combustion configurations (outlined in Section 3.3.4) of which very few have encroached

on the flamelet combustion limit. The logical progression to broaden the validated regime of applicability of the method (and to increase its appeal for widespread industrial use) is to apply stochastic fields to flamelet-combustion configurations. However, as mentioned previously, regardless of the solution strategy employed (Lagrangian or Eulerian) the primary challenge with simulations in this regime remains in determining an adequate closure for the micro-mixing process. To date, premixed stochastic fields simulations have employed relatively simple models for the micro-mixing process and it is unknown if these models are applicable in the flamelet regime in their current form. It is therefore necessary to determine if extending stochastic fields to simulate flamelet combustion would require alternative closures.

Aside from the existing (micro-mixing) modelling challenges of flamelet combustion exhibited by both Eulerian and Lagrangian approaches, an additional aspect of the stochastic field method which is not present in the Lagrangian framework are the discretisation errors. As in all Eulerian methods, the numerical accuracy of the solution depends on the numerical techniques employed to represent the linearised governing equations. A challenge with modelling premixed combustion is the broad range of the magnitude of scalar gradients generated by turbulence and chemical reaction. These gradients must be sufficiently resolved if introduction of numerical errors is to be avoided and correct results (to the level of accuracy of the model) are to be obtained.

For cases with high turbulence intensity (large Karlovitz numbers), turbulent diffusion acts to broaden scalar gradients and can reduce the difficulty in resolving them sufficiently. The resolution of scalar gradients becomes more challenging in flamelet combustion due to dominance of chemical reaction. With increasingly flamelet like conditions (or increasing Damköhler number), scalar gradients further steepen with the most stringent requirements being the resolution of a laminar flame. Therefore, prior to investigating the necessity/benefit of different micromixing closures with the stochastic fields method, the more fundamental issue of resolution requirements and impact on numerical accuracy across the different regimes of turbulent premixed combustion must be addressed. Due to its relative infancy compared to other modelling approaches, a thorough investigation of its limitations and numerical implications of its use have not been reported in academic literature. The primary focus of this work is then:

1. To develop understanding of the numerical resolution requirements of the stochastic field method through simplified and fundamental numerical simulation across a range of premixed combustion conditions.

2. To provide potential avenues for increased computational efficiency and accuracy through formulation and validation of a regime-independent LES-stochastic field methodology that remains numerically accurately across all regimes of premixed combustion.

1.4 Thesis Outline

In this Chapter, a brief introduction to concepts of premixed combustion and turbulence required in this work was presented. Chapter 2 will present the governing equations of fluid flow along with various modelling strategies and closures required for their implementation. More emphasis will be placed on LES as it is the modelling approach used in this work. Chapter 3 presents the turbulent combustion modelling approaches used in this thesis and details the current state of the stochastic field method along with a detailed overview of the different formulations and open questions regarding the method. The final section of Chapter 3 presents the numerical modelling strategy used in this work. Chapter 4 will demonstrate the current capabilities and limitations of the stochastic field method and illustrate a one- and three-dimensional numerical investigation into the numerical resolution requirements. Chapter 5 will build on the conclusions of Chapter 4 and present a numerical framework to mitigate the demanding resolution requirements in the practical use of the stochastic field methodology. Finally, in Chapter 6, the thesis will be concluded with an outline for future work.

Chapter 2

Governing Equation and Numerical Formulation

2.1 Fluid Flow

The evolution of a continuum fluid flow over space and time is described by a set of non-linear, partial differential equations. The non-linearity of these equations arises from the convective transport of momentum, energy and chemical species. Although analytical solutions exist, they are restricted to specific flow conditions and simplified configurations. In more general cases, there do not exist an analytical solutions and therefore numerical solution methods have been employed to solve them. The numerical methods involve discretisation of the equations over a finite set of points within the computational domain. The proceeding equations describe the evolution of a vector/scalar field in a Cartesian coordinate system expressed in Einstein summation notation.

2.1.1 Mass Conservation Equation

The conservation of mass states that no matter can be created or destroyed. The evolution of the mass field is given by

$$\frac{\partial \rho}{\partial t} + \frac{\partial}{\partial x_i}\left(\rho u_i\right) = 0, \tag{2.1}$$

where t is time, x_i is the $i-th$ spatial coordinate, u_i is the velocity component in the $i-th$ direction, and ρ is the density.

2.1.2 Momentum Conservation Equation

Newton's second law states that the rate of change of momentum of a system is equal to the body and surface forces acting on it. The momentum balance can be written as,

$$\frac{\partial}{\partial t}\left(\rho u_i\right) + \frac{\partial}{\partial x_j}\left(\rho u_j u_i\right) = -\frac{\partial p}{\partial x_i} + \frac{\partial \sigma_{ij}}{\partial x_j} + \rho g_i. \tag{2.2}$$

The above equation relates the rate of change of momentum and convective transport to the gravitation acceleration g_i, and the forces given by the viscous stress tensor σ_{ij} and hydrostatic pressure p. For a compressible Newtonian fluid, the components of the stress tensor can be expressed as

$$\sigma_{ij} = \mu\left(\frac{\partial u_j}{\partial x_i} + \frac{\partial u_i}{\partial x_j} - \frac{2}{3}\frac{\partial u_k}{\partial x_k}\delta_{ij}\right), \tag{2.3}$$

where μ is the dynamic viscosity of the mixture which is mainly a function of composition and temperature, and δ_{ij} is the Kronecker delta. The first and second terms represent the isotropic and deviatoric component of the stress tensor respectively. Combining Equation 2.2 and 2.3

$$\frac{\partial}{\partial t}\left(\rho u_i\right) + \frac{\partial}{\partial x_j}\left(\rho u_j u_i\right) = -\frac{\partial p}{\partial x_i} + \frac{\partial}{\partial x_j}\left[\mu\left(\frac{\partial u_j}{\partial x_i} + \frac{\partial u_i}{\partial x_j} - \frac{2}{3}\frac{\partial u_k}{\partial x_k}\delta_{ij}\right)\right] + \rho g_i. \tag{2.4}$$

The complete set of momentum equations in the three coordinate directions are known as the Navier-Stokes equations. Combined with Equation 2.1, they fully describe flow of single component Newtonian fluids.

2.1.3 Species Conservation Equation

When considering reacting flows, in addition to Equations 2.1 and 2.4, additional equations describing the evolution of individual chemical species must be solved. The temporal evolution of the mass fraction, Y, of species α is

$$\frac{\partial}{\partial t}\left(\rho Y_\alpha\right) + \frac{\partial}{\partial x_i}\left(\rho Y_\alpha u_i\right) = -\frac{\partial}{\partial x_i}\left(\rho Y_\alpha V_{\alpha i}\right) + \rho\dot{\omega}_\alpha, \tag{2.5}$$

where Y_α is the mass fraction of the chemical species α, $V_{\alpha i}$ is the $i-th$ component of diffusion velocity, and $\dot{\omega}_\alpha$ is the chemical source term representing the net rate of production/consumption of a species due to chemical reaction. Global mass conservation requires that

$$\sum_{\alpha=1}^{N_\alpha} Y_\alpha V_{\alpha i} = 0. \tag{2.6}$$

The calculation of the diffusion velocities involves inverting an N^2 matrix at every point in space at each instant. This is too computationally demanding for many practical simulation applications. Instead, approximations are often used such as the Hirschfelder and Curtiss [6, 26] approximation, given by

$$V_\alpha X_\alpha = -D_\alpha \frac{\partial X_\alpha}{\partial x_i}, \tag{2.7}$$

where X_α is the mole fraction of species α, and D_α is its diffusion coefficient into the mixture. With the assumption of negligible spatial variation in molecular weight and with the relation between mole and mass fraction

$$Y_\alpha = X_\alpha \frac{W_\alpha}{W}, \tag{2.8}$$

where W_α is the species molecular weight, and W the mixture molecular weight, the diffusion flux can be expressed as

$$Y_\alpha V_{\alpha i} = -\rho D_\alpha \frac{\partial Y_\alpha}{\partial x_i}. \tag{2.9}$$

With unequal species diffusivities, the outstanding issue with this approximation is that it does not satisfy global mass conservation when the diffusion coefficients are not identical. One solution to mitigate this issue is to add a correction velocity, V_{ci}, to Equation 2.9 to enforce mass conservation. Another technique is to apply a correction only to a single species (usually nitrogen in simulations with air) that ensures global mass conservation. However, in the current work, equal species diffusivities is assumed and mass is inherently conserved. More details on correction velocity treatment can be found in [6].

Substituting Equation 2.9 into Equation 2.5 yields the final form of the chemical species transport equation

$$\frac{\partial}{\partial t}\left(\rho Y_\alpha\right) + \frac{\partial}{\partial x_i}\left(\rho Y_\alpha u_i\right) = \frac{\partial}{\partial x_i}\left(\rho D_\alpha \frac{\partial Y_\alpha}{\partial x_i}\right) + \rho\dot{\omega}_\alpha. \tag{2.10}$$

In this formulation, diffusion of species due to temperature gradients (Soret Effects) have been neglected.

2.1.4 Energy Conservation Equation

Depending on the measure of energy employed, the form of the conservation equation takes different forms. For the various definitions and conservation equation forms, refer to [6]. The static enthalpy is comprised of a sensible component and a chemical component through

$$h = \int_T^{T_o} C_p \mathrm{dT} + \sum_{\alpha=1}^{N} Y_\alpha \Delta h_{f,\alpha}, \tag{2.11}$$

where T_o is a reference temperature (usually taken as $298.15K$), $\Delta h_{f,\alpha}$ is the enthalpy of formation of species α. With the common assumption of thermally perfect fluids, the specific heat of the mixture, C_p, is given by

$$C_p = \sum_{\alpha}^{N} Y_\alpha C_{p_\alpha}\left(T\right), \tag{2.12}$$

where C_{p_α} is the specific heat of the individual species.

The energy balance equation can be written as

$$\frac{\partial}{\partial t}\left(\rho h\right) + \frac{\partial}{\partial x_i}\left(\rho h u_i\right) = \frac{\partial p}{\partial t} + \tau_{ij}\frac{\partial u_i}{\partial x_i} + \dot{q} - \frac{\partial q_i}{\partial x_i}. \tag{2.13}$$

where $\dot{q}$ is a source term (radiation, spark, etc.), the first and second term on the RHS represents the temporal evolution of pressure, and viscous heating respectively. In low Mach number flows, they can be neglected [27]. The enthalpy flux q_i in the last term on the RHS is given by

$$q_i = -\lambda\frac{\partial T}{\partial x_i} + \rho\sum_{\alpha=1}^{N} h_\alpha Y_\alpha V_\alpha. \tag{2.14}$$

The first term represents heat diffusion by Fourier's Law and the second represents enthalpy flux generated by diffusion of species with different enthalpies. λ is the thermal

conductivity of the mixture and is calculated through imposition of a mixture Prandtl number

$$\lambda = \frac{\mu C_p}{Pr}. \tag{2.15}$$

Additionally, the second term on the RHS of Equation 2.14 is zero for equal species diffusivities. Thus, Equation 2.14 becomes

$$q_i = \frac{-\mu}{Pr}\frac{\partial h}{\partial x_i}. \tag{2.16}$$

With all the assumptions and neglecting of terms for low Mach number formulations, the final form of the enthalpy equations is

$$\frac{\partial}{\partial t}(\rho h) + \frac{\partial}{\partial x_i}(\rho h u_i) = \frac{\partial}{\partial x_i}\left[\frac{\mu}{Pr}\frac{\partial h}{\partial x_i}\right] + \dot{q}. \tag{2.17}$$

2.1.5 Equation of State

The equation of state provides the final equation required to close the system of equations fully describing fluid flow. It relates the local composition, temperature, and pressure to the density. In this work, an ideal gas is assumed and thus, the equation is

$$\rho = \frac{P W_{mix}}{R_u T}, \tag{2.18}$$

where P is the pressure, T is the temperature, R_u is the universal gas constant (8.315 kJ/kmol-K), and W_{mix} the molecular weight of the mixture determined through

$$\frac{1}{W} = \sum_{k=1}^{N_\alpha} \frac{Y_k}{W_k}, \tag{2.19}$$

where W_k is the species molecular weight.

2.2 Turbulence Modelling

The three main methods of computationally evaluating the governing equations presented in Section 2.1 are *Direct Numerical Simulation* (DNS), *Reynolds Averaged Navier Stokes* (RANS), and *Large Eddy Simulation* (LES). RANS and LES introduce models

for some or all turbulent processes, and they reduce numerical effort needed in the simulation. The main advantage of the modelling approaches of RANS and LES is the flexibility to simulate a specific application with a reduced computational effort, while choosing the amount of detail to be modelled. In the following section the three main approaches for simulating turbulent flow will be described along with their advantages and disadvantages, with the most emphasis being be placed on LES.

2.2.1 Direct Numerical Simulation (DNS)

DNS aims to resolve all scales of turbulence: from the large integral scales to the small Kolmogorov scale. Since all scales are resolved, no modelling of any turbulent scale is necessary. However, as a consequence, very fine computational meshes are required in order to capture the resolve these small scales whose size follow the relationship given in Section 1.2 as

$$\frac{L_t}{\eta} = Re^{3/4} \tag{2.20}$$

Since for industrially applicable turbulent flows, Reynolds numbers can be on the order of $10^5 \sim 10^6$, the scales requiring full resolution will be very small. The number of grid points for a three dimensional computational grid would therefore need to be on the order of $Re^{9/4}$. This means for a Reynolds number of 10^5, the number of computational cells would be on the order of 2×10^{11}. In addition to spatial resolution, DNS requires adequate temporal resolution. As the time-step should be such to resolve the smallest characteristic timescale, a large number of iterations is usually required to complete a simulation.

For reactive flows the computational cost increases further. First, the use of detailed chemical mechanisms increases the number of scalar transport equations that need to be solved. The spatial requirements also increase as the reaction zone (in the premixed flames for example) needs to be resolved with sometimes up to 20 grid points. Finally, the chemical time-scales become the limiting time-scale requiring resolution and usually limit the time-step by several orders of magnitude compared to chemically inert DNS.

Coupled together, the total computational requirement to simulate a moderate Reynolds number reacting flows for a short time can be prohibitive with the current available computing power. Therefore, the applications for DNS are limited to low Reynolds

flow with extremely simple geometries. Apart from the tremendous computational cost required by DNS, it is the most accurate form of simulating turbulent flows. It is often used to validate academic test cases, or to provide data for the development and validation of lower fidelity turbulence modelling methods.

2.2.2 Reynolds Averaged Navier-Stokes

Reynolds Averaged Navier-Stokes (RANS) is the oldest simulation approach and the most commonly used for simulating industrial applications. The main difference between RANS and DNS is the manner in which they solve the flow. In DNS the turbulent flow field is fully resolved and transient. The premise behind RANS is to take advantage of the statistical nature of turbulence and generate a solution of the temporally averaged flow field.

The field variables can be decomposed into time averaged mean ($\overline{\phi}$) and fluctuating components (ϕ')

$$\phi\left(\mathbf{x},t\right)=\overline{\phi}\left(\mathbf{x}\right)+\phi'\left(\mathbf{x},t\right). \tag{2.21}$$

This methodolgy can be applied to time average the governing equation. However, this process generates a number of unclosed terms e.g the Reynolds stresses $\left(\overline{u_i'u_j'}\right)$; the core challenge in the RANS methodology is providing a closure for this term.

The Reynolds stress term is closed by invoking a gradient transport hypothesis requiring specification of a turbulent viscosity. There are three common approaches to model the turbulent viscosity: Algebraic, one- and two- equation models. In the one equation model of Spalart-Allmaras [28], an additional transport equation for turbulent kinetic energy (k) is solved. In the two equation models, in addition to k, the $k-\epsilon$ approach [29] transports the energy dissipation rate (ϵ), and the $k-\omega$ approach [30] transports the specific dissipation rate (ω). Algebraic models do not solve any additional equations but use relatively simple algebraic expressions to link unknown quantities [31, 32].

The resolution of the Reynolds-averaged properties in RANS lends itself to having a much coarser computational domain than DNS, making it more computationally affordable. However, solving only the Reynolds-averaged properties provides limited information on turbulence and transient processes which may be significant in certain applications such as combustion.

2.2.3 Large Eddy Simulation (LES)

A compromise between accuracy and computational cost between the two extremes of fully resolved DNS and mean flow modelling of RANS is Large Eddy Simulation (LES). The premise of LES is to filter the flow field by applying a predetermined filter of width, Δ, to the governing equations.

This filtering procedure operates as a low-pass (wavenumber) filter. It removes the explicit integration of smaller turbulent scales (higher wavenumber) while the large scale turbulent structures are fully resolved. This process is depicted in Figure 2.1 for different size filters. The result of the filtering process on the governing equations is a three dimensional, time-dependant solution. However, similar to RANS, the filtering procedure results in the generation of unclosed Reynolds stress terms that require modelling.

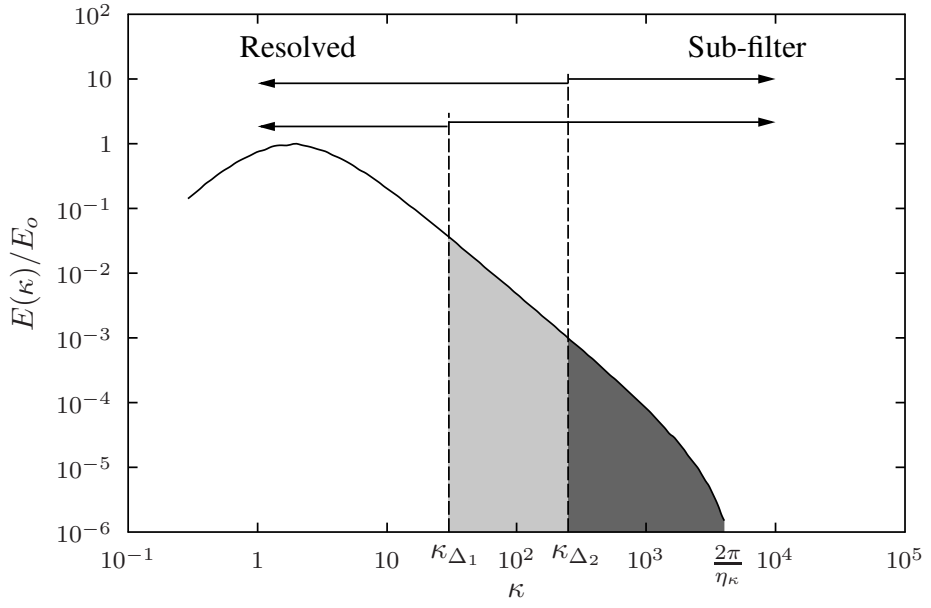

FIGURE 2.1: Resolved and sub-filter ranges on the turbulence spectrum for different filter sizes. κ_Δ represents the filter size specific cut-off wavenumber

It is suggested that the filter used be selected such that 80% of the turbulent kinetic energy is resolved [11]. As such, the filter width usually lies in the inertial range of turbulence where it is generally accepted to be isotropic allowing for simplified closures of the Reynolds stresses compared to the RANS framework. The modelling of the small, unresolved, turbulent scales comes from relations known as *sub-filter scale* models (SFS) which act as small scale turbulence models for the flow. In Figure 2.1, since $\Delta_1 > \Delta_2$, the use of Δ_2 results in a more *physically* resolved flow field. A larger portion of the

turbulent scales are resolved and a smaller portion of turbulent scales require modelling with the SFS models.

Since LES requires filters to (at least) be in the inertial range, the computational grids can be coarser than than DNS but are more refined than RANS. This enables LES to simulate more complex, higher Reynolds number flows for a lower computational cost than that of simulating a similar flow with DNS.

Filtering

The process of filtering involves convolution of a filter function G, with some arbitrary function $f(x)$. In LES, the procedure of separating the resolved large scale structures and filtering out the small scales requires a low pass filtering operation to be conducted on the governing equations through convolution with some arbitrary filter function. The result of this operation is a set of equations describing spatially filtered values. A more complete overview of the filtering operation can be found in Garner *et al.* [33].

The filtering operation of a quantity, ϕ, is given by

$$\overline{\phi}\left(\underline{x},t\right)=\int_{-\infty}^{+\infty}\phi\left(\underline{x}',t\right)G\left(\underline{x}-\underline{x}',\Delta\right)\mathrm{d}\underline{x}', \tag{2.22}$$

where in a similar manner to the Reynolds decomposition, a decomposition can be obtained for the filtered value as

$$\phi=\overline{\phi}+\phi', \tag{2.23}$$

where ϕ' represents the sub-filter fluctuation.

In LES, there are two filtering approaches. With the explicit filter, the filtering process is conducted as an additional step in the solution procedure. The filter type (shape and size) are determined *a priori* and can be independent of the computational mesh. The second approach is an implicit filtering method. In this method the computational grid (and discretisation operators) act as the filter. The primary difference between the explicit and implicit filtering methods is the explicit dependence on the numerical grid spacing ($\Delta=\Delta_x$) for the implicit filtering technique. The differences between the explicit and implicit filters are shown schematically in Figure 2.2. For the explicit filter, an arbitrary number of computational cells is chosen for illustrative purposes.

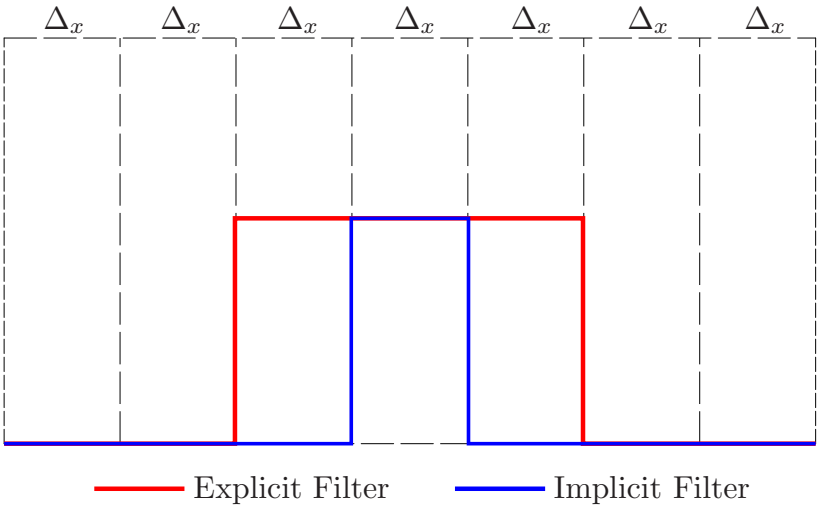

FIGURE 2.2: One-dimensional schematic comparing explicit and implicit filter.

To illustrate the implications of the different filtering methods, a simplified example can be given for the case of a filtered linear advection equation of an arbitrary scalar, ϕ:

$$\frac{\partial \overline{\phi}}{\partial t} = -\overline{u}\frac{\partial \overline{\phi}}{\partial x} + \mathcal{T}_{sfs}(\Delta), \tag{2.24}$$

where in the above equation, $\mathcal{T}_{sfs}(\Delta)$ represents a sub-filter term that accounts for unresolved scales on the evolution of the filtered scalar. Its magnitude is shown to be dependant on the size of the filter width. If this equation is discretised on an arbitrary numerical grid through Taylor expansion with a first order upwind scheme, the result is

$$\frac{\partial \overline{\phi}}{\partial t} = -\overline{u}\frac{\overline{\phi}_i^n - \overline{\phi}_{i-1}^n}{\Delta_x} + \mathcal{T}_{sfs}(\Delta) + \mathcal{O}(\Delta_x). \tag{2.25}$$

Ignoring any influence of temporal discretisation that would be required to evolve the filtered scalar in time, truncation (or numerical) error has been introduced ($\mathcal{O}(\Delta_x)$) due to the discrete approximation of the continuous spatial derivatives on a finite numerical grid. To varying degrees, these truncation errors can manifest themselves as artificial diffusion or dispersion errors [34]. In order to reduce the numerical error, higher order discretisation schemes may be used, or the numerical grid spacing can be reduced.

Considering the explicit filtering method, reducing the grid spacing with a fixed filter size reduces the truncation error leaving the magnitude of $\mathcal{T}_{sfs}(\Delta)$ unchanged. In the case of implicit filtering, or $\Delta = \Delta_x$, any modifications to the grid spacing also changes

the filter size. The new discretised equation then becomes:

$$\frac{\partial \overline{\phi}}{\partial t} = -\overline{u}\frac{\overline{\phi}_i^n - \overline{\phi}_{i-1}^n}{\Delta_x} + \mathcal{T}_{sfs}(\Delta_x) + \mathcal{O}(\Delta_x), \tag{2.26}$$

where the dependency of the sub-filter term has now been changed to the local numerical grid spacing. With this filtering technique, changes in grid spacing influence both the sub-filter modelling component and the truncation error concurrently. This difference is shown in Figure 2.3. This figure shows that reducing Δ_x by half leaves the overall size of the explicit filter unchanged but reduces the implicit filter by the same amount.

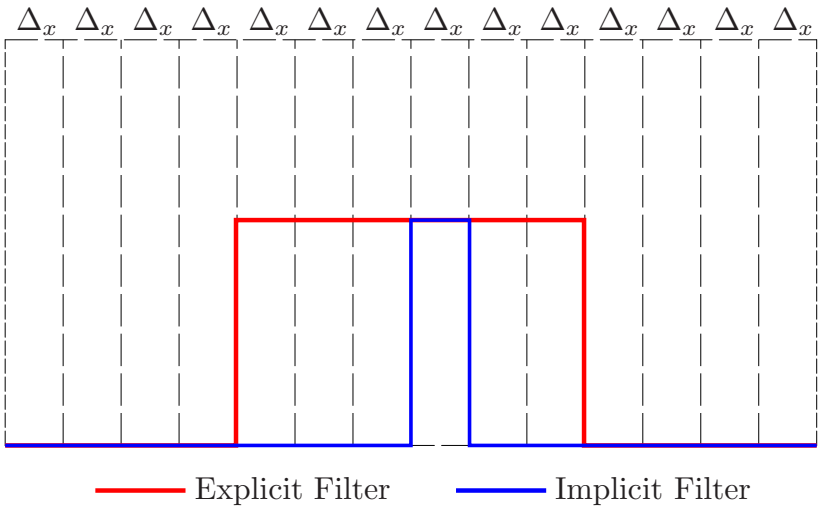

FIGURE 2.3: One-dimensional schematic comparing explicit and implicit filters with refined numerical grid.

Recalling Figure 2.1, different filter sizes result in different physical resolution of the simulation. Thus, the primary challenge with the implicit filtering technique is that changes in numerical grid spacing modifies both physical and numerical resolution concurrently; distinguishing between these two effects within a solution becomes difficult. Nevertheless, due to: 1) the reduced computational cost of the implicit filtering method over the explicit method, and 2) the fine numerical grid resolution and higher order numerical schemes of modern LES, the implicit LES methodology is commonly used.

In the implicit filtering method, for irregular numerical grids, an effective filter width is calculated by

$$\Delta = (\Delta_x \Delta_y \Delta_z)^{1/3}. \tag{2.27}$$

With this, the implicit filter takes on a top-hat distribution given by

$$G\left(\underline{x}-\underline{x}',\Delta\right)=\begin{cases}\prod_{j=1}^{3}\frac{1}{\Delta_j} & |\underline{x}-\underline{x}'|\leq\frac{\Delta}{2}\\ 0, & |\underline{x}-\underline{x}'|>\frac{\Delta}{2}\end{cases} \tag{2.28}$$

where $\prod_{j=1}^{3}\frac{1}{\Delta_j}$ corresponds to a volume averaging of the computational CFD cell.

Favre Filtering

In the case of variable density flows, to avoid treatment of density fluctuation that arise due to filtering, a mass-weighting can be introduced. This procedure is known as Favre filtering and is defined by

$$\overline{\rho}\tilde{\phi}\left(\underline{x},t\right)=\int_{-\infty}^{+\infty}\rho\phi\left(\underline{x}',t\right)G\left(\underline{x}-\underline{x}',\Delta\right)\mathrm{d}\underline{x}', \tag{2.29}$$

and can also be written as

$$\overline{\rho}\widetilde{\phi}=\overline{\rho\phi}. \tag{2.30}$$

Similarly, the decomposition of the density-weighted scalar into a filtered part and sub-filter fluctuation yields

$$\phi=\widetilde{\phi}+\phi''. \tag{2.31}$$

2.3 Filtered Governing Equations

The process of filtering the governing equations requires the use of three fundamental filtering properties:

1. The filtering of a constant, yields the constant: $\overline{b}=b$
2. Linearity of the filtering operator: $\overline{\phi+\psi}=\overline{\phi}+\overline{\psi}$
3. For smoothly varying filter function - Commutation with differentiation:

$$\frac{\overline{\partial\phi}}{\partial x}=\frac{\partial\overline{\phi}}{\partial x.} \tag{2.32}$$

With Favre filtering, due to the presence of density, the filtering operator does not commute with differentiation as it does for conventional filtering. However, if density variations are assumed small then the commutation property is assumed valid.

$$\widetilde{\frac{\partial \phi}{\partial x}} \approx \frac{\partial \widetilde{\phi}}{\partial x} \tag{2.33}$$

2.3.1 Filtered Continuity Equation

Assuming a smoothly varying, arbitrary filter function with fixed filter scale, the continuity equation (Equation 2.1) becomes

$$\frac{\partial \overline{\rho}}{\partial t} + \frac{\partial}{\partial x_i}\left(\overline{\rho u_i}\right) = 0. \tag{2.34}$$

Applying the Favre filter relation yields

$$\frac{\partial \overline{\rho}}{\partial t} + \frac{\partial}{\partial x_i}\left(\overline{\rho}\widetilde{u_i}\right) = 0. \tag{2.35}$$

2.3.2 Filtered Momentum Equation

The filtered momentum equation can be written as

$$\frac{\partial}{\partial t}\left(\overline{\rho u_i}\right) + \frac{\partial}{\partial x_j}\left(\overline{\rho u_j u_i}\right) = -\frac{\partial \overline{p}}{\partial x_i} + \frac{\partial \overline{\sigma}_{ij}}{\partial x_j} + \overline{\rho} g_i. \tag{2.36}$$

Applying the Favre filter relation yields

$$\frac{\partial}{\partial t}\left(\overline{\rho}\widetilde{u_i}\right) + \frac{\partial}{\partial x_j}\left(\overline{\rho}\widetilde{u_j u_i}\right) = -\frac{\partial \overline{p}}{\partial x_i} + \frac{\partial \hat{\sigma}_{ij}}{\partial x_j} + \frac{\partial}{\partial x_j}\left(\overline{\sigma}_{ij} - \hat{\sigma}_{ij}\right) + \overline{\rho} g_i, \tag{2.37}$$

where the hat is not a filter operator but denotes a quantity based on filtered values. Thus, $\hat{\sigma}_{ij}$ is the stress tensor based on Favre filtered values

$$\hat{\sigma}_{ij} = \mu\left(\frac{\partial \widetilde{u_j}}{\partial x_i} + \frac{\partial \widetilde{u_i}}{\partial x_j} - \frac{2}{3}\frac{\partial \widetilde{u_k}}{\partial x_k}\delta_{ij}\right). \tag{2.38}$$

The unknown velocity correlation, $\overline{\rho}\widetilde{u_j u_i}$, can be decomposed as

$$\overline{\rho}\widetilde{u_j u_i} = \overline{\rho}\widetilde{u_j}\widetilde{u_i} + \widetilde{\tau}_{ij}^{sgs}, \tag{2.39}$$

where $\widetilde{\tau}_{ij}^{sfs} = \overline{\rho}\widetilde{u_i'' u_j''}$ is the sub-filter stress tensor (Reynolds stresses) and requires modelling. Following [35], $(\overline{\sigma}_{ij} - \hat{\sigma}_{ij})$ was shown to be at least an order of magnitude smaller than $\widetilde{\tau}_{ij}^{sfs}$ and is neglected.

The final unclosed form of the Favre filtered Navier-Stokes equations is

$$\frac{\partial}{\partial t}\left(\overline{\rho}\widetilde{u_i}\right) + \frac{\partial}{\partial x_j}\left(\overline{\rho}\widetilde{u_j}\widetilde{u_i}\right) = -\frac{\partial \overline{p}}{\partial x_i} + \frac{\partial}{\partial x_j}\left(\hat{\sigma}_{ij} - \widetilde{\tau}_{ij}^{sfs}\right) + \overline{\rho} g_i. \tag{2.40}$$

2.3.3 Filtered Species Conservation Equation

In the governing equation section above, the final form of the species transport equation in Equation 2.10 and enthalpy transport in Equation 2.17 are similar. As such they can be expressed in terms of a general reactive scalar ϕ as

$$\frac{\partial}{\partial t}\left(\rho\phi\right) + \frac{\partial}{\partial x_i}\left(\rho\phi u_i\right) = \frac{\partial}{\partial x_i}\left(\rho D_\alpha \frac{\partial \phi}{\partial x_i}\right) + \dot{\omega}. \tag{2.41}$$

The filtered reactive scalar equation is given by

$$\frac{\partial}{\partial t}\left(\overline{\rho\phi}\right) + \frac{\partial}{\partial x_i}\left(\overline{\rho\phi u_i}\right) = \frac{\partial}{\partial x_i}\left(\overline{\rho D_\alpha \frac{\partial \phi}{\partial x_i}}\right) + \overline{\dot{\omega}}. \tag{2.42}$$

The Favre filtered reactive scalar conservation equation can then be written as

$$\frac{\partial}{\partial t}\left(\overline{\rho}\widetilde{\phi}\right) + \frac{\partial}{\partial x_i}\left(\widetilde{\overline{\rho\phi u_i}}\right) = \frac{\partial}{\partial x_i}\left(\overline{\rho}\overline{D}\frac{\partial \widetilde{\phi}}{\partial x_i}\right) + \overline{\dot{\omega}}, \tag{2.43}$$

where the filtered diffusion flux has been approximated by [6]

$$\overline{\rho D \frac{\partial \phi}{\partial x_i}} = \overline{\rho}\widehat{D}\frac{\partial \widetilde{\phi}}{\partial x_i}, \tag{2.44}$$

where $\widehat{D}$ is a representative diffusion coefficient based on the favre filtered thermochemical state: molecular diffusion for species and thermal diffusion for enthalpy.

In a similar manner to the Navier-Stokes Equations, $\overline{\rho}\widetilde{\phi}\widetilde{u_i}$ can be decomposed as

$$\widetilde{\overline{\rho\phi u_i}} = \overline{\rho}\widetilde{\phi}\widetilde{u_i} + \overline{\rho}\widetilde{\phi'' u_i''}. \tag{2.45}$$

With substitution into Equation 2.43, the unclosed filtered species equation can be written as

$$\frac{\partial}{\partial t}\left(\overline{\rho}\widetilde{\phi}\right)+\frac{\partial}{\partial x_i}\left(\overline{\rho}\widetilde{\phi}\widetilde{u}_i\right)=\frac{\partial}{\partial x_i}\left(\rho D_\alpha\frac{\partial\widetilde{\phi}}{\partial x_i}+\overline{\rho}\widetilde{\phi''u_i''}\right)+\overline{\dot{\omega}}. \tag{2.46}$$

2.3.4 Closures for Governing Equations

The filtering operation shown above resulted in the generation of unknown terms such as the scalar fluxes: $\overline{\rho}\widetilde{u_i''u_j''}$, $\overline{\rho}\widetilde{\phi''u_i''}$, and $\overline{\dot{\omega}_\alpha}$. As these terms cannot be directly calculated from the flow field and they must be modelled.

2.3.4.1 Sub-filter Stress Modelling

The unclosed term pertaining to the filtered Navier-Stokes equation, $\overline{\rho}\widetilde{u_i''u_j''}$, is often closed with an eddy-viscosity model. Eddy viscosity models makes use of the Boussinesq approximation relating mean flow properties to turbulent stresses. Since at the smallest scales of turbulence, turbulent kinetic energy is dissipated by viscous stresses, the eddy-viscosity models approximates the sub-filter stress tensor (τ_{ij}^{sfs}) by a sub-filter viscosity (μ_{sfs}). Generally, eddy viscosity models are computationally inexpensive and have numerically stabilizing properties. The more popular eddy-viscosity model in LES is the Smagorinksy model [36].

The sub-filter stress tensor is represented as

$$\widetilde{\tau}_{ij}=\mu_{sfs}\left(\frac{\partial\widetilde{u_j}}{\partial x_i}+\frac{\partial\widetilde{u_i}}{\partial x_j}-\frac{2}{3}\frac{\partial\widetilde{u_k}}{\partial x_k}\delta_{ij}\right)+\frac{1}{3}\tau_{kk}\delta_{ij}. \tag{2.47}$$

Substituting this equation into Equation 2.40 and using Equation 2.38 yields

$$\frac{\partial}{\partial t}\left(\overline{\rho}\widetilde{u_i}\right)+\frac{\partial}{\partial x_j}\left(\overline{\rho}\widetilde{u_j}\widetilde{u_i}\right)=-\frac{\partial\overline{P}}{\partial x_i}+\frac{\partial}{\partial x_j}\left[\left(\mu+\mu_{sfs}\right)\left(\frac{\partial\widetilde{u_j}}{\partial x_i}+\frac{\partial\widetilde{u_i}}{\partial x_j}-\frac{2}{3}\frac{\partial\widetilde{u_k}}{\partial x_k}\delta_{ij}\right)\right]+\overline{\rho}g_i, \tag{2.48}$$

where for low Mach number flows, the unknown trace of the sub-filter stress tensor is absorbed into a pseudo-pressure term

$$\overline{P}=\overline{p}+\frac{1}{3}\tau_{kk}\delta_{ij}. \tag{2.49}$$

The Smagorinksy model provides the sub-filter viscosity (μ_{sgs}) as

$$\mu_{sfs} = \overline{\rho} C_s \Delta^2 \sqrt{2\widetilde{S_{ij}}\widetilde{S_{ij}}}, \tag{2.50}$$

where C_s is the Smagorinksy constant, Δ is the filter width, and $\widetilde{S_{ij}}$ is the filtered rate-of strain tensor given by

$$\widetilde{S_{ij}} = \frac{1}{2}\left(\frac{\partial \widetilde{u_j}}{\partial x_i} + \frac{\partial \widetilde{u_i}}{\partial x_j}\right). \tag{2.51}$$

The Smagorinksy model generally gives good predictions of dissipation, but was shown to be too dissipative in certain areas such as in transitional flow, flows with discontinuities, and near walls. This is primarily associated with the Smagorinksy constant being uniform in all regions of the flow. A more flexible approach is to dynamically calculate the constant. The Dynamic-Smagorinksy model [37, 38] uses the scale similarity hypothesis to infer information about the smallest resolved scales though a test-filtering procedure which is then used to dynamically calculate the constant.

An additional method to bypass this excess dissipation was to neglect the SGS models all together. This method is known as the Implicit Large Eddy Simulation (ILES). ILES attempts to use the truncation error and the numerical viscosity generated by numerical discretisation errors in place of the sub-filter viscosity model that the Classic LES modelling uses [39]. This method however, has problems of its own. Its behaviour depends on the numerical scheme used, more specifically, the spectral properties of the truncation error generated. An example of such numerical formulations is available in Thornber *et al.* [40].

2.3.4.2 Scalar Flux Closure

The chemical species interpretation of the Favre filtered reactive scalar transport equation (Equation 2.46) leads to the unclosed turbulent scalar flux, $\overline{\rho}\widetilde{Y_\alpha'' u_i''}$. This term is commonly modelled though a gradient transport assumption by

$$\overline{\rho}\widetilde{Y_\alpha'' u_i''} = -\overline{\rho}\frac{\mu_{sgs}}{Sc_t}\frac{\partial \widetilde{Y_\alpha}}{\partial x_i}, \tag{2.52}$$

where μ_{sgs} is the turbulent viscosity provided by Equation 2.50 and Sc_t is the turbulent Schmidt number. It should be mentioned that in weakly turbulent premixed flames, in

the presence of heat release generated pressure gradients, counter-gradient diffusion has been observed. Therefore, the standard gradient diffusion closure may not always be applicable [6, 41].

2.3.4.3 Energy Equation Closures

For the enthalpy interpretation of Equation 2.46, the enthalpy flux is closed with a gradient transport assumption in a similar form to the scalar flux term described above.

$$\overline{\rho}\widetilde{h''u_i''} = -\overline{\rho}\frac{\mu_{sgs}}{Pr_t}\frac{\partial\widetilde{h}}{\partial x_i}, \tag{2.53}$$

where Pr_T is the turbulent Prandtl number, and c_p is the mixture specific heat at constant pressure.

Chapter 3

Turbulent Premixed Combustion Modelling and Numerical Framework

3.1 LES Turbulent Premixed Combustion Models

The highly non-linear nature of the reaction source term means that composition and temperature fluctuations have a substantial impact on the filtered reaction rate. Therefore, simply evaluating the source term with filtered quantities can lead to substantial errors in the predicted chemical source term. In general

$$\overline{\omega_\alpha \left(\underline{Y}, T\right)} \neq \omega_\alpha \left(\overline{\underline{Y}}, \overline{T}\right), \tag{3.1}$$

where $\underline{Y}$ is a mass fraction vector, T is temperature and $\overline{\dot{\omega}_\alpha}$ is the reaction rate appearing in Equation 2.46. As such, the effect of sub-filter fluctuations on the closure of the filtered reaction rate source term needs to be modelled.

An additional challenge in the modelling of turbulent premixed combustion is that under certain numerical (and physical) configurations, the flame may exist entirely sub-filter. This may not be strictly an issue if there are a sufficient number of computational cells in a given filter width, however, in typical LES simulations the assumption that the filter scale is equal to the numerical grid spacing ($\Delta = \Delta_x$) results in a change from unburnt

to burnt composition over a range of the order of one filter width. Poor resolution of the gradient across the flame can lead to numerical diffusion, enhancing burning velocity [41]. Even if the preheat zone is captured adequately, the reaction zone still requires proper resolution which may not be possible for large filter widths. As this region can be an order of magnitude smaller than the preheat zone, it places more stringent criteria on the mesh/filter requirement for full resolution.

To help identify the turbulence-flame interactions that exist below the filter-scale (or sub-filter combustion regime), the regime diagram shown in Figure 1.5 was modified by Pitsch [41] to account for computational parameters replacing the integral length scale parameters by those at thee LES filter-width, Δ. The updated figure is shown in Figure 3.1

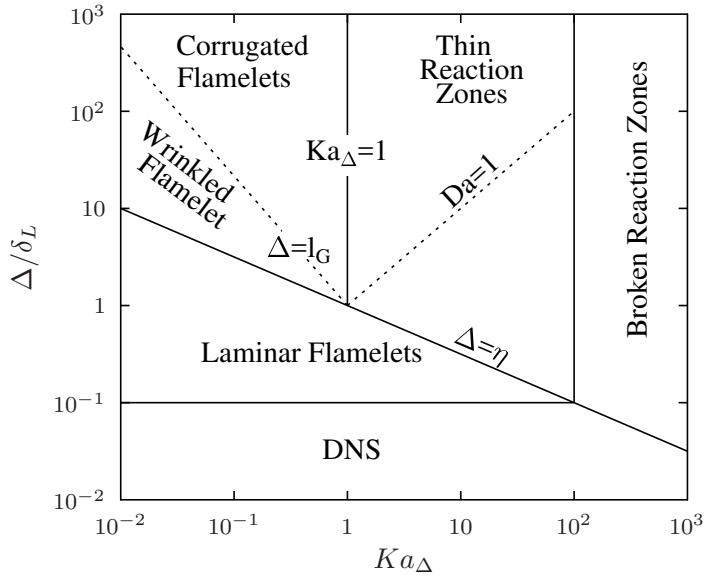

FIGURE 3.1: Premixed combustion regime diagram

Where the numerical configuration of the LES simulation resides on this diagram influences the choice of combustion model that can/should be used as different models have different inherent fundamental assumptions in their derivation. For details and reviews of the available models refer to [6, 41–43] and references therein.

In the proceeding sections, an overview will be given for the Artificially Thickened Flame (ATF) model, and probability density function methods (PDF). In this section, more detail will be provided for the ATF model as elements of this model are used in

Chapter 5 and a detailed discussion of PDF methods that are the focus of this thesis will be presented in Section 3.2.

3.1.1 Artificially Thickened Flame (ATF)

The approach of the artificially thickened flame model is to accurately propagate a flame on a coarse grid, and was first proposed by Butler and O'Rourke [44]. The unresolved flame is thickened by a factor, F, to allow adequate flame resolution on typical LES grids while maintaining the laminar flame speed. The thickening factor scales the unresolved flame as

$$\delta_L^1 = F\delta_L^0, \tag{3.2}$$

where δ_l^1 is the thickness of the thickened flame, δ_L^0 is the unthickened flame thickness, and F is the thickening factor. F is determined by

$$F = \frac{n\Delta_x}{\delta_L^0}, \tag{3.3}$$

and is a function of the local numerical grid spacing, Δ_x, and the desired number of grid points across the laminar flame, n. This value of n is limited by the number of grid points required to resolve all species (major and radicals) within the reaction zone. The ATF model thickens the flame by increasing the diffusion coefficient of species and temperature by the thickening factor, but maintains the laminar flame speed by reducing the reaction rate by the same thickening factor. This behaviour can be illustrated through Equation 3.4 where if a one-step reaction mechanism is employed for the reaction rate constant, then

$$s_L^1 \propto \left(D_{th}^1 R^1\right) =\propto \left(D_{th}^0 F \frac{R^0}{F}\right) = s_L^o \tag{3.4}$$

where the superscript "1" denotes the thickened properties.

The thickened species transport equation is given as

$$\frac{\partial}{\partial t}\left(\rho Y_\alpha\right) + \frac{\partial}{\partial x_i}\left(\rho Y_\alpha u_i\right) = \frac{\partial}{\partial x_i}\left(\rho F D_\alpha \frac{\partial Y_\alpha}{\partial x_i}\right) + \frac{1}{F}\dot{\omega}_\alpha. \tag{3.5}$$

In turbulent flows, the thickening procedure modifies how the flame interacts with turbulence. This can be illustrated through the modification of the nominal Damköhler

number $\left(Da^0\right)$. From Equation 1.15, the modified Damköhler number becomes

$$Da^1 = \frac{L_T}{u'}\frac{s_L^0}{\delta_L^1} = \frac{Da^0}{F}. \tag{3.6}$$

Thus, with thickening comes a reduction in Da by the factor F. The consequence of this is that the flame fronts become less sensitive to resolved scale turbulent motions and more sensitive to strain effects.

With artificial thickening, turbulent scales smaller than $F\delta_L^o$ no longer interact with the flame and structures larger than $F\delta_L^o$ may have a reduced ability to interact with it. This artificial suppression of smaller scale wrinkling will modify the total flame surface area of the flame influencing the resultant turbulent flame speed. To account for this, the loss of flame surface wrinkling due to artificial thickening is counteracted by the introduction of an efficiency factor E. Equation 3.5 becomes

$$\frac{\partial}{\partial t}\left(\rho Y_\alpha\right) + \frac{\partial}{\partial x_i}\left(\rho Y_\alpha u_i\right) = \frac{\partial}{\partial x_i}\left(\rho F E D_\alpha \frac{\partial Y_\alpha}{\partial x_i}\right) + \frac{E}{F}\dot{\omega}_\alpha. \tag{3.7}$$

The efficiency factor is a parameter that takes into account the effect of unresolved turbulence on the flame by evaluating unresolved flame surface generation (or sub-filter wrinkling). It is defined as

$$E = \frac{\Xi(\delta_L^0)}{\Xi(\delta_L^1)}, \tag{3.8}$$

where $\Xi(\delta_L^1)$ represents the sub grid scale wrinkling factor of the thickened flame, and $\Xi(\delta_L^0)$ represents the sub grid scale wrinkling factor of the unthickened flame. Various authors [14, 22, 45] have proposed different algebraic models for computing this wrinkling factor as functions of local thermo-physical properties such as u', s_L, and filter scale Reynolds number Re_Δ.

Charlette *et al.* [14] adopted a power-law dependence of sub-grid wrinkling yielding a sub-filter wrinkling factor of

$$\Xi = \left(1 + \min\left[\frac{\Delta}{\delta_L^0}, \Gamma\left(\frac{\Delta}{\delta_L^0}, \frac{u'_\Delta}{s_L^0}, Re_\Delta\right)\frac{u'_\Delta}{s_L^0}\right]\right)^\beta, \tag{3.9}$$

where the effective straining function Γ is

$$\Gamma\left(\frac{\Delta}{\delta_L^0}, \frac{u'_\Delta}{s_L^0}, Re_\Delta\right) = [((f_u^{-a} + f_\Delta^{-a})^{-1/a})^{-b} + f_{Re}^{-b}]^{-1/b}, \tag{3.10}$$

and,

$$f_u = 4\left(\frac{27C_k}{110}\right)^{1/2}\left(\frac{18C_k}{55}\right)\left(\frac{u'_\Delta}{s_l^0}\right)^2, \tag{3.11}$$

$$f_\Delta = \left[\frac{27C_k\pi^{4/3}}{110}\times\left(\left(\frac{\Delta}{\delta_L^0}\right)-1\right)\right]^{1/2}, \tag{3.12}$$

$$f_{Re} = \left[\frac{9}{55}\exp\left(-\frac{3}{2}C_k\pi^{4/3}Re_\Delta^{-1}\right)\right]^{1/2}\times Re_\Delta^{1/2}, \tag{3.13}$$

with

$$\begin{aligned} a &= 0.60 + 0.20\exp[-0.1(u'_\Delta/s_L^0)] - 0.2\exp[-0.01\Delta/\delta_L^0], \\ b &= 1.4 \end{aligned} \tag{3.14}$$

In deriving their model, Charlette *et al.* [14] assumed that $\Delta/\delta_L^0 \gg 1$ however, with the computational meshes of today, this criteria is not always satisfied and was relaxed in the modification of Wang *et al.* [46]. The modified form of Equation 3.9 is

$$\Xi = \left(1+\min\left[\frac{\Delta}{\delta_l^0}-1, \Gamma\left(\frac{\Delta}{\delta_L^0}, \frac{u'_\Delta}{s_L^0}, Re_\Delta\right)\frac{u'_\Delta}{s_L^0}\right]\right)^\beta. \tag{3.15}$$

Some attractive features of ATF are its relatively cheap computational cost, simple implementation into codes, and the ability for chemistry to be evaluated directly from Arrhenius rate expressions. Additionally, this modelling approach correctly recovers the DNS limit in the case of decreasing filter size.

However, some of its drawbacks are that with complex chemical mechanisms producing thin layers of combustion radicals, the thickening factor may need to be quite large. Additionally, with a constant thickening factor, unphysical alterations in heat and species transport may occur away from the flame. To overcome this last issue, the Dynamically Thickened Flame (DTF) approach [46, 47] may be used, or the use of flame sensors [48, 49] to dynamically turn on thickening only in the presence of flames.

3.2 Transported PDF Method

The Transported Probability Density Function (PDF) approach represents one of the more advanced approaches for turbulent combustion modelling and works by solving a transport equation for a joint-PDF. Its derivation is free from assumptions regarding flame structure and it simulates the evolution of the one-point, one time PDF for a number (N_s) of conditioning variables. The conditioning variables may be the thermochemical state variables (the scalar PDF approach) and can also include the velocity vector (the joint-velocity-scalar PDF approach). A major advantage of the PDF approach is the non-linear chemical source term appears in closed form in the instantaneous transport equation of the PDF. This lack of pre-supposed flame structure makes it one of the more promising candidates for modelling applications that may experience a wide variety of combustion regimes. A comprehensive review PDF methods up to 2010 can be found in [50]

3.2.1 Sub-filter Probability Density Function

Within the LES context, the sub-filter PDF represents the distribution of scalars within a filter volume. For a single scalar ϕ_α, the one-point marginal PDF (P_α) is defined as

$$P_\alpha = \delta\left(\psi_\alpha - \phi_\alpha\right), \tag{3.16}$$

where ψ_α represents the sample space of scalar ϕ_α, and δ is the *Dirac*-function. In combusting flows, multiple scalars (species and enthalpy) are commonly used as conditioning variables. As such, the joint (fine grained [51]) PDF $\left(\mathcal{F}\left(\underline{\psi};\underline{x},t\right)\right)$ of the entire set of scalars $\underline{\psi} = [\psi_1, ..., \psi_{N_s}]$ can be constructed as a product of the marginal PDF of each scalar. This joint PDF is denoted as the joint-composition PDF and is given by

$$\mathcal{F}\left(\underline{\psi};\underline{x},t\right) = \prod_{\alpha=1}^{N_s} \delta\left(\psi_\alpha - \phi_\alpha(\underline{x},t)\right). \tag{3.17}$$

A similar filtering operation conducted on the on the governing equations in Section 2.2.3 can be applied to the PDF. Following [52, 53], a density weighting can also be introduced to incorporate density variations. The result is a density weighted sub-filter density function (FDF), $\widetilde{P}_{sfs}\left(\underline{\psi};\underline{x},t\right)$. The Favre filtering operation of the PDF takes on the

form

$$\overline{\rho}\widetilde{P}_{sfs}\left(\underline{\psi};\underline{x},t\right)=\int_{V}\rho\mathcal{F}\left(\underline{\psi};\underline{x}',t\right)G\left(\underline{x}-\underline{x}',\Delta\right)\mathrm{d}V'. \tag{3.18}$$

This expression describes the probability of observing values of scalar in the interval $\psi_\alpha < \phi_\alpha < \psi_\alpha + \mathrm{d}\psi$ within a filter volume.

With the assumption of equal diffusivities, the exact filtered transport equation for the joint composition FDF is given as [21, 52, 53]:

$$\begin{aligned}\frac{\partial\overline{\rho}\widetilde{P}_{sfs}}{\partial t}+\frac{\partial\overline{\rho}\widetilde{u}_i\widetilde{P}_{sfs}}{\partial x_i}-\frac{\partial}{\partial x_i}\left[\Gamma\frac{\partial\widetilde{P}_{sfs}}{\partial x_i}\right]+\sum_{\alpha=1}^{N_s}\frac{\partial}{\partial\psi_\alpha}\left[\overline{\rho}\dot{\omega}_\alpha\widetilde{P}_{sfs}\right]=\frac{\partial}{\partial x_i}\left[\overline{\rho u''|\underline{\psi}}\widetilde{P}_{sfs}\right]\\-\sum_{\alpha=1}^{N}\sum_{\beta=1}^{N}\frac{\partial^2}{\partial\psi_\alpha\partial\psi_\beta}\left[\left(\frac{\mu}{Sc}\overline{\frac{\partial\phi_\alpha}{\partial x_i}\frac{\partial\phi_\beta}{\partial x_i}\middle|\underline{\phi}=\underline{\psi}}\right)\widetilde{P}_{sfs}\right],\end{aligned} \tag{3.19}$$

where spatial and temporal dependencies have been dropped for compactness. In Equation 3.19 $\Gamma = \overline{\rho}D$ represents the total molecular diffusion coefficient. The first, second and third terms on the L.H.S correspond to the temporal evolution of the sub-filter PDF, the physical space transport of the sub-filter PDF due to the filtered velocity, and the physical space transport of the sub-filter PDF due to molecular transport respectively. The fourth term on the L.H.S changes the sub-filter PDF shape due to chemical reaction ($\dot{\omega}$) and represents one of the core advantages of the PDF formulation; the chemical source term appears in closed form. The terms on the R.H.S remain unclosed and require modelling. The first term on the R.H.S represents the sub-filter PDF transport due to turbulent fluctuations (turbulent flux) and is commonly closed with a gradient diffusion assumption [54] similar to Equation 2.52.

$$\overline{u''|\underline{\psi}}\widetilde{P}_{sgs}(\underline{\psi})=-\frac{\mu_{sgs}}{Sc_t}\frac{\partial\widetilde{P}_{sgs}}{\partial x_i}. \tag{3.20}$$

If the PDF is conditioned on velocity, this term does not require modelling and appears in closed form [55]. The last term on the R.H.S is the micromixing term and representing the effect of molecular diffusion on the sub-filter PDF.

The challenges associated with this modelling strategy is that due to the high dimensionality of the PDF equation (which is equal to the number of conditioning variables), solving this equation directly using finite differencing techniques can be very expensive and intractable for most practical applications. Additionally, the micromixing term

requires modelling as closing this term requires information on composition gradients which inherently are not available through single point PDFs. The latter point constitutes the primary research challenge for PDF methods and will be discussed further in Section 3.2.2.

Provided that the micro-mixing effects are modelled adequately (and that the PDF equation is solved accurately), in principle, the joint-scalar transported probability density function approach is applicable in both Reynolds-Averaged (RANS) and Large-Eddy Simulations (LES) across all modes of turbulent combustion – including the limiting cases of non-premixed and perfectly-premixed combustion.

To ease the computational burden of solving Equation 3.19, less computationally expensive solution methodologies have been proposed for approximating the PDF. Although deterministic methods exist such as the Direct Quadrature Method of Moments (DQMOM) closure [55, 56], the most popular approaches for approximating the PDF are Monte Carlo approaches. Two types of Monte Carlo methods to solve PDF equation can be found in literature: The Lagrangian Monte Carlo method, and Eulerian Field Monte Carlo method.

The majority of transport PDF simulations to date have employed Lagrangian particle Monte Carlo methods. In this method, the PDF is represented by an ensemble of Lagrangian particles that evolve according to stochastic ordinary differential equations that are statistically equivalent to the PDF transport equation. The particles that evolve in the computational domain are mesh free, and this mesh independence means discretisation errors commonly encountered in Eulerian based equations are almost non-existent. Although Lagrangian approaches have the advantage of not introducing errors due to discretisation of spatial gradients, errors are partially reintroduced by the interpolation required to obtain the statistical moments in physical space [50]. The primary disadvantage of this Lagrangian method arises in the potential large statistical error (or statistical under-resolution). Due to the mesh independence a sufficient quantity of particles may not always be present at a given spatial location for adequate/reliable calculation of statistical moments such as the mean and variance. Additionally, as the local density is obtained from an ensemble of the masses of the particles, sparsity of the particles may lead to an oscillatory density field which may impact the stability of the simulation.

In the stochastic field method, stochastic partial differential equations (SPDE) equivalent to the transport PDF equation are solved. The resulting ensemble of these stochastic fields represent the approximate PDF. The stochastic field method used in this work is described in more detail in Section 3.3

3.2.2 Micromixing Modelling

In the PDF methodologies described above, the common challenge that exists between both methods is obtaining closure for the last term on the R.H.S of Equation 3.19. This term is commonly known as the "micromixing" term and represents the evolution of the joint-PDF due to molecular diffusion. Modelling of this micromixing term is the core research challenge in PDF modelling community.

This term can be considered to be comprised of 2 parts: the physical mixing process, and the time-scale of the mixing [57]; both requiring modelling. The mixing model determines *how* the PDF changes due to the mixing process, and the mixing frequency closure determines *how fast* it changes. It has been shown that the choice of mixing and frequency model are not independent [58] and varies for the given application [59, 60].

There exists a variety of different closures for *how* the PDF mixes. For a comprehensive review up to 2015 of all the different closures, along with their underlying assumptions and modification to address their shortcomings, refer to Celis and Figueira da Silva [60] and the references therein. Here only the commonly employed Interaction by Exchange with the Mean (IEM) [61] or the Linear Mean Square Estimation [62] is discussed as it is the closure adopted in this thesis.

According to [11, 55, 63, 64], every micromixing model is required to exhibit a certain set of physical and mathematical properties. These are:

- Conservation of means: The mixing process should not affect the mean compositions
- Variance Decay: The variances should decay at the correct rate which implies the scalar dissipation is captured correctly
- Boundness: scalar quantities should remain within their allowable regions

In addition to the above fundamental properties, other less strict (but desirable) characteristics are also outlined:

- Linearity and Independence [65]
  - Linearity: The evolution equation for scalar properties should remain unchanged when subject to linear transformation.
  - Independence: The evolution of one scalar should not affect the evolution of another (for interaction matrices, any non-zero off diagonal values will violate this). If independence is satisfied so is linearity.
- Localness: The mixing model should mix locally in composition space (discussed further in Section 3.2.3)
- PDF Relaxation: The PDF should relax to Gaussian distribution for statistically homogeneous systems
- Inclusion of Re, Sc, and Da effects.

and more recently

- Dispersion-consistency [64]: At sufficiently high Reynolds numbers, the scalar field is determined entirely by turbulence. Therefore, the scalar flux is unaffected by molecular mixing and so should its rate of change.

Interaction by Exchange with the Mean

Aside from being one of the most widely used micromixing models it is also one of the simplest and computationally inexpensive. In this model, the particle composition relaxes towards the local mean composition over the scalar mixing timescale τ_ϕ. The model is given as

$$\sum_{\alpha=1}^{N}\sum_{\beta=1}^{N}\frac{\partial^2}{\partial\psi_\alpha\partial\psi_\beta}\left[\left(\frac{\mu}{Sc}\overline{\frac{\partial\psi_\alpha}{\partial x_i}\frac{\partial\psi_\beta}{\partial x_i}\middle|\underline{\phi}=\underline{\psi}}\right)\widetilde{P}_{sfs}\right]= \frac{\overline{\rho}}{\tau_\phi}\sum_{\alpha=1}^{N_s}\frac{\partial}{\partial\psi_\alpha}\left[\left(\psi_\alpha-\widetilde{\phi}_\alpha(\underline{x},t)\right)\widetilde{P}(\underline{\psi})\right] \tag{3.21}$$

Being a pair-wise exchange model, this micromixing model inherently satisfies the three fundamental properties of mixing models. However, it is does not possess the localness property, nor does it relax to a Gaussian. An alternative to the IEM is the Interaction by Exchange with the Conditional Mean (IECM)[66]. This model was developed to extend the IEM to satisfy the dispersion-consistency criterion. In the IECM variant, the composition is relaxed towards the mean composition conditioned on velocity as well as position.

3.2.3 High Damköhler Limit and Localness

In the case of high Damkohler number combustion, molecular transport and chemical reaction are tightly coupled and combustion most often corresponds to the flamelet regime. In this regime, fast reaction steepens scalar gradients giving rise to a reaction sheet type combustion where reactants are rapidly converted to products [50]. Therefore, if a mixing model is to capture mixing correctly, it must not violate how mixing occurs in physical space; the composition field immediately neighbouring a fluid particle dictates how it mixes. Since generally the composition fields are smooth, a spatial neighbourhood corresponds to a neighbourhood in composition space. Therefore, if the mixing model mixes locally in composition space, it can be deduced that it mixes locally in physical space and is not in violation of the physical mixing process [55].

If non-local mixing models such as the IEM are used in the flamelet regime, un-physical mixing can occur. For example, in non-premixed combustion, the thin reaction sheet and non-local mixing could result in mixing of cold fuel and oxidiser across the reaction zone without the composition evolving thorough the flame. This non-physical mixing at very high Da was demonstrated for a non-premixed flame where in certain cases, using a mixing model that did not possess the localness property led to quenching of the flame [63, 64]. Similarly, in premixed combustion, there would be mixing of unburnt reactants and burnt products without reaction which is not physical and can result in erroneous flame speed calculations.

This mixing behaviour is in contrast to the lower Da regions (distributed reaction zones in Figure 1.5) where it was shown by Correra [67] that at low Da, the choice of mixing model is not as important. The difference between the IEM and other models such as the Euclidean Minimum Spanning Trees (EMST) [63] or Modified Curl(MCD) [68] is

insignificant due to finite rate of the chemical reactions and the dominance of turbulence on mixing (turbulent dispersion theory [69]).

3.2.4 Mixing Time-scale

In addition to *how* particles are mixed, *how fast* also has an influence on overall influence of the micromixing term. It is commonly assumed that the scalar mixing time-scale is proportional the turbulence time-scale [70]

$$\frac{1}{\tau_\phi} = \frac{C_\phi}{\tau_T}, \tag{3.22}$$

where C_ϕ is a non-dimensional parameter known as the scalar-to-mechanical time-scale ratio, and τ_T is the time-scale of the integral scale turbulent motions. C_ϕ that is often assumed to have a value of 2.0. However, this value is not universal and has been shown to also vary [71] depending on the application and micromixing model used. As an example, in the RANS context, using the EMST for a premixed flame at a Da$\approx$ 1, Stöllinger and Heinz [59] illustrated that the appropriate value of C_ϕ was 12.

Choosing an optimal, value of for this coefficient is an *ad hoc* process. Various authors [59, 71] have shown that by applying a non-constant C_ϕ, the results of simulations can improve substantially when paired with mixing models that have previously shown to cause un-physical results [63, 64, 72] with more traditional values of C_ϕ. This also helped strengthen the conclusion that different micromixing models require different values of C_ϕ. Although varying C_ϕ and determining it through trial and error is generally better than assuming a constant incorrect value, it is quite time consuming, and can still lead to poor results as burning modes and scale dependencies vary in space and time. Various authors [57, 71] have proposed methods for generalising the calculation of C_ϕ by considering local flow conditions in its calculation (such as composition, Reynolds number) or by solving an additional transport equation for scalar variance. An interested reader is referred to these works as detailing these models is outside the scope of this thesis.

The large focus of research in development of micromixing models and expressions for C_ϕ have been within the RANS-PDF community. The need for more accurate representation of C_ϕ in RANS comes from the need to accurately represent scalar mixing by scales that

are unresolved by the RANS methodology. It has been proposed that in LES, because of the broader range of resolved turbulent scales, the representation of scalar mixing provided by the traditional IEM micromixing model and mixing timescale closure and may be adequate [73]; a conclusion confirmed in [74–76].

3.3 LES Stochastic Field Formulation

An alternative approach to the Lagrangian particle method, is the Eulerian stochastic field (SF) method which was initially proposed by Valiño [23] and then Sabel'nikov and Soulard [25] using a different approach. In this method, the joint scalar PDF is constructed through an ensemble of N_f, Eulerian stochastic fields $\zeta^n(\underline{x},t) = \left[\zeta_1^n, ..., \zeta_{N_s}^n\right]$. The joint scalar PDF can be constructed as

$$\mathcal{F}(\underline{\psi};\underline{x},t) = \frac{1}{N_f}\sum_{n=1}^{N_f}\prod_{\alpha=1}^{N_s}\delta\left[\phi_\alpha - \zeta_\alpha^n(\underline{x},t)\right]. \tag{3.23}$$

Through convolution of the joint scalar PDF with a filter function, the sub-filter PDF defined in terms of stochastic fields can be obtained in a similar manner as Equation 3.18

The premise behind the stochastic field method is deriving stochastic partial differential equations (SPDEs) that are stochastically representative/equivalent of the closed form of the transported PDF equation.

$$\begin{aligned}&\frac{\partial\overline{\rho}\widetilde{P}_{sfs}}{\partial t} + \frac{\partial\overline{\rho}\widetilde{u_i}\widetilde{P}_{sfs}}{\partial x_i} - \frac{\partial}{\partial x_i}\left[\Gamma_e\frac{\partial\widetilde{P}_{sfs}}{\partial x_i}\right] + \sum_{\alpha=1}^{N_s}\frac{\partial}{\partial\psi_\alpha}\left[\overline{\rho}\dot{\omega}_\alpha\widetilde{P}_{sfs}\right] = \\ &\frac{\overline{\rho}}{\tau_\phi}\sum_{\alpha=1}^{N_s}\frac{\partial}{\partial\psi_\alpha}\left[\left(\psi_\alpha - \widetilde{\phi}_\alpha(\underline{x},t)\right)\widetilde{P}(\underline{\psi})\right],\end{aligned} \tag{3.24}$$

where the conditional turbulent flux and micromixing term in the unclosed equation (Equation 3.19) were modelled with the gradient diffusion closure of Equation 3.20 and the IEM model of Equation 3.21 respectively. In the above equation, $\Gamma_e = \overline{\rho}\left(D + D_t\right)$ is the total diffusion coefficient.

The resultant SPDEs govern the evolution of a stochastic scalar field. Valiño [23] was the first to propose a method of generating these SPDEs using an Itô interpretation of

the stochastic integral, and Sabel'nikov and Soulard [25] using the Stratonovich interpretation. In either interpretation, the resultant set of SPDEs represents the stochastic 3D evolution of a joint composition PDF and is purely Eulerian in nature. Each individual stochastic field does not represent a particular realization of a real field, but instead, form a stochastic system equivalent to it - that is, moments arising from the stochastic field equations will be identical to the modelled PDF transport equation of Equation 3.24.

Stochastic fields is an attractive way to approximate a transported PDF for turbulent reacting flows for a few reasons: It guarantees a density field that is continuous and differentiable in space and it can exploit similar Eulerian solution methods and domain decomposition schemes implemented for the momentum equations easing the implementation process into existing codes.

3.3.1 Itô Formulation

Using the Itô interpretation of Valiño [23] with the IEM (Equation 3.21) and gradient diffusion closure, the stochastic field SPDEs evolve according to

$$\begin{aligned}\overline{\rho}\mathrm{d}\zeta_\alpha^n = &-\overline{\rho}\widetilde{u}_i\frac{\partial\zeta_\alpha^n}{\partial x_i}\mathrm{d}t + \frac{\partial}{\partial x_i}\left(\overline{\rho}(D+D_T)\frac{\partial\zeta_\alpha^n}{\partial x_i}\right)\mathrm{d}t + \overline{\rho}\sqrt{2\,(D+D_T)}\frac{\partial\zeta_\alpha^n}{\partial x_i}dW_i^n \\ &- \frac{\overline{\rho}}{\tau_{sfs}}\left(\zeta_\alpha^n - \widetilde{\phi_\alpha}\right)\mathrm{d}t + \overline{\rho}\dot{\omega}_\alpha(\underline{\zeta}^n)\mathrm{d}t, \end{aligned} \tag{3.25}$$

A fundamental assumption with this particular formulation is that the stochastic fields are smooth on the scale of the filter width (they contain no hidden "sub-filter" scales) and are thus fully resolved on the grid size level.

The first and second term on the R.H.S of Equation 3.25 represent physical space advection of the stochastic fields in physical space due to the filtered momentum fields and spatial diffusion of the fields respectively. Interaction between the fields of a corresponding scalar occurs due to the second last term on the R.H.S (or the micromixing term). The Favre filtered values of the scalar ϕ_α required in this term is the mean of all the stochastic fields of the corresponding scalar, α, obtained with

$$\widetilde{\phi}_\alpha = \langle\zeta_\alpha\rangle = \frac{1}{N_f}\sum_{n=1}^{N_f}\zeta_\alpha^n. \tag{3.26}$$

The third term on the R.H.S represents the stochastic contribution to the SPDE and includes an increment of a Wiener process (dW) with zero mean and dt variance. The stochastic term differs for every field and is independent of spatial location.

Each stochastic field satisfies the mass conservation and boundness of the scalar it represents because as the scalar tend to extrema, the gradients tend to zero and the stochastic contribution vanishes. As the number of fields $N_f \rightarrow \infty$, the filtered stochastic term tends to zero [27]

$$\left\langle \overline{\rho}\sqrt{2\left(D+D_T\right)}\frac{\partial \zeta_\alpha^n}{\partial x_i}dW_i^n \right\rangle \rightarrow 0. \tag{3.27}$$

With these aforementioned attributes, the stochastic fields are smooth on the scale of the filter width, continuous and differentiable in space, and continuous but not differentiable in time. A full derivation of the stochastic field SPDEs with the Itô interpretation can be found in [23, 74].

3.3.2 Stratonovich Formulation

Sabel'nikov and Soulard [25] used the Stratonovich interpretation and derived a set of SPDEs in the form

$$\begin{aligned} &\overline{\rho}\mathrm{d}\zeta_\alpha^n + \overline{\rho}\widetilde{u}_j\frac{\partial \zeta_\alpha^n}{\partial x_j}\mathrm{d}t + \frac{\overline{\rho}}{\tau_{sfs}}\left(\zeta_\alpha^n - \widetilde{\phi_\alpha}\right)\mathrm{d}t - \overline{\rho}\dot{\omega}_\alpha\left(\underline{\zeta}^n\right)\mathrm{d}t \\ &\quad = -\overline{\rho}\left(u_j^g + u_j^d\right)\frac{\partial \zeta_\alpha^n}{\partial x_j}\mathrm{d}t, \end{aligned} \tag{3.28}$$

where the terms on the L.H.S represent identical processes to those described above. The terms arising from the Stratonovich interpretation are on the R.H.S. The first term on the R.H.S (u_j^g) represents a stochastic velocity and is defined as

$$u_j^g = \sqrt{2\left(D+D_T\right)} \circ \frac{\mathrm{d}W_j^n}{\mathrm{d}t}, \tag{3.29}$$

where $\circ$ denotes the Stratonovich interpretation of the stochastic integral. The second term (u_j^d) is a drift velocity u_j^d and accounts for spatial variations of the diffusion coefficient and is given by

$$u_j^d = \frac{1}{2}\frac{\partial}{\partial x_j}\left(D+D_T\right) - \frac{1}{\overline{\rho}}\frac{\partial}{\partial x_j}\left[\overline{\rho}\left(D+D_T\right)\right], \tag{3.30}$$

Unlike the formulation of Valiño [23], smoothness of the stochastic fields is not necessary with this interpretation, however, at the scale of the filter width, both formulations are smooth and the advantage of the less stringent smoothness restriction is quite minor. Additionally, compared to Equation 3.25, as the number of fields $N_f \to \infty$, the filtering of the stochastic contribution is non-zero [27]

$$\left\langle \overline{\rho}\sqrt{2\left(D+D_T\right)}\frac{\partial \zeta_\alpha^n}{\partial x_i}dW_i^n \right\rangle \to -\overline{\rho}\frac{\partial^2 \zeta_\alpha}{\partial {x_j}^2}, \tag{3.31}$$

and corresponds to a diffusion term.

Regardless of the different physical interpretations and mathematical approaches, it was shown in [25, 50] that the two formulations are mathematically equivalent and both are equivalent representations of Equation 3.19. In fact, [77] illustrated that the two formulations produce very similar results. To date, the only known definite advantage of the Stratonivich interpretation over the Itô is the ability to use implicit schemes [27, 77].

3.3.3 Extension to Low Reynolds Number

The stochastic field formulations presented above were derived for high Reynolds number flows. In [24], Valiño proposed modifications to the original 1998 formulation to ensure consistency in the case of low Reynolds number. The desire was to obtain the correct limiting behaviour of the sub-filter PDF that limit - that is, the stochastic fields should become less stochastic as the turbulent diffusivity (D_T) tends to zero. This condition is obtained in two separate cases:

1. In the case of laminar flow.
2. In the limit of fully a resolved flow field.

In the case of laminar flow, the stochastic fields should reduce exactly to the transport equation that govern the evolution of the conditioning variable. In the case of a fully resolved flow field, the flow is still turbulent, but all scales are resolved. As such, there is no sub-filter turbulent transport or mixing. In both of these cases, the sub-filter PDF should decay towards a *Dirac*. In the formulation given in Equation 3.25, this low

(filter) Reynolds number limiting behaviour was not obtained due to the presence of the molecular diffusion (D), in the stochastic term.

The modified formulation of the Itô formulated stochastic fields was achieved by decomposition of the diffusion term in the PDF transport equation (Equation 3.19) through substitution of P_{sfs} by its definition in the Stochastic field sense (Equation 3.23). A complete derivation can be found in [24, 78]. The decomposed PDF transport equation is then

$$\begin{aligned}
&\frac{\partial \overline{\rho}\widetilde{P}_{sfs}}{\partial t} + \frac{\partial \overline{\rho}\widetilde{u_i}\widetilde{P}_{sfs}}{\partial x_i} + \sum_{\alpha=1}^{N_s} \frac{\partial}{\partial \psi_\alpha}\left[\overline{\rho}\dot{\omega}_\alpha \widetilde{P}_{sfs}\right] = \\
&-\sum_{\alpha=1}^{N} \frac{\partial}{\partial \psi_\alpha}\left[\frac{\partial}{\partial x_i}\left\langle \overline{\rho}\left(D + D_T\right)\widetilde{\frac{\partial \zeta_\alpha}{\partial x_i}}\middle| \underline{\phi} = \underline{\psi}\right\rangle \widetilde{P}_{sfs}\right] \\
&+\sum_{\alpha=1}^{N}\sum_{\beta=1}^{N} \frac{\partial^2}{\partial \psi_\alpha \partial \psi_\beta}\left[\left\langle \overline{\rho} D_T \widetilde{\frac{\partial \zeta_\alpha}{\partial x_i}\frac{\partial \zeta_\beta}{\partial x_i}}\middle| \underline{\zeta} = \underline{\psi}\right\rangle \widetilde{P}_{sfs}\right] \\
&+\sum_{\alpha=1}^{N}\sum_{\beta=1}^{N} \frac{\partial^2}{\partial \psi_\alpha \partial \psi_\beta}\left[\left\langle \overline{\rho} D \widetilde{\frac{\partial \zeta_\alpha}{\partial x_i}\frac{\partial \zeta_\beta}{\partial x_i}}\middle| \underline{\zeta} = \underline{\psi}\right\rangle \widetilde{P}_{sfs}\right] \\
&-\sum_{\alpha=1}^{N}\sum_{\beta=1}^{N} \frac{\partial^2}{\partial \psi_\alpha \partial \psi_\beta}\left[\left\langle \overline{\rho} D \widetilde{\frac{\partial \phi_\alpha}{\partial x_i}\frac{\partial \phi_\beta}{\partial x_i}}\middle| \underline{\phi} = \underline{\psi}\right\rangle \widetilde{P}_{sfs}\right],
\end{aligned} \tag{3.32}$$

The primary assumption in deriving the new stochastic field formulations is that, because the stochastic fields are smooth at the resolved scales, their contribution is on the same order as the mean gradients [24]. This relationship is expressed by:

$$\begin{aligned}
&\sum_{\alpha=1}^{N}\sum_{\beta=1}^{N} \frac{\partial^2}{\partial \psi_\alpha \partial \psi_\beta}\left[\left\langle \overline{\rho} D \widetilde{\frac{\partial \zeta_\alpha}{\partial x_i}\frac{\partial \zeta_\beta}{\partial x_i}}\middle| \underline{\zeta} = \underline{\psi}\right\rangle \widetilde{P}_{sfs}\right] - \sum_{\alpha=1}^{N}\sum_{\beta=1}^{N} \frac{\partial^2}{\partial \psi_\alpha \partial \psi_\beta}\left[\left\langle \overline{\rho} D \widetilde{\frac{\partial \phi_\alpha}{\partial x_i}\frac{\partial \phi_\beta}{\partial x_i}}\middle| \underline{\phi} = \underline{\psi}\right\rangle \widetilde{P}_{sfs}\right] \\
&\qquad = \sum_{\alpha=1}^{N}\sum_{\beta=1}^{N} \frac{\partial^2}{\partial \psi_\alpha \partial \psi_\beta}\left[\left\langle \overline{\rho} D \widetilde{\frac{\partial \phi'_\alpha}{\partial x_i}\frac{\partial \phi'_\beta}{\partial x_i}}\middle| \underline{\phi} = \underline{\psi}\right\rangle \widetilde{P}_{sfs}\right].
\end{aligned} \tag{3.33}$$

These terms roughly cancel out against the contribution of the fluctuating filtered scalar gradients.

Substitution of the relationship in Equation 3.33 into Equation 3.32 yields:

$$\begin{aligned}
&\frac{\partial \overline{\rho}\widetilde{P}_{sfs}}{\partial t} + \frac{\partial \overline{\rho}\widetilde{u_i}\widetilde{P}_{sfs}}{\partial x_i} + \sum_{\alpha=1}^{N_s} \frac{\partial}{\partial \psi_\alpha}\left[\overline{\rho}\dot{\omega}_\alpha \widetilde{P}_{sfs}\right] = \\
&-\sum_{\alpha=1}^{N} \frac{\partial}{\partial \psi_\alpha}\left[\frac{\partial}{\partial x_i}\left\langle \overline{\rho}\left(D + D_T\right)\widetilde{\frac{\partial \zeta_\alpha}{\partial x_i}}\middle|\underline{\phi} = \underline{\psi}\right\rangle \widetilde{P}_{sfs}\right] \\
&+\sum_{\alpha=1}^{N}\sum_{\beta=1}^{N} \frac{\partial^2}{\partial \psi_\alpha \partial \psi_\beta}\left[\left\langle \overline{\rho} D_T \widetilde{\frac{\partial \zeta_\alpha}{\partial x_i}\frac{\partial \zeta_\beta}{\partial x_i}}\middle|\underline{\zeta} = \underline{\psi}\right\rangle \widetilde{P}_{sfs}\right] \\
&-\sum_{\alpha=1}^{N}\sum_{\beta=1}^{N} \frac{\partial^2}{\partial \psi_\alpha \partial \psi_\beta}\left[\left\langle \overline{\rho} D \widetilde{\frac{\partial \phi'_\alpha}{\partial x_i}\frac{\partial \phi'_\beta}{\partial x_i}}\middle|\underline{\phi} = \underline{\psi}\right\rangle \widetilde{P}_{sfs}\right],
\end{aligned} \tag{3.34}$$

In the PDF transport equation given above, the IEM model is used to close the last term on the R.H.S. In this case however, the micromixing model is related to the sub-filter part of the scalar dissipation compared to the previous formulation where it modelled both the resolved and sub-filter contributions.

Using standard methods [23, 24, 27, 74], the stochastic field equations can be derived. The modified evolution of the stochastic fields is then given by:

$$\begin{aligned}
\overline{\rho}\mathrm{d}\zeta_\alpha^n = &-\overline{\rho}\widetilde{u}_i\frac{\partial \zeta_\alpha^n}{\partial x_i}\mathrm{d}t + \frac{\partial}{\partial x_i}\left(\overline{\rho}(D + D_T)\frac{\partial \zeta_\alpha^n}{\partial x_i}\right)\mathrm{d}t + \overline{\rho}\sqrt{2D_T}\frac{\partial \zeta_\alpha^n}{\partial x_i}dW_i^n \\
&- \frac{\overline{\rho}}{\tau_{sfs}}\left(\zeta_\alpha^n - \widetilde{\phi_\alpha}\right)\mathrm{d}t + \overline{\rho}\dot{\omega}_\alpha(\underline{\zeta^n})\mathrm{d}t.
\end{aligned} \tag{3.35}$$

It can be seen that the new formulation is consistent with the desired low Reynolds number limit. As turbulent diffusivity approaches zero, the stochastic term vanishes, $\zeta_\alpha^n \rightarrow \widetilde{\phi_\alpha}$, and the stochastic fields reduce to the transport equation of the scalar that ζ represents. However, this new formulation is also consistent in the high Reynolds number limit. For sufficiency high Reynolds number, $D_T >> D$, and both the 1998 [23] and 2016 [24] formulations reduce to approximately the same form.

3.3.4 Stochastic Fields for Premixed Combustion

Following successful validation of the stochastic fields approach in a range of non-premixed combustion scenarios [79–84], a smaller number of stochastic fields simulations of premixed combustion have been reported. Using the 1998 formulation of [23],

premixed stochastic fields simulations have been conducted for a low Reynolds number swirl flame [75], a piloted Bunsen flame [85], and for a bluff body flames [86, 87]. To date only a few studies [78, 88, 89] have been conducted with the modified stochastic field equations provided by [24]. It was shown in [89] that for a laminar flame, the non-vanishing stochastic term of the 1998 formulation led to incorrect flame predictions compared to the simulations with the modified stochastic term. Similar results were obtained in [88] for the very low Reynolds number Cambridge slot burner flame [90]. The numerical simulations of the rod stabilised V-flame showed that compared to experiment, the 1998 formulation of stochastic fields led to a 54% over-prediction in flame angle/burning velocity compared to an 18% over-prediction obtained with the modified stochastic field formulation.

In general, the results of these simulations is encouraging for the application of stochastic fields in the simulation of turbulent premixed combustion. More importantly, the relatively good agreement with experiment within these simulations was obtained with a micro-mixing model (the IEM) that was unchanged from the non-premixed modelling efforts. The sensitivity of the choice of nominal C_ϕ in conjunction the IEM model was investigated by Dodoulas and Navarro-Martinez [85] where it was observed that the flame structure was not significantly altered through variation of this particular parameter. These results were similar to the conclusions of [76] using the Lagrangian particle LES-PDF formulations of the same test case. These similar conclusions strengthen the hypotheses that the effect of C_ϕ in LES is minor compared to the dependency observed in RANS context [57, 71].

However, even with the lack of sensitivity seen for this modelling approach, the use of the IEM micromixing model in premixed LES-PDF has not been rigorously justified to extend to all premixed combustion regimes. Its preliminary (and continued) use in simulations generally arises from its computational convenience and a lack of application of stochastic fields modelling to sufficiently flamelet-combustion dominated flames. Investigations of stochastic particle-based transported-PDF modelling in flamelet combustion regimes suggest that turbulent flame predictions can be improved by applying alternative micro-mixing models that enforce localness [59, 63] and also account for preferential molecular transport [91]. However, the necessity of these properties in the context of stochastic fields LES is unknown as such models have not yet been adapted for use with the stochastic fields approach. The relative success of the IEM in LES-PDF methods

is speculated to be due to the increased resolved mixing and the smaller contribution of sub-filter mixing [73]. However, the necessity for different closures for the micromixing term may arise with application of stochastic fields LES to increasingly (sub-filter) flamelet like premixed combustion conditions where scalar mixing would then be governed by increasingly unresolved scales (for example, simulation of a combustion device at increasingly higher pressure). This increased scale separation between the resolved and scalar mixing scales (similar to that of RANS) at these conditions will perhaps place more stringent requirements on the choice of mixing and frequency models.

Within Monte Carlo simulations in general, ensuring an adequate sample size is necessary to obtain an accurate and unbiased estimate of statistics quantities. Statistical convergence was analysed in the introductory stochastic fields papers of [23, 25], however, these were under simplified conditions. A more practical investigation of the effect of field number on SF-LES predictions was investigated in the context of 3D LES in the work of [85]. They analysed statistical resolution by simulating a premixed Bunsen flame [92] using 1, 4, and 16 fields with a fine grid resolution. It was shown that increasing the number of fields generally improved the prediction of axial velocity in all three flames simulated, although some discrepancies did exist at some locations. Most of the species predictions also showed similar behaviour. Although no absolute convergence was seen, it was suggested that using 8-16 fields was adequate. Here, absolute convergence is defined as independence of the solution from any successive increase in field number. This investigation provided an initial estimate for required field number to be used with stochastic fields but did not provide any specific dependencies to field requirements at different premixed combustion conditions. Their conclusions are not expected to be applicable across all turbulent premixed combustion regimes as the number of samples required to reconstruct a discrete PDF will vary depending on its shape (or variance). The sub-filter variance of a PDF is expected to vary depending on the sub-filter combustion regime; a larger variance would generally require more fields than that for PDF with smaller variance. To date, no explicit investigation into this relationship has been conducted. In order to ensure that stochastic field simulations are adequately resolved statistically, establishing field requirements as a function of different (sub-filter) combustion regimes is necessary.

More fundamentally than statistical resolution, as stochastic fields is an Eulerian methodology, it is suspected that it may be susceptible to similar inherent modelling challenges

associated with any Eulerian based premixed combustion modelling framework, namely; numerical errors as a product of poor numerical resolution. Numerical resolution requirements of the stochastic fields equations in premixed combustion LES have not been discussed explicitly in academic literature.

Each stochastic field contains a reaction front that "resembles" a premixed flame. Strictly, the reaction fronts in the stochastic fields are not required to correspond to actual flame fronts in a physical flow, and therefore the term "reaction front" is used to avoid confusion. In general, the combined effects of an exchange with the mean micro-mixing model (that has the effect of drawing the fields towards their correspondingly thicker filtered field) and an eddy-diffusivity model for the unresolved turbulent transport is to thicken the individual stochastic fields. In the absence of unresolved turbulent transport, the stochastic fields reaction front thickness should converge to the laminar flame thickness. Conversely, the upper limit on reaction-front thickness would be in the case of perfect mixing. In this case, the stochastic field reaction fronts will be equal to the ensemble average of all the stochastic fields. Therefore, the thermal thickness of the stochastic fields reaction fronts is expected to be bound by the thermal thickness of an unstrained laminar premixed flame and the thermal thickness of the ensemble-averaged (RANS) or resolved (LES) temperature field. From this, it can be concluded that the averaged thickness of the reaction-front of individual stochastic fields is necessarily less than or equal to the thickness of the ensemble average of all the stochastic fields.

In the context of LES, the average thickness of an individual stochastic field reaction front is expected to depend on the effective filter length scale and the sub-filter combustion regime. Karlovitz numbers much greater than unity (i.e. broken reaction zones) have the effect of thickening instantaneous flame fronts [19]. Therefore, higher Karlovitz numbers should also thicken the stochastic field reaction fronts, reducing numerical resolution requirements. Conversely, the most stringent resolution requirements are expected for low Karlovitz number flames that characterise combustion in the flamelet regime. Although not the focus of their study, Advić *et al.* (using the modified stochastic field formulation of [24]) briefly investigated the effect of spatial resolution on the stochastic field predictions of a laminar flame. Their simulations showed a strong dependence of the predicted flame speed on the different grid resolutions tested. This dependence is expected however. Through analysis of Equation 3.35 in the limiting case of $D_T = 0$, it can be seen that this particular stochastic field formulation would reduce to a reactive

scalar transport equation for each conditioning reactive scalar. Consequently, in order to accurately predict the laminar flame correctly, the stochastic field will necessarily require an adequate numerical grid resolution to do so. Although not strictly a stochastic field simulation per se, this particular investigation by these authors confirms the necessity for stochastic field simulations to have sufficient numerical resolution and provides a requirement for numerical resolution of stochastic fields in the limiting case of a laminar flame ($\mathrm{Ka} = 0$); a resolution equivalent to DNS simulations.

Comparatively, the numerical grid requirement for the ATF [14, 22, 44, 45] is not as strict, and it can better predict the correct laminar flame speed for a given numerical grid spacing. In the ATF method (as discussed in Section 3.1.1), the scalar fields are artificially thickened by a thickening factor F to sufficiently resolve all the scalar gradients, reducing the magnitude of numerical errors introduced into the solution. The insensitivity to the choice of numerical grid arises from the fact F is evaluated through an *a priori* defined resolution of the laminar flame on the employed numerical grid. The consequence is that coarse numerical grids can be used for turbulent flame simulation and still preserve the correct flame speed in the case of a laminar flame.

As the numerical resolution requirements of stochastic fields are suspected to be dependant on combustion regime, it is essential to establish an understanding of the impact of numerical grid resolution on the predictive capability of stochastic fields across these regimes and how any numerical error that arises from poor resolution is manifested. As low Karlovitz number combustion is prevalent in most premixed combustion applications (including spark-ignition engines and industrial gas turbines), the computational implications of applying stochastic fields to simulate these flamelet-like combustion regimes needs to be established. It is not evident *a priori* whether a given grid spacing will be sufficient to numerically resolve the individual stochastic fields in different combustion regimes, and numerical resolution requirements need to be investigated numerically.

3.4 Numerical Framework

The stochastic fields framework is implemented within the block-structured BOFFIN (Boundary Fitted Flow Integrator) computational fluid dynamics code [85, 93]. The code is a second order accurate finite volume method based on fully implicit low-Mach-number formulation using a staggered storage arrangement. For the momentum equation convection term, an energy conserving discretisation scheme is used and all other spatial derivatives are approximated by standard second order central differences. A total variation diminishing (TVD) scheme is used for the convection terms in the scalar conservation equations to ensure boundness.

The stochastic field equations are solved using a weak first order temporal approximation with accuracy $\mathcal{O}\left(\sqrt{\Delta t}\right)$ based on the Euler–Maruyama scheme [94]. The chemical source terms are solved using an in-house Newton method-based stiff solver.

3.4.1 Stochastic Fields Formulation

Due to the consistency in the low Reynolds number limit, in this thesis, the modified stochastic field equations (Equation 3.35) of Valiño [24] is used. Traditionally, in stochastic field simulations, filtered moments of scalars are obtained by ensemble averaging all the instantaneous stochastic fields as in Equation 3.26. Subsequently, the filtered density required in the LES momentum equations is obtained by

$$\frac{1}{\overline{\rho}} = \frac{1}{N}\sum_{n=1}^{N}\frac{1}{\rho^n} \tag{3.36}$$

where ρ^n is the local density on field n determined from the equation of state for an ideal gas.

For low number of samples, stochastic noise may have an impact of the stability of the solution. Therefore, in this work, the SF formulation of Prasad [27] is adopted. In this formulation, auxiliary species transport equations are solved for all α scalars. After the stochastic fields are solved at a given time step, the auxiliary equation is advanced with closure of the filtered chemical source term achieved through the ensemble of the stochastic field reaction rates as:

$$\overline{\dot{\omega}_\alpha}(x,t) = \frac{1}{N}\sum_{n=1}^{N}\dot{\omega}_\alpha^n(x,t). \tag{3.37}$$

The density required in the LES equations is then calculated by the equation of state using the auxiliary species composition.

Included in the stochastic field formulation proposed by Prasad [27], is a scaling for the mechanical-to-scalar time-scale ratio. It is given as:

$$C_\phi = C_\phi^0\left(\frac{\mu_L}{\mu_{sgs}} + 1\right), \tag{3.38}$$

where $C_\phi^0 = 2$. This scaling was derived to ensure low Reynolds number consistency for the high Reynolds number stochastic field formulations used in [27]. It ensures the correct limiting behaviour at both high Reynolds number, and laminar flow conditions. In the limit of sufficiently large Reynolds number, $\mu_{sgs} >> \mu_{sgs}$ and $C_\phi \to 2$. In the case of laminar flow, $\mu_{sgs} \to 0$ and mixing becomes infinitely fast. The latter case has the effect of removing any contributions of the stochastic term in the respective stochastic field formulation. Although this behaviour is inherent in the modified stochastic field formulation of Equation 3.35, this particular scaling is used nonetheless to scale C_ϕ at states between these two extremes.

3.4.2 Wiener Term

The Wiener process (dW) is determined by time-step increments $dt^{1/2}\eta_i^n$ where η_i^n is the Wiener term increment of field n in the $i-th$ coordinate direction. It is determined by a weak first order approximation using a dichotomic random vector $\{-1, 1\}$ [25, 94]. The algorithm of distributing Wiener term increments involves generating normally distributed random numbers for the first half of the total number of fields. Depending on the sign of the random number, the increment obtains the dichotomic vector value corresponding to same sign; Negative signed random numbers are given a value of -1 and positive signed numbers, +1. Each field in the first half of the total number of fields is assigned a complement in the second half which is offset by $N_f/2$. Thus, consistency with the weak approximation in providing the correct mean and variance is achieved by enforcing complementary fields to have opposite signs. As such, the number of fields is restricted to an even number. In a final step, to avoid introduction of any correlation

into the solution through consistent negative correlation of field complement, after the initial distribution of Wiener term increments is complete, the distribution is randomly shuffled.

3.4.3 Thermo-chemical Model

In this thesis, similar to the work of [46], premixed combustion kinetics are modelled using a one-step reaction model for methane-air flames,

$$CH_4 + 2O_2 \rightarrow CO_2 + 2H_2O. \tag{3.39}$$

The fuel reaction rate is modelled by the Arrhenius law,

$$\dot{\omega}_{CH_4} = A \cdot \left(\frac{\rho Y_{CH_4}}{M_{CH_4}}\right)^{n_{CH_4}} \left(\frac{\rho Y_{O_2}}{M_{O_2}}\right)^{n_{O_2}} \exp\left(-\frac{E_a}{RT}\right), \tag{3.40}$$

where T, Y_{CH_4}, Y_{O_2}, M_{CH_4}, M_{O_2} and R denote temperature, fuel and oxygen mass fractions, corresponding molar masses and the universal gas constant, respectively. The pre-exponential factor, the activation energy and the model exponents are $A = 1.1 \times 10^{10}$ (cgs), $E_a = 20,000$ cal/mol, $n_{CH_4} = 1.0$ and $n_{O_2} = 0.5$. The use of such simple chemical modelling is justified by the focus of the thesis on evaluation of the numerical resolution requirements of the stochastic fields approach, rather than assessing the physical accuracy of the stochastic fields approach.

Temperature dependent thermodynamic properties are modelled with NASA polynomials, and the mixture viscosity is modelled with Wilkes law. Due to the unity Lewis number assumption in the stochastic fields formulation, the laminar Schmidt and Prandtl numbers are both set equal to 0.7. These assumptions lead to a laminar flame speed $S_L = 0.38$ m/s, a thermal thickness $\delta_L = 0.408$ mm, and a burnt gas adiabatic temperature $T_b = 2328$ K in atmospheric and stoichiometric conditions.

Chapter 4

Numerical Requirements of the Stochastic Field Approach

The grid spacing required in order to numerically resolve a reaction-diffusion front varies depending on the numerical discretisation employed, the details of the chemistry and transport models employed, and the numerical accuracy desired. For high-accuracy simulation of premixed combustion with a detailed chemistry model, more than twenty points may be required within each reaction-diffusion front. Whereas five points within a reaction diffusion front may be taken as an absolute minimum requirement for less accurate engineering simulations with simple (e.g. single-step) chemistry models [14]. Low-order numerical methods and TVD schemes used for some LES of turbulent reacting flows can remain stable even when the governing equations are under resolved, providing numerical diffusion that spreads the reaction fronts across multiple grid points.

In implicitly-filtered LES, the effective filter length scale used in modelling for the unclosed sub-filter scale terms usually depends on the grid spacing. Previous stochastic fields LES studies [75, 80–82, 85, 86] have all set the filter length scale equal to the grid spacing (or the cube root of the cell volume as in Equation 2.27). As demonstrated in Section 2.2.3, when the filter length scale depends on the grid spacing, the effects of numerical resolution errors cannot be distinguished from scale-dependence of the sub-grid modelling. Vreman *et al.* [95] investigated the effects of numerical error in non-reacting LES by changing the filter scale independently from the grid spacing. For a fixed filter scale they found significant differences in LES predictions between simulations with the

grid spacing equal to either the filter scale or one half of the filter scale. They did not proceed to refine the grid to the extent that grid-independence of the predictions was demonstrated, presumably due to the computational expense of further refining the three-dimensional grid. The approach of refining the numerical resolution while keeping the filter length scale unchanged is also appropriate for assessment of numerical error and resolution requirements in the stochastic fields equations and this approach is employed in this section. Due to the computational expense of highly-resolved three-dimensional stochastic fields simulations, the numerical resolution requirements are assessed across a wide range of combustion regimes using a simple one-dimensional test case relating to a stationary planar freely-propagating turbulent flame, before verifying the conclusions from the one-dimensional study in a three-dimensional LES of a turbulent premixed Bunsen flame and of a statistically planar flame propagating in decaying homogeneous-isotropic turbulence.

The particular goal of this chapter is to establish the dependence of the non-dimensional thickness of the reaction-fronts of individual stochastic fields on the combustion regime. The approach adopted here is to solve the stochastic fields equations with a fixed filter length scale, but to reduce the numerical grid spacing relative to the filter scale in order to ensure that the individual stochastic fields are numerically resolved. From this approach it is possible to ascertain a thickness of the individual stochastic fields, and therefore determine under what conditions they are adequately resolved by a grid spacing equal to the filter scale.

4.1 One-Dimensional Freely-propagating Turbulent Flame

The analysis undertaken for the one-dimensional test cases represents a planar flame propagating through a medium with constant turbulence properties. The turbulence is specified by two independent parameters: the RMS velocity fluctuation, and a turbulent length scale. The results of the simulation may be interpreted either in the context of RANS or LES. In either case, a model for the turbulent diffusivity and mixing time-scale is required to close the stochastic field equations used in this study (Equation 3.35). Details of the closures employed are discussed in the proceeding section.

RANS

In the context of RANS, the planar turbulent premixed flame is statistically homogeneous in the directions orthogonal to the mean propagation direction. The model for turbulent diffusivity takes on the form of an algebraic closure which resembles the form of the k-equation closure given in [11]:

$$D_T = \frac{C_\mu u' L_T}{Sc_T}, \tag{4.1}$$

where $Sc_T = 0.7$ and $C_\mu = 0.09$. The mixing frequency required for the micro-mixing term is modelled by

$$\frac{1}{\tau_T} = \frac{C_\phi u'}{L_T}. \tag{4.2}$$

LES

Large Eddy Simulation is inherently three-dimensional, however, in regions where the local resolved flame front is thin relative to the curvature radius of the resolved flame front, molecular and turbulent transport across the resolved flame front is approximately one-dimensional in the direction normal to the local resolved flame surface. It is then appropriate to consider the local propagation of the resolved flame front as locally similar to the propagation of a planar turbulent flames subject to turbulence with properties of the equal sub-filter scale turbulence.

The one-dimensional simulations in this context may be interpreted loosely as representing the transport along a line passing perpendicularly through a LES-resolved flame front, assuming that the LES-resolved flame front propagation is quasi-steady and unaffected by: other flame fronts, curvature, or resolved strain (except to the extent that the resolved strain results in generation of sub-filter scale velocity fluctuations characterised by u'_Δ). The sub-filter scale diffusivity and dissipation time scales required in Equation 3.35 are then modelled by Equation 4.1 and Equation 4.2, replacing the turbulence length scale L_T with the filter scale Δ, and the turbulent velocity u' with the sub-filter scale velocity fluctuation u'_Δ. According to these simple interpretations, the results of an LES solution would converge to those of an unsteady RANS solution in the limit where the filter scale approaches the integral length scale, however it should be noted

that using a filter scale that is of the order of the integral scale violates the basic premise that the LES filter scale should be in the inertial range.

The sub-models for the sub-filter scale turbulent diffusivity and dissipation time scale that depend on a notional LES filter length scale Δ and the corresponding sub-filter scale velocity fluctuation u'_Δ are

$$D_T = \frac{C_{\mu\Delta} u'_\Delta \Delta}{Sc_T}, \tag{4.3}$$

where $Sc_T = 0.7$ and $C_{\mu\Delta} = 0.09$. The mixing frequency is modelled by

$$\frac{1}{\tau_T} = \frac{C_\phi u'_\Delta}{\Delta}. \tag{4.4}$$

4.1.1 Turbulence Parameters - Estimation of u′

To close the above equations for turbulent diffusivity and mixing frequency in either the RANS or LES context, a model is required for the RMS velocity fluctuations. To obtain this, the turbulence parameters u' and L_T are first non-dimensionalised using the laminar flame thermal thickness, δ_L, and the laminar flame speed, s_L, in order to obtain the filter-to-flame length scale ratio δ_L/Δ, and the Karlovitz number [41]:

$$Ka^2 = \frac{u'^3 \delta_L}{s_L^3 L_T}. \tag{4.5}$$

In LES, the sub-filter scale RMS velocity is a function of the filter length scale Δ. Here, conventional scaling arguments are used to estimate the dependence of u'_Δ on Δ. The assumption that Δ is in the inertial range of the turbulence decay means that the dissipation occurs at scales smaller than Δ. Within this region, the rate of sub-filter turbulent kinetic energy dissipation ϵ_Δ is independent of length-scale (or Δ) and can be approximated equal to the Reynolds averaged turbulent kinetic energy dissipation rate ϵ. As in Equation 1.10, the dissipation rate scales with

$$\epsilon \sim \frac{u'^3}{L_T}, \tag{4.6}$$

and therefore

$$\epsilon_\Delta \sim \frac{u'^3_\Delta}{\Delta}. \tag{4.7}$$

Since in the inertial range we assume that $\epsilon_\Delta = \epsilon$, combining Equation 4.5, Equation 4.6, and Equation 4.7, provides an estimate for the sub-filter scale RMS velocity as a function of the filter length-scale and Karlovitz number,

$$u'_\Delta = s_L K a^{2/3} \left(\frac{\Delta}{\delta_L} \right)^{1/3}. \tag{4.8}$$

With the assmptions outlined in the previous section, the velocity fluctuations for the RANS context can be obtained by simply replacing Δ with L_T.

The presented scaling argument provides a complete set of models for the parameters appearing in Equation 3.35. The closures are not expected to be quantitatively accurate, but will be used to demonstrate the behaviour of the stochastic fields under the various conditions tested in the proceeding work.

4.1.2 Thermo-physical Configuration

For filter length scales in the inertial sub-range of the turbulence spectrum, from the scaling analysis shown above, the filter scale Karlovitz number Ka_Δ is equal to the integral scale Karlovitz number, $\mathrm{Ka}_\Delta = \mathrm{Ka}$ [14]. Since LES relies on selection of a filter length scale in the inertial sub-range, the effect of choosing different ratios of the filter length scale to laminar flame thickness (Δ/δ_L) for simulation of a particular turbulent flame regime can be investigated by fixing Karlovitz number and evaluating the corresponding sub-filter scale velocity fluctuation as in Equation 4.8

The thermo-physical configurations chosen for this test case were selected to demonstrate resolution requirements spanning different combustion regimes from the Corrugated Flamelet ($\mathrm{Ka} \approx 0.5$), to Thin Reaction Zones regime ($\mathrm{Ka} \approx 50.0$). The filter width ratios were chosen to correspond to conditions similar to those expected in the 3D LES simulations in the proceeding sections. Full details of the range of filter widths, Karlovitz numbers, and stochastic field numbers used in the study are outlined in Table 4.1.

4.1.3 Performance Metrics

Of particular interest in this study is how the numerical resolution of the individual stochastic fields affect the resolved flame front speed s_{T_Δ}, and thickness δ_c of the filtered

TABLE 4.1: One-dimensional simulation thermo-physical configurations

Ka	0.5, 1, 5, 10, 20, 30, 40, 50
Δ/δ_{th}	1, 2.5, 5.0
Δ/Δ_x	1, $\gg 1$
Number of stochastic fields	512

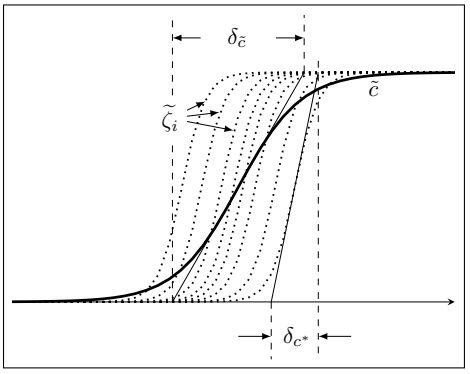

FIGURE 4.1: A schematic diagram showing the δ_{c^*} thickness of the individual stochastic fields progress variable profiles (dashed lines) and the $\delta_{\tilde{c}}$ thickness of the resolved progress variable field (solid line)

progress variable field, since both of these factors influence the overall turbulent flame dynamics that would arise in a full 3D LES. In order to characterise the resolution of the individual stochastic fields, the stochastic field reaction-front thickness for each individual field is evaluated and ensemble averaged according to

$$\delta_{c^*} = \left\langle \frac{1}{|\nabla \zeta_i|_{max}} \right\rangle ; i \in 1, \ldots, N. \tag{4.9}$$

This process is illustrated in Figure 4.1. This quantity is referred to as the *average stochastic field thickness* and will be used as a metric to define the resolution of a given simulation configuration.

The turbulent flame speeds presented in the proceeding analysis are determined through the global consumption rate given by the rate of conversion of products through the turbulent flame brush.

$$S_T = -\frac{1}{\rho_u Y_{u,f} A_0} \int_V \dot{\omega}_F dV \tag{4.10}$$

where ρ_u is the unburnt gas density, $Y_{u,f}$ is the fuel mass fraction in the unburnt gas, and A_0 is the flow cross sectional area.

4.1.4 Numerical Configuration

The numerical domain was comprised of simple inflow-outflow boundary conditions at the left and right boundaries respectively. An overly conservative isotropic grid spacing was used to ensure that there was a minimal influence of numerical errors in the simulations with the relatively low order numerical schemes used in the code. The grid spacing was chosen such that at each test point there were at least 20 grid points within an average stochastic field thickness for the "well-resolved", stochastic fields solutions. This grid spacing was deemed independent as the relative property change between successive grid refinements was approximately $\pm 0.05\%$. As a consequence of this, each of the thermo-physical conditions tested employed a different number of grid points.

4.1.5 Results and Discussion

Freely-Propagating Turbulent Flame - RANS

The one-dimensional RANS model is applied to the freely-propagating turbulent premixed flame for a range of u'/S_L and L_T/δ_L, and the turbulent flame speed predictions are reported in Figure 4.2 alongside DNS data of a freely propagating stoichiometric methane-air flame of Nivarti and Cant [15].

Given the assumptions and simplifications of the one-dimensional simulations, the results compare well with the DNS. The differences are expected to be because the closure for the turbulent viscosity employed in these simulations is based on scaling arguments only. For a more accurate representation of the turbulent viscosity, the pre-multiplying coefficient could have been tuned with supplementary turbulent flame data.

Even though use of non-local mixing models is known to be inaccurate in Lagrangian particle RANS-PDF modelling of premixed flames [57], the RANS-stochastic fields simulations using the IEM model successfully describes the correct premixed combustion behaviour seen in the data of Nivarti and Cant [15] namely the onset of the "bending" whereby the increase of turbulent flame speed saturates at higher u'/s_L due to the local saturation of flame surface density. In order be able to conclude definitively if the bending effect occurs, larger values of u'/s_L would need to be analysed.

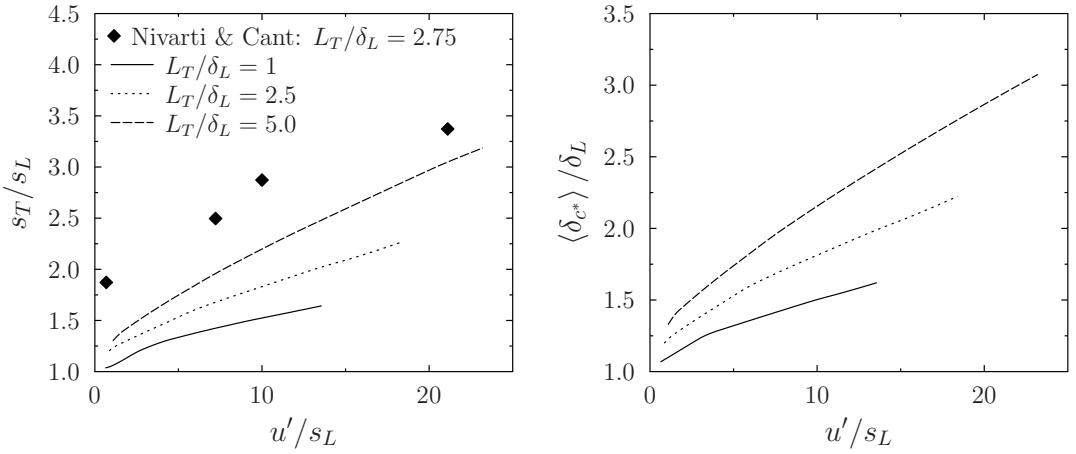

FIGURE 4.2: One-dimensional RANS stochastic fields results for freely-propagating turbulent flame. Normalised turbulent flame speed (left) and normalised average stochastic field thickness (right) versus u'/S_L for $L_T/\delta_L = 1,\ 2.5,\ 5$. Results plotted along with DNS data of Nivarti and Cant [15].

The relative success of non-local mixing models in the context of the stochastic fields PDF implementation in premixed combustion applications may be that as the stochastic fields are continuous in space, and a portion of the scalar dissipation process is accounted for by the spatial diffusion term in the stochastic fields equation which is absent in the Lagrangian-PDF formulation. As illustrated by Subramaniam and Pope [63], non-local mixing is not physically representative of the true mixing process. Thus, non-local micromixing models draw the composition into highly improbable regions of composition space which can lead to errors in flame speed. The introduction of the coupling between the spatial diffusion and reaction (representing a true physical process) in the stochastic field formulation may draw the compositions in the stochastic fields solutions towards a more physically-plausible composition manifold across the reaction front and, to varying extents, counteract the (non-physical) influence of a non-local micromixing model.

In order to evaluate the resolution requirements of the stochastic fields equation, the thermal thicknesses of the reaction fronts on the individual stochastic fields, δ_c^*, are evaluated as indicated in Figure 4.1 and ensemble averaged. The average thickness of the RANS stochastic fields is presented in Figure 4.2, showing that the thickness reduces towards the laminar flame thickness as $u'/S_L \to 0$. The thickness remains on the order of the laminar flame thickness across a wide range of turbulence conditions for the smaller filter width ratio. Resolution requirements in RANS simulations in general must be such to resolve the large scale flow features that drive the integral scale turbulence (i.e. length scales greater than L_T). However, when coupled with the stochastic fields approach that

is seen to require resolution of scales close to the much smaller laminar flame thickness, it is then necessary to dramatically increase grid resolution requirements when applied to premixed combustion.

Freely-Propagating Turbulent Flame - LES

In the context of LES, in addition to the well-resolved flame speed and stochastic field thickness distributions with changing turbulent conditions, the results are compared to the commonly assumed LES filter scale of $\Delta = \Delta_x$. Here, the $\Delta = \Delta_x$ results are denoted as the *coarse* simulations.

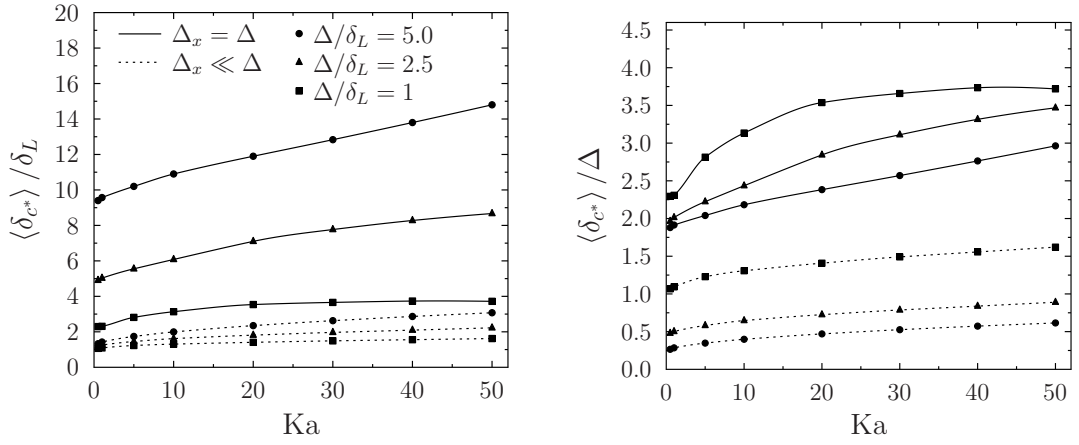

(A) Averaged stochastic field thickness normalised by laminar flame thickness

(B) Averaged stochastic field thickness normalised by filter width

FIGURE 4.3: Normalised averaged stochastic field thickness variation with Ka for $\Delta/\delta_L = 1,\ 2.5,\ 5$. Legend applied to both figures.

Figure 4.3 shows the results for both coarse and well resolved simulations for the average stochastic field thickness normalised by the laminar flame thickness (Figure 4.3a) and the filter width used in the corresponding simulation (Figure 4.3b). Figure 4.3a shows that for the well resolved simulations, the average thickness of the stochastic field reaction-fronts is on the order of the laminar flame thickness at low Karlovitz numbers and increases with Karlovitz number and filter length scale due to the increasing contribution of sub-filter scale diffusivity. A similar trend can be seen for the coarse simulations, however, the effect of numerical thickening is evident through large differences seen between the well resolved and coarse simulations. Additionally, numerical errors are highlighted from the large deviation of reaction front thickness compared to the laminar flame thickness as the Karlovitz number tends to zero. In the absence of numerical

errors, towards this limit, all cases *should* converge to a ratio of unity (or the laminar flame thickness); a behaviour not experienced by setting $\Delta_x = \Delta$.

Figure 4.3b on the other hand shows that if setting $\Delta_x = \Delta$, the absolute minimum of five grid points necessary within a reaction front ($\delta_{c^*}/\Delta_x \geq 5$) in order to give acceptable numerical resolution is not satisfied anywhere in the wide range of combustion conditions tested. Additionally, the numerical effects on stochastic field reaction front thickness is evident from the $\Delta_x = \Delta$ results at low Karlovitz number. For the $\Delta/\delta_L = 2.5, 5$ cases, the reaction front thickness is sufficiently smaller than the filter width and thus, numerical thickening acts to broaden the reaction front (or the scalar gradients) so that they extend across at least twice the grid spacing. This is evident from the $\Delta/\delta_L = 2.5, 5$ cases converging to $\langle\delta_{c^*}\rangle/\Delta \approx 2$ as Karlovitz number approaches zero.

An instantaneous output of the one-dimensional simulations is shown in Figure 4.4 to help illustrate the behaviour seen in Figure 4.3. In this figure, $\Delta/\delta_L = 1$ at Ka=1 and $\Delta/\delta_L = 5$ at Ka=50 outputs are shown for both well-resolved and coarse simulations as they represent the extreme conditions of those tested in the one-dimensional study.

From Figures 4.4a and 4.4b, it can be seen that for $\Delta/\delta_L = 1$ at Ka=1, both well-resolved and coarse simulations produce similar stochastic field distributions. Although still under-resolved by the definition of a minimum of 5 grid-points within a reaction-front (see Figure 4.3b), the small grid spacing of the coarse simulation results in less visible numerical spearing of the stochastic field reaction-fronts leading to average stochastic field thickness similar to those of the well-resolved simulation. Figures 4.4c and 4.4d, on the other hand, show the results for $\Delta/\delta_L = 5$ at Ka=50. These figures illustrate a more obvious degradation in smoothness and stochastic field reaction-front resolution for the coarse simulations. It can be seen that the large grid spacing (as a consequence of setting $\Delta_x = \Delta$) numerically smears the stochastic field reaction-fronts over at least two grid points, drastically increasing their thickness relative to the well-resolved simulations.

The numerical thickening of reaction fronts is an error that changes the physical predictions of the simulation in two main ways. First, the broadening of scalar gradients is expected to affect the local propagation speed of the reaction fronts in the stochastic fields. Second, the numerically-thickened reaction fronts are less susceptible to wrinkling by the resolved turbulence leading to an under-prediction in the overall resolved flame surface area.

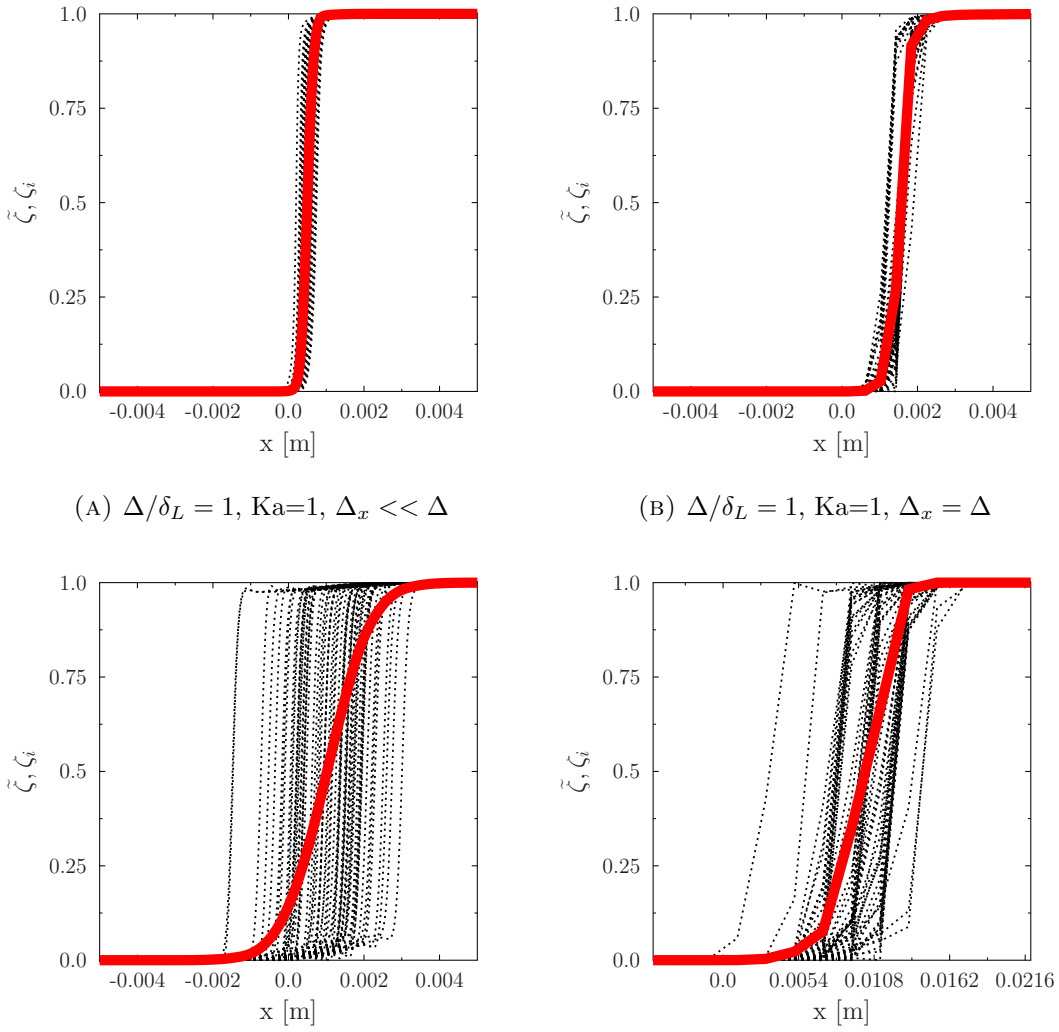

(A) $\Delta/\delta_L = 1$, Ka=1, $\Delta_x << \Delta$

(B) $\Delta/\delta_L = 1$, Ka=1, $\Delta_x = \Delta$

(C) $\Delta/\delta_L = 5$, Ka=50, $\Delta_x << \Delta$

(D) $\Delta/\delta_L = 5$, Ka=50, $\Delta_x = \Delta$

FIGURE 4.4: Example output of one-dimensional "LES" simulations for well-resolved and coarse grid resolutions. Red line denotes the filtered scalar field, $\widetilde{\zeta}$.

Figure 4.5a shows the results of the filter scale turbulent flame speed where the effect of the numerical thickening of scalar gradients is shown. For all filter width ratios tested, the $\Delta_x = \Delta$ cases result in varying degrees of over-prediction of sub-filter flame propagation speeds with the deviation increasing with increasing filter-width ratio and Karlovitz number. More importantly, as the Karlovitz number decreases to zero, the $\Delta_x = \Delta$ simulations do not converge to $s_{T_\Delta}/s_L = 1$ meaning the laminar flame speed is not recovered in these cases; a limiting behaviour that must be satisfied. Only the results for $\Delta/\delta_L = 1$ show reasonable agreement which indicates that even with approximately 3 grid points within a reaction front (see Figure 4.3b), *acceptable* predictions of flame speed may be obtained.

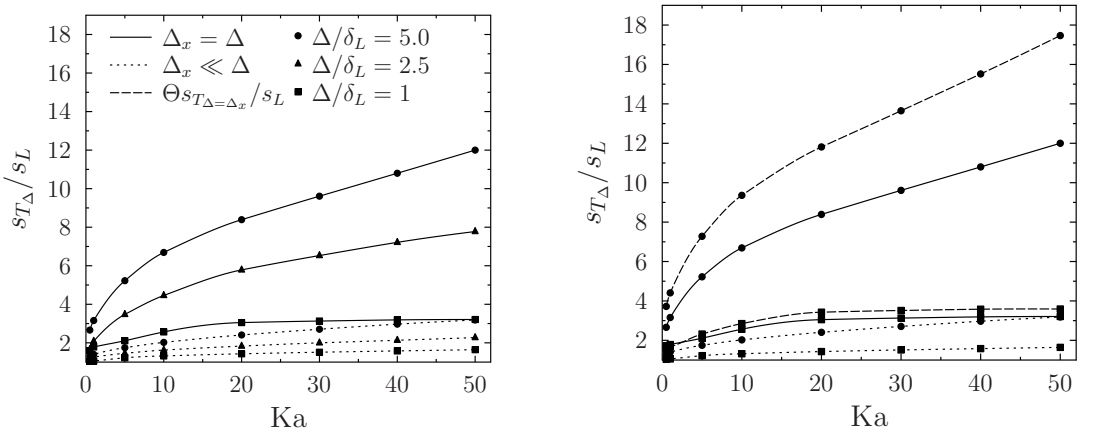

(A) Normalised sub-filter flame speed.

(B) Normalised sub-filter flame speed adjusted for lost flame surface area

FIGURE 4.5: Normalised sub-filter flame speed variation with Ka for $\Delta/\delta_L = 1,\ 2.5,\ 5$. Legend applied to both figures.

The effect of the numerical thickening on the under-prediction of flame surface area and its impact on consumption rate cannot be obtained directly from the one-dimensional simulations but it can be estimated using established models for sub-filter scale flame wrinkling in the context of Artificially Thickened Flame modelling [14, 22]. The efficiency function developed by Charlette *et al.* [14] provides an estimate for the contribution to flame surface area from turbulent motions below a particular length scale. Evaluating this efficiency function for the reaction front thicknesses of the well-resolved and coarse simulations, and taking their ratio, (Θ), gives an estimate for the proportion of the flame surface area remaining after the numerical thickening. The impact of the loss of flame surface area on burning rate due to numerical thickening is illustrated in Figure 4.5b by multiplying the propagation speed data for $\Delta_x = \Delta$ by Θ.

For clarity within Figure 4.5b, the adjusted flame speeds are only shown for the $\Delta/\delta_L = 1$ and 5 cases. The magnitude of the adjustment to the coarse flame propagation data increases with increasing filter width due to the increase in numerical thickening associated with larger filter widths for a given Karlovitz number. It can be seen that even for a filter width of $\Delta/\delta_L = 5$, which is common in current laboratory scale flame simulations, an almost 50% increase in turbulent flame speed is observed. This indicates a substantial proportion of flame surface area is neglected in stochastic fields when setting $\Delta = \Delta_x$.

4.1.6 Comparison of Stochastic Field Formulation

In this sub-section, the two Itô stochastic field formulations presented in Section 3.3 are compared, namely the high-Reynolds number 1998 formulation [23] and the low-Reynolds number 2016 formulation [24]. The purpose of this study is to analyse if the two formulations yield different predicitons and under what combustion conditions this might occur. This simplified investigation is performed as a necessary precursor to the 3D LES simulations in the proceeding section. It aims to help justify the choice of stochastic field formulation to be used in the 3D LES and to understand if/how the results of the simulation will be influenced by the inherent assumptions specific to a formulation.

The comparison between the formulations is made by analysing the predictions of sub-filter flame speeds over a range of filter widths and Karlovitz numbers. The flame speeds are obtained in a similar manner to the simulations in Section 4.1.5, namely, an "LES" of a one-dimensional freely-propagating turbulent flame. The numerical set-up is identical to that outlined in the section above, however, additional simulations are conducted with the high Reynolds number formulation of [23].

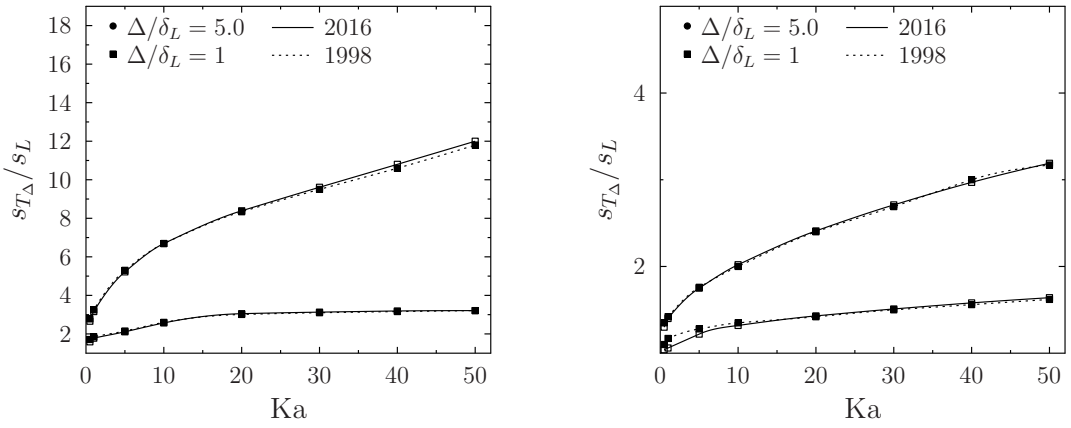

(A) $\Delta_x = \Delta$ (B) $\Delta_x \ll \Delta$

FIGURE 4.6: Normalised sub-filter flame speed variation with Ka for $\Delta/\delta_L = 1, 5$ comparing stochastic field formulations

It can be seen from Figure 4.6 that for increasing Karlovitz number (which is analogous to increasing Reynolds number for a fixed filter width), the results of both the formulations at a given configuration yield similar values of normalised flame speed, with the results of the $\Delta/\delta_L = 5$ simulations generally showing smaller deviations. These results

are consistent with the high Reynolds number limiting behaviour of both formulations outlined in Section 3.3 and in [24]. As the Karlovitz number decreases towards zero, the predictions of the two formulations begin to diverge with the 1998 formulation consistently over-predicting the flame speed. This over-prediction of the 1998 formulation over the 2016 was also seen in the low Reynolds number rod stabilized V-flame simulated in [88].

The coarse simulations in Figure 4.6a show almost identical evolutions of normalised flame speed across all Karlovitz numbers. For the $\Delta/\delta_L = 1$ case, at Karlovitz number of 0.5, the differences in flame speeds is approximately 3.1% while for the $\Delta/\delta_L = 5$ case it is approximately 2.2%. As the Karlovitz number increases, the differences between the simulations decrease and converge (to less than 1%) at a Karlovitz number of approximately 15 for $\Delta/\delta_L = 1$ and 3 for $\Delta/\delta_L = 5$. The relatively small differences seen in these sets of simulation at low Karlovitz numbers can be attributed to the increased numerical diffusion present at these coarse resolutions (see Section 4.1.5) and increased (numerical) scalar dissipation as a consequence.

This differences exhibited with the coarse simulations between the 1998 and 2015 formulation can also be seen by comparing the contributions of the Wiener term and micromixing terms produced by both models for a given simulation. Figures 4.7 and 4.8 show instantaneous magnitudes for the Wiener term and micromixing terms for the coarse simulations at a Karlovitz number of 1 and 50 respectively for different filter widths. Figure 4.7 shows that even at a Karlovitz number of 1, for a larger filter width (and thus larger Reynolds number) the contribution of terms is very similar for the 1998 and 2015 stochastic field formulations. Differences arise at the $\Delta/\delta_L = 1$ case which helps explain the marginal differences in flame speed seen in this particular regime in Figure 4.6. Figure 4.8 on the other hand, shows that at a Karlovitz number of 50, for $\Delta/\delta_L = 1$ and $\Delta/\delta_L = 5$, the contributions of the Wiener and micromixing terms are effectively identical across the 1998 and 2015 stochastic field formulations.

For the well-resolved simulations in Figure 4.6b the general trends exhibited by the coarse simulations remains the same except for larger deviation of flame speeds at larger Karlovitz number with respect to the coarse simulations. The differences between the two formulations at Ka=0.5 is 6% and 3.7% for $\Delta/\delta_L = 1$ and $\Delta/\delta_L = 5$ respectively. The Karlovitz number of convergence of the two formulations remains very close to

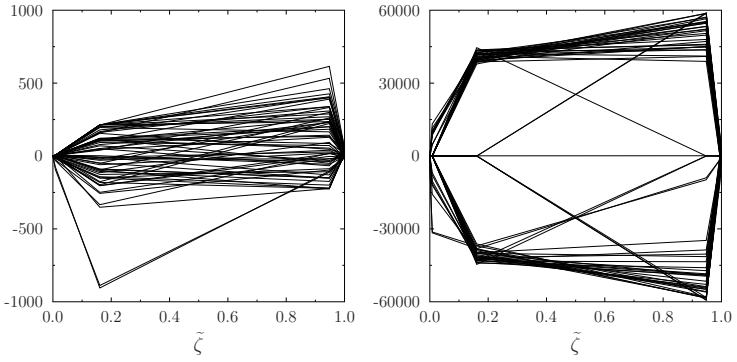

(A) $\Delta/\delta_L = 1$, 1998 model

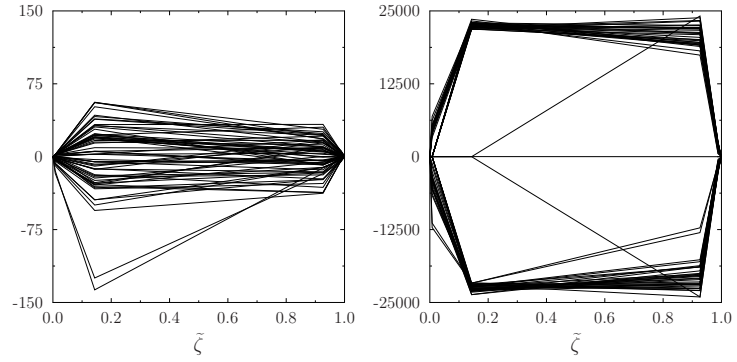

(B) $\Delta/\delta_L = 1$, 2015 model

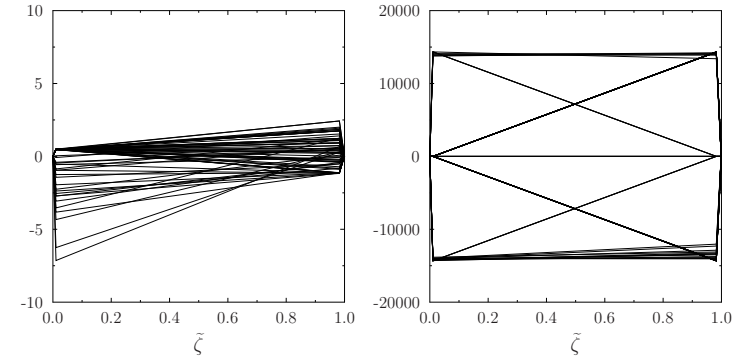

(C) $\Delta/\delta_L = 5$, 1998 model

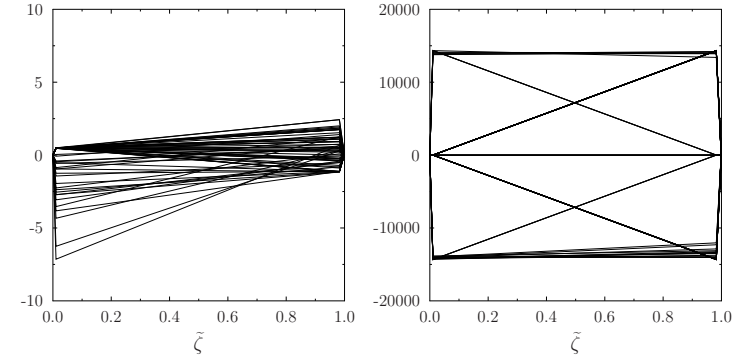

(D) $\Delta/\delta_L = 5$, 2015 model

FIGURE 4.7: Instantaneous conditional magnitudes of the micromixing (left) and Wiener (right) terms in Equation 3.35 of different fields for coarse simulations. Results shown for $\Delta/\delta_L = 1$ and $\Delta/\delta_L = 5$ at Ka=1. Magnitudes are conditioned on $\widetilde{\zeta}$.

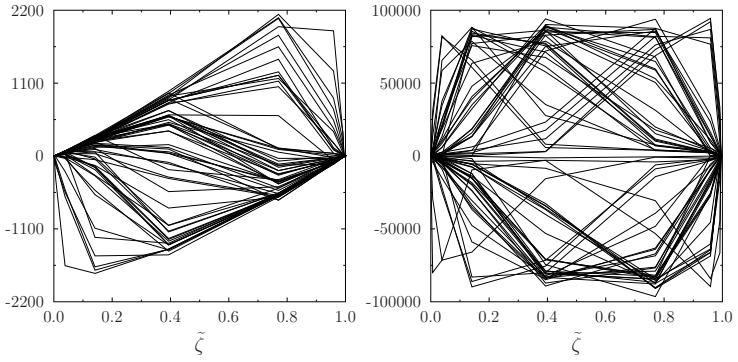

(A) $\Delta/\delta_L = 1$, 1998 model

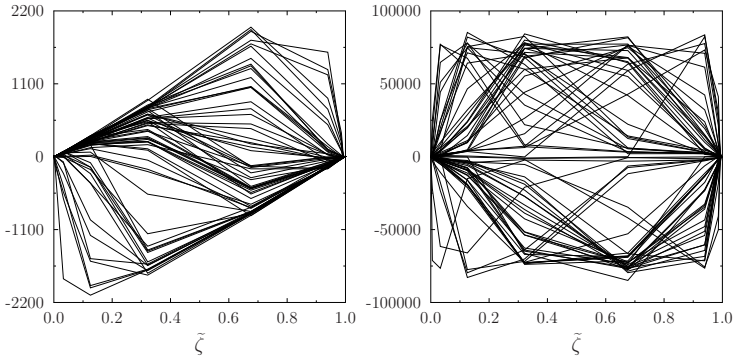

(B) $\Delta/\delta_L = 1$, 2015 model

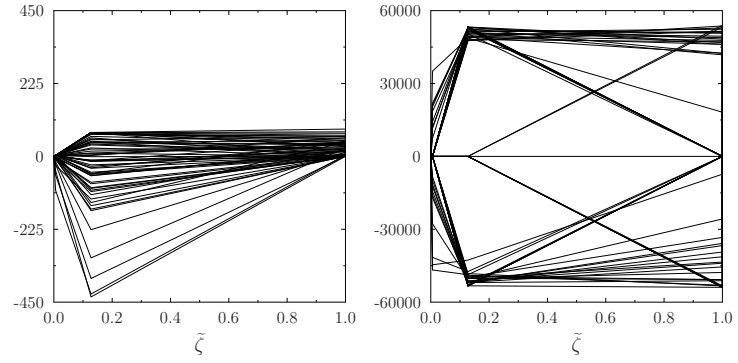

(C) $\Delta/\delta_L = 5$, 1998 model

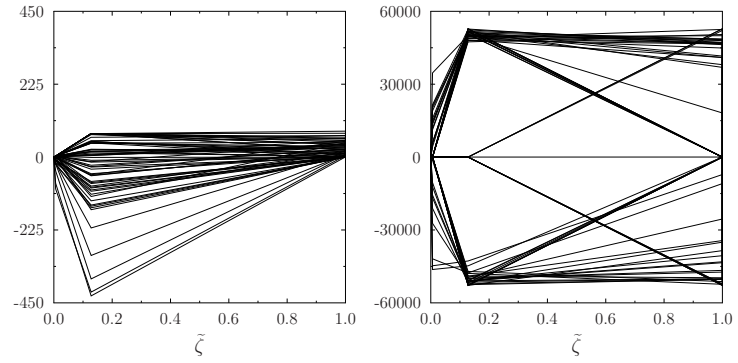

(D) $\Delta/\delta_L = 5$, 2015 model

FIGURE 4.8: Instantaneous conditional magnitudes of the micromixing (left) and Wiener (right) terms in Equation 3.35 of different fields for coarse simulations. Results shown for $\Delta/\delta_L = 1$ and $\Delta/\delta_L = 5$ at Ka=50. Magnitudes are conditioned on $\widetilde{\zeta}$.

those for the coarse simulations increasing from 15 to approximately 20 for $\Delta/\delta_L = 1$ and from 3 to approximately 5 for $\Delta/\delta_L = 5$. An increase that is likely an artefact of the reduction of numerical errors. Through Equation 4.3, an effective turbulent viscosity can be obtained for these Karlovitz numbers. Analysis shows that at these particular Karlovitz numbers of convergence for both the $\Delta/\delta_L = 1$ and $\Delta/\delta_L = 5$ cases, the turbulent viscosity is approximately two orders of magnitude greater than the molecular viscosity. This dominance of turbulence results in the 1998 formulation [23] obtaining a similar form to the 2016 [24] formulation. This justifies the similar predictions of the two models and verifies the expected high-Reynolds number similarities between the two formulations outlined in [24]. Similar to the coarse simulation, the magnitudes of the contributions of the Wiener term and micromixing terms are shown in Figures 4.9 and 4.10. These figures show almost identical trends as those observed in Figures 4.7 and 4.8 and the conclusions remain the same.

Interestingly, the $\Delta/\delta_L = 1$ results for the well-resolved simulations shows an increase in deviation from Ka=0.5 to Ka=1 (up to 10% from 6%), a trend not seen by any other configuration tested. The reason for this decrease in deviation at Ka=0.5 from Ka=1 between the two formulations is likely due to the convergence of the two stochastic field equations to the same functional form as Ka$\rightarrow$ 0. This convergence of the functional form of the two formulations is a result of the numerical framework (namely C_ϕ scaling - Equation 3.38) used in this thesis. With this particular scaling, as Ka$\rightarrow$ 0, $C_\phi \rightarrow \infty$ resulting in the dominance of scalar dissipation and the convergence of the stochastic field equations to the perfect mixing limit. This results in the stochastic field equation, of either formulation, obtaining a functional form of a deterministic reactive scalar transport equation (or the DNS limit - Equation 2.10). According to [24], this convergence towards perfect mixing as Ka$\rightarrow$ 0 is a necessary limit in the stochastic field formulation in order to recover the laminar flame speed in the absence of (sub-filter) turbulence. However, without adequate modification of C_ϕ, this limiting behaviour is not inherent to the 1998 formulation as the stochastic term does not vanish in this limit. Therefore, the use of this particular C_ϕ scaling in this numerical framework imposes this low-Reynolds number limiting behaviour on the 1998 model making both formulations consistent in the limit of Ka=0; a feature the scaling was designed to have [27]. That is, both formulations will recover the correct laminar flame speed in the limit of Ka$\rightarrow$ 0. Therefore, what is seen in Figure 4.6b with the decrease in deviation from Ka=1 to

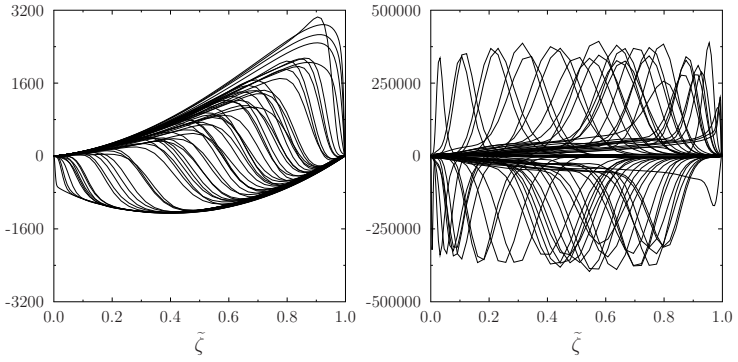

(A) $\Delta/\delta_L = 1$, 1998 model

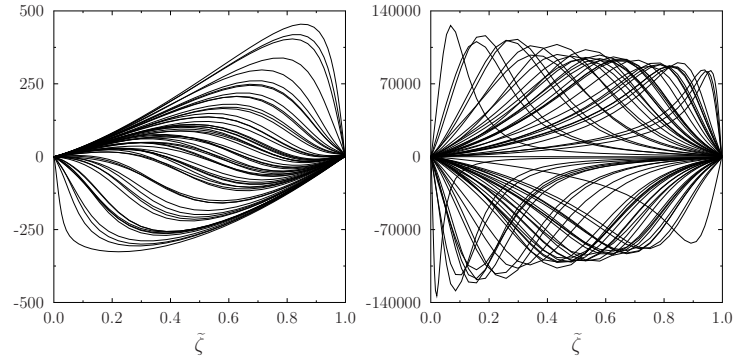

(B) $\Delta/\delta_L = 1$, 2015 model

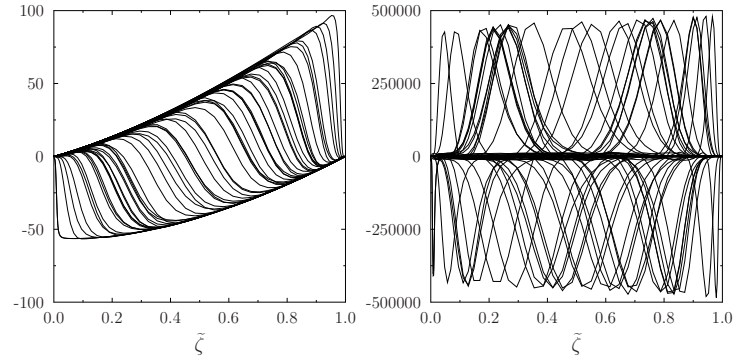

(C) $\Delta/\delta_L = 5$, 1998 model

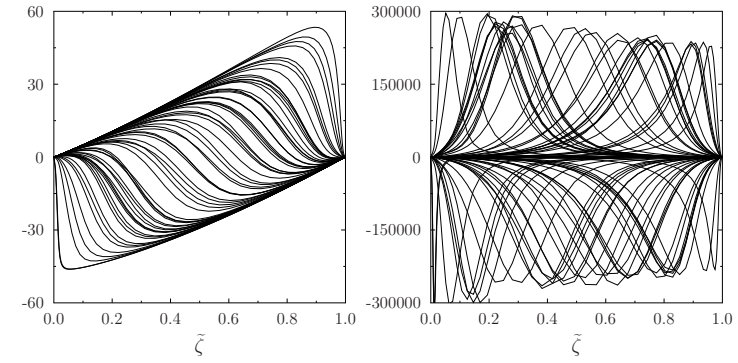

(D) $\Delta/\delta_L = 5$, 2015 model

FIGURE 4.9: Instantaneous conditional magnitudes of the micromixing (left) and Wiener (right) terms in Equation 3.35 of different fields for well-resolved simulations. Results shown for $\Delta/\delta_L = 1$ and $\Delta/\delta_L = 5$ at Ka=1. Magnitudes are conditioned on $\widetilde{\zeta}$.

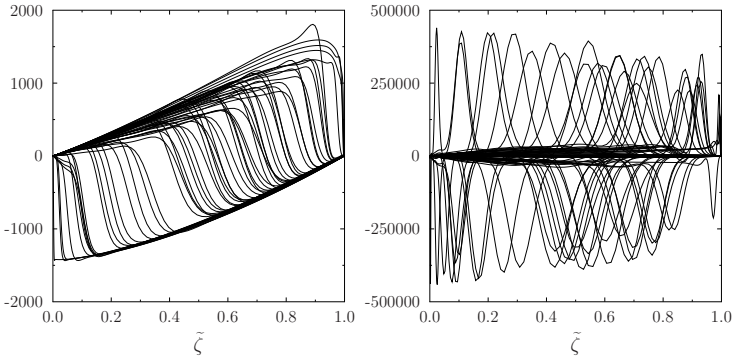

(A) $\Delta/\delta_L = 1$, 1998 model

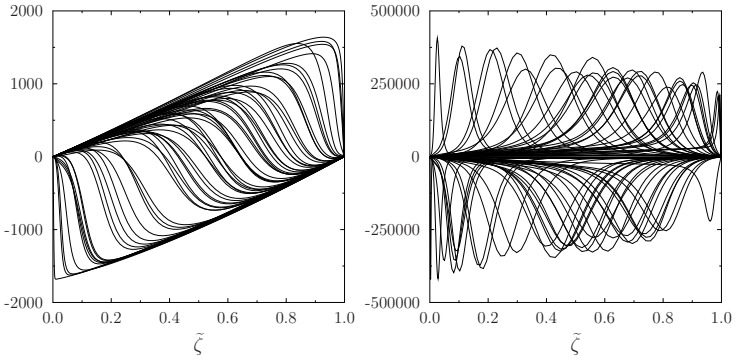

(B) $\Delta/\delta_L = 1$, 2015 model

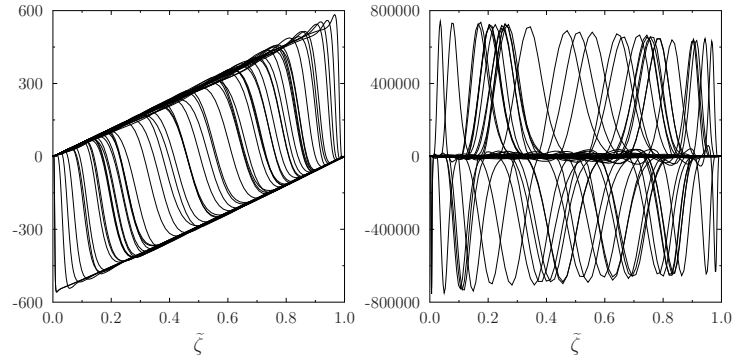

(C) $\Delta/\delta_L = 5$, 1998 model

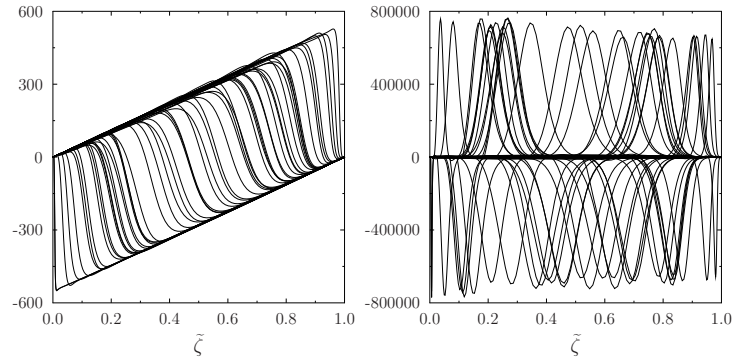

(D) $\Delta/\delta_L = 5$, 2015 model

FIGURE 4.10: Instantaneous conditional magnitudes of the micromixing (left) and Wiener (right) terms in Equation 3.35 of different fields for well-resolved simulations. Results shown for $\Delta/\delta_L = 1$ and $\Delta/\delta_L = 5$ at Ka=50. Magnitudes are conditioned on $\widetilde{\zeta}$.

Ka=0.5 is the beginning of the "re-convergence" of the two formulations towards the perfect mixing limit. In fact, for sufficiently small Karlovitz numbers, both formulations yield a normalised flame speed of unity.

This investigation has shown that in both with the particular numerical framework used here, in high- and very low-Reynolds number limits, the two formulations can produce similar results that are consistent with the necessary limiting behaviour. What remains an open investigation is understanding the differences between the two formulations at moderate Reynolds number (or $\Delta/\delta_L \approx 1$ and Ka≈ 1). However, the enforcing of the low-Reynolds number limiting behaviour on the 1998 formulation through the micromixing term suggest that with more appropriate micromixing modelling, the stochastic field simulations of either formulation can produce similar results. Investigation into the specific physical processes behind the differences at moderate Reynolds number (and possible mitigations) is beyond the scope of this thesis and warrants further investigation.

4.2 Turbulent Bunsen Flame LES

In this thesis, the piloted turbulent premixed Bunsen flame of Chen *et al.* [92] was simulated as this flame is well studied in literature. Prasad and Gore [96] used the FSD concept in the RANS context and Pitch and De Legeneste [97] used a level-set approach for LES. The majority of the simulations of this flame in the RANS context [57, 59, 71] were conducted to analyse, develop, and testing micromixing models in the Lagrangian PDF framework. This particular flame is attractive as a test case because this Bunsen flame uses the same burner for three different nozzle exit velocities leading to varying levels of turbulence-chemistry interaction. Therefore, with the same configuration, models can be tested for a range of premixed combustion conditions. More recently, this flame has been analysed in the context of LES for the composition FDF in the Lagrangian particle framework [76], and Eulerian Stochastic Field framework [85].

The burner, shown in Figure 4.11, is comprised of a main jet stream of premixed stoichiometric methane-air ejected from a nozzle of diameter $D = 12[mm]$, surrounded by a stabilizing laminar pilot stream of burnt stoichiometric methane-air combustion products estimated to have a velocity of $U_{pilot} = 1.32[m/s]$ following [85]. The details of

TABLE 4.2: Global operating conditions of the three flames

Flame	F1	F2	F3
$U_j\,[m/s]$	65	50	30
Re	52500	40300	24200
$k_c\,[m^2/s^2]$	12.7	10.8	3.82

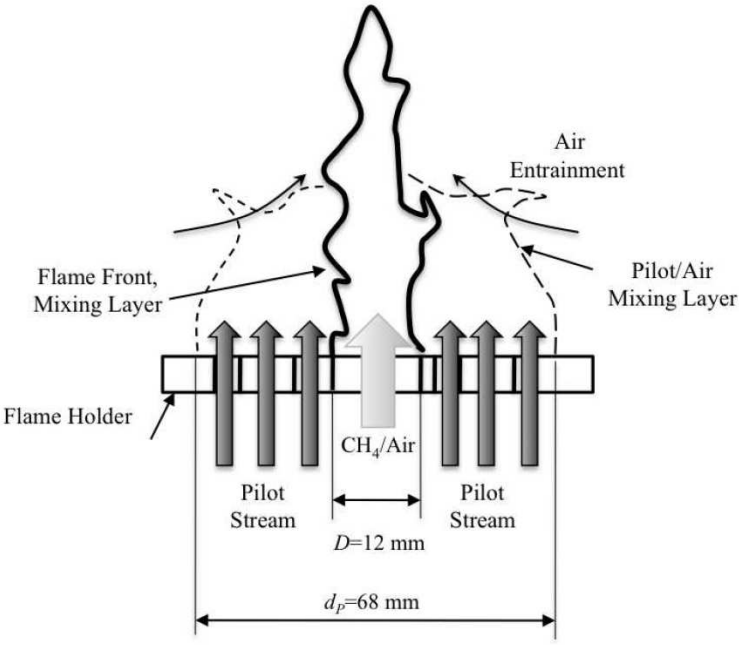

FIGURE 4.11: Schematic of the Chen et al. [92] taken from [85]

the jet exit velocity (U_j) , Reynolds number Re, and centreline kinetic energy (k_c) are shown in Table 4.2. The composition of the jet and the pilot are given in Table 4.3. The burner itself is surrounded by an axial co-flow of air at a velocity of $U_{air} = 0.22[m/s]$ and temperature of $T_{air} = 298[K]$.

TABLE 4.3: Pilot Stream Composition

Species	
Y_{O_2}	5.00E-4
Y_{H_2O}	0.1236
Y_{CO_2}	0.15
Y_{CO}	7.800E-4
Y_{H_2}	3.00E-5
Y_{OH}	1.20E-4
Y_{N_2}	0.7247

Due to the cool burner surface, significant heat losses were reported and remains one of the primary sources of uncertainty in simulating these flames. Consequently, pilot

temperatures different from the adiabatic flame temperature of 2245[K] have been used: 1936[K] [91], 2005[K] [71, 76], and 1785[K] [57, 71, 85]. The latter corresponding to losses up to 20%. In the present work, the pilot temperature is taken to be 1785[K].

The results of present simulation will be compared to the experimentally available data which include radial profiles of the mean velocity, turbulent kinetic energy, mean and variance of the temperature, and mean mass fractions of CH_4, CO_2, CO, O_2, OH, and H_2O. The mass fractions were obtained using 2D Rayleigh Thermometry, and the one-dimensional combined Raman, Rayleigh, and laser-induced predissociation fluorescence technique. The published error in the measurements of the mean velocity is estimated to be less than 1%, and the error of the mean temperature is expected to be less than 10%. The error in the measurements of minor species (CO, H_2, OH) is within 20% to 25%, and the major is between 8% and 15% [92].

In addition to the mean flow parameters of the flame, Chen *et al.* [92] also provide estimates of time and length scales at the centre of the nozzle. Details are given in Table 4.4. The estimated Ka and Da numbers place these simulation in the thin reaction zones regime as shown in Figure 4.12. However, as reported in Chen *et al.* [92], they are quite approximate and change considerably within the flame.

TABLE 4.4: Estimate of timescales, Ka and Da of F1-F3 Flames. Additional data available in [92]

Flame	$\tau_c\,[ms]$	$\tau_t\,[ms]$	$\tau_\eta\,[ms]$	$s_L\,[m/s]$	$u'\,[m/s]$	$\delta_{th}\,[mm]$	$\delta_t\,[mm]$	Da	Ka
F1	0.44	0.51	0.04	0.4	4.7	0.175	2.4	1.16	11
F2	0.44	0.65	0.06	0.4	3.7	0.175	2.4	1.48	7.33
F3	0.44	1.10	0.13	0.4	2.18	0.175	2.4	2.5	3.38

Numerical Setup

The computational domain used in these simulations has an axial length of $x/D = 15$ and transverse length of $y/D = 15$. Two different computational grids are used: a fine grid characterised by 0.5 mm grid spacing at the inlet, and a coarse grid characterised by 1.0 mm grid spacing at the inlet.

In addition to the coarse ($\Delta_x = \Delta = 1.0$ mm) and fine ($\Delta_x = \Delta = 0.5$ mm) simulations, a third case is conducted which is denoted as the *improved resolution* case. The improved

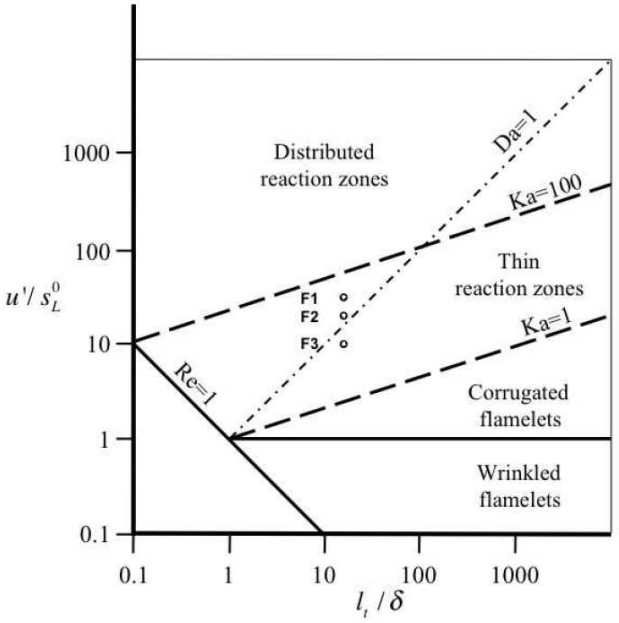

FIGURE 4.12: Location of F1-F3 flames on premixed regime diagram [85]

resolution case is characterised by a numerical grid spacing set to half the filter width of the coarse simulation ($\Delta_x = 0.5$ mm, $\Delta = 1.0$ mm). The purpose of this simulation to reduce the influence of numerical errors from modelling errors present within the stochastic fields framework in a similar manner to the work of Vreman *et al.* [95].

In all the simulations, the grids are Cartesian, with a uniform region of grid around the inlet with transverse extent equal to twice the nozzle diameter. In the axial direction, the grid spacing increases linearly. The turbulent inflow is modelled with the digital filter based method of Klein *et al.* using the mean and RMS velocity profiles from [92] and by assuming a constant integral length scale of $1.2mm$. The velocity profiles imposed in these simulations were obtained from experiment at $x/D = 0.04$ removing the necessity to resolve the jet rim on the computational mesh.

A total of sixteen stochastic fields in the form of the 2016 Valiño formulation [24] (Equation 3.35) are used in the three-dimensional simulations. The 2016 formulation was chosen to maintain consistency with the one-dimensional simulations, however, the choice of formulation is not expected to influence the results of the proceeding simulations for the following reasons: First, the numerical resolutions used in these 3D simulations are far from those used in the well-resolved one-dimensional simulations. Comparing the coarse and well-resolved, one-dimensional simulation results of Figure 4.6, the numerical resolution generally has a larger impact on the predicted flame speed compared to the choice of

stochastic field formulation. Second, Stöllinger and Heinz [59] provided a estimation of combustion regime along the T=1500K iso-surface for the F3 flame and illustrated that the Karlovitz number was generally well above 1. From the results shown in Figure 4.6, at higher Karlovitz numbers, the choice of formulation becomes inconsequential. Thus, these two points together support the decision to use the 2016 formulation and that the influence of the choice of stochastic field formulation will have a marginal impact on the proceeding 3D LES solution compared to the overarching influence of numerical errors that this particular LES is attempting to investigate.

In this thesis, only the F3 and F1 cases were simulated as they represent the extreme conditions available for this series of flame. Each simulation for either flame was run for a total of 18 flow-through times: eight for stabilization of the flow and to remove transients, and ten for obtaining statistics. The convective velocity of the shear layer was used to determine a flow-through time and was approximated through [98]

$$U_c = U_{jet}\left(\frac{1+r\sqrt{s}}{1+\sqrt{s}}\right), \tag{4.11}$$

where $r = U_{coflow}/U_{jet}$ and $s = \rho_{coflow}/\rho_{jet}$. The convective velocity is approximately $21m/s$ for the F3 case and $41.5m/s$ for the F1 case leading to a flow-through time of about 8.5ms and 4.3ms respectively. Therefore, the total simulation time was approximately 155ms and 78ms for the F3 and F1 cases respectively. The computational time-step for the F3 and F1 cases are $4.6\mu s$ and $2.3\mu s$ respectively.

Due to the use of single-step chemistry and the omission of certain chemical species, the pilot composition was modified from that outlined in [92] and is given in Table 4.5.

Table 4.5: Pilot Stream Composition

Species	Chen *et al.* [92]	Current Work
Y_{O_2}	5.00E-4	5.00E-4
Y_{H_2O}	0.1236	0.1236
Y_{CO_2}	0.15	0.15
Y_{CO}	7.800E-4	-
Y_{H_2}	3.00E-5	-
Y_{OH}	1.20E-4	-
Y_{N_2}	0.7247	0.7259

The spatially-filtered momentum equations are closed with the constant-coefficient Smagorinsky model for the sub-filter scale turbulent stresses [36], with a constant (C_s) equal to

0.09. The turbulent diffusivity is modelled assuming turbulent Schmidt and Prandtl numbers of 0.7.

4.2.1 Flame Structure

An illustration of the instantaneous filtered temperature fields for an individual stochastic field from the three simulations is shown as colour maps on a plane through the burner centreline in Figure 4.13 for the F3 flame, and Figure 4.14 for the F1. A qualitative analysis of these figures show that a stochastic field in the coarse simulation exhibits less fine-scale structures than the other simulations. The colour maps of the improved resolution and fine simulation on the other hand show arguably similar levels of wrinkling. Given that the LES filter widths between the coarse and improved resolution are the same, the difference in observed wrinkling indicates this absence of finer scales is a product of numerical diffusion and thickening of the instantaneous field reaction front. The effect of numerical thickening is demonstrated by evaluating the inverse average progress variable gradient magnitude of the stochastic fields conditioned on the progress variable giving maximum heat release, $\langle |\nabla \zeta_{c,(i)}| \mid \zeta_{c,(i)} = 0.68 \rangle^{-1}$. For the F3 case, this analysis determined that the inverse average progress variable gradient magnitude on the stochastic fields for the coarse, improved resolution, and fine simulations are 2.68 mm, and 1.8 mm, and 1.71 mm respectively. For the F1 case, the average stochastic field thicknesses are determined to be 3.5 mm, 2.3 mm, and 2.3 mm for the coarse, improved resolution, and fine simulations respectively. The similar thicknesses of the improved resolution and the fine simulations illustrate that the stochastic field thickness is set by the numerical resolution, even with $\Delta = 2\Delta_x$.

The larger average stochastic field thickness obtained for the F1 case is a product of the increased turbulence intensity present in this particular flame. The consequence of this increased average stochastic field thickness is an increase in the resolution of the respective F1 and F3 simulations. For the F3 flame, the average number of grid points in a stochastic field reaction front is on the order of 2.6, 3.6, and 3.4 for the coarse, improved resolution, and fine simulations, while for the F1 the respective resolutions were 3.5, 4.6, and 4.6. As such, from the one-dimensional investigation and analysis in the preceding section, the improvement in resolution generates the expectation that, in general, the results of the F1 simulations should be in better agreement with experiment.

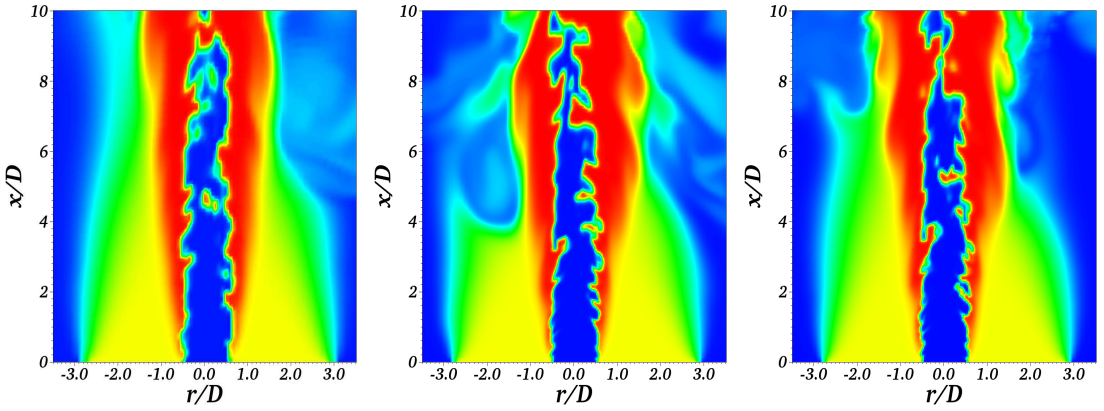

FIGURE 4.13: Instantaneous temperature field of an individual field from the F3 flame LES with $\Delta_x = \Delta = 1.0$ mm (left),$\Delta_x = 0.5$ mm & $\Delta = 1.0$ mm (mid), and $\Delta_x = \Delta = 0.5$ mm (right).

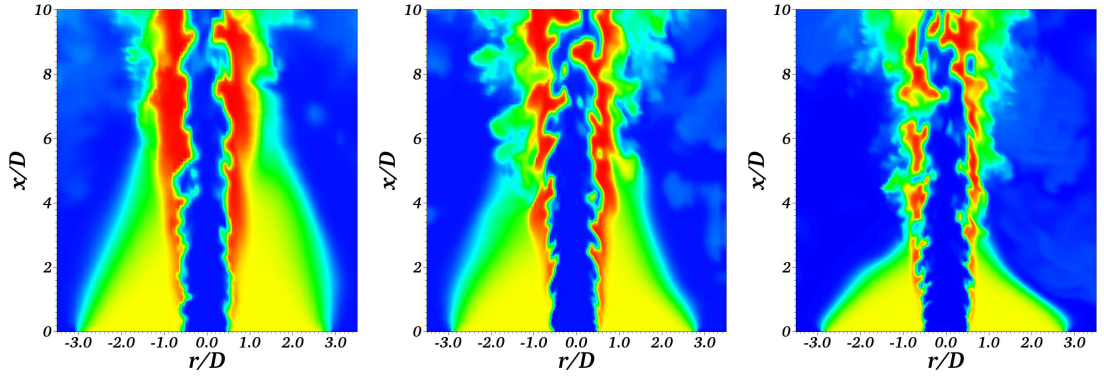

FIGURE 4.14: Instantaneous temperature field of an individual field from the F1 flame LES with $\Delta_x = \Delta = 1.0$ mm (left),$\Delta_x = 0.5$ mm & $\Delta = 1.0$ mm (mid), and $\Delta_x = \Delta = 0.5$ mm (right).

Reactive Scalar Distributions

For the F3 and F1 cases respectively, the radial variation of the time-averaged filtered methane and oxygen mass fraction are shown in Figure 4.15 and Figure 4.17, and carbon dioxide and water vapour in Figure 4.16 and Figure 4.18.

Overall, the scalar distribution shown for the F3 case in Figure 4.15 and 4.16 clearly show an under predicted flame height with a substantial difference between the coarse, and the improved and fine resolution cases, with the latter two showing almost identical scalar predictions across all reactive scalars.

The methane and oxygen mass fraction in Figure 4.15, to varying extents, are under-predicted across all simulations at every axial station. The oxygen mass fraction appears to exhibit an excessive co-flow entrainment rate, however, the degradation in oxygen

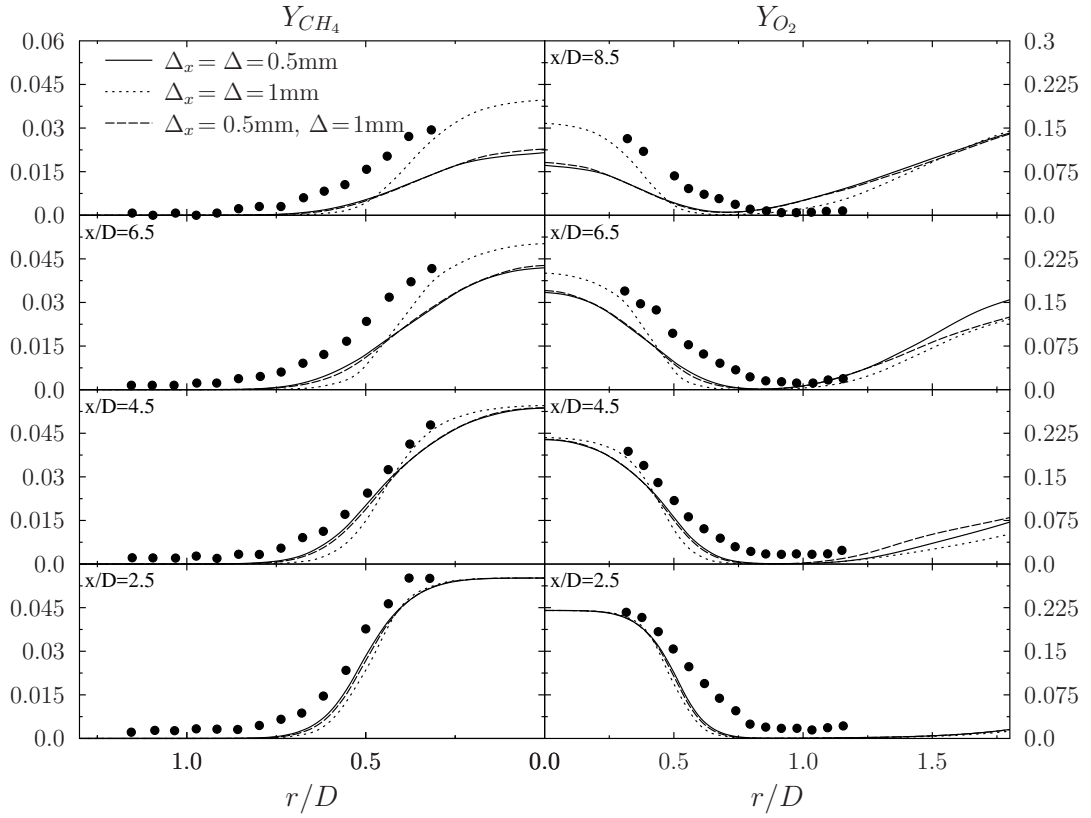

FIGURE 4.15: F3 radial distributions of the time-averaged methane mass fraction $\langle\widetilde{Y_{CH_4}}\rangle$ and oxygen mass fraction $\langle\widetilde{Y_{O_2}}\rangle$ at various axial locations. Symbols denote experimental measurements.

mass fraction with radial (and axial) location is likely due simply to the incorrectly predicted flame position. The similarity of the results between the different filter and grid spacings in the near jet region at $x/D = 2$ is a product of the high turbulence intensity in this region [57] compared to the downstream locations and to the increased numerical resolution as a consequence of the thickening of the reaction front in this region.

To a lesser extent, similar behaviour can be seen in the scalar distributions of the F1 simulations shown in Figure 4.17 and Figure 4.18, however, in this particular flame, the under-prediction of the flame height is comparatively small. The methane mass fraction distributions are predicted very well for all three simulations except for the final station at $x/D = 10.5$ where a slight under-prediction is seen. Similarly, the oxygen mass fractions are predicted well for small radial distances but progressively deviate with increasing radial location.

Trends similar to those seen in the F3 simulations can be seen in the distributions of

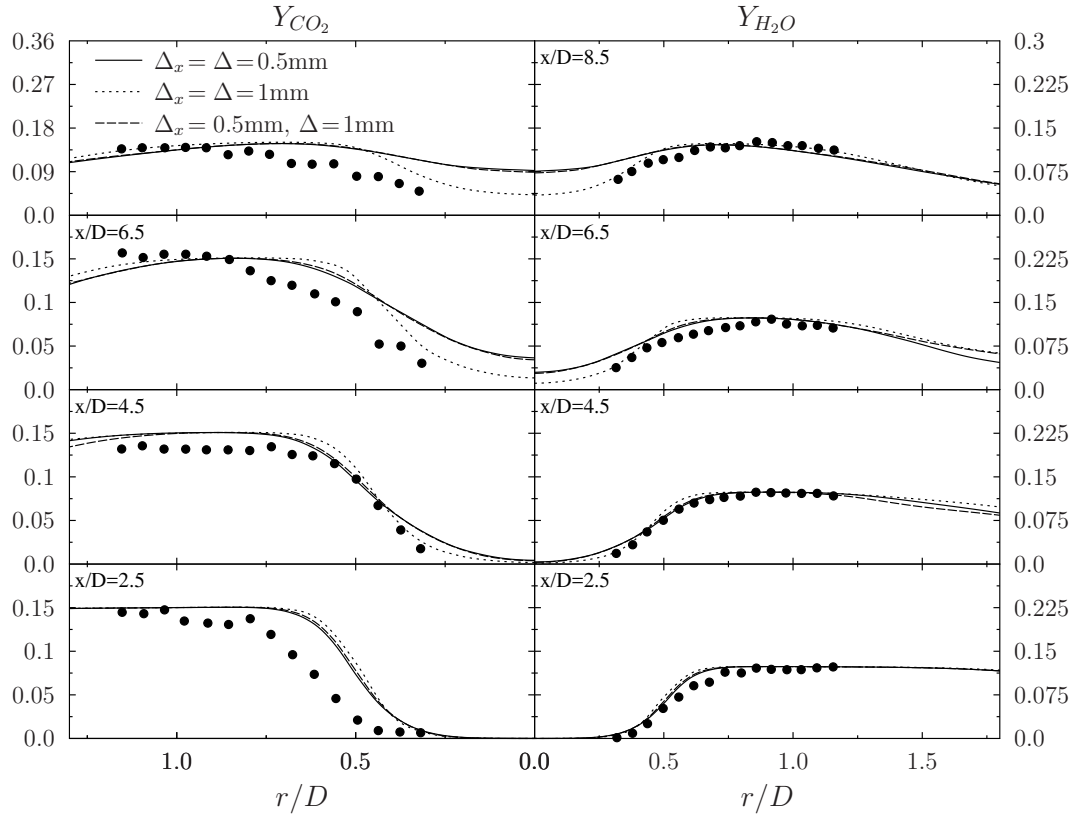

FIGURE 4.16: F3 radial distributions of the time-averaged carbon dioxide mass fraction $\langle\widetilde{Y_{CO_2}}\rangle$ and water vapour mass fraction $\langle\widetilde{Y_{H_2O}}\rangle$ at various axial locations. Symbols denote experimental measurements.

products for the F1 case in Figure 4.18. The water vapour mass fractions are predicted very well across at all axial stations with the fine simulation slightly under-predicting at $r/D = 0.75$ at the first axial station. A similar under-prediction can be seen at the same axial location for carbon dioxide. However, the overall improved predictions of methane and oxygen generally result in similarly good predictions of carbon dioxide. This under-prediction of product mass fractions and a slight over-prediction of oxygen mass fraction at the first axial station for the fine F1 simulation may elude to an excessive co-flow entrainment rate.

The under-predicted flame height across both the F3 and F1 simulations can be largely attributed to varying degrees of over-predicted reaction rate. This is identifiable by deficient centreline distribution of reactants and excess centreline of products compared to experiment. The excessive reaction rate is likely attributed to: (i) numerical errors due to the linearisation of the stochastic field equations; (ii) sensitivity to the inlet velocity and scalar fields imposed; (iii) accuracy of the stochastic field LES modelling.

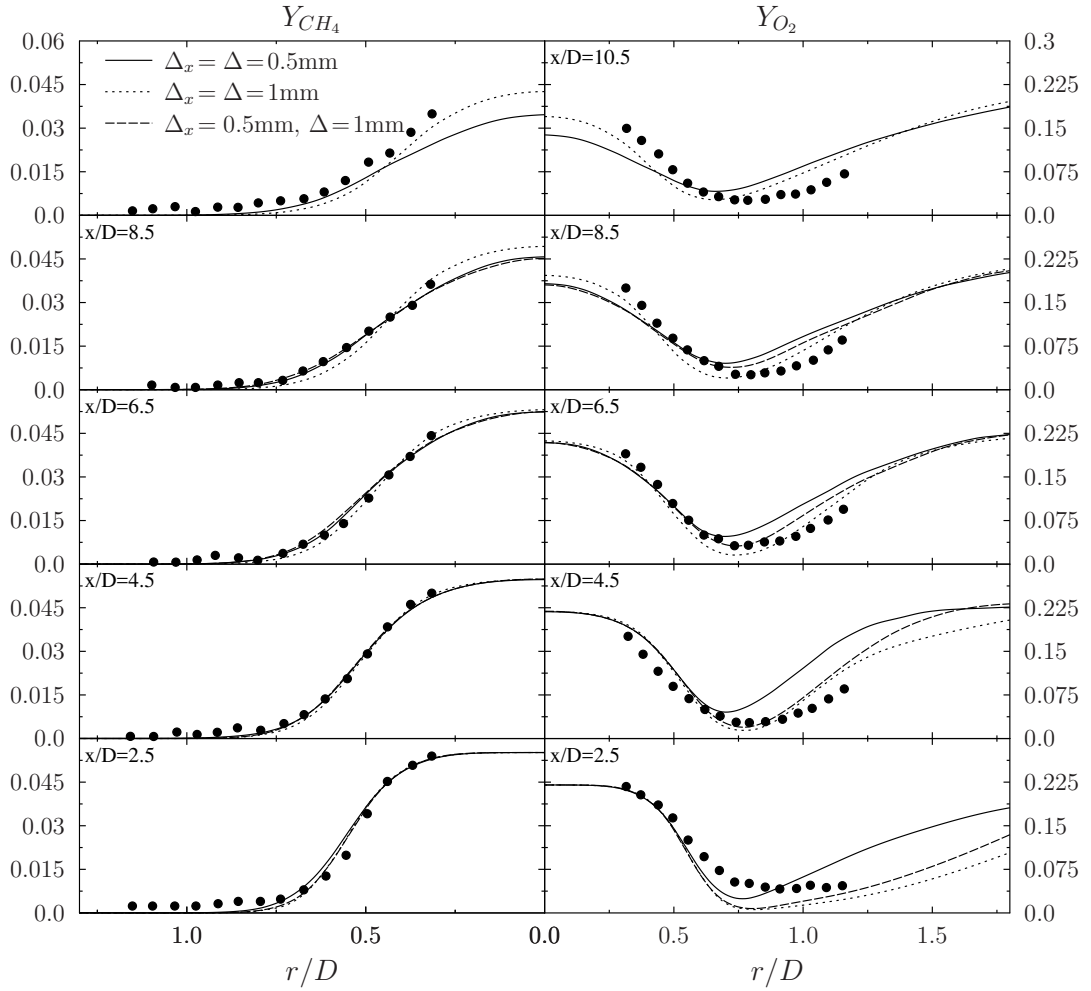

FIGURE 4.17: F1 radial distributions of the time-averaged methane mass fraction $\langle\widetilde{Y_{CH_4}}\rangle$ and oxygen mass fraction $\langle\widetilde{Y_{O_2}}\rangle$ at various axial locations. Symbols denote experimental measurements.

The effect of numerical errors on the solution is evident from the differences observed between the simulations with $\Delta_x = 1$mm and $\Delta_x = 0.5$mm. For a well resolved, unstrained, freely propagating laminar flame simulation, the 1-step mechanism employed in this study yields a laminar flame speed of 0.3825 m/s; close to the accepted value of laminar flame speed of stoichiometric methane-air at 300K. However, at the numerical grid resolutions present in these simulations, the laminar flame speeds are 1.3m/s and 0.7m/s for the $\Delta_x = 1.0$ and $\Delta_x = 0.5$ grid spacings respectively - a difference solely influenced by increased numerical diffusion. Based on the well established idea that numerical errors are a function of numerical grid spacing (for a given numerical order of accuracy) the expectation would then be that the coarse simulation would have the shortest flame height of all the simulations.

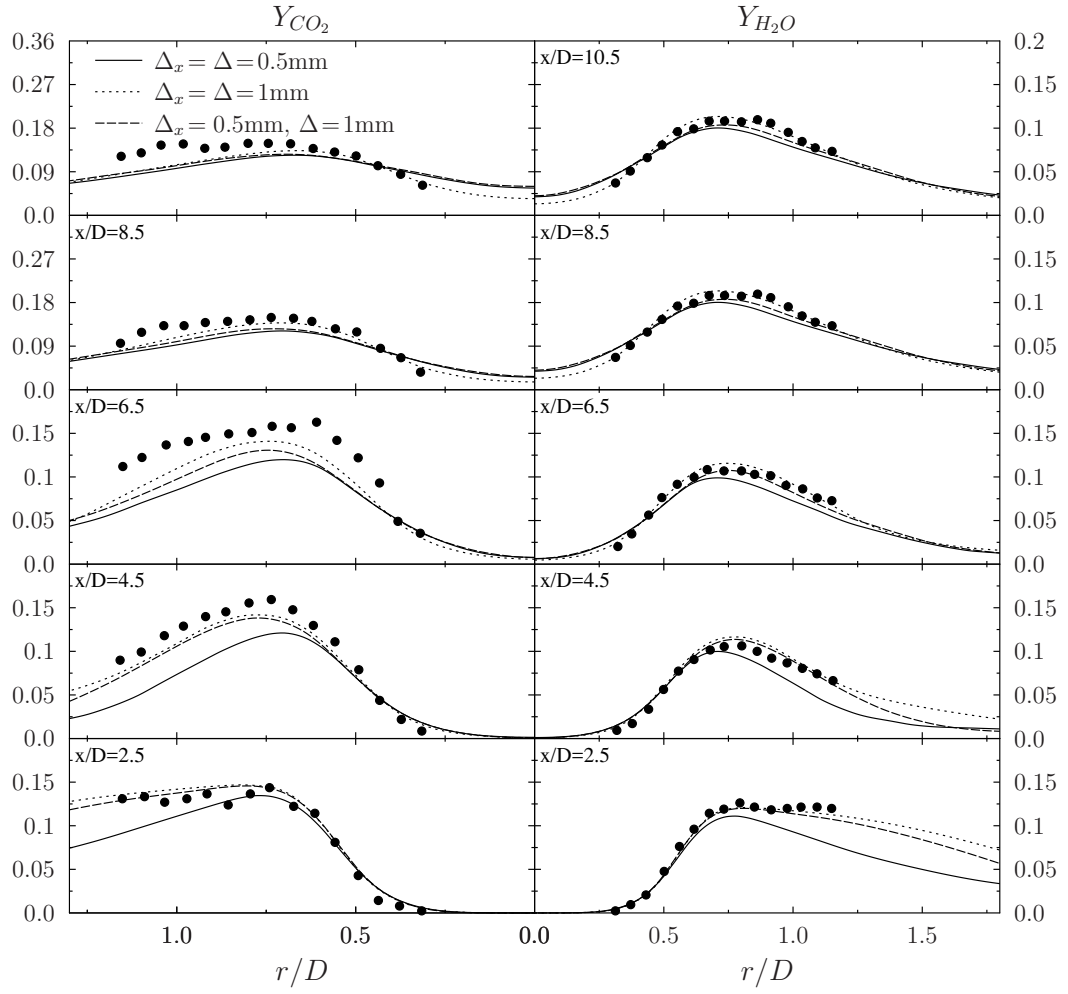

FIGURE 4.18: F1 radial distributions of the time-averaged carbon dioxide mass fraction $\langle\widetilde{Y_{CO_2}}\rangle$ and water vapour mass fraction $\langle\widetilde{Y_{H_2O}}\rangle$ at various axial locations. Symbols denote experimental measurements.

In addition to numerical errors increasing diffusion rates, as mentioned in the previous section, the increased numerical diffusion numerically thickens the flame and reduces its ability to be wrinkled by resolved scale turbulence. It is evident that even with the coarse simulations having almost double the laminar flame speed compared to the fine simulation, the overall burning rate in these particular simulations is primarily dominated by the generation of flame surface. This suppression of turbulent flame surface area ultimately results in a reduced local turbulent flame speed for the coarse simulation with respect to the more numerically resolved simulations.

Figure 4.19 shows radial distributions of normalised axial velocity for the F1 ($U_o = 65.0$ m/s) and F3 flame ($U_o = 30.0$ m/s). Compared with experiment, the normalised velocity profiles for the F3 case exhibit a more obvious degradation in agreement with increasing

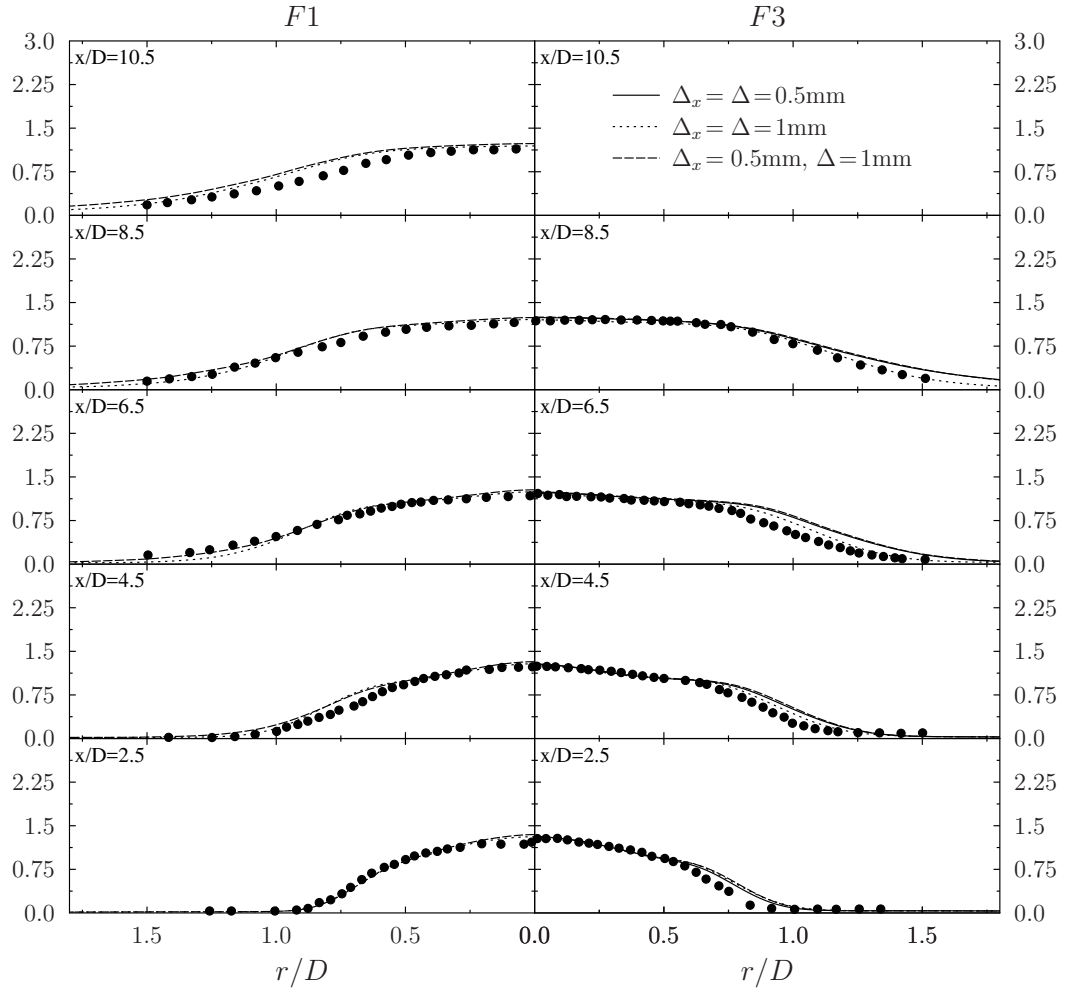

FIGURE 4.19: Radial distributions of the time-averaged normalised axial velocity at various axial locations for Flames F1 and F3. Symbols denote experimental measurements.

radial distance from the centreline. At all axial stations, the improved and fine resolution simulations are almost identical and over-predict the velocity to a greater extent than the coarse. The F1 velocity distributions on the other hand show that all three simulations produce almost identical results with a marginal over-prediction at the final axial station.

The sensitivity of the velocity field to the prediction of reactive scalar distribution can be seen by the difference in velocity field predictions between the F3 and F1 flames, however, it remains fairly weak. The primary observation is that under-prediction of reactive scalars leads to over-predictions of axial velocity. This is because the location of the flame front has a direct influence on the thermal expansion and acceleration of combustion gases through the flame. Therefore, the primary contribution to the

over-prediction of axial velocity is suspected to be the over-predicted reaction rate (or under-predicted flame height).

4.2.2 Influence of Stochastic Field Formulation

In Section 4.2, justification for the use of the 2015 stochastic fields formulation was given on the basis of the expected combustion regime indicated by [59], and from the one-dimensional simulations of Section 4.1.6 that illustrated that for the conditions expected in the Bunsen case being analysed, the differences between the models is likely insignificant. Nevertheless, to verify these assumptions, the more flamelet-like flame, the F3, was simulated with the 1998 formulation with the coarse, improved resolution, and the well-resolved configurations to directly compare the two formulations. The objective of this particular investigation is to assess if the choice of formulation influences the simulation predictions for the numerical configurations used in this thesis. The results for the time-averaged methane mass fractions of both stochastic field formulations is shown in Figure 4.20.

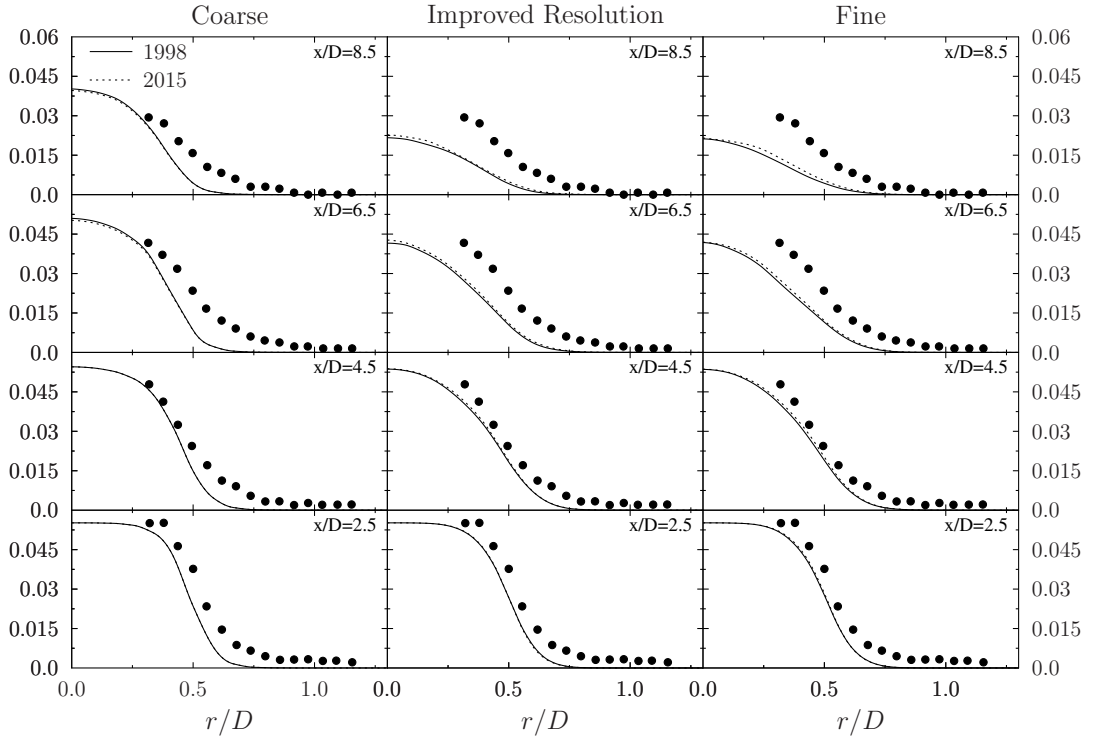

FIGURE 4.20: Comparison of methane mass fraction $\langle \widetilde{Y_{CH_4}} \rangle$ distributions between the 1998 and 2015 stochastic field formulation for various filter and grid sizes.

As expected, Figure 4.20 shows that the predictions of both models are effectively identical for all computational grids tested. The coarse simulation shows profiles that are indistinguishable at all axial stations. For the fine and improved resolution simulations, the results of both models are identical at the $x/D = 2.5$ station and, although negligible, a slight deviation of the profiles can be seen to grow with each downstream axial station. This is due to the change of combustion regime to increasingly flamelet like conditions with downstream location. This miniscule deviation at $x/D = 8.5$ may suggest that towards the flame tip, the numerical combustion regime is beginning to encroach on the limit of validity of the high-Reynolds number assumption that yields similar functional forms of the 1998 and 2015 stochastic field models. If the combustion regime were to become more flamelet-like than that experienced in the F3, then perhaps a more distinguishable difference between stochastic field formulations would be visible. Nevertheless, the results of these comparisons of stochastic field formulation confirms that in this thesis, with the numerical configurations used, the results of the simulations are independent of the choice of stochastic field formulation.

4.2.3 Sensitivity to Inflow Conditions

In addition to the effects of numerical diffusion on flame propagation speed mentioned above, an additional influence on the flame height prediction are inlet boundary condition. In this particular case, as the physical boundary conditions have been taken as in [85], the sensitivity to the numerical boundary conditions are analysed - specifically, the prescribed turbulent integral length-scale.

A single (constant) integral length-scale used in these simulation equal to 1.2 mm in the premixed jet portion of the burner which is approximately half the experimentally-measured centreline value. A single value was used due to a limitation in the synthetic digital turbulence generation method of Klein *et al.* [99] in that a spatially varying integral length scale is not easily implemented into the method. With this limitation, and since the experimentally measured integral length scale decreases in size from approximately 2.4 mm at the centreline to effectively zero at the jet boundary, a constant (and approximate) midpoint value was used. The consequence of this assumed constant integral length scale in the premixed jet is that the turbulent length scales in proximity to the jet boundary are over-predicted. Implications of this over-prediction is that the

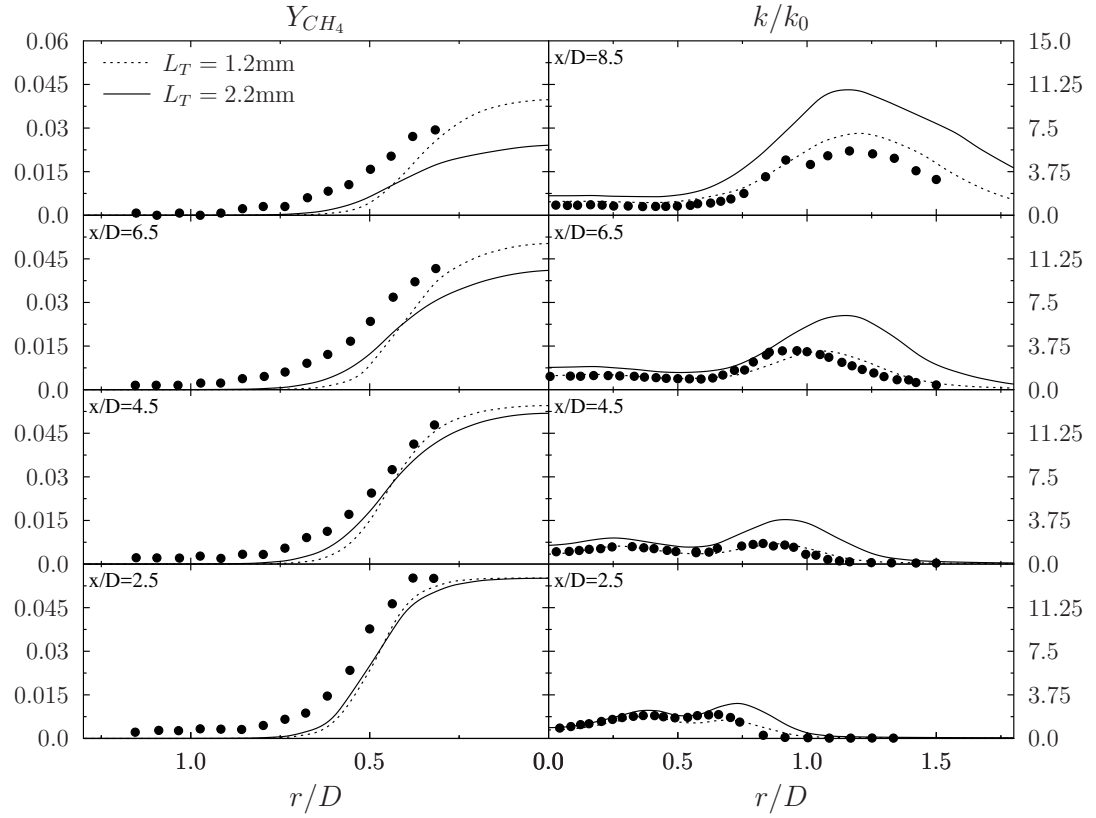

FIGURE 4.21: F3 radial distributions of the time-averaged methane mass fraction $\langle\widetilde{Y_{CH_4}}\rangle$ and turbulent kinetic energy at various axial locations for different inflow integral length-scales. Symbols denote experimental measurements. Symbols denote experimental measurements.

larger turbulent scales in this region lead to an under-prediction of turbulent kinetic energy dissipation rate since that is proportional to the ratio of estimated versus actual integral length scale size. The consequence is then excessive turbulent kinetic energy at the downstream locations. A secondary effect of the larger mixing length-scales in this region is an an over predicted turbulent diffusivity leading to unrealistic mixing.

To investigate the sensitivity of the prescription of integral length scale on the solution, additional simulations were conducted of the F3 flame using the coarse resolution. The integral length-scale was increased (and kept constant) with velocity RMS distributions kept the same between the different simulations. The results are shown in Figure 4.21. From this figure, the turbulent kinetic energy is larger at all locations for a larger integral length-scale. The effect of the larger integral length-scale is an even shorter flame height, and radial species profiles that are more diffused. The relatively good agreement with the experimental values of the coarse simulation with $L_T = 1.2$ mm is therefore deemed to be due to a better approximation of the average turbulent length scales across the

inlet when used in the digital filter turbulence generation method with the coarser grid spacing.

4.3 Statistically-Planar Premixed Flame

Numerical experiments in the form of DNS are often conducted as methods of creating/-validating numerical models and investigating specific physical phenomenon that may be difficult to determine experimentally. These numerical experiments involve greatly simplified computational configurations due to their computational cost and to ensure well defined boundary conditions. In the area of premixed turbulent combustion, these computational experiments commonly take the form of a premixed flame embedded in a turbulent field with the flame separating the domain into two parts; the reactant, and the product side. The imposed turbulent conditions within these numerical experiments vary depending on what is being investigated, but can range from maintained to decaying isotropic turbulence.

The decaying turbulence configurations usually involve turbulence being introduced with the fresh reactants through the domain inlet allowing the turbulence to decay spatially. Because the flame propagates in the direction of the inlet, the position of the flame is maintained at a specified location within the computational domain by modulation of the inflow velocity. This particular configuration is beneficial for obtaining temporal statistics as the simulations can theoretically be run indefinitely. However, a consequence of this spatial evolution of turbulence is that any analyses of turbulence-chemistry interaction requires knowledge of the conditions present at the location of the flame. Additionally, if not controlled and initialised properly, this configuration may be susceptible to development of flame speed instabilities due to the turbulent flame propagating into progressively higher intensity turbulence. A method to mitigate these drawbacks is to have a turbulence field that evolves temporally and but remains spatially homogeneous. In this configuration, no turbulence is introduced into the domain and the initial turbulent field is allowed to decay in time. The flame does not remain stationary in this case and propagates towards the reactant stream within the domain. Although reducing some of the complexities associated with the introduction of turbulence through the inlet, this configuration is limited to analysing temporally evolving flame behaviour; the length of the simulations is dictated by the decay time of turbulence or the domain size.

In the maintained turbulence configurations, turbulence is unnaturally forced to remain at a specified condition [100]. The benefit of this configuration is that it is designed to analyse flame-turbulence interaction at targeted turbulent conditions removing uncertainty associated with local flame conditions and turbulence decay. The drawback is the forcing routines are complex and can substantially increase the computational overhead associated with already expensive DNS simulations.

In this thesis, LES simulations of a statistically-planer premixed flame in temporally decaying isotropic turbulence with no turbulent inflow are conducted. The specific objectives of these simulations are to compare numerical effects of different LES-stochastic field configurations rather than analysing detailed combustion phenomena.

Thermo-Physical Configuration

The thermo-physical configuration of the LES simulations is given in Table 4.6 and was chosen as a compromise between conditions representative of practical combustion applications [101], and computational cost and volume of the desired number of computations. The initial combustion regime under these conditions is characterised under the thin reaction zones.

TABLE 4.6: Thermo-physical condition of the statistically-planar premixed flame

u'/S_L	L_T/δ_L	Ka	Re_T
7.88	10	7	682

It should be mentioned, that for certain thermo-physical conditions, thermo-diffusive instabilities may exist [6]. Due to the $Le = 1$ assumption inherent to the numerical formulation in this thesis, the turbulent flame examined will be thermo-diffusively stable [102]. Hydrodynamic instabilities, however, may still be present.

The hydrodynamic instabilities are a result of thermal expansion across a planar flame. However, these hydrodynamic instabilities are dominant in weakly turbulent flames. Therefore, the initial stages of flame propagation in the proposed simulations are expected to be dominated by turbulence. However, as the turbulence intensity decays, the influence of instabilities on flame propagation are expected to grow [103]. The extent of their influence will be determined by the length of the simulation. If they develop,

their presence will be manifested through rapid growth of the observable turbulent flame speed.

Numerical Setup

The numerical configuration for these simulations corresponds to a premixed flame embedded in a three-dimensional computational domain of decaying isotropic turbulence. The longitudinal direction of the computational domain has a length $L_x/\delta_L = 120$ and the transverse directions $L_y/\delta_L = 60$. As such there are approximately six integral-length scales across the shortest length of the domain ($L_y/L_T = 6$). The left and right computational boundaries were inflow and outflow respectively, and all the transverse boundaries were periodic. All the simulations were run for a total of four integral scale eddy turnover times. A list of all numerical configurations tested is given in Table 4.7

TABLE 4.7: Numerical configurations examined for the statistically planar premixed flame. Identifiers: (c) -coarse, (f) - fine

Case	$L_x \times L_y \times L_z$	Δ/δ_L	Δ/Δ_x	N_f
A	$720 \times 360 \times 360$	0.166	1	1
B_c_N_f	$60 \times 30 \times 30$	2	1	1,8,16
B_f_N_f	$240 \times 120 \times 120$	2	4	1,8,16,32
C_c_N_f	$30 \times 15 \times 15$	4	1	1,8,16,32
C_f_N_f	$240 \times 120 \times 120$	4	8	1,8,16,32,64

The simulations were initialised by first generating a turbulent velocity field for the numerical grid of case A with S3D [104] using the Passot-Pouquet model spectrum [105]. The initial velocity fields for cases B and C were generated by explicitly filtering the velocity field of Case A with a top-hat filter. The width of the filter correspond to the filter width required in the respective cases. Once filtered, the velocity field was interpolated onto the different numerical grids for the corresponding filter width. No interpolation errors are expected because the numerical grids of the coarse and fine cases are integer multiples of one another and have corresponding nodes.

The initial thermo-chemical state of the turbulent simulations was generated by superimposing a premixed laminar flame solution (obtained with BOFFIN) within the filtered turbulent velocity field. The initial premixed laminar flame profile was obtained using the same numerical grid resolution of the corresponding case it was initialising. This was done to avoid any transients in the initial stages of the simulation that may have

arisen due to the numerical spearing caused by imposing overly resolved laminar flame solution on a coarser numerical grid.

For Cases B and C, the spatially-filtered continuity and momentum equations are closed with the constant-coefficient Smagorinsky model for the sub-filter scale turbulent stresses [36], with constant (C_s) equal to 0.09. The turbulent diffusivity is modelled assuming turbulent Schmidt and Prandtl numbers of 0.7.

For the LES of Case A, the grid spacing of the computational mesh resulted in a resolution of the Kolmogorov length-scale of $\eta/\Delta_x \approx 1$. Therefore, the turbulent diffusivity is expected to be much smaller than the laminar viscosity. As such, in this particular simulation, the turbulent viscosity was set to zero.

In the results presented, time is non-dimensionalised by the integral time scale, τ_0, based on the initial conditions given in Section 4.3. An instantaneous snapshot of each simulation at a non-dimensional time of 2.5 is given in Figure 4.22 displaying the iso-contour corresponding to a progress variable value of 0.68; the progress variable value corresponding to the maximum reaction rate for the given thermo-chemical model used in this study.

It can be seen that throughout all the simulations, similar large scale structures/features appear to be captured across all the simulations to some extent. In comparing the specific effects of the filter width, case C show noticeably less small-scale features compared to case B, which is expected due to the larger filter width. For the coarse cases ($\Delta = \Delta_x$), the effect of numerical resolution can be seen by the less smooth rendering of the flame surface features.

In Figure 4.23, a comparison of time-evolving flame characteristics are shown for cases A, B_f_32, and C_f_64. Within this figure distinct phases of the flame evolution can be identified. Up to a non-dimensional time of approximately 1.75, turbulence wrinkles the initially flat flame surface and a transient phase can be seen. Eventually an equilibrium is reached which can be identified through arrival at the global (peak) turbulent flame speed. Finally, in the last phase, turbulence decays and the flame surface begins to smoothen resulting in a slight decay of flame speed. From this decaying behaviour of the final phase, it would appear that within the time interval simulated, the flame remains hydro-dynamically stable.

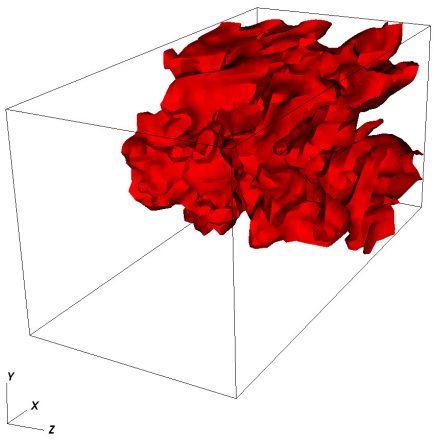

(A) Case B_c_16

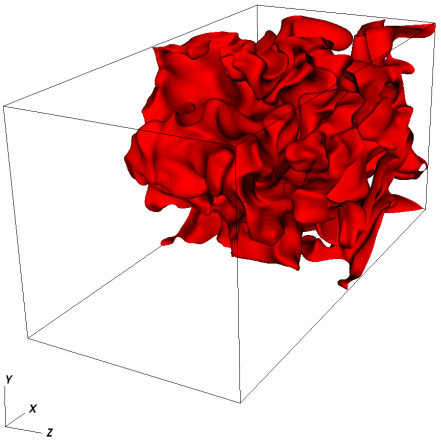

(B) Case B_f_32

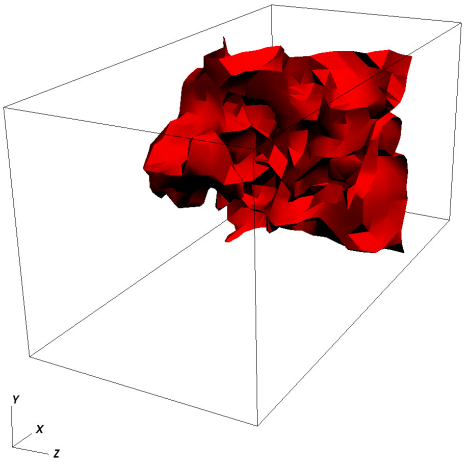

(C) Case C_c_32

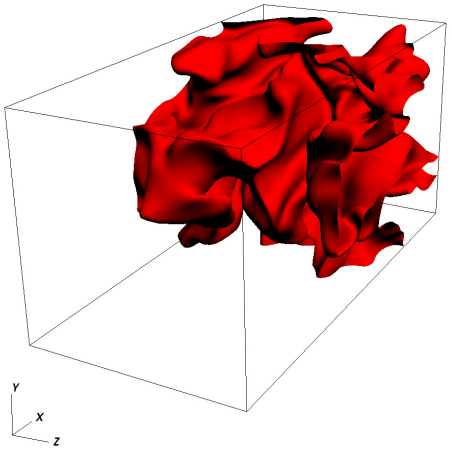

(D) Case C_f_64

FIGURE 4.22: Iso-contours of $\tilde{c} = 0.68$ for the various simulations at non-dimensional time of 2.5

The time variation of characteristic thicknesses are shown in Figure 4.23a. Both the evolution of the mean flame brush thickness and the stochastic field thickness show excellent agreement between the stochastic field simulations at both filters widths. Of particular interest are the results of the evolution of the mean stochastic field thickness. It can be seen from this figure that the stochastic field thickness is weakly dependant on the choice of filter width at this given thermo-physical configuration.

As expected, the effect of increasing the filter width is that the resolved turbulent flame surface area (left plot in Figure 4.23b) progressively decreases with increasing filter

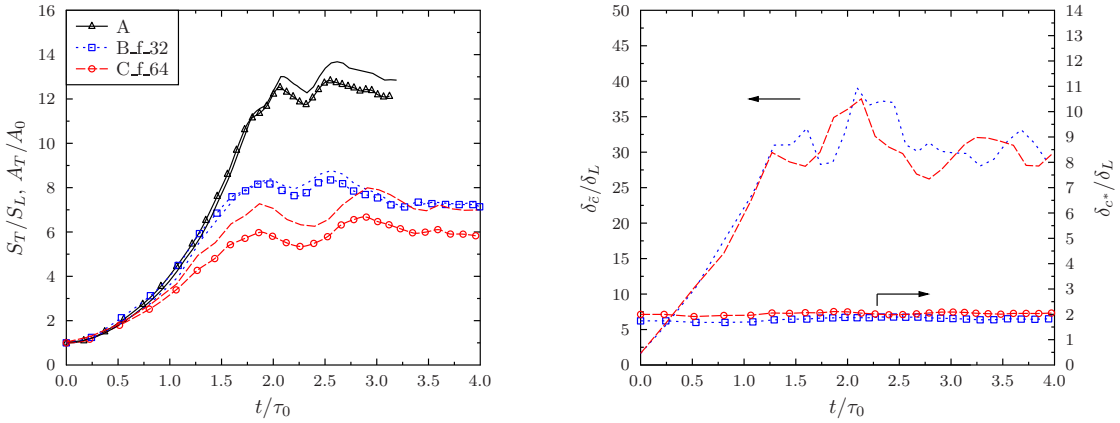

(A) Normalised turbulent flame speed (lines) and turbulent surface area (symbols)

(B) Non-dimensional mean flame brush thickness (lines) and mean stochastic field thickness (symbols)

FIGURE 4.23: Comparison of temporal evolution of cases A, B_f_32, and C_f_64.

width (this was shown qualitatively in Figure 4.22). However, this trend is also seen with the turbulent flame speed predictions. The desire within the LES-SF framework (and turbulent premixed combustion modelling in general) is that the predictions of turbulent flame speed be filter-width independent. This would result in similar flame speed predictions regardless of the resolved flame surface area. The differences seen here between the various simulations would suggest the presence of errors and that the sub-filter flame speed predictions are incorrect.

Achieving the objective that the model predictions be filter-scale independent relies upon the stochastic field simulations being adequately resolved numerically, and all sub-models closed accurately. Even though these particular stochastic field simulations have improved numerical resolution over their $\Delta = \Delta_x$ counterparts, they are not necessarily free of numerical errors as is evident from the initial non-dimensional flame speed at a non-dimensional time of zero (corresponding to a laminar flame) being greater than unity. As such, these particular simulations may still be susceptible to some numerical effects. The numerical effects being (to varying extents) suppression of resolved scale wrinkling due to numerical smearing of gradients; a behaviour demonstrated in previous sections of this chapter. However, given that these particular stochastic field simulations are relatively well resolved (they have approximately one-third the resolution of the well resolved LES), this numerical thickening effect is expected to be quite small in comparison to the general effects of a larger turbulent diffusivity from the use of larger filter widths.

Taking into consideration that the numerical resolution between the stochastic field simulations of cases B_f_32, and C_f_64 are identical, the differences between the stochastic field simulations alludes to the possibility of deficiencies within the the closures used within stochastic field.

4.3.1 Effect of Numerical Resolution

To illustrate the sensitivity of stochastic field predictions on the numerical resolution, a comparison between the temporal evolution of flame parameters for cases B_c_16 and B_f_32 are shown in Figure 4.24, and cases C_c_32 and C_f_64 in Figure 4.25.

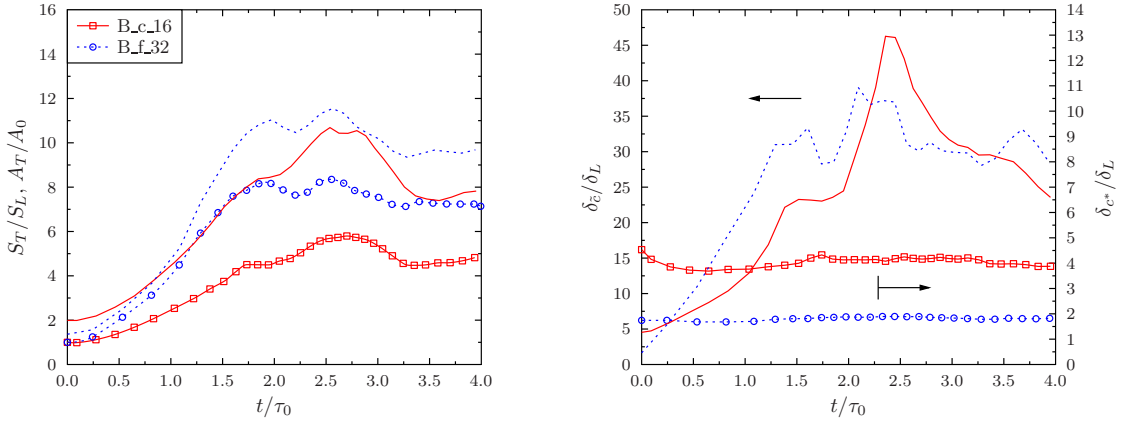

(A) Normalised turbulent flame speed (lines) and turbulent surface area (symbols)

(B) Non-dimensional mean flame brush thickness (lines) and mean stochastic field thickness (symbols)

FIGURE 4.24: Comparison of temporal evolution of cases B_c_16, and B_f_32

In general, case B_c exhibits better qualitative agreement to case B_f than C_c does to C_f. This is attributed primarily to the increasing numerical errors present within the simulations as the grid coarsens.

In previous sections, it was concluded that under-resolution leads to numerical thickening of scalar gradients which reduces the ability for the resolved flame front to be wrinkled by resolved scale turbulence. In this set of simulations, this effect can be seen by the differences in resolved flame surface area between the coarse (c) and fine (f) grids cases for a given filter width. The severity of the reduction provides an indication to the degree of under-resolution present in the corresponding simulation.

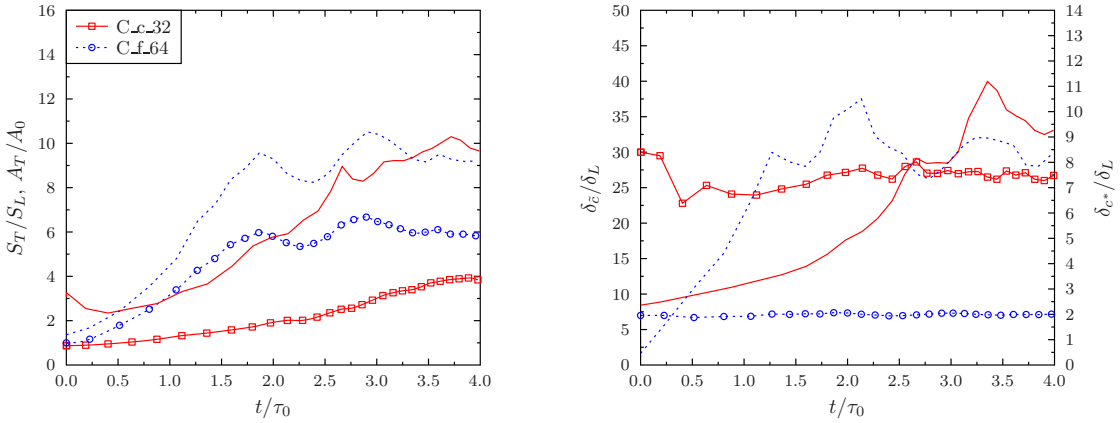

(A) Normalised turbulent flame speed (lines) and turbulent surface area (symbols)

(B) Non-dimensional mean flame brush thickness (lines) and mean stochastic field thickness (symbols)

FIGURE 4.25: Comparison of temporal evolution of cases C_c_32, and C_f_64

Coupled with this reduction in resolved flame surface area is a modification to the temporal evolution of turbulent flame speed. The reduced efficiency for small scale turbulence to wrinkle the initially flat flame leads to slower development of the turbulent flame. This is evident from the shorter development time seen for case B_c than for case C_c.

In both cases B_c and C_c, the average stochastic field thickness can be seen to be much larger than for the fine grid counterpart for the corresponding case. In both fine grid cases, the resultant stochastic field resolution (δ_{c^*}/Δ_x) was approximately four. The stochastic field thickness for the coarse grid cases have, on average, approximately two grid points within a stochastic field reaction front. This resolution represents the lower limit for premixed flames since it is a consequence of numerical discretisation that there should be at least one partially-reacted point (two grid spacings) inside the flame. These results indicate once again that the stochastic field reaction front thickness is predominantly influenced by the numerical grid spacing; an observation also supported by results for the one-dimensional flame analysis in Section 4.1 and from the Bunsen Flame in Section 4.2.

4.4 Conclusions

In this chapter, the sensitivity of the stochastic field method to the numerical grid spacing was investigated through simulation of three different configurations: a one-dimensional pseudo-turbulent freely propagating flame, a 3D LES of a piloted premixed laboratory Bunsen flame, and a 3D LES of a freely propagating flame in decaying homogeneous isotropic turbulence.

The one-dimensional simulations aimed to parametrise the stochastic field reaction front thickness as a function of Karlovitz number, filter width, and numerical grid spacing. Although a simplified study, it was shown that in grid independent simulations of premixed turbulent combustion, the reaction front thicknesses arising from the Stochastic field solution can be on the order of the laminar flame thickness as the Karlovitz number tends towards zero, irrespective of the filter width chosen.

Setting the filter scale equal to the grid spacing, as is common practice in LES, leads to substantial errors in predicted flame speed when compared to the grid independent simulations as a result of the numerical thickening of under-resolved scalar gradients. A suspected consequence of the numerically-thickened stochastic fields reaction fronts is that they are less susceptible to wrinkling by the resolved turbulence which would result in an under-prediction in the overall flame surface area, and therefore turbulent flame speed. However, the one-dimensional nature of the simulation made investigating this impossible and was therefore only approximated using well established relations of flame surface wrinkling models from the Artificially Thickened Flame Model. (and this suggests the lost wrinkling more than compensates for the effect of numerical diffusion)

The three-dimensional LES of a laboratory turbulent premixed Bunsen flame confirmed that the stochastic fields solution is not numerically accurate when the grid spacing is equal to the filter length scale, but demonstrated that the velocity field solution is relatively insensitive to further refinement of the numerical grid spacing compared to the effect on the reactive scalar field.

It was also shown that the conclusions from the one-dimensional simulations on the effect of numerical thickening of stochastic field reaction fronts on flame surface generation and turbulent flame speed were correct. The simulation where the grid spacing was equal to

the filter width produced a total turbulent flame speed that was lower than the improved resolution case as a consequence of the suppression of flame surface generation.

In order to avoid uncertainties concerning the inflow conditions to be used within the LES of the Bunsen flame, a three-dimensional LES of a freely propagating flame in decaying homogeneous isotropic turbulence was conducted for different filter widths and numerical resolutions. This set of LES simulations further confirmed the conclusions drawn from the previous investigations within this chapter, specifically, the sensitivity of the stochastic field solution to the numerical grid spacing. It also indicated possible inaccuracy of the established closures (IEM and gradient transport) of the stochastic field model.

Although the stochastic fields method is an attractive way to apply transported probability density function approach to turbulent reacting flows, the spatial resolution requirements become very demanding when applied to turbulent premixed combustion. The general requirement is that the grid spacing should be finer than the filter scale and the same order of magnitude as the laminar flame thickness. This is impractical for many industrial applications involving high pressure combustion. Techniques such as artificial thickening should be considered in order to reduce the resolution requirements while retaining the key advantages of the stochastic fields method, or alternatively, approaches such as AMR.

Chapter 5

The Thickened Stochastic Field Approach

5.1 Introduction

In Chapter 4 it was shown that in order to solve the stochastic fields equations accurately it can be necessary to have a numerical grid spacing finer than the LES filter length-scale as flame-like structures may arise that are thinner than the filter scale. This increased numerical resolution can substantially increase the oversell computational cost required for a stochastic fields simulation, specifically, as the sub-filter Karlovitz number approaches zero. Conversely, following the conventional practice of setting the LES filter length-scale equal to the numerical grid spacing can lead to substantial numerical error for two reasons. First, numerical diffusion caused by under-resolution changes the local propagation speed of the reaction fronts in the stochastic fields solution. Second, wrinkling of the reaction fronts by resolved turbulence is reduced because the numerical diffusion increases the thickness of the fronts.

The Artificially Thickened Flame (ATF) approach [14, 22] (described in Section 3.1.1) has been introduced as a means to ensure accurate numerical resolution of premixed reaction fronts in LES. In the ATF approach, the governing equations for composition and energy are modified in order to yield thicker reaction fronts that can be resolved accurately on a given numerical grid. Importantly, the artificial thickening ensures a predetermined number of grid-points sufficiently resolves (numerically) all reactive

scalars. Without thickening, the poor resolution of these scalars may introduce numerical errors into the solution whose magnitude is dependant on both the numerical grid and numerical methods employed.

The consequence of the numerical thickening procedure artificially modifies the influence of turbulence on (thickened) flame surface wrinkling dynamics. More specifically, the thickening procedure acts as pseudo-filtering operation and removes the resolution/generation of small scale flame surface convolutions below the artificial thickening scale. In order to compensate for this lost flame surface on the propagation speed of the resolved flame front, an *efficiency function* model is employed. The efficiency function model accounts for effects of un-resolved flame wrinkling on the overall burning rates, and the quality of the predictions of the ATF approach depends on the accuracy of the efficiency function modelling employed.

With this ability for the ATF approach to accurately resolve and propagate turbulent flame fronts on arbitrary numerical grids, and the potentially prohibitive numerical resolution that is required in stochastic field simulation of premixed flamelet combustion, the objective of this chapter is then to set out a new approach for stochastic fields-PDF simulation that uses artificial thickening to ensure an accurate numerical solution on an arbitrary numerical grid. The extent to which the thickened stochastic fields approach retains the ability of PDF methods to accurately describe turbulence-chemistry interactions depends on the amount of thickening employed. In the case where numerical resolution is sufficient, no thickening is applied and the standard stochastic fields formulation is recovered.

5.2 Development of the Thickened Stochastic Fields (TSF) Approach

The TSF approach is best introduced by first reviewing the formulation of the ATF approach. Consider a reactive scalar transport equation:

$$\rho\frac{\partial \underline{Y}}{\partial t} = -\rho u_j \frac{\partial \underline{Y}}{\partial x_j} + \frac{\partial}{\partial x_j}\left(\rho D \frac{\partial \underline{Y}}{\partial x_j}\right) + \underline{\dot{\omega}}(\underline{Y}), \tag{5.1}$$

where $\underline{Y}$ is the vector of species mass fractions and enthalpy, u_j is the jth component of the velocity vector, D is the laminar diffusivity (assumed equal for all species), and $\underline{\dot{\omega}}$ is the vector of chemical source terms.

5.2.1 The Thickened Flame Model

The ATF transport equations [22] are obtained by applying the transformation $\underline{x}' = F\underline{x}$ and $t' = Ft/E$ [22] to Eq. 5.1,

$$\rho\frac{\partial\underline{Y}}{\partial t'} = -\rho E v_j\frac{\partial\underline{Y}}{\partial x'_j} + \frac{\partial}{\partial x'_j}\left(\rho DEF\frac{\partial\underline{Y}}{\partial x'_j}\right) + \frac{E}{F}\underline{\dot{\omega}}(\underline{Y}), \tag{5.2}$$

where the convection velocity v_j is given by the solution of the similarly-transformed Navier-Stokes equations [106]. Here, F and E denote the thickening factor and efficiency function respectively. In most previous applications of the ATF approach, following [14, 22], the thickened scalar transport equation Equation 5.2 has been coupled with un-thickened LES making the assumption that Ev_j is equal to the resolved velocity from the LES simulation $\widetilde{u}_j$. The effect of F and E can be understood by considering the solution of a stationary freely-propagating planar premixed flame ($\partial/\partial t' = \partial/\partial t = 0$). The flame thickness given by Equation 5.2 is thickened by the factor F and the propagation speed is faster by a factor E compared respectively to the flame thickness δ_L and flame speed S_L given by solution of Equation 5.1.

Thickening the species transport equations by factor F with $E = 1$ has the attractive feature that numerical resolution requirements are reduced while laminar flame speeds are unaffected. The turbulent flame speed, however, depends on the increase in flame surface area caused by wrinkling of the flame front. The amount of wrinkling depends (at least) on the ratio of turbulent velocity fluctuations to the laminar flame speed u'/S_L, and the ratio of the turbulence length scales to the laminar flame thickness, L_T/δ_L. Since thickening of a flame front reduces the degree to which turbulence will wrinkle it, the efficiency function E is then used as a correction factor to account for un-resolved flame wrinkling on the propagation speed of the resolved flame surface.

The various models used in the ATF approach for determining a function for E are derived empirically from DNS data. Theoretically, the methods used to derive E in the thickened flame context is generalised such that no assumption on premixed flame

regime is made. As such, dominant physical processes at low and high Ka regimes (such as preferential diffusion and flame stretch and strain) can be contained within the ATF framework and the model for E to the extent that they are captured in the DNS data used to derive it. For the efficiency function given in Equation 3.9, effects of stretch and strain can be included by using laminar flame thickness (δ_L) and flame speeds (s_L) that account for these effects [107].

The efficiency function E is defined in [14, 22] as the ratio of the wrinkling factor, Ξ, of the thickened and un-thickened flames,

$$E_{TF} = \frac{\Xi_\Delta \left(u'_{\Delta,TF}/S_L, \Delta_{TF}/\delta_L \right)}{\Xi_\Delta \left(u'_{\Delta,TF}/S_L, \Delta_{TF}/F\delta_L \right)}. \tag{5.3}$$

The sub-filter wrinkling factor Ξ_Δ, is a parameter describing the ratio between the total flame surface area present within a filter volume and its projection in the direction normal to flame propagation [108]. It can also be defined in term of the ratio of the sub-filter turbulent flame speed $S_{T\Delta}$ and the laminar flame speed S_L. The sub-filter turbulent flame speed is local propagation speed of the reaction-front resolved by the LES simulation[14]. Thus, the wrinkling factor can be expressed as:

$$\frac{S_{T\Delta}}{S_L} = \frac{A_{sfs}}{\Delta^2} = \Xi_\Delta. \tag{5.4}$$

Modelling for the sub-filter flame wrinkling in the context of Thickened Flame modelling has been proposed initially by Colin *et al.* [22] and Charlette *et al.* [14] as functions of the non-dimensional sub-filter velocity fluctuations u'/S_L and the non-dimensional filter size Δ_{TF}/δ_L. Here, $\Delta_{TF} = F\delta_L$ is the effective filter scale in the Thickened Flame model. In general, the effective filter scale Δ_{TF} implied by the Thickened Flame model can be different from the filter length scale Δ used in modelling of the LES momentum equations. Thus, thickening the flame front by factor F reduces the non-dimensional filter size to $\Delta/F\delta_L$. This results in a reduction in the sub-filter turbulent flame speed by factor $1/E$. This process is illustrated in Figure 5.1.

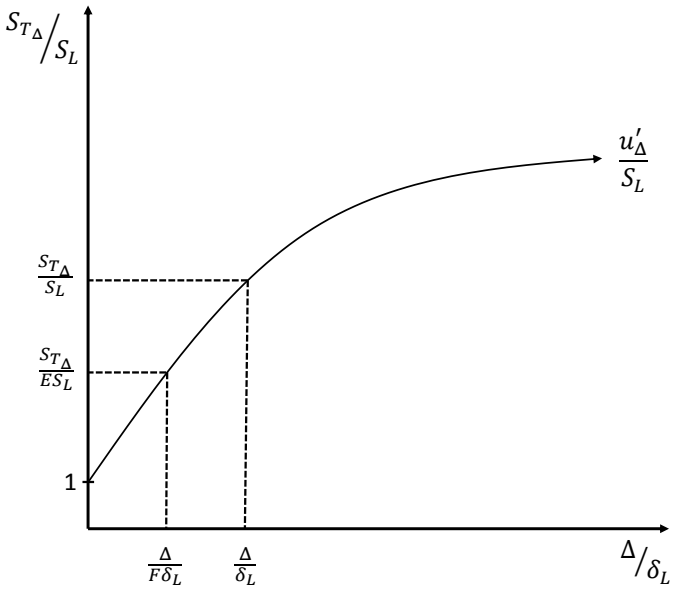

FIGURE 5.1: The dependence of wrinkling factor $S_{T\Delta}/S_L$ on Δ/δ_L and u'_Δ/S_L, indicating the reduction in Ξ_Δ due to thickening by factor F.

5.2.2 The Thickened Stochastic Fields Model

The unmodified stochastic fields equation is given by Valiño *et al.* [24] as,

$$\begin{aligned}\overline{\rho}\mathrm{d}\underline{\zeta}_{(i)} = &-\overline{\rho}\widetilde{u_j}\cdot\frac{\partial\underline{\zeta}_{(i)}}{\partial x_j}\mathrm{d}t+\frac{\partial}{\partial x_j}\left(\overline{\rho}(D+D_T)\frac{\partial\underline{\zeta}_{(i)}}{\partial x_j}\right)\mathrm{d}t+\overline{\rho}\sqrt{2D_T}\frac{\partial\underline{\zeta}_{(i)}}{\partial x_j}dW_{j\,(i)}\\&-\frac{\overline{\rho}}{\tau_T}\left(\underline{\zeta}_{(i)}-\widetilde{\underline{\zeta}}\right)\mathrm{d}t+\overline{\rho}\dot{\underline{\omega}}(\underline{\zeta}_{(i)})\mathrm{d}t.\end{aligned}\tag{5.5}$$

The thickened stochastic field equation is obtained by applying to Equation 5.5 the same transformation that produces the ATF model: $\mathbf{x}' = F\mathbf{x}$, $t' = Ft/E$, and, since the Wiener increment vector $\mathbf{dW}$ has dimension $\sqrt{t}$, its transformation becomes $\mathbf{dW}' = \sqrt{F/E}\mathbf{dW}$. This results in an equation of the following form:

$$\begin{aligned}\overline{\rho}\mathrm{d}\underline{\zeta}_{(i)} = &-\overline{\rho}E\widetilde{v_j}\cdot\frac{\partial\underline{\zeta}_{(i)}}{\partial x'_j}\mathrm{d}t'+\frac{\partial}{\partial x'_j}\left(\overline{\rho}(D+D'_T)EF\frac{\partial}{\partial x'_j}\underline{\zeta}_{(i)}\right)\mathrm{d}t'+\overline{\rho}\sqrt{2D'_TEF}\frac{\partial\underline{\zeta}_{(i)}}{\partial x'_j}dW'_{j\,(i)}\\&-\frac{\overline{\rho}E\left(\underline{\zeta}_{(i)}-\widetilde{\underline{\zeta}}\right)}{F\tau'_T}\mathrm{d}t'+\frac{\overline{\rho}E\dot{\underline{\omega}}(\underline{\zeta}_{(i)})}{F}\mathrm{d}t'.\end{aligned}\tag{5.6}$$

In principle the convection velocity vector $\tilde{\mathbf{v}}$, turbulent diffusivity D'_T, and dissipation time scale τ'_T come from solution of similarly-transformed LES momentum equations. However if, following Colin *et al.* [22], the thickened scalar equations are coupled with un-thickened LES momentum equations then the velocity vector $\tilde{\mathbf{u}}$, turbulent diffusivity

D_T, and dissipation time scale τ_T from the un-thickened LES should be scaled as: $\tilde{\mathbf{v}} = \tilde{\mathbf{u}}/E$, $D'_T = D_T/EF$, and the turbulence timescale to be used in Equation 5.6 is then $\tau_T'^{-1} = C_{\phi\Delta}(DEF + D_T)/(F\Delta)^2$.

The transformation of the stochastic fields equation has the effect that the solution for a steady-state planar freely-propagating turbulent flame modelled by Equation 5.6 is thickened by factor F and the propagation speed is increased by factor E relative to the solution of Equation 5.5. The thickening factor, F, can therefore be set in order to obtain satisfactory numerical resolution on a particular computational grid. The efficiency function, E, should then be set in order to account for the reduction in resolved flame surface area that results from thickening of the stochastic fields equation.

5.2.3 The Efficiency Function

The specification of the efficiency function for the TSF model relates to the wrinkling of the reaction fronts in the stochastic fields solution, rather than the wrinkling of physical flames considered in the conventional ATF model. The characteristic thickness δ_{c^*}, and propagation speed S_{c^*}, of the reaction fronts in the stochastic fields solution are in general different from the thickness and speed of the corresponding laminar flame. However, the wrinkling dynamics of the reaction fronts are assumed to be governed by the same wrinkling factor, Ξ_Δ. This assumption is justified because in both ATF and TSF, the wrinkling dynamics of reaction fronts in the flamelet regime are dominated by the combination of resolved convection, sub-filter turbulent transport, diffusion, and reaction processes. The efficiency function for the TSF model (Equation 5.6) is then given by,

$$E_{TSF} = \frac{\Xi_\Delta\left(u'_{\Delta,TSF}/S_{c^*}, \Delta_{TSF}/\delta_{c^*}\right)}{\Xi_\Delta\left(u'_{\Delta,TSF}/S_{c^*}, \Delta_{TSF}/F\delta_{c^*}\right)}, \tag{5.7}$$

where the effective filter scale of the TSF is $\Delta_{TSF} = F\delta_{c^*}$. Similar to [22], the sub-filter wrinkling of the thickened fields is normalised to account for the possible wrinkling of the thickened field. In general Δ_{TSF} can be different from the filter scale Δ used to evaluate the model for the turbulent diffusivity in Equation 5.6.

Previous studies have developed models for the function Ξ_Δ on the basis of theory and empirical information from direct numerical simulations and laboratory measurements of

flame response [14, 22]. The purpose of the TSF approach however is to provide simulation results that maintain the same flame propagation speeds as the underlying stochastic fields modelling when the computational grid spacing is increased. The modelling for Ξ_Δ should not seek to improve the agreement between the stochastic fields model and DNS or experiment, rather it should fit to predictions of the numerically accurate underlying un-thickened stochastic fields framework. Improving the physical accuracy of the underlying stochastic fields modelling is outside the scope of the present thesis. The functional dependence of the wrinkling factor on the filter-scale turbulence properties $\Xi_\Delta(u'_\Delta/S_L, \Delta/\delta_L)$ is therefore obtained from stochastic fields simulations across a range of conditions. The set up of one-dimensional stochastic fields simulations in order to obtain data for δ_{c^*}/δ_L and S_{c^*}/S_L is presented in the next Section.

5.2.4 Determination of Wrinkling Factor from 1D Stochastic Fields Simulations

The dependence of the sub-filter scale turbulent flame speed and reaction-front thickness on filter-scale turbulence properties is evaluated in a one-dimensional stochastic fields simulation of a freely-propagating planar turbulent flame. The one-dimensional approach neglects the effects that curvature and bulk strain have on the local propagation of reaction-fronts in stochastic fields LES of premixed combustion, but has the advantage that the simulations are computationally less expensive compared to three-dimensional LES and still represent the transport processes normal to the resolved reaction front that dominate the dynamics of the resolved reaction front. The framework and numerical setup are identical to those used in the one-dimensional simulations in Chapter 4 and can be found in Section 4.1.

Evaluation of E_{TSF}

S_{c^*}/S_L and δ_{c^*}/δ_L required in Equation 5.7 are evaluated over a wide range of range of u'_Δ/S_L and Δ/δ_L corresponding to a wide range of premixed combustion regimes. 512 stochastic fields are used for the one-dimensional simulations with uniform computational grid spacing selected to ensure at least 16 points within the reaction fronts in each case.

The average consumption speed of the reaction front of the individual stochastic fields is evaluated by calculating the overall consumption speed of the ensemble average of the stochastic fields. In this statistically-stationary case, the overall consumption speed of the ensemble average of the stochastic fields is necessarily equal to the averaged consumption speed of the individual stochastic fields ($S_{c^*} = S_{T\Delta}$). The consumption speed is evaluated through

$$S_{T\Delta} = S_{c^*} = \frac{1}{\rho_u Y_f A} \int_V \frac{1}{N_s} \sum_{i=1}^{N_s} \dot{\omega}_{(i)} \mathrm{dV}, \tag{5.8}$$

where ρ_u is the unburnt gas density, Y_f the mass fraction of fuel in the premixed reactants, A the domain cross sectional area, N_s represents the number of stochastic fields, and $\dot{\omega}_{(i)}$ the instantaneous reaction rate on field i. Due to the stochastic nature of the consumption speed given by Eq. 5.5, the values reported are those averaged over time.

The average thicknesses of the individual stochastic fields is evaluated as

$$\langle \delta_{c^*} \rangle = \frac{1}{N_s} \sum_{i=1}^{N_s} \frac{1}{|\nabla \zeta_{(i)}|_{max}}. \tag{5.9}$$

Similar to the consumption speed, the average stochastic field thickness reported is also the time averaged value.

The resultant data sets are approximated by fitting power-law functions of u'_Δ/S_L and Δ/δ_L in the general form similar to that employed by Charlette *et al.* [14],

$$f_i(u'_\Delta/S_L, \Delta/\delta_L) = \left(1 + A_i \left(\frac{u'_\Delta}{S_L}\right)^{a_i} \left(\frac{\Delta}{\delta_L}\right)^{b_i}\right)^{\beta_i}. \tag{5.10}$$

The ranges of u'_Δ/S_L and Δ/δ_L used to fit the coefficients in Eq. 5.10 correspond to ranges of Karlovitz number Ka $\in (0.5 - 50)$ and filter length scale ratios $\Delta/\delta_L \in (1 - 5)$ that are representative of practical LES simulations of premixed combustion in internal combustion engines and gas turbines. A least squares fit to the data yields $[A_S, a_S, b_S, \beta_S] = [0.083, 0.627, 0.48, 1.4]$ for $f_S = S_{c^*}/S_L$ and $[A_\delta, a_\delta, b_\delta, \beta_\delta] = [0.081, 0.6, 0.47, 1.48]$ for $f_\delta = \delta_{c^*}/\delta_L$. The curve-fits give excellent agreement across the relevant parameter space, as shown in Fig. 5.2.

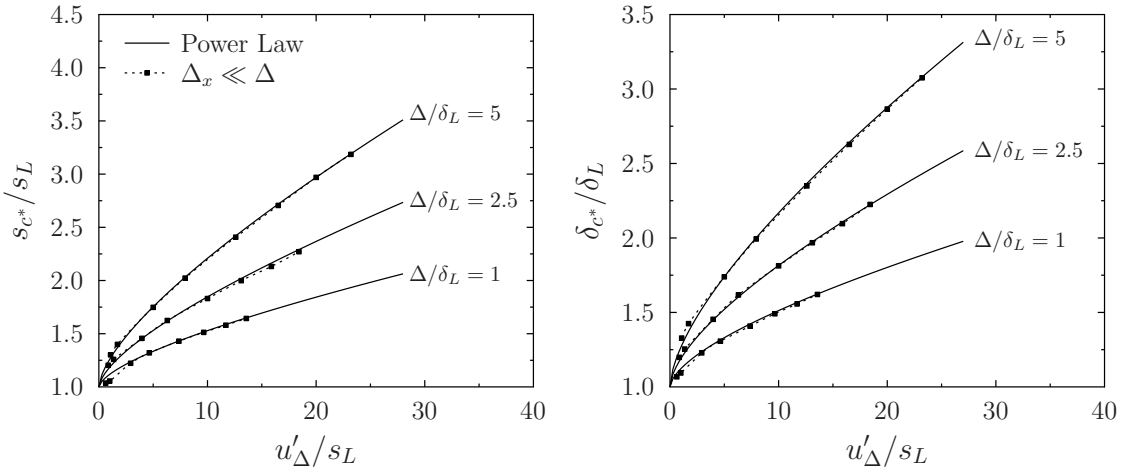

FIGURE 5.2: Wrinkling factor S_{c^*}/S_L (left) and non-dimensional reaction front thickness δ_{c^*}/δ_L (right) versus sub-filter turbulence intensity u'_Δ/S_L for well-resolved stochastic fields ($\Delta_x \ll \Delta$), stochastic fields simulation with $\Delta_x = \Delta$, and the curve fit to the well resolved data given by Eq. 5.10

For illustrative purposes, the differences between the empirically fit wrinkling factor of the TSF model and the algebraic wrinkling factor of Fureby [109] are shown in Figure 5.3. Not surprisingly, the two wrinkling factors yield different results. However, it is not to say that one is more correct than the other as comparisons between other algebraic flame wrinkling models also produce different results - see [110]. The expected difference between the TSF wrinkling factor and the algebraic model arises from the fact that the wrinkling factor derived for this TSF framework is not necessarily a wrinkling factor in the traditional sense. Since the numerically accurate stochastic field solution is sought, here, E_{TSF} is modelling the underlying stochastic fields predictions. The algebraic wrinkling factor of [109] on the other hand attempts to predict the DNS data on which it has been derived. In this particular case, the factor E_{TSF} accounts for physical processes and for the effect of loss of flame surface area from filtering to the extent that the effects are accounted for by the modelled IEM/stochastic fields equations in 1D. The only similarity shared by these two models is that in the limiting case of laminar or fully resolved flow, the efficiency functions decay to unity - a necessary limiting behaviour

With an appropriate model for the dependence of the sub-filter scale turbulence velocity fluctuation u'_Δ on the filter length scale, and with knowledge of the laminar flame speed and thickness, the TSF efficiency function, E_{TSF}, can be evaluated through the following steps:

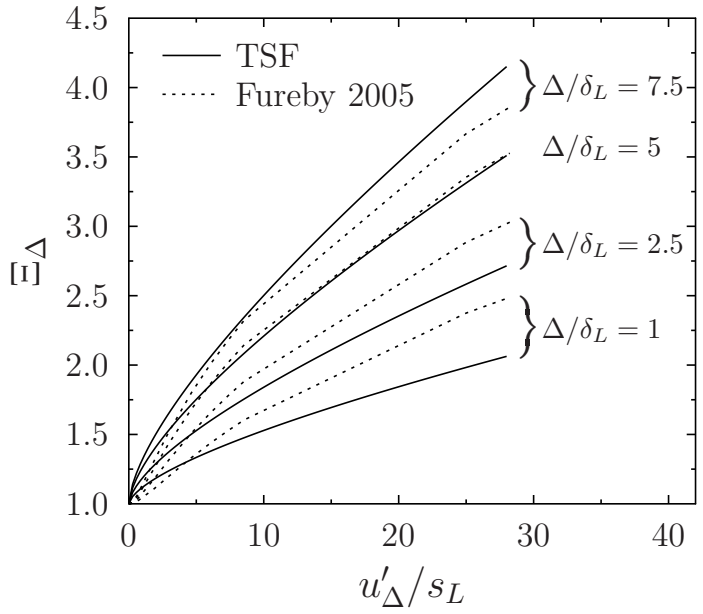

FIGURE 5.3: Comparison of wrinkling factor obtained through empirical fit of 1D stochastic field simulations and the algebraic wrinkling factor of [109].

1. Evaluate u'_Δ for the stochastic fields filter scale Δ;
2. Evaluate δ_{c^*}/δ_L and S_{c^*}/S_L corresponding to u'_Δ/S_L and Δ/δ_L using Eq. 5.10;
3. Evaluate $F = n\Delta_x/\delta_{c^*}$ and $\Delta_{TSF} = n\Delta_x$, where n is the minimum number (e.g. 5-7) of grid spacings Δ_x required within the reaction-front thickness δ_{c^*};
4. Calculate $u'_{\Delta,TSF}$ for the effective thickened stochastic fields filter scale Δ_{TSF};
5. Evaluate Eq. 5.7 for E_{TSF} using the power law curve fit Eq. 5.10 for the wrinkling factors.

Calculation of the sub-filter scale velocity fluctuations required for the evaluation of E_{TSF} (as outlined in Sec. 5.2.4), follows the procedure used in the traditional ATF approach derived in [22]. The sub-filter scale velocity fluctuations in the TSF approach are evaluated as

$$u'_{\Delta,TSF} = c_2\Delta^3|\nabla \times (\nabla^2(\tilde{\mathbf{u}}))|, \tag{5.11}$$

where $\tilde{\mathbf{u}}$ is the resolved velocity vector corresponding to filter scale Δ and $c_2 = 2.0$ is a model constant [22]. The use of this relation ensures zero velocity fluctuation in the limit of a planar laminar flame, which also enforces the correct asymptotic behaviour of the TSF framework in this limit.

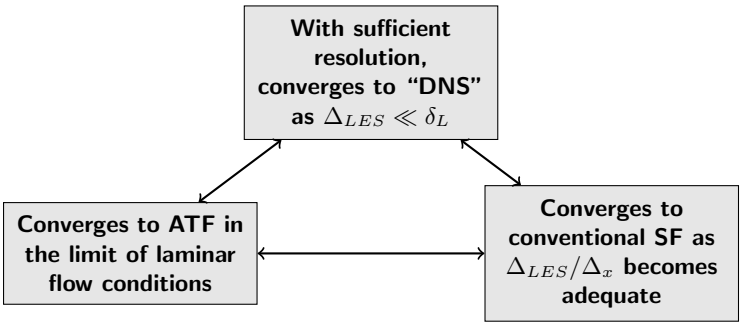

FIGURE 5.4: Asymptotic behaviour of TSF.

5.2.5 Flame Sensor

An additional aspect of any artificial thickening of the scalar equations is that it is typically necessary only in regions of the flow containing unresolvable reaction fronts. Thickening in regions where it is not required leads to an unnecessary loss of simulation fidelity, for example by over-predicting the rate of fuel-air premixing in partially-premixed combustion systems. To overcome this, Durand *et al.* [111] introduced dynamic thickening by a flame sensor, Ω, to remove the effects of thickening away from reaction fronts. In this work, this particular form of sensor is denoted as the *traditional* sensor and is given by

$$\Omega = 16\left(c\left(1-c\right)\right)^2, \tag{5.12}$$

where c is a relevant progress variable bound by zero and unity. $\Omega > 0$ indicates the presence of a flame front and $\Omega = 0$, its absence. The thickening factor in the scalar transport equations are then rewritten as

$$F = 1 + (F_0 - 1)\Omega, \tag{5.13}$$

where F_0 is the nominal thickening factor determined as a function of the grid spacing and the desired number of grid points within the reaction front.

A flame sensor can also be applied in the thickened stochastic fields approach, however, a problem arises with the use of the traditional sensor due to the typical use of the filtered progress variable field to evaluate the sensor. Evaluating it using the filtered progress variable obtained by ensemble averaging the stochastic fields may result in an individual stochastic fields' reaction front to be thickened non-uniformly with respect to the other fields; the extent of the thickening disparity depends on the fields position relative to

the resolved flame front. This is simply a consequence of the shape of the sensor and its maximum value of unity occurring at $\tilde{c} = 0.5$. This behaviour is illustrated in Figure 5.5 where the variation of the progress variable of selected individual stochastic fields ($\zeta_{(i)}$) with respect to the ensemble averaged progress variable ($\tilde{c}$) is shown for a one-dimensional flame with low (left) and high (right) sub-filter variance. The traditional flame sensor evaluated with the filtered progress variable is also presented. Figure 5.5 shows that if using $\tilde{c}$ to activate the sensor, depending on the sub-filter variance, individual fields towards the leading or trailing edge of the resolved flame front may not be thickened to the desired extent.

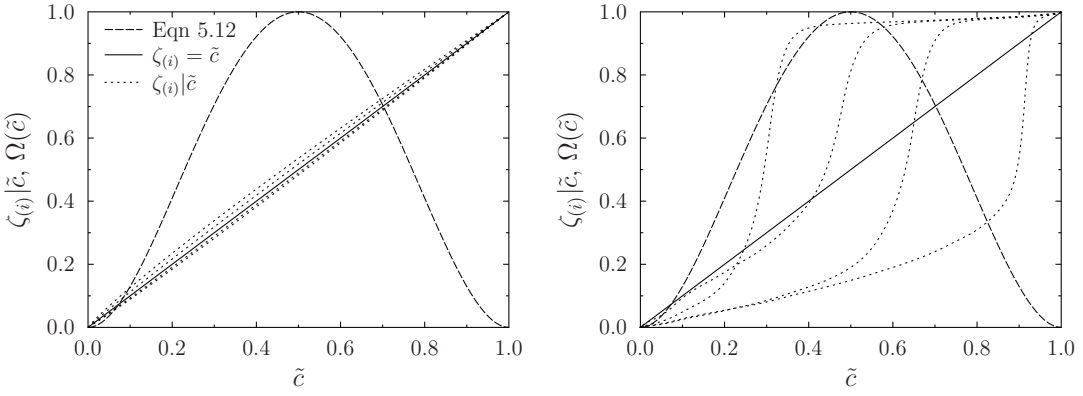

FIGURE 5.5: Illustration of thickening seen by 4 different individual fields for low sub-grid variance (left) and large sub-grid variance (right)

The first step to mitigate the potential heterogeneous thickening of each field is to simply evaluate the flame sensor on each field using an equivalent progress variable,

$$\Omega_{(i)} = 16\zeta_{(i)}^2 \left(1 - \zeta_{(i)}\right)^2, \tag{5.14}$$

where $\Omega_{(i)}$ denotes the sensor on an individual field. The principle drawback with this particular sensor is the maximum thickening occurs at a progress variable value of 0.5. Thickening is typically necessary in the region of $0.6 < \zeta_{(i)} < 0.8$ where the reaction rate is greatest and reactive scalar gradients are steepest. Therefore, using this sensor in its current form results in a thickening factor which may be less than the prescribed factor in the region of interest. Analysis of the one-step reaction mechanism employed in this work shows that the maximum reaction rate occurs at a progress variable value of about 0.68. At this value the thickening factor is about 75% of the maximum thickening prescribed.

The desire is to then to broaden the region of thickening of each stochastic field to ensure the entirety of the reaction zone of each field exhibits the same amount of artificial thickening across all the fields. This new sensor is known as the *broadened* sensor and is described by

$$\Omega_{(i)} = \frac{\tanh\left[\beta_1\left(16\zeta_{(i)}^2\left(1-\zeta_{(i)}\right)^2\right)\right]}{\tanh\beta_1}, \tag{5.15}$$

where β_1 is a broadening parameter greater than unity that broadens the thickening zone for each field and determines how quickly the sensor approaches unity for $\tilde{c} > 0$ and $\tilde{c} < 1$. Although β_1 is tunable, its minimum value should be such that in the absence of sub-filter variance (and the recuperation of Equation 5.12), the flame sensor should be approximately unity (or 0.99) at the progress variable value of maximum reaction rate. With the thermochemical model employed in this work, the minimum value of β_1 was determined to be approximately 3.5.

Although the activation of artificial thickening locally on each field may provide a benefit on the individual fields, maintaining consistency between the thickening seen by the potentially thickened momentum equation and the thickening seen on individual fields becomes difficult. Therefore, it is desirable to have a single "global" sensor that is seen by both momentum and scalar stochastic field equations.

Care must be taken when determining a method in obtaining a single sensor as simply taking an ensemble mean of the local flame sensors on every field is inadequate as the ensemble averaged sensor will be different to the thickening required on a particular stochastic field. Additionally, an ensemble averaged flame sensor will almost always be less than unity due to the weighting of number of fields and their dispersion. A consequence of this is that a fully activated "global" sensor and consistency between scalar and momentum equations would only be achieved in the limiting case of the absence of sub-filter variance.

With these facts in mind, the calculation of a single sensor can be achieved if the weighting of each field during the calculation of a global sensor can be redistributed. Here, the weighting is such that the field with the most activated flame sensor at a given spatial location, bears the full weighting of the ensemble average. This is also achieved through evaluation of the maximum sensor value between all the fields as,

$$\Omega(\mathbf{x}, t) = \max(\Omega_{(i)}(\mathbf{x}, t)). \tag{5.16}$$

This approach yields the desirable limiting behaviour that:

1. The traditional sensor evaluated with the filtered progress variable field is recovered in the limit of negligible sub-filter variance
2. Within the resolved flame brush, the sensor is fully activated with $\Omega = 1$
3. The regions of thickening of the stochastic fields scalar equations is consistent with the thickening of the LES momentum field

Arrhenius Rate Flame Sensor

Although simulation fidelity can be increased with the introduction of a flame sensor in general, the performance and applicability of the sensor above for different cases (such as partially premixed combustion) is sensitive to the definition of progress variable. Additionally, it does not consider changes in composition that may result in more resolvable reaction fronts for a given numerical grid spacing. By considering this compositional change in the calculation of the flame sensor (and thus applied thickening factor), the simulation fidelity can be increased further through application of appropriate levels of local flame activation, as opposed to possible "over-thickening" by ignoring them.

Leiger, Poinsot, and Veynante [48] introduced a flame sensor based on reaction rate. Information on mixture composition is inherently included in this sensor through use of the reaction rate magnitude which is a function of the local composition. The sensor takes the form:

$$\Omega = \tanh\left(\frac{\beta_2 \dot{\omega}}{\dot{\omega}_{max}}\right), \tag{5.17}$$

where β_2 is a broadening parameter. Although the authors suggest that β_2 is greater than unity, it is suggested here that β_2 be a greater than at least 2.6 as this value guarantees in the case of the reaction rate approaching the maximum, the sensor tends to unity.

The issue with defining a sensor based on this type of expression with the use of a detailed chemical mechanism for the species production/destruction rates, the choice of reaction rate to activate the sensor is non-trivial. In the work of Leiger et al. [48], they employed an "Arrhenius-like" expression different to their one-step chemical mechanism to calculate the presence of a reaction zone. In this work a similar methodology is

proposed, however, the expression used to monitor the activity of the reaction zone *is* an Arrhenius expression of an irreversible, one-step global reaction. The reason for this modification is that a single step mechanism better represents the chemical reaction pathway than an Arrhenius type expression which would require tuning (likely from a single step mechanism anyway).

The issue with triggering the flame sensor with a one-step mechanism is that is that an irreversible one-step mechanism may have different equilibrium compositions compared to a detailed mechanism; a consequence of the presence of slower and reversible reactions in detailed schemes. Therefore, in order to be able to use the one-step reaction rate sensor to accurately detect a reaction zone that is representative of the detailed mechanism, a mapping from the composition and progress of the detailed mechanism to the composition and progress of the irreversible one-step global mechanism is required.

With the dependencies introduced, the expression for the reaction rate required in Equation 5.17 takes on the form:

$$\dot{\omega}(z^*, c^*) = A \left[\frac{\rho Y_o^*(z^*, c^*)}{W_f}\right]^m \left[\frac{\rho Y_f^*(z^*, c^*)}{W_f}\right]^n \exp\left(\frac{-T_a}{T^*(z^*, c^*)}\right), \tag{5.18}$$

where W_f and W_o denote the molar mass of the fuel and oxidiser respectively, ρ the mixture density, T_a the reaction activation temperature, A the pre-exponential constant, and m and n exponents. The "starred" mass fractions (Y) and temperature (T) refer to the respective quantities in the composition space (z^*, c^*) of the irreversible one-step mechanism. These quantities are determined through the following expressions:

$$Y_o^*(z^*, c^*) = Y_o^u(z^*) + c^*(z^*)\left[Y_o^b(z^*) - Y_o^u(z^*)\right] \tag{5.19}$$

$$Y_f^*(z^*, c^*) = Y_f^u(z^*) + c^*(z^*)\left[Y_f^b(z^*) - Y_f^u(z^*)\right] \tag{5.20}$$

$$T^*(z^*, c^*) = T^u(z^*) + c^*(z^*)\left[T^b(z^*) - T^u(z^*)\right] \tag{5.21}$$

where superscript u and b indicates unburnt ($c^* = 0$) and burnt ($c^* = 1$) quantities respectively. The values of unburnt quantities are determined through a simple linear mixing rule between the pure oxidiser ($z^* = 0$) and pure fuel ($z^* = 1$) states, and burnt quantities are assumed to vary linearly towards the stoichiometric equilibrium compositions. The expressions for the variation of these quantities are given in Table 5.1 and shown schematically in Figure 5.6.

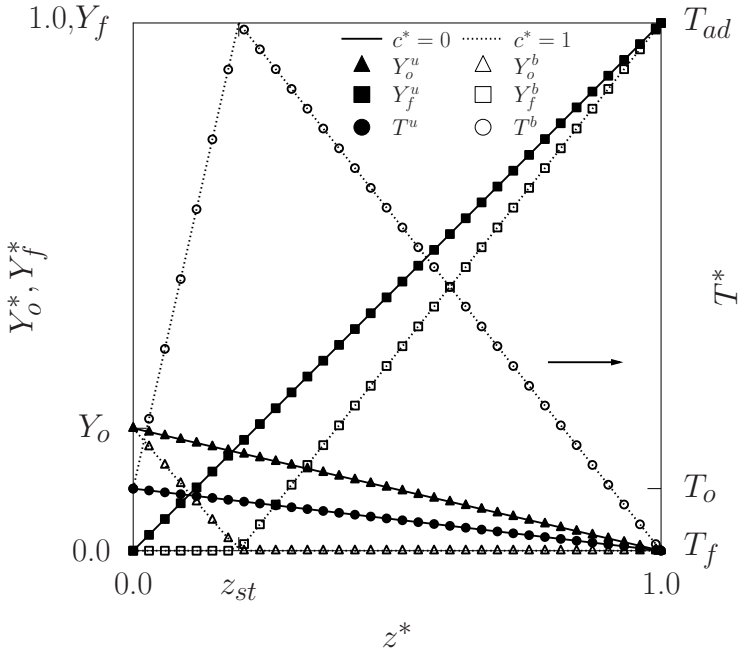

FIGURE 5.6: Schematic of equilibrium profiles outlined in Table 5.1

TABLE 5.1: Mixing and Equilibrium Profiles for Sensor

Quantity	Unburnt	Burnt
$Y_o(z)$	$Y_{\text{ox}}^o(1-z)$	$Y_{\text{ox}}^o \max(0, 1-z/z_{st})$
$Y_f(z)$	$Y_f^o z$	$Y_f^o \max(0, \frac{z-z_{st}}{1-z_{st}})$
$T(z)$	$T_o + z(T_f - T_o)$	$T_o + z(T_{ad} - T_o)/z_{st}$ if $z \leq z_{st}$ $T_{ad} - (T_{ad} - T_f)\frac{z-z_{st}}{1-z_{st}}$ if $z > z_{st}$

With all the possible states known from the above expressions, in order to evaluate Equation 5.17, z^* and c^* must be determined. These values are obtained from the mapping of the composition and progress space of the detailed mechanism to those of the one-step mechanism. The mapping is given by:

$$\tilde{z}(\mathbf{x}, t) = z^*, \tag{5.22}$$

and

$$\tilde{c}(\mathbf{x}, t) = c^*, \tag{5.23}$$

where $\tilde{z}$ is the filtered mixture fraction, $\tilde{c}$ the filtered, normalised progress variable. The filtered mixture fraction is evaluated by

$$\tilde{z}(\mathbf{x},t) = z_{st}\left(\frac{s\tilde{Y_f}(\mathbf{x},t) - \tilde{Y_o}(\mathbf{x},t)}{Y_{\text{ox}}^o} + 1\right), \tag{5.24}$$

where $\tilde{Y_f}(\mathbf{x},t)$ and $\tilde{Y_o}(\mathbf{x},t)$ are the local filtered fuel and oxidiser mass fractions, Y_{ox}^o the mass fraction of oxidiser in the oxidiser stream, and z_{st} the stoichiometric mixture fraction. The progress variable can be defined arbitrarily through,

$$\tilde{c}(\mathbf{x},t) = \frac{\tilde{Y_\alpha}(\mathbf{x},t) - Y_\alpha^u\left[\tilde{z}(\mathbf{x},t)\right]}{Y_\alpha^b\left[\tilde{z}(\mathbf{x},t)\right] - Y_\alpha^u\left[\tilde{z}(\mathbf{x},t)\right]}, \tag{5.25}$$

where $Y_\alpha^u\left[\tilde{z}(\mathbf{x},t)\right]$ and $Y_\alpha^b\left[\tilde{z}(\mathbf{x},t)\right]$ are the unburnt and burnt states of the species chosen to define the progress variable as functions of the local filtered composition.

In order to evaluate Equation 5.17, a value for $\dot{\omega}_{max}$ is required. This value is obtained by differentiating Equation 5.18 and finding the maximum:

$$\frac{\partial}{\partial c}\dot{\omega}(\tilde{z}^*,\tilde{c}^*) = 0, \tag{5.26}$$

Once differentiated two approaches can be taken to solve the resultant equation. First, is to assume a global maximum reaction rate that occurs at $z^* = z_{st}$. This assumption simplifies the differentiated expression resulting in an equation for which an analytical solution exists for determining $\dot{\omega}_{max}$ and its corresponding $c^*(z_{st})$. Second, is to assume a dependence of the reaction rate on the mixture fraction and evaluate a corresponding value of c^* providing $\dot{\omega}_{max}(z^*)$. In this case, no analytical solution exists and only numerical solutions are possible. Therefore, for the second approach and on-the-fly use, an iterative solution is necessary. For increased computational efficiency, the values can be can be pre-computed and stored as a lookup table.

Similar to the flame sensor shown in the previous section, this Arrhenius rate sensor can be used in the context of TSF. The flame sensor can be evaluated on an individual field through

$$\Omega_{(i)} = \tanh\left(\frac{\beta_2\dot{\omega}_{(i)}}{\dot{\omega}_{max}}\right), \tag{5.27}$$

where the subscript i denotes the quantities determined on each field. The global sensor can then be evaluated as in Equation 5.16. The evaluation of the reaction rate for sensor

activation on each field is obtained through:

$$\dot{\omega}(\eta^*_{(i)}, \zeta^*_{(i)}) = A \left[\frac{\rho Y^*_o(\eta^*_{(i)}, \zeta^*_{(i)})}{W_f}\right]^m \left[\frac{\rho Y^*_f(\eta^*_{(i)}, \zeta^*_{(i)})}{W_f}\right]^n \exp\left(\frac{-T_a}{T^*(\eta^*_{(i)}, \zeta^*_{(i)})}\right), \quad (5.28)$$

where an equivalent irreversible one-step composition space of progress variable, $\zeta^*_{(i)}$, and mixture fraction, $\eta^*_{(i)}$, are evaluated on each field i and mapped to by the corresponding filtered field values. The calculation of equilibrium composition and overall methodology remains as outlined above with the appropriate substitution of the filtered fields, z, and c, made with the stochastic field equivalent η, and ζ, respectively.

5.3 Turbulent premixed Bunsen flame LES

In this section, the TSF framework is tested with 3D LES simulations of the premixed Bunsen flame of Chen *et al.* [92]. The numerical setup and configuration can be found in Section 4.2. In the simulations presented in this section, no flame sensor is applied to the TSF framework and the results for the base TSF formulation is presented. For the efficiency function, it was assumed that there was no local variation in the laminar flame speed and lmainar flame thickness due to strain and themo-physical property variation. The values of both S_L and δ_L used in Equation 5.7 were obtained for a laminar stoichiometric methane-air flame at 300K.

5.3.1 Estimated Resolution Requirements

The stochastic field reaction front thicknesses reported in Figure 5.2 and approximated by Equation 5.10 may be used to estimate the resolution requirements for stochastic field LES presented here. In the case of the Bunsen flame simulated in this study [92], the thermal thickness of a laminar stoichiometric methane-air flame is $0.41mm$ (using the one-step chemistry model described above), the filter length scale selected is $1mm$, and the Karlovitz number is reported to range between 1 and 10 [92]. These Karlovitz numbers (corresponding to $u'_\Delta/S_L = 1.3$ and 6.2 respectively) lead to the prediction that $\delta_{c^*}/\delta_L = 1.3 - 1.7$, given $\Delta = 1mm$. Imposing a minimum requirement of 5 grid spacings within the stochastic field reaction front thickness δ_{c^*} then dictates a maximum grid spacing of 0.11 - 0.14 mm for fully-resolved stochastic fields simulation. Compared

to the usual practice of setting the grid spacing equal to the LES filter scale, this estimate suggests a numerically-resolved stochastic field solution would require a grid spacing of 11-14% of the filter scale, implying 360-750 times more grid points in a three-dimensional simulation. The resolution requirements of the stochastic fields approach may be even more daunting in simulation of industrial combustion systems for which the ratio of filter length scale to laminar flame thickness might need to be an order of magnitude greater than in the laboratory Bunsen flame example. The need for sub-filter scale resolution around the stochastic field reaction fronts suggest that the TSF approach or an Adaptive Mesh Refinement (AMR) approach may be needed in order to obtain numerically-accurate stochastic fields predictions for practical systems.

A known disadvantage of thickened flame approaches is that application of the thickening factor and the efficiency function affects the chemical time scales in the fluid, and consequently changes the Damköhler and Karlovitz numbers describing the turbulence-chemistry interactions. The Damköhler number (Da= $L_T s_L/u'\delta_L$) and Karlovitz number (Ka= $(u'^3\delta_L/S_L^3 L_t)^{1/2}$) change by E/F and $(F/E^3)^{1/2}$ respectively. Since the turbulent diffusivity and micromixing terms in Equation 5.6 lead to a stochastic field reaction front thickness that is greater than the corresponding laminar flame thickness by the factor $f_\delta = \delta_{c^*}/\delta_L$ described by Equation 5.10, the TSF requires a thickening factor that is smaller than for the conventional ATF approach by the same factor f_δ. In the case of the Bunsen flame LES in this study, the thickening factor is expected to be 1.3-1.7 times less than in a conventional thickened flame LES with the same filter scale. The undesirable effect of thickening on the Damköhler and Karlovitz numbers is therefore generally smaller for the TSF approach compared to the conventional ATF approach, and the correct chemical time scale and the conventional stochastic fields model is recovered in the limit of adequate resolution, for which no thickening is required.

5.3.2 Bunsen Flame Analysis

Below, the results for the LES simulation of the F3 and F1 flames are shown. For each flame, two sets of simulations are conducted; one simulation solves the stochastic field equation (Equation 5.5) and the second solves the TSF equation (Equation 5.6). Both simulations in both flames adopt the conventional practice of setting the grid spacing

equal to the LES filter scale, and based on the characteristic grid-spacing for these simulations, $\Delta_x = \Delta = 1mm$.

The instantaneous filtered temperature fields taken on a plane through the burner centre-line for an individual stochastic field in each of the two simulations is shown in Figure 5.7 for the F3 flame, and Figure 5.8 for the F1. Due to application of the TSF model, the images show that the flame thickness increases and the flame wrinkling decreases; the effects being more obvious in the case of the F3 flame where the thickening requirement is expected to be larger. The result of this is the F3 flame height predicted by the thickened stochastic fields increases. In both cases, it can be seen that through the unmodulated application of artificial thickening, the pilot stream away from the core premixed jet is highly diffused.

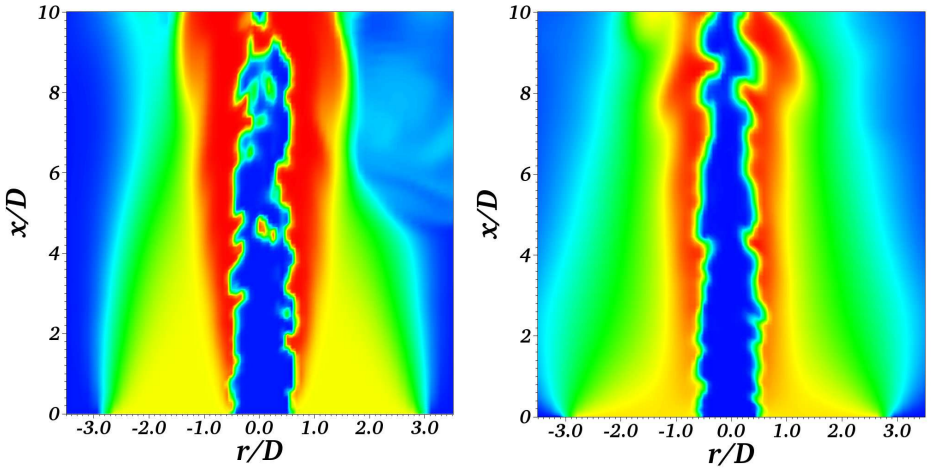

FIGURE 5.7: Instantaneous temperature field of an individual field from the F3 flame LES with $\Delta_x = \Delta = 1.0$ mm for Traditional stochastic fields (left), and thickened stochastic fields (right).

The different flame thicknesses in the two simulations are quantified by evaluating an indicative stochastic fields reaction front thickness given by the inverse average progress variable gradient magnitude on the stochastic fields conditioned on the progress variable giving maximum heat release, $\langle |\nabla \zeta_{c,(i)}| \mid \zeta_{c,(i)} = 0.68 \rangle^{-1}$. For the F3 Flame, application of the TSF model leads to the average thickness of the stochastic field reaction fronts increasing from 2.68 mm in the conventional stochastic fields simulation to 4.9 mm in the Thickened solution, while in the F1 case, it increases from 3.5 mm to 4.85mm – confirming that in both cases, the TSF approach delivers the target five grid spacings within the stochastic field reaction fronts.

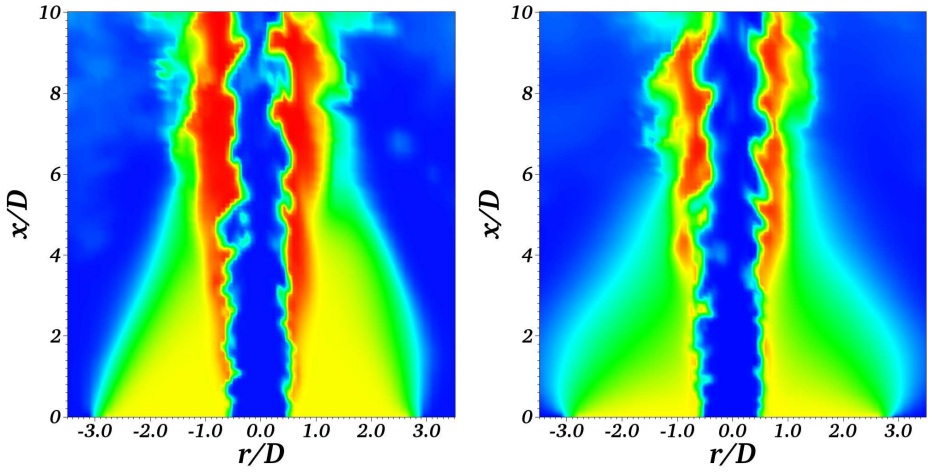

FIGURE 5.8: Instantaneous temperature field of an individual field from the F1 flame LES with $\Delta_x = \Delta = 1.0$ mm for Traditional stochastic fields (left), and thickened stochastic fields (right).

Plots of time-averaged u'_Δ are shown in Figure 5.9. It can be seen from the figure that in both flames, in the near-burner regions, the velocity in the pilot stream ($r/D > 1$) remains laminar. With progressive downstream location, the entire flow-field becomes turbulent and the magnitude of sub-filter velocity fluctuations within the flame (at approximately $r/D = 0.5$) decreases. Also shown is the time-averaged u'_{TSF}. The increased magnitude of this quantity is a result of the change of length-scale in the TSF method.

The consequence of this decrease in u'_Δ within the flame with downstream location is that the combustion becomes more flamelet-like. From the anslysis of Chapter 4, the implications are that the resolution should become more stringent and require a larger thickening factor. Indeed, this behaviour can be seen in Figure 5.10 where the time-averaged TSF thickening and efficiency factor are shown.

In the near-burner region at large r/D, both F1 and F3 thickening factors in this region are effectively identical. As the flow is more laminar in this region, the TSF framework is attempting to fully resolve a more laminar flame resulting in a very large thickening factor compared to the region in the vicinity of the turbulent jet. This large thickening factor in the large r/D regions justifies the overly diffused temperature distribution seen in Figures 5.7 and 5.8. Closer to the jet at $r/D < 1$, due to the larger turbulence intensity that acts to thicken the premixed reaction fronts, the required thickening factor is substantially smaller than in the pilot region. This behaviour is further exemplified

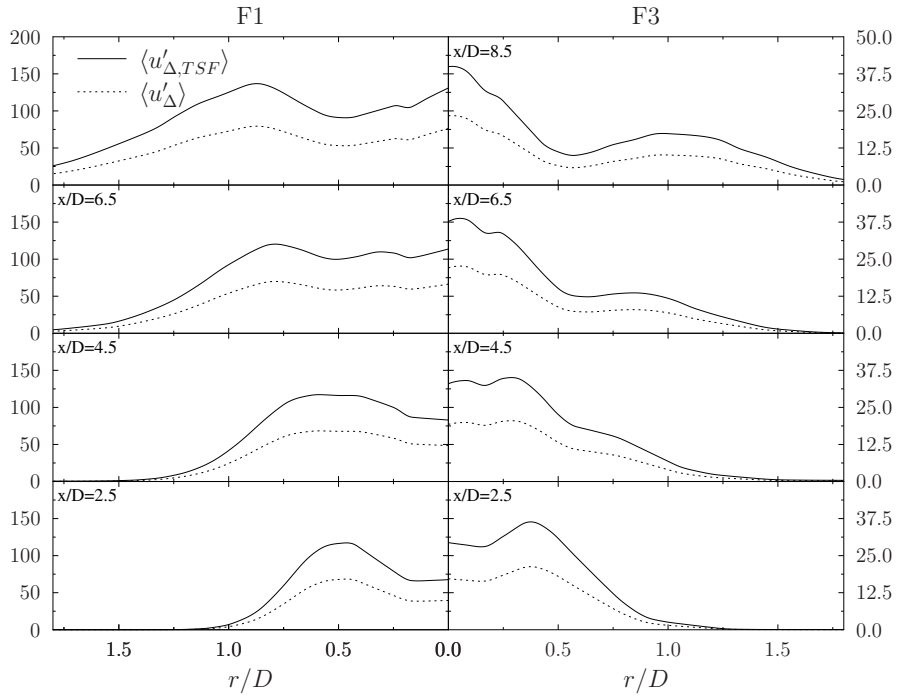

FIGURE 5.9: Radial distributions of time-averaged sub-filter velocity fluctuations at various axial locations for the F1 and F3 flames. Units are in [m/s].

by comparing the thickening factor required in the F1 flame with that of the F3. Since the F1 flame exhibits higher turbulence intensity, its thickening factor is smaller than the corresponding F3 thickening factor at the same axial location.

The balance between the thickening factor and turbulence intensity explained above may justify the relatively flat radial distributions of efficiency function seen for both flames. However, due to larger thickening factor required in the F3 simulation, the efficiency function is generally seen to be larger.

Irrespective of the difference in magnitude of the thickening factor and efficiency function for either flame, in the vicinity of the flame front (around $r/D = 0.5$) both flames exhibit a decrease in sub-filter velocity fluctuations with downstream location (as shown in Figure 5.9). This is manifested as an increase in thickening factor with respect to the surrounding spatial locations that exhibit a higher turbulence intensity. The result is that the average thickening factor from locations $x/D = 2.5$ to $x/D = 8.5$ increases from approximately 2 to 4 and from approximately 4 to 7 for the F1 and F3 flame respectively.

The radial variation of the time-averaged filtered methane and oxygen mass fraction

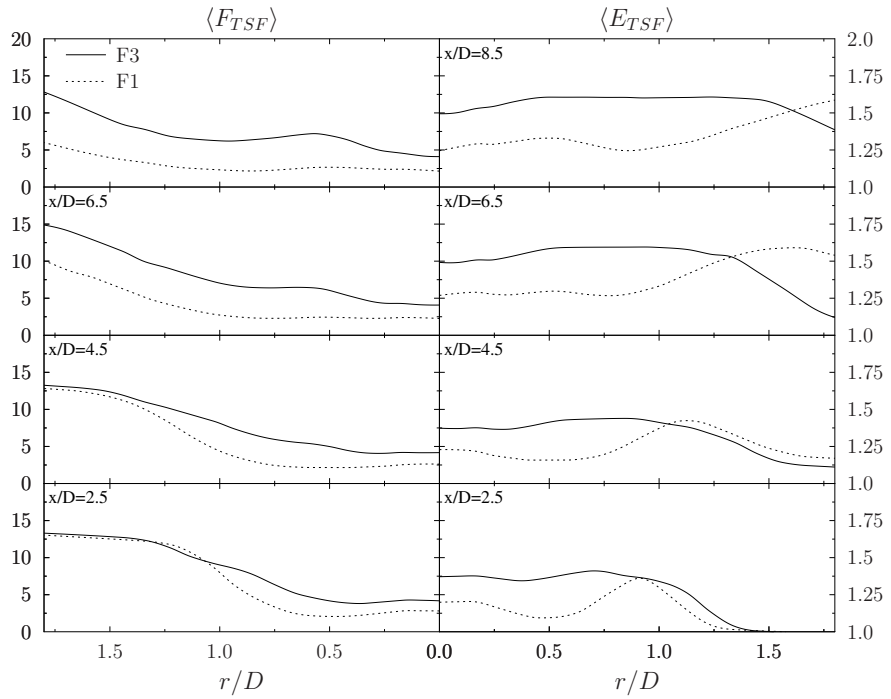

FIGURE 5.10: Radial distributions of time-averaged TSF efficiency function and thickening factor at various axial locations for the F1 and F3 flames.

are shown in Figure 5.12 and Figure 5.13, and carbon dioxide and water vapour in Figure 5.14 and Figure 5.15 for the F3 and F1 flames respectively.

The radial distributions of the reactants in Figure 5.12 for the F3 flame show a larger impact of artificial thickening on the solution than those for the F1 flame in Figure 5.13. This is expected due to the relatively small amount of thickening observed for F1 flame, which in itself, is the primary indicator of the under-resolution exhibited by the unthickened stochastic field simulations.

As mentioned in Chapter 4, under-resolution affects the flame speed in three main ways: first, numerical diffusion increases the local propagation speed of the individual stochastic field reaction fronts; second, thickening of the stochastic field reaction fronts caused by the numerical diffusion reduces the amount of flame wrinkling produced by a given velocity field; third, the numerical viscosity reduces the strength of small-scale eddies that wrinkle the reaction fronts.

The result of the artificial thickening in this method is to produce a numerically accurate stochastic field solution and overcome the effects of numerical thickening outlined

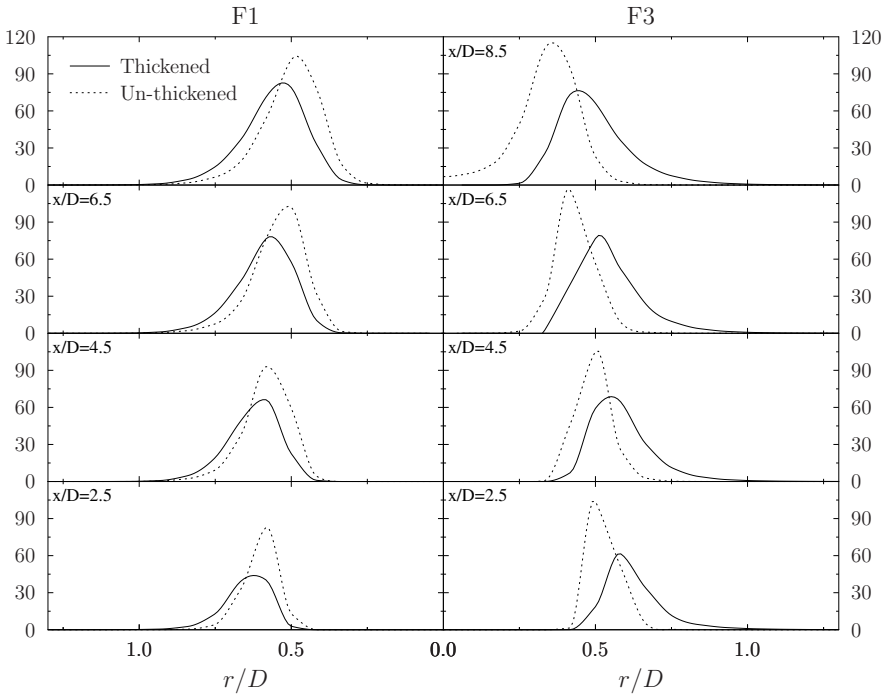

FIGURE 5.11: Radial distributions of the time-averaged methane reaction rate $\langle \dot{\omega}_{CH_4} \rangle (\mathrm{kg/m^3 - s})$ at various axial locations comparing the thickened and Un-thickened Stochastic Field.

above. As shown in Figure 5.11, the TSF simulations results in a decrease in the overall reaction rate (and consequently flame speed) relative to the un-thickened stochastic field simulations. This results in a slightly longer flame from the TSF simulations. The difference between the reaction rate for the un-thickened and thickened stochastic field simulations is smaller for the F1 flame than for the F3 due to the fact that it is more resolved than the F3 flame.

For the F3 flame, the TSF simulations resulted in overall improvements in the prediction of both reactants (Figure 5.12) and products (Figure 5.14). The improved reaction rate prediction meant that the excess consumption of reactants (and over-production of products) in the un-thickened simulations were corrected to yield reactive scalar distributions in better agreement with experiment. To a lesser extent, the same behaviour can be seen in the case of the F1 flame where a slight improvement of the TSF simulations can be seen in the case of the reactants compared to the un-thickened simulation (Figure 5.13). From the "good agreement" of product species from the un-thickened simulations, the improved numerical accuracy of the TSF simulations results in product distributions (Figure 5.15) that appear to worsen. Given the increased numerical accuracy of the TSF method, the under-predicted product mass fractions is expected to be the correct

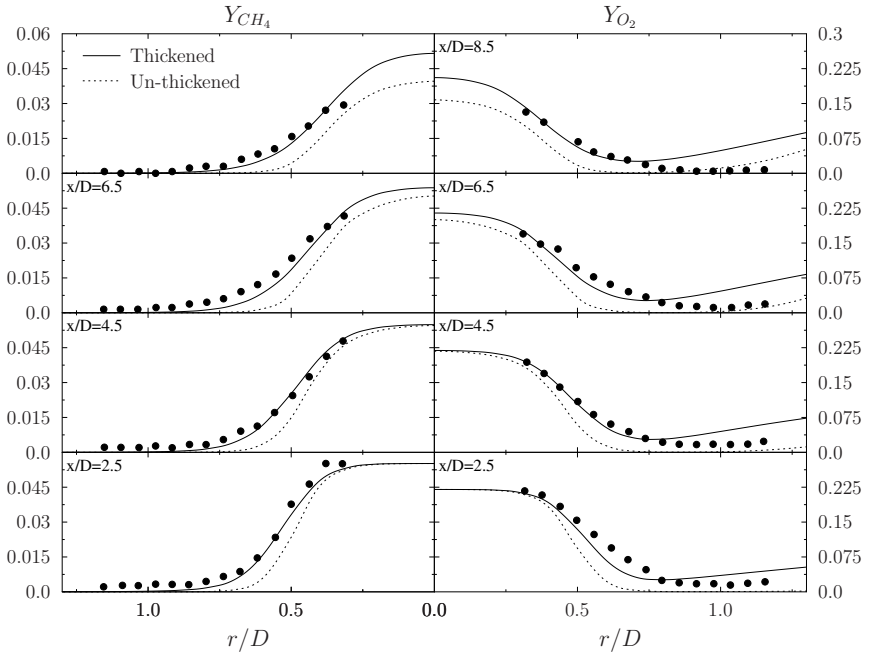

FIGURE 5.12: F3 radial distributions of the time-averaged methane mass fraction $\langle \widetilde{Y}_{CH_4} \rangle$ and oxygen mass fraction $\langle \widetilde{Y}_{O_2} \rangle$ at various axial locations comparing the thickened and un-thickened stochastic field.

solution for the given numerical setup. In fact, the predictions of the TSF method in the case of the F3 and F1 flames (including the under-predicted product species of the F1 case) are not unique to this set of simulations and are similar to trends and results obtained in [57, 85].

In both F1 and F3 flames, for all reactive scalars except methane, the poor results at larger r/D are a consequence of excessive artificial thickening at the pilot and co-flow interface region due to the absence of a flame sensor. The impact of flame sensors on the predictions is examined in Section 5.4.

Distribution of the time-averaged filtered temperature are shown in Figure 5.16. Irrespective of the improvements of reactive scalars predictions in the TSF framework, mean temperatures are over-predicted as in the un-thickened simulations. This over-prediction is similar to those obtained by [46] who also employ the one-step reaction model used in this thesis. This over-predictions is suspected to be a consequence of the absence of carbon monoxide/dioxide chemistry [46].

Figure 5.17 shows radial distributions of normalised axial velocity for the F1 ($U_o = 65.0$ m/s) and F3 ($U_o = 30.0$ m/s) flames. Due to thermal expansion across the flame front, the mean velocity field is affected by the predicted flame location. The mean

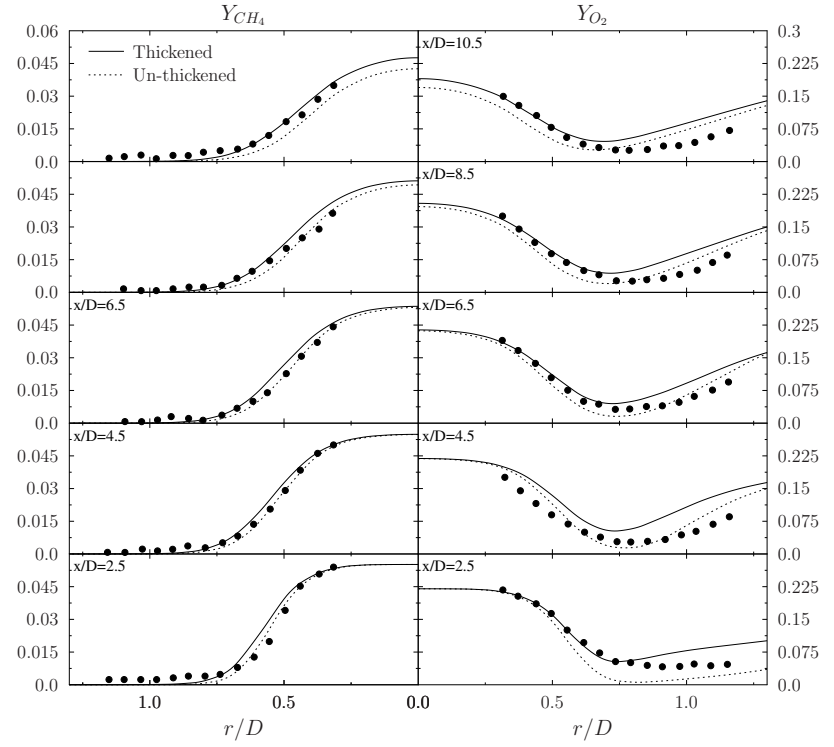

FIGURE 5.13: F1 radial distributions of the time-averaged methane mass fraction $\langle \widetilde{Y}_{CH_4} \rangle$ and oxygen mass fraction $\langle \widetilde{Y}_{O_2} \rangle$ at various axial locations comparing the thickened and un-thickened stochastic field.

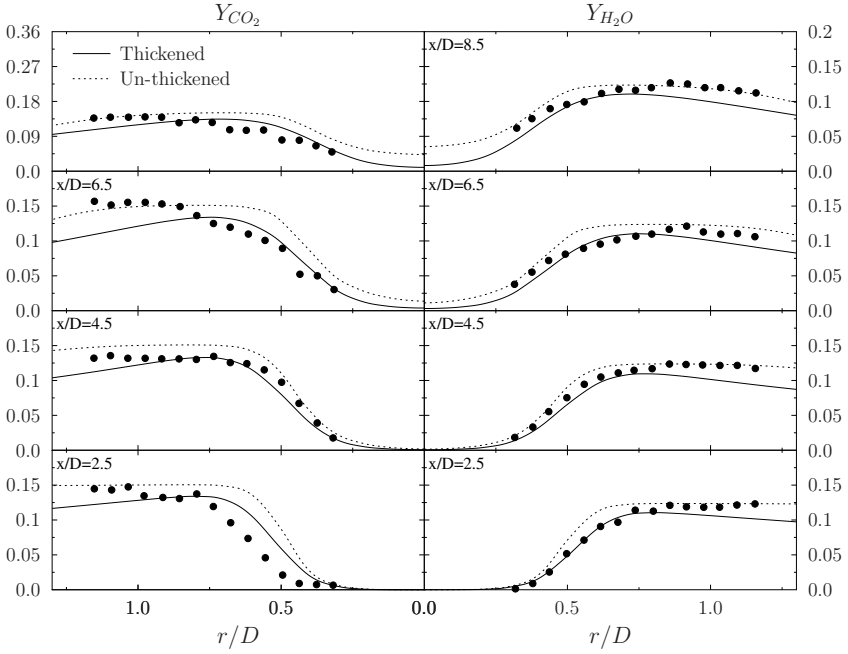

FIGURE 5.14: F3 radial distributions of the time-averaged carbon dioxide mass fraction $\langle \widetilde{Y}_{CO_2} \rangle$ and water vapour mass fraction $\langle \widetilde{Y}_{H_2O} \rangle$ at various axial locations comparing the thickened and un-thickened stochastic field.

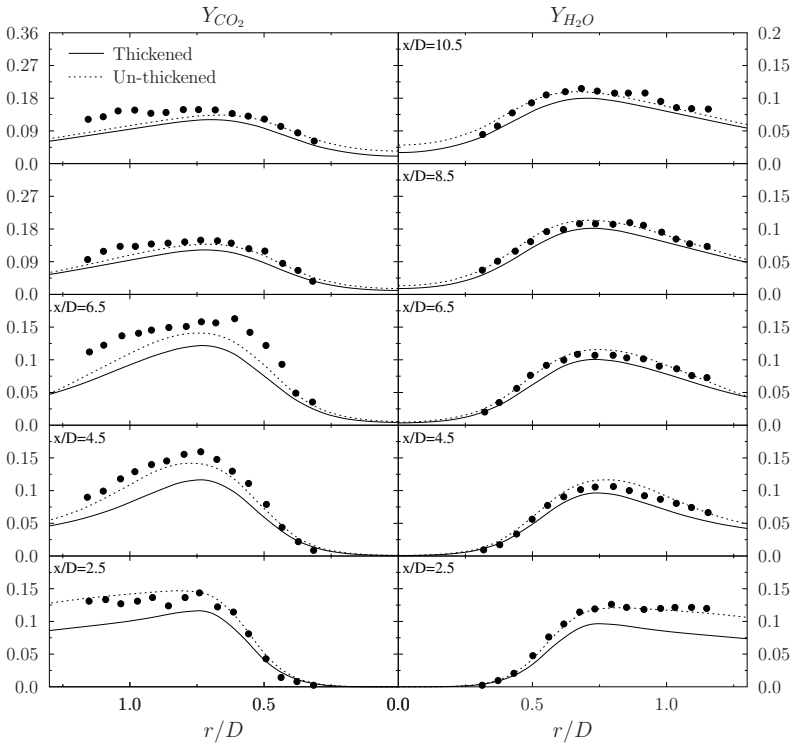

FIGURE 5.15: F1 radial distributions of the time-averaged carbon dioxide mass fraction $\langle \widetilde{Y}_{CO_2} \rangle$ and water vapour mass fraction $\langle \widetilde{Y}_{H_2O} \rangle$ at various axial locations comparing the thickened and un-thickened stochastic field.

axial velocity in both flames shows reasonable agreement across both stochastic field methodologies, but as the flame height in the TSF simulations are better predicted, the axial velocity predictions of the TSF approach shows closer agreement to experiment.

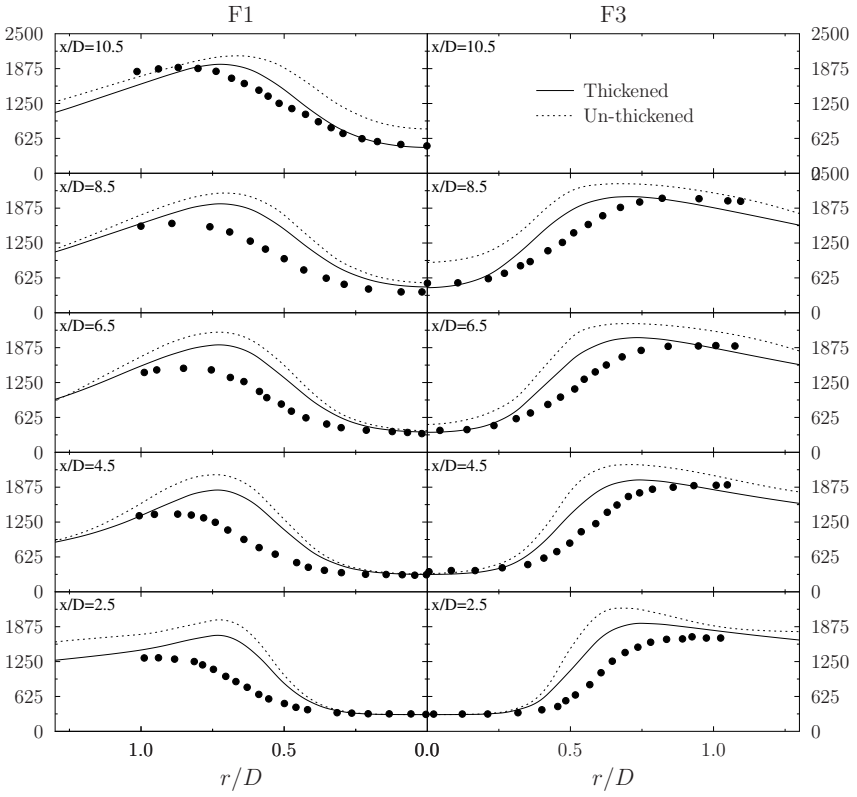

FIGURE 5.16: Radial distributions of the time-averaged filtered temperature $\langle \widetilde{T} \rangle$ for the F1 and F3 flames at various axial locations comparing the thickened and un-thickened stochastic fields.

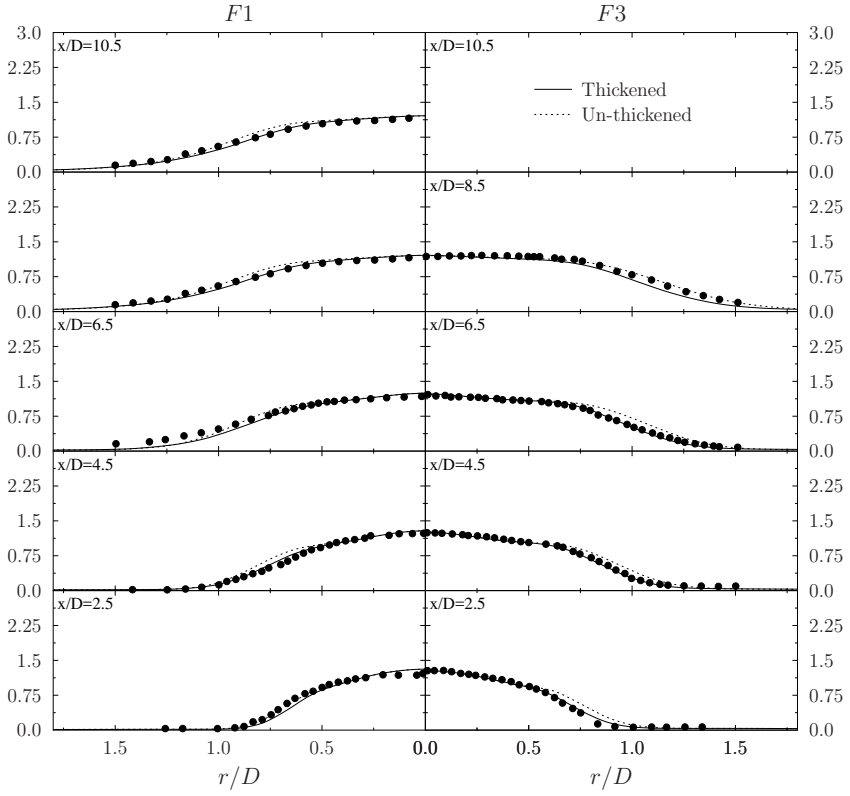

FIGURE 5.17: Radial distributions of the time-averaged normalised axial velocity at various axial locations comparing the thickened and un-thickened stochastic fields for Flames F1 and F3.

5.4 Flame Sensor

In this section, the sensitivity of the TSF solution to the inclusion of a flame sensor and to the value of the corresponding broadening factor is investigated. In the first part, the impact of the choice of flame sensor with nominal broadening factor is analysed. The second part assesses the sensitivity of the choice of broadening factor for the various sensors.

5.4.1 A Priori Flame Sensor Analysis

In Figure 5.18, the different sensors are analysed for a range of mixture fractions (zero to stoichiometric) and progress variables (zero to unity) with the nominal broadening factors given in the captions of the figures. Also shown is the iso-line, $c(z)$, corresponding the the progress variable of maximum reaction rate. Figure 5.18a shows the distribution of flame sensor activation for the traditional sensor. From this figure it is obvious that there is no dependence on mixture fraction and that the sensor value at the maximum reaction rate decreases as mixture fraction approaches zero. Figure 5.18b shows the distribution of the broadened sensor. Although there is still no dependence on composition, the broadening of the sensor profile though the hyperbolic tangent ensures that there is more activation of the flame sensor at the maximum reaction rates that stretch into lower values of mixture fraction.

It should be noted, that although the location of the iso-line in Figure 5.18 indicates the maximum reaction rate, it does not indicate the magnitude. For decreasing mixture fractions towards zero, the magnitude of the maximum reaction rate decreases and therefore, the thickening required can also decrease though accompaniment of more resolvable scalar gradients. Therefore it may be concluded that to a certain extent the broadened sensor captures this behaviour although perhaps coincidentally.

This behaviour is taken into account deliberately in the Arrhenius rate sensor shown in Figure 5.18c. With the sensor normalised by the maximum reaction rate obtained at the stoichiometric mixture fraction (z_{st}), the flame sensor activity is highest at mixture fractions close to stoichiometry at the progress variable for maximum reaction rate. It then reduces along the maximum reaction rate iso-line as the mixture fraction approaches zero. When normalising by the maximum reaction rate as a function of the local mixture

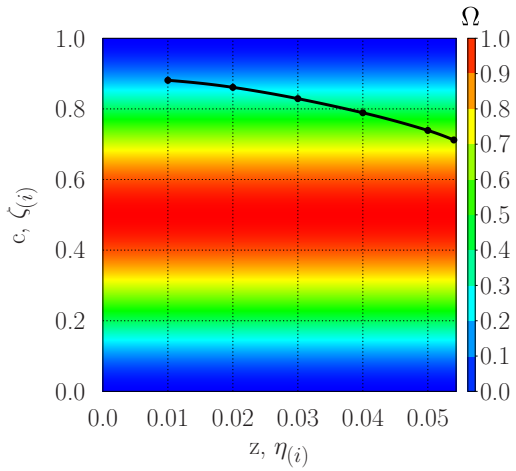

(A) The *traditional* flame sensor of Equation 5.12

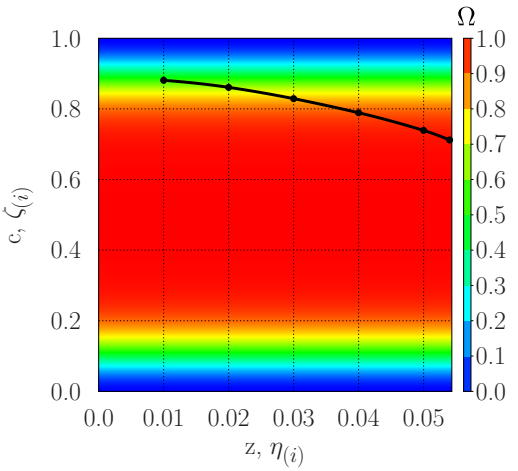

(B) The *broadened* flame sensor of Equation 5.15 with $\beta_1 = 3.5$

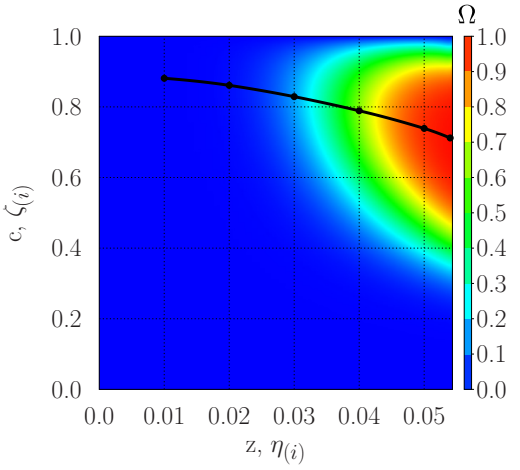

(C) Reaction rate sensor of Equation 5.17 with $\beta_2 = 2.6$. $\dot{\omega}_{max} = \dot{\omega}_{st}$.

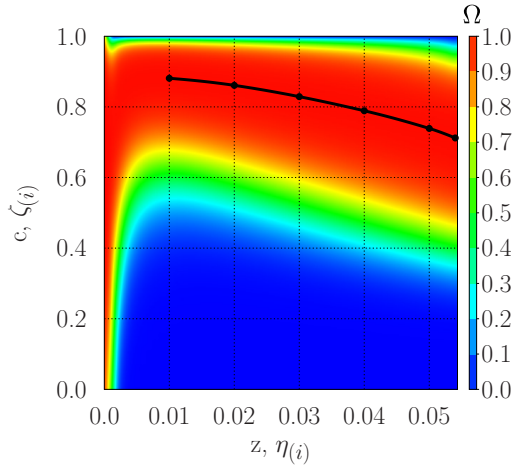

(D) Reaction rate sensor of Equation 5.17 with $\beta_2 = 2.6$. $\dot{\omega}_{max} = \dot{\omega}(z)_{max}$

FIGURE 5.18: Example compositions of activity of different flame sensors across representative compositions for methane-air system with $T_f = T_o = 300K$.

fraction, full activation of the sensor can be seen following the maximum reaction rate isoline. As the mixture fraction approaches zero, as does the maximum reaction rate causing Equation 5.17 to be activated for all values of progress variable at $z = 0$. This indicates that within a simulation, if using this method of normalisation, the oxidiser stream (and correspondingly the pure oxidiser stream) will be thickened to the maximum prescribed thickening factor unless appropriate numerical remedies are taken. As it stands, this limiting behaviour contradicts the primary benefit of a flame sensor to begin with and will therefore be avoided in the proceeding 3D LES.

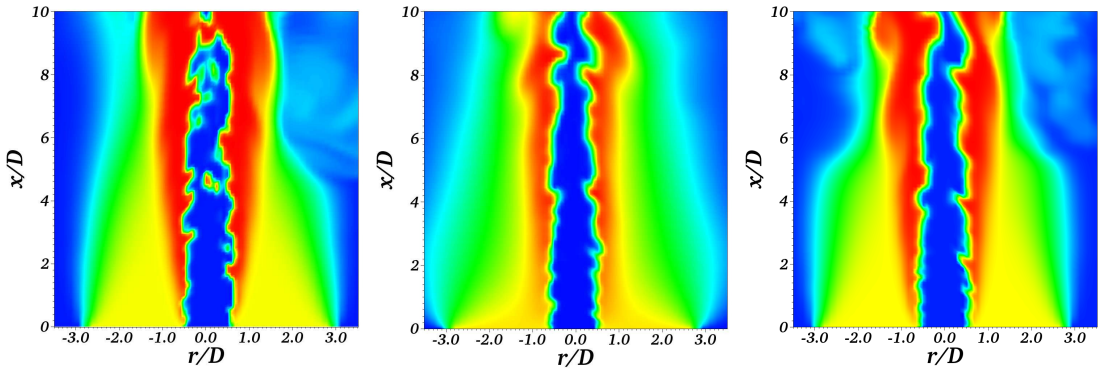

FIGURE 5.19: Instantaneous temperature field of an individual field from the F3 flame LES with $\Delta_x = \Delta = 1.0$ mm for traditional stochastic fields (left), and thickened stochastic fields with no sensor (middle) and thickened stochastic fields with flame sensor (right).

5.4.2 Bunsen Flame Analysis

To assess the effect of choice of flame sensor on the TSF simulation results, additional simulations of the F1 and F3 cases were conducted with the three flame sensors given in Section 5.2.5 namely: the traditional, broadened, and Arrhenius rate sensors. In the case of the broadened sensor, β_1 was set to a value of 3.5 and for the Arrhenius rate sensor, β_2 was set to the nominal value of 2.6. The reaction rate used for normalisation in the Arrhenius sensor was that based on maximum reaction rate determined at the stoichiometric mixture fraction (z_{st}). For clarity the proceeding section, where the conclusions and trends are the same for both F3 and F1 flames, only the F1 is shown.

Figures 5.19 and 5.20 show an extension of the instantaneous filtered temperature field colour maps shown in Section 5.3.2 to include the temperature map of the solutions with the broadened flame sensor. From these figures it can be seen that the inclusion of the sensor concentrates the artificial thickening to the interface of the pilot and jet streams. An effect inferred by an obvious reduction in the diffusion of the pilot stream with the ambient air.

The concentration of the thickening to the interface of the jet and pilot can be seen through contour maps of the instantaneous thickening factors obtained in the TSF framework for the F3 (Figure 5.21) and F1 (Figure 5.22). The thickening factor in both simulations is unity outside of the flame since the flame sensor tends to zero in this region. Inside the flame, the value of the thickening factor varies due to the dependence

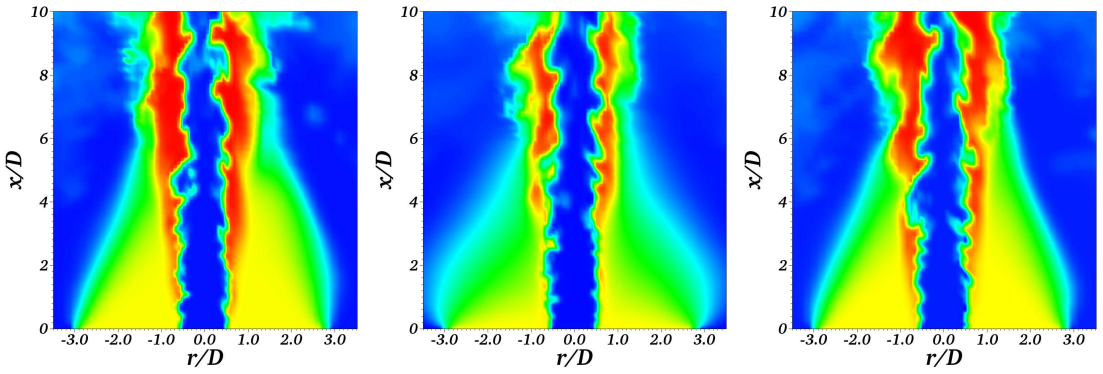

FIGURE 5.20: Instantaneous temperature field of an individual field from the F1 flame LES with $\Delta_x = \Delta = 1.0$ mm for traditional stochastic fields (left), and thickened stochastic fields with no sensor (middle) and thickened stochastic fields with flame sensor (right).

on the local value of u'_Δ/S_L in Equation 5.10. In both cases, the peak value of the thickening factor within the flame increases with downstream axial location.

For the F3 flame, in the near-field the peak thickening factor is typically in the range 2-4, and it is mostly in the range 4-7 downstream of $x/D = 5$. The F1 flame on the other hand exhibits less thickening, generally around 1-3, increasing slightly to around 2-4 after $x/D = 7$. The thickening factor tends to increase downstream because of the decay of u'_Δ away from the jet inlet leading to the combustion becoming more flamelet-like and thereby increasing the resolution requirement. These thickening factors may be compared with the static thickening factor of $F = 8$ used in [46] for ATF simulations of the F3 flame with a grid spacing of 0.8 mm, and for the value of approximately 12 required with the characteristic grid spacing used here. Figures 5.21 and 5.22 show that the thickening factor required by the TSF approach can be significantly less than the value required in the Thickened Flame model, reducing unwanted effects of the thickening on the chemical time scale, the Damköhler number and the Karlovitz number.

The magnitude of mean thickening factor and efficiency function for the F1 and F3 flames with a flame sensor are shown Figure 5.23. For comparison, the results for the no-sensor simulations are also shown. Similar to Figures 5.21 and 5.22, this figure also shows the difference in magnitude of thickening required by the F1 and F3 flame. More importantly, this figure clearly shows is that the inclusion of a sensor drastically modifies the spatial distribution of thickening factor and efficiency function. Specifically, it removes the excess and undesired diffusion of scalars that are not in the vicinity of the flame front.

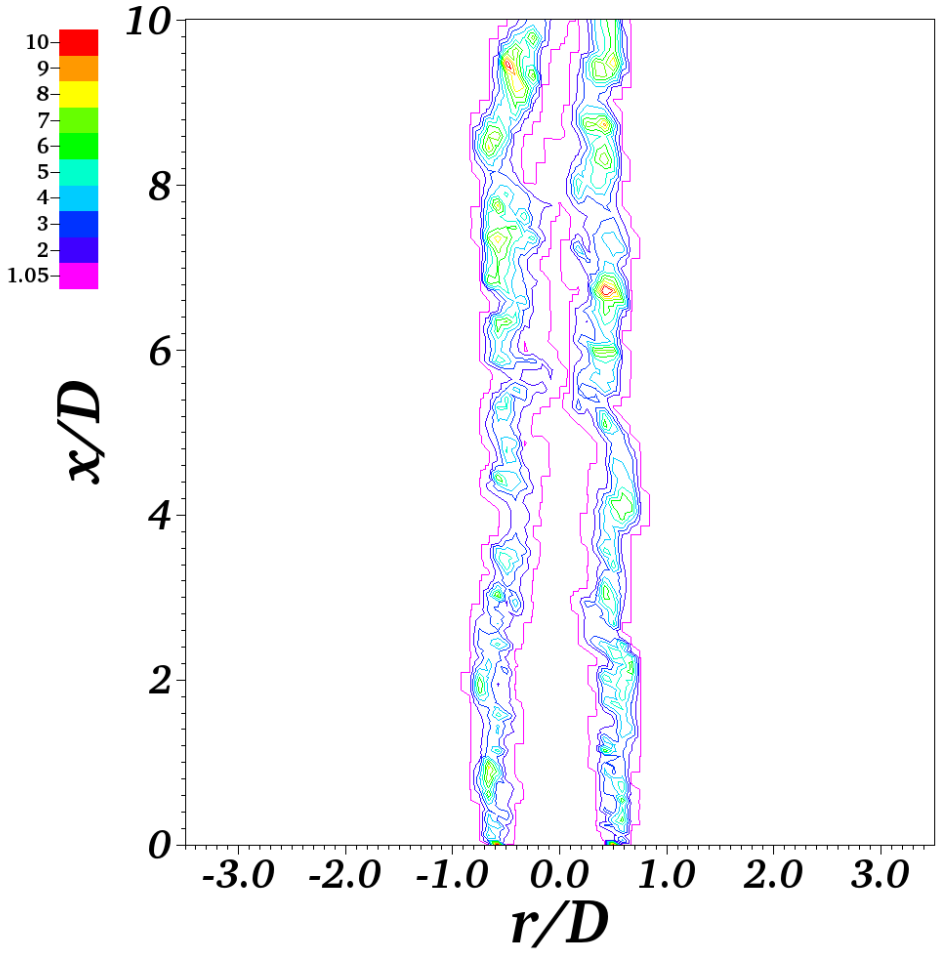

FIGURE 5.21: Instantaneous contours of thickening factor in the thickened stochastic fields simulation of the F3 Flame.

The impact of including a flame sensor (and the difference between the various types) on the solution can be seen through radial mass fraction distributions of carbon dioxide and oxygen in Figures 5.25 and 5.24 respectively for the different sensors. In both the F3 and F1 flames, the mass fraction predictions between the various sensors show an almost indistinguishable difference. However, the inclusion of a flame sensor in general has a substantial influence on the solution, specifically in the $r/D > 1$ regions.

As indicated from the figures above, the inclusion of a sensor allows for unaltered mixing and entrainment of the ambient air into the flame due to the removal of artificial thickening in these regions. It can be seen in both the F1 and F3 flames that the solution with no sensor artificially increases the diffusion of the pilot and ambient air which can

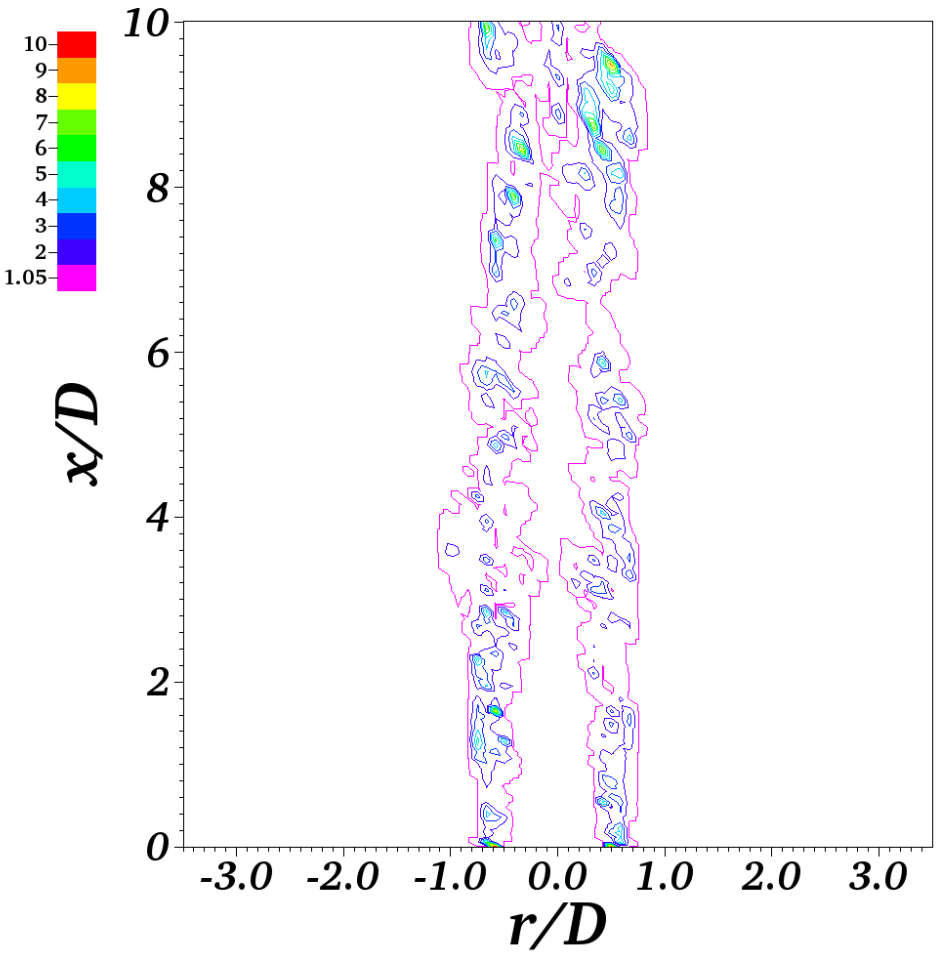

FIGURE 5.22: Instantaneous contours of thickening factor in the thickened stochastic fields simulation of the F1 Flame.

be identified with the higher/lower mass fractions of oxygen and carbon dioxide receptively at larger r/D. In both F1 and F3 cases, the inclusion of the sensor substantially improves the mixing predictions compared to experiment at larger r/D.

5.4.3 Sensitivity to Flame Sensor Type

The relative insensitivity of the predictions between the different sensors can be investigated through analysis of the global flame sensor seen by a particular field. Scatter plots of the global flame sensor seen by a single, arbitrary field versus progress variable are shown in Figure 5.26 along with a solid line indicating the value of the particular flame sensor calculated on that field. Shown along side the scatter plots is the corresponding,

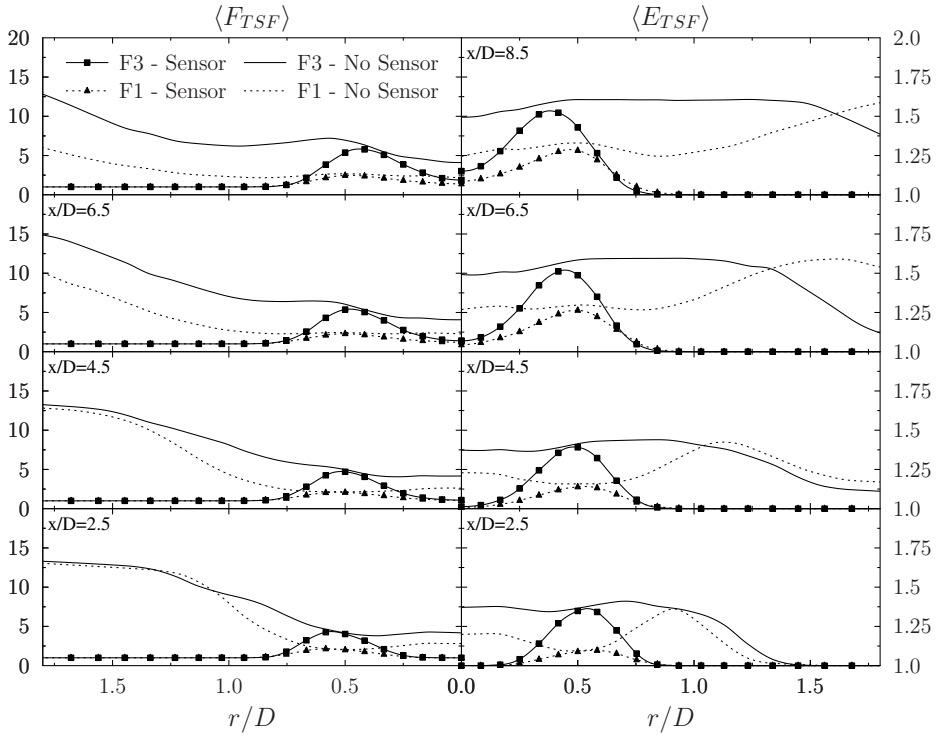

FIGURE 5.23: Comparison of sensor and no-sensor radial distributions of mean efficiency function (E_{TSF}) and thickening factor (F_{TSF}).

50 bin discrete PDF of global sensor activation magnitude for the particular sensor being analysed.

Figure 5.26a shows the results for the traditional sensor. Also shown with the PDF of this particular sensor, is the discrete PDF of the traditional sensor on the same arbitrary stochastic field in the limiting case that $\zeta_{(i)} = \tilde{c}$. From the scatter plot, the inclusion of the *max* operation in the global sensor (along with field dispersion) draws points towards $\Omega = 1$ that spans a wider range of progress variable values than it would otherwise span. As a consequence, the corresponding probability of obtaining a global sensor that is fully activated on a particular field has increased substantially.

The width of the broadened range of activated $\zeta_{(i)}$ with $\Omega = 1$ provides an indication to the amount of overlap between thickening profiles of the various fields. In general, for a large amount of overlap of fields, it is expected that the majority of the points be clustered at $\Omega = 1$. Conversely, as the overlap decreases (or the fields become "isolated"), the points will begin to cluster towards the solid line on that particular field.

An additional influence on the location of the points on the scatter plot is the location of a stochastic field relative to the mean flame brush. The aforementioned behaviour of

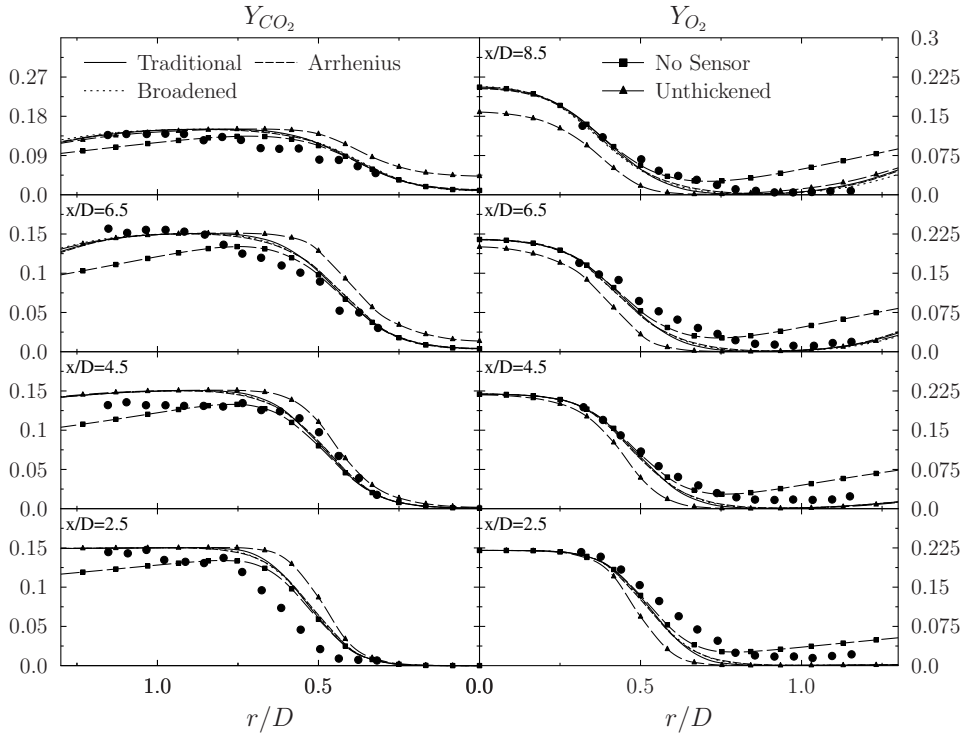

FIGURE 5.24: Radial distributions of the time-averaged carbon dioxide mass fraction $\langle \widetilde{Y}_{CO_2} \rangle$ and oxygen mass fraction $\langle \widetilde{Y}_{O_2} \rangle$ at various axial locations comparing the the effect of different flame sensors with TSF for the F3 Flame

Ω and overlap is most applicable to a field located in the centre of the flame brush. For a stochastic field that is preferentially located at the leading or trailing edge of the mean flame brush, in addition to the above behaviour, there will be a larger concentration of points towards $\zeta_{(i)} = 1$ and $\zeta_{(i)} = 0$ respectively.

The severity of overall migration of points towards the solid line on a scatter plot may hint at the solution being statistically under-resolved. This is because for a low number of fields and a large sub-filter variance, field dispersion will be high and overlap at a minimum. However, it should be mentioned that the amount of overlap between fields is a function of both the number of fields and the value of β; A small number of fields with large β may provide the same amount of visible overlap as many fields with a small value β. Therefore, even with a sufficient visible overlap of the fields, the simulation is not guaranteed to be statistically resolved and other methods of ensuring this need to be taken.

The behaviour described above is exaggerated through broadening of the sensor profile as shown in Figure 5.26b. For this sensor the extent of progress variables with $\Omega = 1$ is

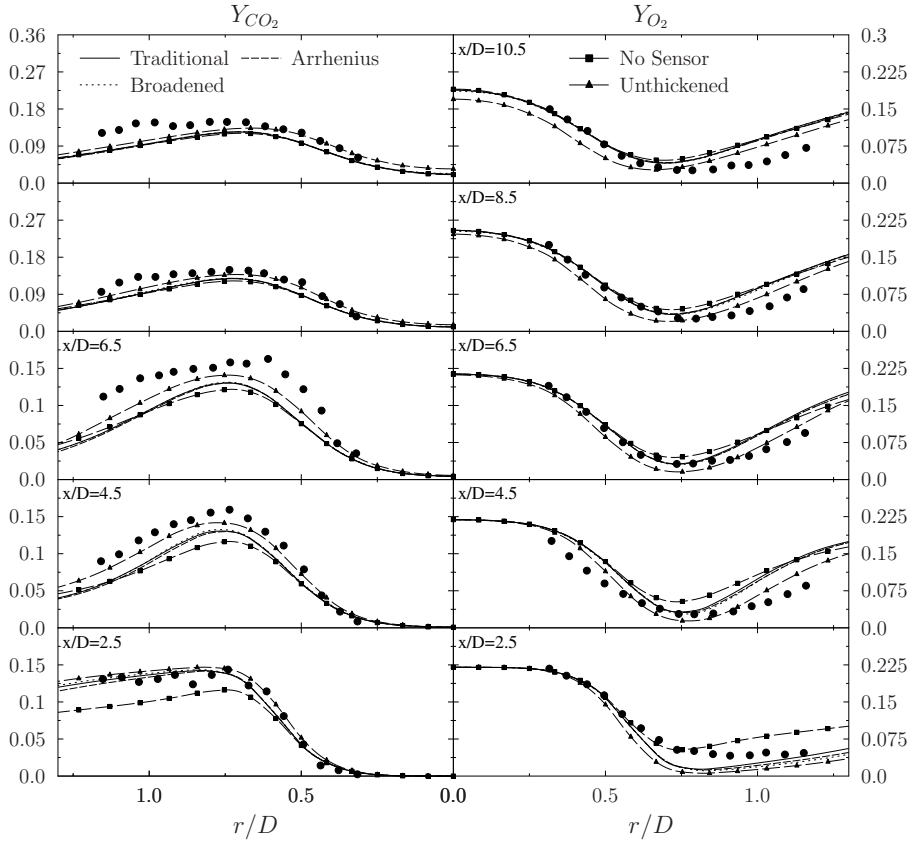

FIGURE 5.25: Radial distributions of the time-averaged carbon dioxide mass fraction $\langle \widetilde{Y}_{CO_2} \rangle$ and oxygen mass fraction $\langle \widetilde{Y}_{O_2} \rangle$ at various axial locations comparing the effect of different flame sensors with TSF for the F1 Flame

increased greatly through the process of increasing the minimum value of flame sensor activation for a given progress variable. The points that where previously hovering around lower flame sensor values with the traditional sensor are swept back through the broadening. This corresponds directly to an increases in the probability of finding a fully activated sensor as seen through the discrete PDF.

Figure 5.26c shows the effect of the Arrhenius rate sensor. Contrary to the symmetry in progress variable space about $\zeta = 0.5$ of the other sensors, this particular sensor shows strong asymmetry and, as intended, a bias towards the progress variable of maximum reaction rate. As a consequence of this bias, it shares certain similarities with the broadened sensor, namely the forcing of larger progress variable values to have a larger flame sensor activity. The relaxing of this enforcement at lower progress variable values is accompanied by a substantially larger region of sparsely located activation values. Regardless of the preference of this sensor to different extreme regions within progress variable space, a high concentration of points can still be seen at $\Omega = 1$, which, due to

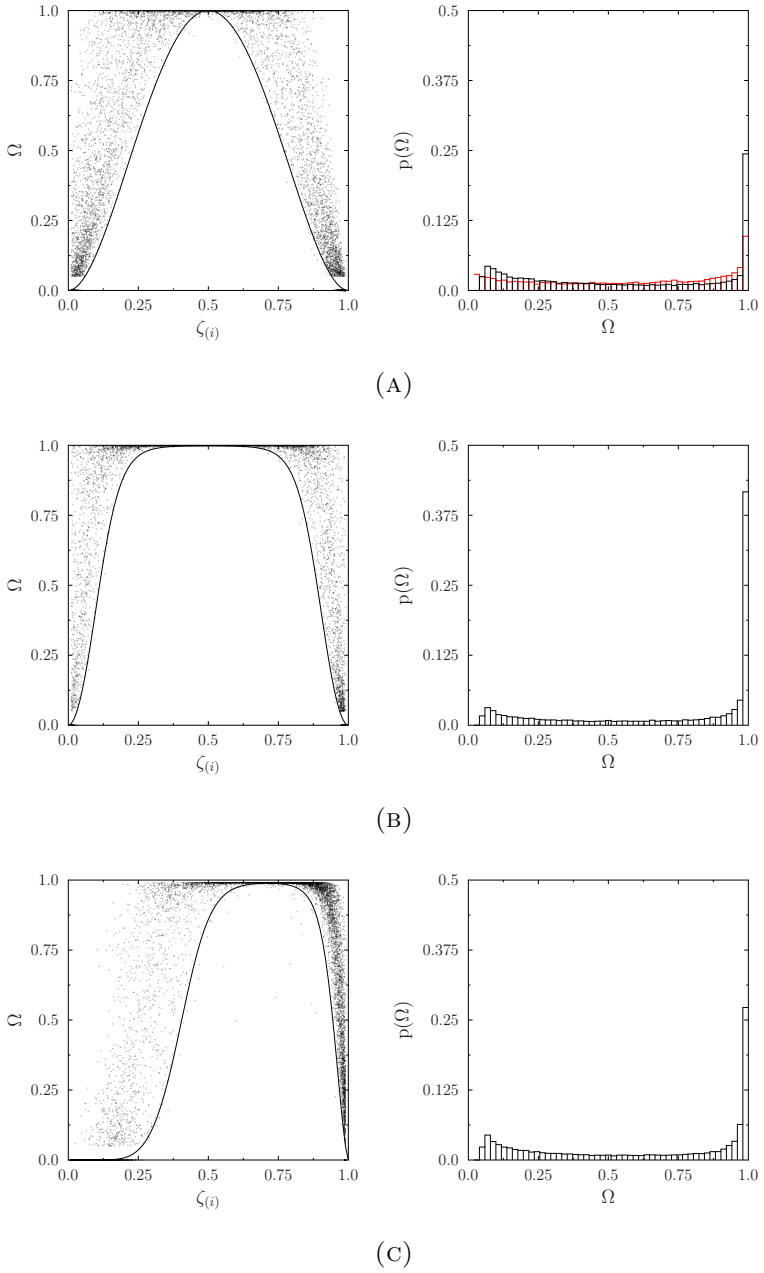

FIGURE 5.26: F1 Flame. Left: Scatter plot of global flame sensor and progress variable of a single field. Right: PDF of global flame sensor

the dispersion of fields, spans a broader range of progress variables; a behaviour shared by all the sensors analysed. This can also be seen in the corresponding PDF.

From these scatter plots, the relative insensitivity of choice of flame sensor is likely a consequence of the *max* operation in the global flame sensor formulation. The objective of the *max* operation is to create a single activated region to be seen by all fields, however, the consequence is that through the dispersion of the fields, the actual active

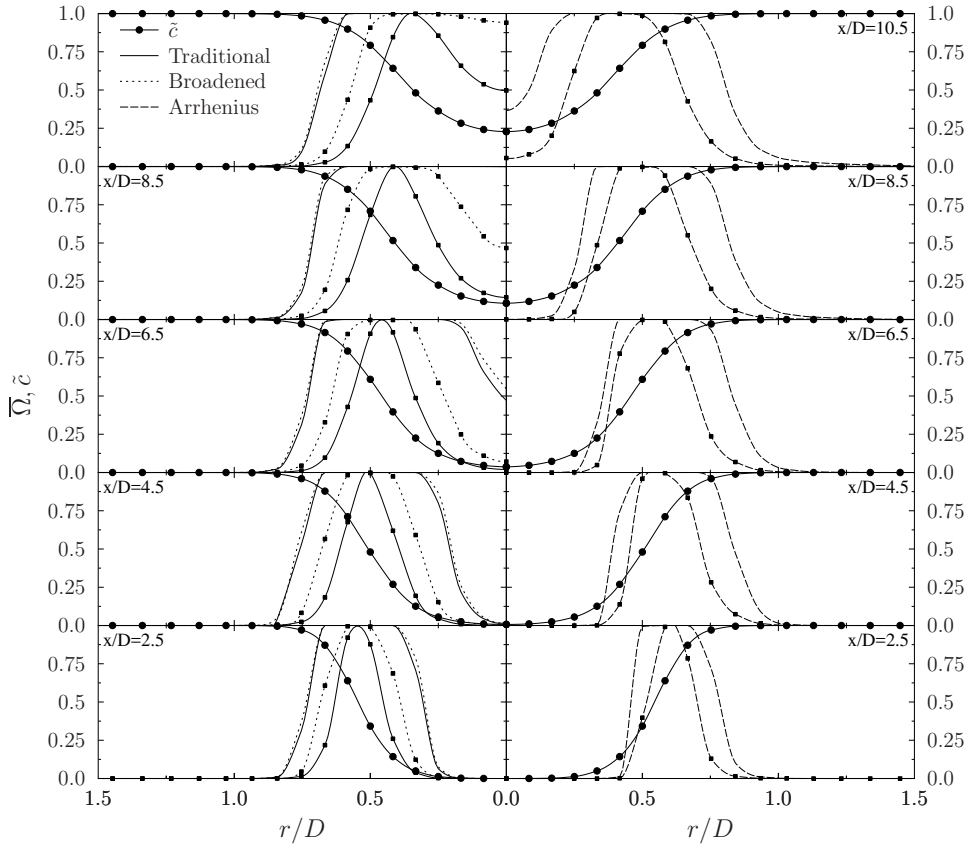

FIGURE 5.27: Radial distributions of the time-averaged global flame sensor at various axial locations for the F1 flame. Symbols indicate global sensor distribution when $\zeta_{(i)} = \tilde{c}$

region on a particular field (and thus the global sensor) can be much broader than intended. Therefore, the effective broadening factor, β_{eff}, is larger than the prescribed broadening factor.

To exemplify this influence, Figure 5.27 shows the radial distribution of the temporally averaged global flame sensor for the three simulations discussed at the beginning of Section 5.4.2. In addition to this, the figure also shows the global sensor distribution for the case where $\zeta_{(i)} = \tilde{c}$. The spatial distributions of the traditional and broadened sensor in the case of $\zeta_{(i)} = \tilde{c}$ are quite different, yet the global sensor determined in the TSF framework with these two sensors is effectively identical.

Comparatively, the Arrhenius sensor shows a slightly narrower profile with a much slower broadening of the sensor with downstream location. Interestingly, this figure highlights the principle difference between the broadened sensors and the Arrhenius rate sensors. In the near field, the reaction rate is lower than in the downstream location and as a

consequence, the sensor profile is narrower compared the broadened sensors which use a geometric interpretation of the flame to establish activation. The result is that the flame sensor is located preferentially towards $\tilde{c} = 1$, however, even with this preferential position, the artificial broadening of this sensor is sufficiently large such that the benefit of a reaction rate based sensor is mostly hidden. These slight differences between the Arrhenius sensor and the others may justify the diminishing (although minor) differences seen in Figures 5.24 and 5.25.

From the results of the TSF simulations and the distribution of points within the scatter plots in Figure 5.26, it can be concluded that apart from the Arrhenius rate sensor in the near-field, due to the dispersion of the fields and the *max* operator, the sensors are artificially broadened to the point that the choice of sensor becomes inconsequential. This artificial broadening has the effect that as it increases, the solution will approach the limiting case were no sensor is used; globally, $\Omega = 1$. This limiting behaviour can be seen in the scatter plots for the broadened and Arrhenius rate sensors with increased broadening factors shown in Figure 5.28. Irrespective of how broad the sensor is set locally on the field, the resultant clustering of point at $\Omega = 1$ spans a broader progress variable range.

As a consequence of this, the effect of increasing the broadening factor on the solution is that it is expected to asymptotically approach the no-sensor solution. For example, the effect of modifying the broadening factor in the Arrhenius rate sensor is shown in Figure 5.29 and as expected, as the broadening factor approaches infinity, the results approach the no-sensor solution.

5.4.4 Comparison to ATF

Artificially Thickened Flame simulations were conducted and compared to the results of the TSF simulations. The objective of these set of simulations was not to scrutinise the underlying numerical models of the ATF or the ATF's ability to model this particular flame as this has already been conveyed in a previous work [46]. Instead these simulations simply provide a basis of comparison to the proposed TSF methodology.

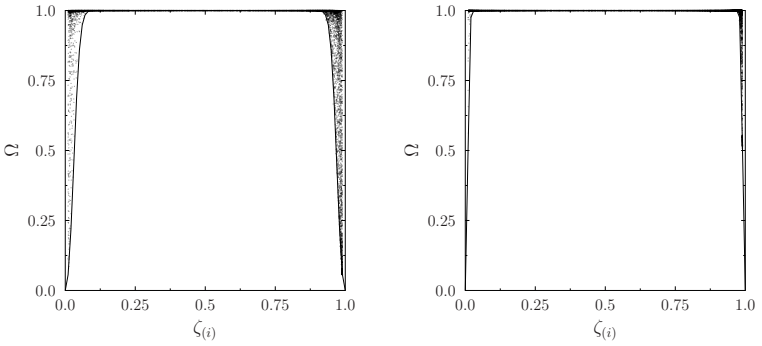

(A) Scatter plot of increasing β_1 for the broadened sensor. Left: $\beta_1 = 35$, Right: $\beta_1 = 350$

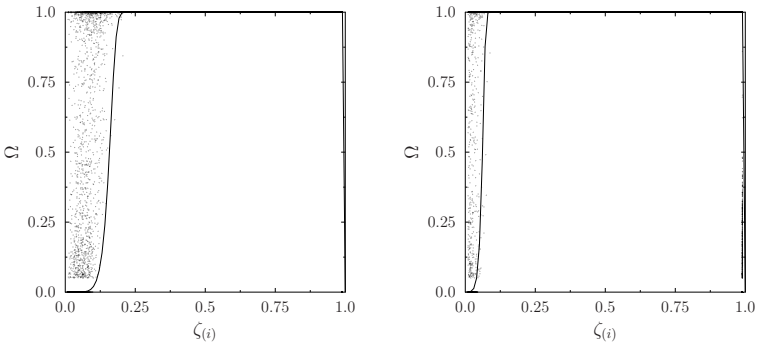

(B) Scatter plot of increasing β_2 for the Arrhenius rate sensor . Left: $\beta_2 = 10^3$, Right: $\beta_2 = 10^6$

FIGURE 5.28: Scatter plot of global flame sensor and progress variable of a single field comparing broadening factors for the F1 Flame

The ATF simulations were conducted with the exact same numerical configurations as the TSF simulations presented in Section 5.4.2 using the traditional sensor. The main differences in the ATF simulations relative to the TSF simulations were:

1. The absence of the *max* operation in the flame sensors
2. A constant thickening factor of 12 was used instead of a variable thickening factor as in the TSF

In the ATF simulations, the efficiency function of Charlette et al. [14] was used, with β in Equation 3.9 taking on a value of 0.5 as suggested in [14]. The sub-filter scale velocity fluctuations required to evaluate Equation 3.9 were determined with the ATF scale equivalent of Equation 5.11 [22]. The results of the simulations are shown in Figure 5.31 for the F1 and in Figure 5.30 for the F3.

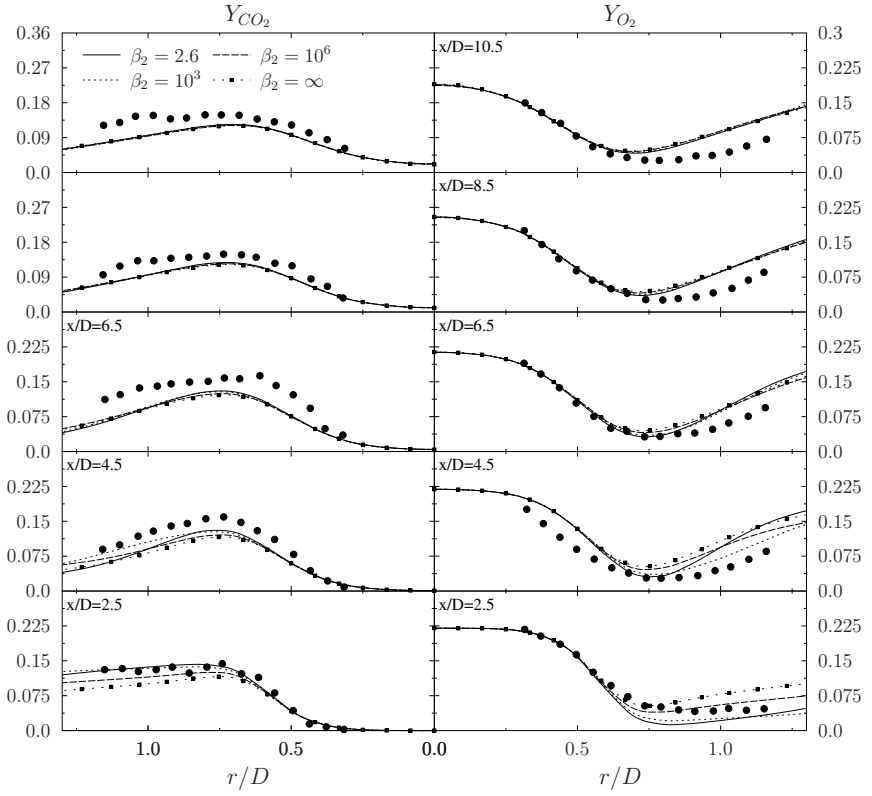

FIGURE 5.29: Comparison of effect of modification of β_2 in the Arrhenius rate sensor for the F1 Flame with TSF

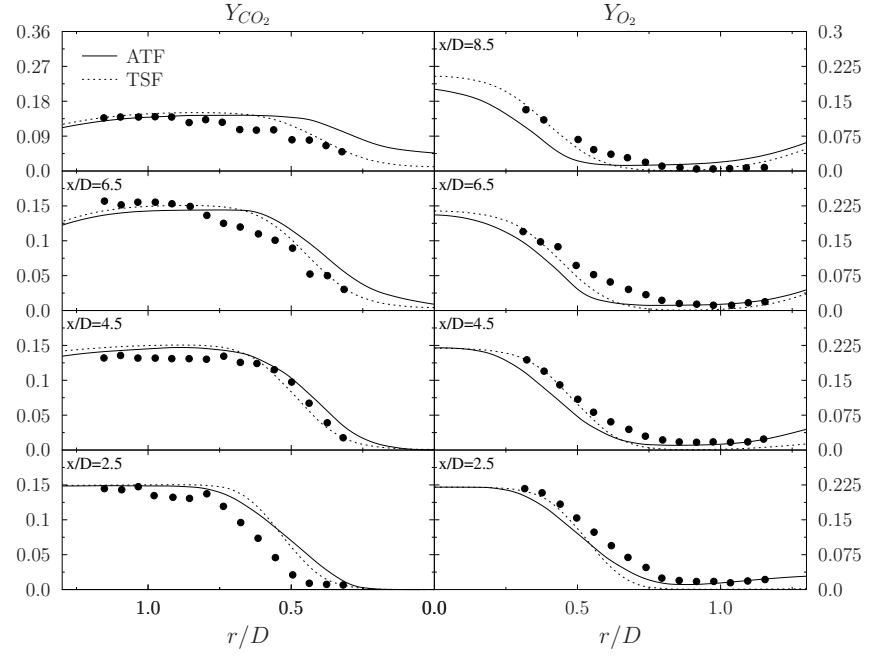

FIGURE 5.30: Radial distributions of the time-averaged carbon dioxide mass fraction $\langle \widetilde{Y}_{CO_2} \rangle$ and oxygen mass fraction $\langle \widetilde{Y}_{O_2} \rangle$ at various axial locations comparing ATF with TSF for the F3 Flame

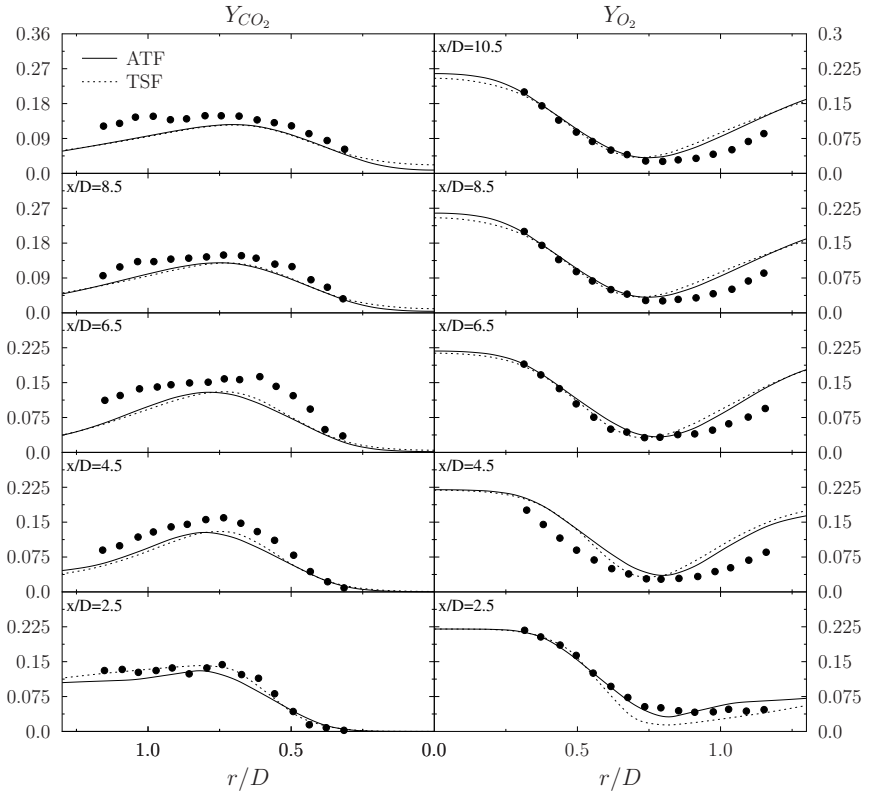

FIGURE 5.31: Radial distributions of the time-averaged carbon dioxide mass fraction $\langle \widetilde{Y}_{CO_2} \rangle$ and oxygen mass fraction $\langle \widetilde{Y}_{O_2} \rangle$ at various axial locations comparing ATF with TSF for the F1 Flame

Apart from CO_2 which was also difficult to capture in the TSF and un-thickened SF simulations, the agreement between ATF and TSF is very good across both flames which give credence to the proposed TSF framework. The under-predicted flame height of the ATF simulations shown here can be explained by the choice of β. In the ATF simulations of [46] a dynamic β formulation was used and the authors obtained excellent results for all the flames (F1-F3). To illustrate the benefit of their method over the use of a constant β, they also conducted additional simulations with a constant β of 0.2. The results of this particular simulation resulted in an over-predicted flame height and overall under-predicted product mass fraction compared to the dynamic formulation.

To assess the impact of β on the ATF predictions within the numerical configuration used here, an additional simulation of the F3 flame using $\beta = 0.2$ was also conducted and the results are shown in Figure 5.32. Similar to the results of [46], setting $\beta = 0.2$ resulted in a longer flame and under-estimated product mass fraction with respect to the $\beta = 0.5$ results. However, the results in general are in better agreement with experimental measurements, and closer to the predictions of the TSF framework. This

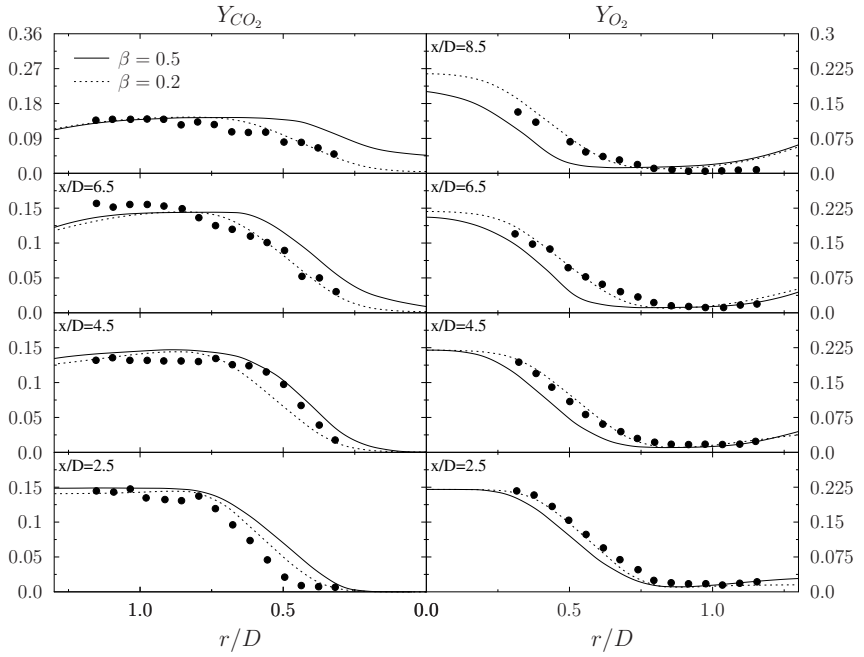

FIGURE 5.32: Radial distributions of the time-averaged carbon dioxide mass fraction $\langle \widetilde{Y}_{CO_2} \rangle$ and water vapour mass fraction $\langle \widetilde{Y}_{O_2} \rangle$ at various axial locations comparing the the effect of different values of β in Equation 3.9 for the F3 Flame

comparison highlights the sensitivity of the ATF method to the choice of β and the benefit of implementing a dynamic formulation.

In addition to the comparison of different values of β, additional ATF simulations were conducted using the three sensors described above to observe if they resulted in more substantial differences in predictions from those seen in the TSF simulations. From Figure 5.33,even in the absence of the *max* operation, it can be seen that although some differences can be observed closer to the jet rim, there is still a minor impact on the simulation predictions with the Arrhenius rate sensor giving arguably the best results. Therefore, the reintroduction of the *max* operation in the flame sensor (and the broadening of the thicken region as a consequence) used in the TSF framework may explain the indistinguishable results seen for the TSF sensor comparisons.

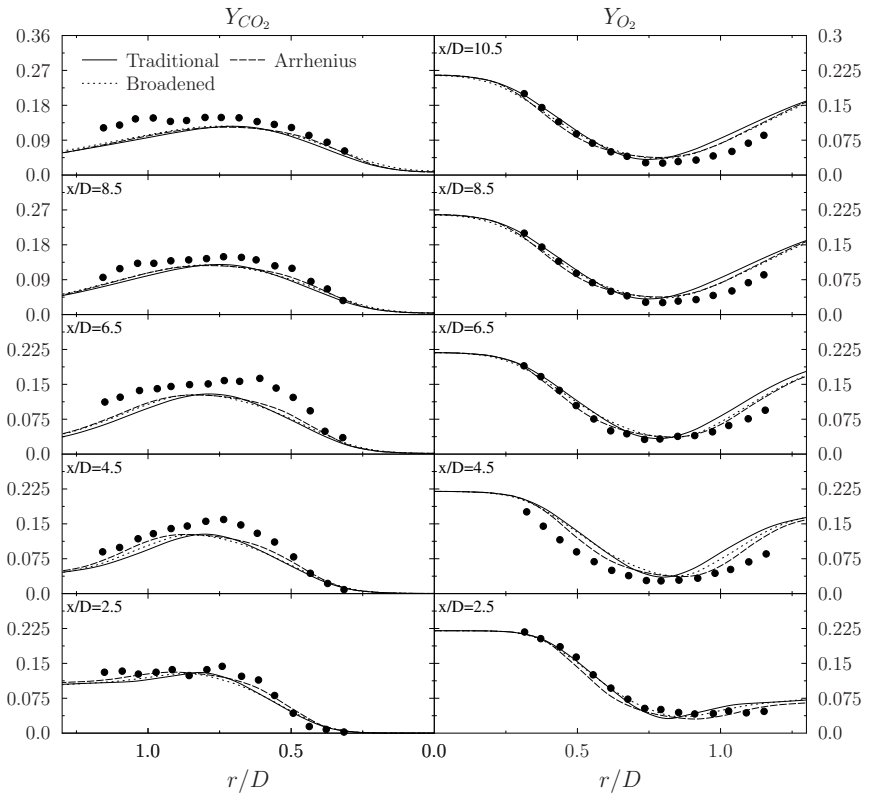

FIGURE 5.33: Radial distributions of the time-averaged carbon dioxide mass fraction $\langle \widetilde{Y}_{CO_2} \rangle$ and water vapour mass fraction $\langle \widetilde{Y}_{O_2} \rangle$ at various axial locations comparing the the effect of different flame sensors with ATF for the F1 Flame

5.5 Conclusions

Full-resolution stochastic fields simulations are not currently available due to prohibitive computational effort required. Such fully-resolved stochastic fields simulations of premixed turbulent combustion will be facilitated by application of AMR approaches, however introduction of AMR-stochastic fields LES is beyond the scope of this study. Instead, in this chapter, a thickened Stochastic Fields (TSF) approach was proposed. This modelling approach seeks to ensure adequate numerical resolution of the stochastic fields equation in premixed turbulent combustion with reduced computation time. This framework bridges between the conventional stochastic fields and conventional Thickened-Flame approaches depending on the sub-grid combustion regime and the numerical grid spacing utilised. In the limit of full-resolution, it converges towards Direct Numerical Simulation. A method for determining the thickening factor required and an efficiency function model are provided based on data from one-dimensional stochastic fields simulations of freely-propagating turbulent premixed flames. The efficiency function accounts for the loss of resolved flame surface area caused by applying the thickening transformation to the stochastic fields equations. The numerical implementation of the TSF approach requires only a minor modification of any stochastic fields code.

Included in the thickened stochastic fields approach presented was a new form of "global" flame sensor specific to this framework that ensured consistency between the thickening factor seen by the a stochastic fields and potentially thickened LES momentum equations. This new global flame sensor maintained the limiting behaviour of the TSF framework while allowing the use of any form of flame sensor previously used in conventional Artificially Thickened Flame (ATF) simulations.

In addition to the global sensor, a new flame sensor was proposed that modified a previously established sensor based on a reaction rate formulation. The reaction rate used to trigger the activation of the sensor proposed here is that of a one-step global reaction as opposed to a general Arrhenius rate expression. The formulation presented allows this sensor to be used with arbitrary chemical mechanisms and ensures that the flame sensor is activated in the correct regions without the need for excessive tuning. The benefit of reaction rate based sensors over geometrically activated sensors is that they inherently account for changes in composition that may reduce local thickening requirements.

The TSF approach was tested by performing LES of a laboratory Bunsen flame. The results demonstrated that the TSF method avoids numerical errors arising in stochastic fields simulations where the grid spacing is set equal to the filter scale, and produces results that agree closely with the experimental measurements when a flame sensor is introduced. The thickening factor required in the TSF approach is generally less than in the conventional ATF approach, and this promises superior modelling of flame-turbulence interactions compared to the ATF approach. The TSF approach therefore may permit numerically-accurate simulation of industrially-relevant premixed combustion systems with several orders of magnitude fewer grid points than are required for accurate solution of the un-thickened stochastic fields approach.

In addition to verifying the baseline TSF approach, it's sensitivity to the choice of flame sensor and broadening factor were investigated. It was seen that due to the proposed form of the global flame sensor and the sub-filter dispersion of the fields, the global flame sensor was artificially broadened to levels above those prescribed. Even with small nominal broadening factors, the amount of artificial broadening was substantial enough to yield TSF solutions what were effectively independent of the choice of flame sensor. Increasing the broadening factor had the undesirable effect that it pushed the solution towards that of one with no sensor. As such, it is recommended that the choice of sensor and broadening factor be based on the desired behaviour of the sensor to be recovered as the sub-filter variance approaches zero. For the broadened sensor, $\beta_1 = 3.81$ is recommended, and for the Arrhenius rate sensor, $\beta_1 = 2.6$.

Overall the TSF predictions are in good agreement with experiment. The simple addition of thickening terms in the TSF equation thereby yields a computationally-efficient and accurate alternative to full-resolution stochastic fields simulations, which remain computationally prohibitive without adoption of AMR techniques.

Chapter 6

Conclusion and Future Work

This thesis provided initial insight into resolution requirements of Stochastic Fields for modelling of turbulent premixed combustion. In Chapter 4, numerical resolution requirements with the Itô interpretation of the Stochastic Fields framework were investigated. Three different test cases were simulated. First, one-dimensional simulations were conducted for a range of filter widths, Karlovitz numbers, and two numerical grid resolutions. The purpose of these simulations was to establish a relationship between these flame characterising parameters and the average resolution (requirements) of a stochastic fields. It was shown that under certain conditions, for numerically well-resolved stochastic field simulations, a stochastic field thickness can approach the laminar flame thickness and that setting the grid spacing equal to the filter width (which is commonly employed in LES) can lead to substantial errors in predicted flame speed.

This investigation into numerical resolution requirements was extended into 3D LES simulations of a laboratory Bunsen flame. Similar to the one-dimensional simulations, effects of resolution in this configuration were investigated by fixing the filter width and modifying the underlying numerical grid spacing. It was shown that for the lowest (and to a lesser extent the highest) Reynolds number Bunsen flame solution was not numerically accurate by setting the grid spacing equal to the filter width and that the scalar fields were more effected by numerical resolution than the velocity field. Additionally, it was shown that numerical thickening introduced from under-resolution led to reduced generation of flame surface and consequently, a reduction in total turbulent flame speed.

To remove any uncertainty associated with the imposition of boundary conditions used in the laboratory Bunsen flame simulations, a final simulation set of a statistically planar flame propagating in isotropic decaying turbulence was performed. Two filter widths were tested along with two numerical grid resolutions for a total of four numerical configurations. The effects of setting the grid spacing equal the the filter width confirmed the observation of both the one-dimensional and 3D Bunsen flame studies. The transient nature of these simulations highlighted an additional effect of numerical diffusion; that the numerical thickening of flame lead to a slower flame response to the initial turbulent field and a lag to its overall evolution. For the improved resolution cases at different filter widths, the differences in the total flame speed predictions also indicated possible inaccuracies of the established closures (IEM and gradient transport) of the stochastic field model.

From the observations of Chapter 4, the established resolution requirements (specifically at low Ka numbers) are too great for practical use. Chapter 5 introduced a thickened stochastic field framework as a potential method to provide a numerically accurate solution and avoid the excessive computational cost of fully resolved stochastic field simulations.

A method for calculating the thickening factor and efficiency function required in the proposed thickened stochastic field framework was presented. The efficiency function was developed empirically from a series of one-dimensional stochastic fields simulations of freely-propagating turbulent premixed flames. Simulations of the laboratory Bunsen flame were used as initial validation. The results showed good agreement with experiment except for excessive thickening in regions of pure mixing which was expected. Additional validation was conducted by comparing the thickened stochastic field results with results from simulations using the artificially thickened flame model. The results of the two modelling approaches yielded similar results providing confidence in the general approach of the thickened stochastic field framework. It was shown that the thickening factor required in the thickened stochastic fields approach is generally less than in the conventional Artificially Thickened Flame approach while still providing comparable results.

To mitigate this excessive mixing, a global flame sensor specific to the thickened stochastic fields framework was developed and applied to the initial formulation. This sensor

ensures consistency between the thickening factor seen by the all stochastic fields and a potentially thickened LES momentum field while still maintaining the underlying effect from the addition of established flame sensors. The results of the thickened stochastic field simulations with this flame sensor drastically improved the agreement with experiment. Within the application of this global sensor, the effect of various flame sensors commonly used in the Artificially Thickened Flame approach were compared. Additionally, a variation to a reaction rate sensor based off a Arrhenius rate expression was developed and tested. It was determined that due to the dispersion of the Stochastic Fields and the nature of the global flame sensor, the thickened stochastic field solution was effectively independent of the choice of flame sensor. It was therefore recommended to use the thickening factor requiring the least computational effort in conjunction with nominal broadening factors when generating the global flame sensor.

6.1 Future Work

Stratonovich versus Itô interpretations

In this work, only the Itô interpretation of the Stochastic Field framework was investigated. Even though the Stratonovich and Itô interpretations are mathematically equivalent, they produce different discretised forms of the SPDE and require different numerical implementations and algorithms to adhere to the underlying stochastic calculus used in their derivations (see [77]). This implies that numerical errors may propagate through the solution differently yielding different numerical behaviour. Although preliminary work on passive scalars has shown the results to be quite similar, how the errors manifest themselves (if at all) between the two interpretations in the context of under-resolved premixed combustion remains to be investigated.

Comparison of Low and High Reynolds number Stochastic Field Models

In Section 4.1.6 the 1998 [23] and 2015 [24] stochastic field formulations were briefly compared. This study illustrated that for the conditions present in the 3D LES conducted in this study, the choice of model was insignificant to the results. However, the

one-dimensional study highlighted that at moderate-to-low (sub-filter) Reynolds number, the choice of formulation yields a different flame speed predictions. If stochastic fields is to be extended to industrially relevant simulations, this particular regime, the choice of model, and the influence of micromixing models requires further investigation.

Adaptive Statistical Resolution

To further reduce the computation cost of Stochastic Fields simulation and ensure a statistically converged solution, an additional Stochastic Fields formulation can be developed that enables local adaptation of the number of stochastic fields used to evaluate statistics. This approach is highly advantageous because varying statistical sample sizes would be required/expected in the vicinity of the flame front which may only be in a small region of a combustor. This would further facilitate the accurate and computationally feasible application of the Stochastic Fields approach to industrially-relevant combustion systems. A description of the methodology and preliminary framework is presented in Appendix A.

Micromixing

In this work, different closures for the micromixing term in the Stochastic Field framework were not investigated. Turbulent premixed LES simulations to date have shown a lack of sensitivity to how C_ϕ is modelled. However, it is expected that to facilitate the extension of Stochastic Fields into industrially-relevant combustion systems that may exhibit more flamelet like combustion, a more rigorous and in-depth investigation into micromixing closures required at different premixed combustion regimes is necessary. A possible 3D test case for this investigation would be that of the Kobayashi Bunsen flame [112, 113].

Bibliography

[1] BP Statistical review of world energy, "BP statistical review of world energy, June 2015," no. June, pp. 2003–2005, 2015.

[2] International Energy Agency (IEA), "World Energy Outlook 2014," p. 207, 2014.

[3] European Parliament and Council of the European Union, "REGULATION (EC) No 715/2007 OF THE EUROPEAN PARLIAMENT AND OF THE COUNCIL of 20 June 2007 on type approval of motor vehicles with respect to emissions from light passenger and commercial vehicles (Euro 5 and Euro 6) and on access to vehicle repair and maintenance information," *Official journal of the European Union*, vol. L171, no. December 2006, pp. 1–16, 2007.

[4] M. Jahanmiri, *Particle Image Velocimetry: Fundamentals and Its Applications*. Goteborg, Sweden, 2011.

[5] I. Glassman and R. A. Yetter, *Combustion*. Elsevier Inc, 4th ed., 2008.

[6] T. Poinsot and D. Veynante, *Theoretical and Numerical Combustion*. R.T. Edwards, Inc., 2005.

[7] F. Williams, *Combustion Theory*. Benjamin Cummings, 1985.

[8] O. L. Gülder, "Burning velocities of ethanol-isooctane blends," *Combustion and Flame*, vol. 56, no. 3, pp. 261–268, 1984.

[9] A. N. Kolmogorov, "A refinement of previous hypotheses concerning the local structure of turbulence in a viscous incompressible fluid at high reynolds number," *Journal of Fluid Mechanics*, vol. 13, no. 01, pp. 82–85, 1962.

[10] V. M. Tikhomirov, *Equations of Turbulent Motion in an Incompressible Fluid*, pp. 328–330. Dordrecht: Springer Netherlands, 1991.

[11] S. B. Pope, *Turbulent Flows*. Cambridge University Press, 2000.

[12] R. Borghi, *Recent Advances in aeronautical science*. Pergamon Press, 1984.

[13] N. Peters, "The turbulent burning velocity for large-scale and small-scale turbulence," *Journal of Fluid Mechanics*, vol. 384, p. 107–132, 1999.

[14] F. Charlette, C. Meneveau, and V. Veynante, "A power-law flame wrinkling model for LES of premixed turbulent combustion Part I: non-dynamic formulation and initial tests," *Combustion and Flame*, vol. 131, no. 1, pp. 159 – 180, 2002.

[15] G. Nivarti and S. Cant, "Direct numerical simulation of the bending effect in turbulent premixed flames," *Proceedings of the Combustion Institute*, vol. 36, no. 2, pp. 1903–1910, 2017.

[16] G. Damköhler, "Der einfluss der turbulenz auf die flammengeschwindigkeit in gasgemischen," *Zeitschrift für Elektrochemie und angewandte physikalische Chemie*, vol. 46, no. 11, pp. 601–626, 1940.

[17] C. Turquand D'Auzay, "Numerical modelling of compressible turbulent premixed hydrogen flames."

[18] K. Bray, M. Champion, and P. A. Libby, "The interaction between turbulence and chemistry in premixed turbulent flames," in *Turbulent Reactive Flows* (R. Borghi and S. N. B. Murthy, eds.), (New York, NY), pp. 541–563, Springer US, 1989.

[19] N. Peters, *Turbulent Combustion*. Cambridge University Press, 2000.

[20] S. P. Chincholkar and J. G. Suryawanshi, "Gasoline direct injection: An efficient technology," *Energy Procedia*, vol. 90, pp. 666 – 672, 2016.

[21] S. B. Pope, "Lagrangian PDF Method for Turbulent Flows," *Annu. Rev. Fluid Mech.*, vol. 26, no. 1, pp. 23–63, 1994.

[22] O. Colin, F. Ducros, D. Veynante, and T. Poinsot, "A thickened flame model for large eddy simulations of turbulent premixed combustion," *Physics of Fluids*, vol. 12, no. 7, pp. 1843–1863, 2000.

[23] L. Valiño, "A Field Monte Carlo Formulation for Calculating the Probability Density Function of a Single Scalar in a Turbulent Flow," *Flow, Turbulence and Combustion*, vol. 60, no. 2, pp. 157–172, 1998.

[24] L. Valiño, R. Mustata, and K. Ben Letaief, "Consistent behavior of eulerian monte carlo fields at low reynolds numbers," *Flow, Turbulence and Combustion*, vol. 96, no. 2, pp. 503–512, 2016.

[25] V. Sabel'nikov and O. Soulard, "Rapidly decorrelating velocity-field model as a tool for solving one-point Fokker-Planck equations for probability density functions of turbulent reactive scalars," *Physical Review E - Statistical, Nonlinear, and Soft Matter Physics*, vol. 72, no. 1, pp. 1–22, 2005.

[26] J. O. Hirschfelder, F. Curtiss, and R. B. Bird, *Molecular theory of gases and liquids*. John Wiley & Sons, Inc, 1954.

[27] V. N. Prasad, *Large eddy simulation of partially premixed turbulent combustion*. Phd thesis, Imperial College London, 2011.

[28] P. Spalart and S. R. Allmaras, "A One-Equaiion Turbulence Model for Aerodynamic Flows," *30th Aerospace Sciences Meeting & Exhibit*, vol. 1, pp. 5–21, 1992.

[29] W. P. Jones and B. E. Launder, "The prediction of laminarization with a 2-equation model of turbulence," *International Journal of Heat and Mass Transfer*, vol. 15, p. 301, 1972.

[30] D. C. Wilcox, "Reassessment of the scale-determining equation for advanced turbulence models," *AIAA Journal*, vol. 26, no. 11, pp. 1299–1310, 1988.

[31] B. Baldwin and H. Lomax, "Thin Layer Approximation and Algebraic Model for Separated Turbulent Flows," *AIAA 16th Aerospace Science Meeting*, p. 9, 1978.

[32] A. H. Glasser, S. C. Jardin, and G. Tesauro, "Numerical solution of the resistive magnetohydrodynamic boundary layer equations," *Physics of Fluids*, vol. 27, no. 5, p. 1225, 1984.

[33] E. Garnier, N. Adams, and P. Sagaut, *Large Eddy Simulation for compressible flows*. Springer Netherlands, 2009.

[34] D. Anderson, J. Tannehill, and R. Pletcher, *Computational Fluid Mechanics and Heat Transfer*. CRC Press, 2015.

[35] B. Vreman, B. Geurts, and H. Kuerten, "Subgrid-modelling in LES of compressible flow," *Applied Scientific Research*, vol. 54, no. 3, pp. 191–203, 1995.

[36] J. Smagorinsky, "General Circulation Experiments With the Primitive Equations," *Monthly Weather Review*, vol. 91, no. 3, 1963.

[37] M. Germano, U. Piomelli, P. Moin, and W. H. Cabot, "A dynamic subgrid-scale eddy viscosity model," *Physics of Fluids A: Fluid Dynamics*, vol. 3, pp. 1760–1765, 1991.

[38] D. K. Lilly, "A Proposed Modification of the Germano-Subgrid-Scale Closure Method," *Physics of Fluids A: Fluid Dynamics*, vol. 4, no. 3, pp. 633–635, 1992.

[39] W. J. Grinstein, F. F. and Margolin, L. G. and Rider, *Implicit Large Eddy Simulation: Computing Turbulent Fluid Dynamics*. Cambridge University Press, 2007.

[40] B. Thornber, A. Mosedale, D. Drikakis, D. Youngs, and R. J. R. Williams, "An improved reconstruction method for compressible flows with low Mach number features," *Journal of Computational Physics*, vol. 227, no. 10, pp. 4873–4894, 2008.

[41] H. Pitsch, "Large-Eddy Simulation of Turbulent Combustion," *Annual Review of Fluid Mechanics*, vol. 38, no. 1, pp. 453–482, 2006.

[42] D. Veynante and L. Vervisch, "Turbulent combustion modeling," *Progress in Energy and Combustion Science*, vol. 28, no. 3, pp. 193–266, 2002.

[43] S. Candel, D. Veynante, F. Lacas, N. Darabiha, and C. Rolon, "Current Progress and Future Trends in Turbulent Combustion," *Combustion Science and Technology*, vol. 98, no. 4-6, pp. 245–264, 1994.

[44] T. D. Butler and P. J. O'Rourke, "A numerical method for two dimensional unsteady reacting flows," *Symposium (International) on Combustion*, vol. 16, no. 1, pp. 1503–1515, 1977.

[45] C. Angelberger, D. Veynante, F. Egolfopoulos, and T. Poinsot, "Large eddy simulations of combustion instabilities in premixed flames," *Proceedings of the Summer Program 1998, Center for Turbulence Research*, pp. 61–82, 1998.

[46] G. Wang, M. Boileau, and D. Veynante, "Implementation of a dynamic thickened flame model for large eddy simulations of turbulent premixed combustion," *Combustion and Flame*, vol. 158, no. 11, pp. 2199–2213, 2011.

[47] F. Charlette, C. Meneveau, and V. Veynante, "A power-law flame wrinkling model for LES of premixed turbulent combustion Part II: dynamic formulation," *Combustion and Flame*, vol. 131, no. 1, pp. 181 – 197, 2002.

[48] J. P. Legier, T. Poinsot, and D. Veynante, "Dynamically thickened flame LES model for premixed and non-premixed turbulent combustion," *Proceedings of the Summer Program*, pp. 157–168, 2000.

[49] F. Proch and A. M. Kempf, "Numerical analysis of the Cambridge stratified flame series using artificial thickened flame LES with tabulated premixed flame chemistry," *Combustion and Flame*, vol. 161, pp. 2627–2646, Oct. 2014.

[50] D. C. Haworth, "Progress in probability density function methods for turbulent reacting flows," *Progress in Energy and Combustion Science*, vol. 36, no. 2, pp. 168–259, 2010.

[51] S.B.Pope, "PDF Methods for Turbulent Reactive Flows," *Progress in Energy and Combustion Sciences*, vol. 11, pp. 119–192, 1985.

[52] P. J. Colucci, F. A. Jaberi, P. Givi, and S. B. Pope, "Filtered density function for large eddy simulation of turbulent reacting flows," *Physics of Fluids*, vol. 10, no. 2, pp. 499–515, 1998.

[53] F. Gao and E. E. O'Brien, "A large-eddy simulation scheme for turbulent reacting flows," *Physics of Fluids A: Fluid Dynamics*, vol. 5, no. 6, p. 1282, 1993.

[54] T. M. Eidson, "Numerical Simulation of the Turbulent Rayleigh-Benard Problem using Subgrid Modelling," *Journal of Fluid Mechanics*, vol. 158, pp. 245–268, 1985.

[55] R. O. Fox, *Computational Models for Turbulent Reacting Flows*. Cambridge: Cambridge University Press, 2003.

[56] V. Raman, H. Pitsch, and R. O. Fox, "Eulerian transported probability density function sub-filter model for large-eddy simulations of turbulent combustion," *Combustion Theory and Modelling*, vol. 10, no. 3, pp. 439–458, 2006.

[57] M. Stöllinger and S. Heinz, "PDF modeling and simulation of premixed turbulent combustion," *Monte Carlo Methods and Applications*, vol. 14, no. 4, pp. 343–377, 2008.

[58] R. R. Cao, H. Wang, and S. B. Pope, "The effect of mixing models in PDF calculations of piloted jet flames," *Proceedings of the Combustion Institute*, vol. 31 I, no. 1, pp. 1543–1550, 2007.

[59] M. Stöllinger and S. Heinz, "Evaluation of scalar mixing and time scale models in PDF simulations of a turbulent premixed flame," *Combustion and Flame*, vol. 157, no. 9, pp. 1671–1685, 2010.

[60] C. Celis and L. F. Figueira Da Silva, "Lagrangian mixing models for turbulent combustion: Review and prospects," *Flow, Turbulence and Combustion*, vol. 94, pp. 643–689, 2015.

[61] J. Villermaux and J. C. Devillon, "Représentation de la redistribution des domaines de ségrégation dans un fluide par un modéle d'interaction phénoménologique.," *Proceedings of the Second International Symposium on Chemical Reaction Engineering*, pp. 1–13, 1972.

[62] C. Dopazo and E. E. O'Brien, "An approach to the autoignition of a turbulent mixture," *Acta Astronautica*, vol. 1, pp. 1239–1266, 1974.

[63] S. Subramaniam and S. B. Pope, "A mixing model for turbulent reactive flows based on Euclidean minimum spanning trees," *Combustion and Flame*, no. 4, pp. 487–514, 1998.

[64] S. B. Pope, "A model for turbulent mixing based on shadow-position conditioning," *Physics of Fluids*, vol. 25, no. 11, 2013.

[65] S. B. Pope, "Consistent modeling of scalars in turbulent flows," *Physics of Fluids*, vol. 26, no. 2, pp. 404–408, 1983.

[66] S. B. Pope, "On the relationship between stochastic Lagrangian models of turbulence and second-moment closures," *Physics of Fluids*, vol. 6, no. 2, p. 973, 1994.

[67] S. M. Correa, "A direct comparison of pair-exchange and IEM models in premixed combustion," *Combustion and Flame*, vol. 103, no. 3, pp. 194–206, 1995.

[68] J. Janicka, W. Kolbe, and W. Kollmann, "Closure of the Transport-Equation for the Probability Density-Function of Turbulent Scalar Fields," *Journal of Non-Equilibrium Thermodynamics*, vol. 4, no. 1, pp. 47–66, 1979.

[69] G. I. Taylor, "Diffusion By Continuous Movements," *Proceedings of the London Mathematical Society*, vol. 2, pp. 196–212, 1921.

[70] D. B. Spalding, "Concentration fluctuations in a round turbulent free jet," *Chemical Engineering Science*, vol. 26, no. 1, pp. 95–107, 1971.

[71] R. P. Lindstedt and E. M. Vaos, "Transported PDF modeling of high-Reynolds-number premixed turbulent flames," *Combustion and Flame*, vol. 145, no. 3, pp. 495–511, 2006.

[72] A. Mura, F. Galzin, and R. Borghi, "A unified pdf-flamelet model for turbulent premixed combustion," *Combustion Science and Technology*, vol. 175, no. 9, pp. 1573–1609, 2003.

[73] V. Raman and H. Pitsch, "A consistent LES/filtered-density function formulation for the simulation of turbulent flames with detailed chemistry," *Proceedings of the Combustion Institute*, vol. 31 II, no. 2, pp. 1711–1719, 2007.

[74] I. Dodoulas, *Application of LES-PDF Methods on Turbulent Reacting Flows*. PhD Thesis, Imperial College London, 2015.

[75] W. P. Jones, A. J. Marquis, and V. N. Prasad, "LES of a turbulent premixed swirl burner using the Eulerian stochastic field method," *Combustion and Flame*, vol. 159, no. 10, pp. 3079–3095, 2012.

[76] S. L. Yilmaz, M. B. Nik, P. Givi, and P. A. Strakey, "Scalar Filtered Density Function for Large Eddy Simulation of a Bunsen Burner," *Journal of Propulsion and Power*, vol. 26, no. 1, pp. 84–93, 2010.

[77] a. Garmory, *Micromixing Effects in Atmospheric Reacting Flows*. Phd thesis, Cambridge University, 2007.

[78] T. Brauner, *Large Eddy Simulation of Premixed and Stratified Turbulent Combustion*. Phd thesis, Imperial College London, 2016.

[79] L. Mustata, R.and Valiño, C. Jiménez, W. P. Jones, and S. Bondi, "A probability density function Eulerian Monte Carlo field method for large eddy simulations: Application to a turbulent piloted methane/air diffusion flame (Sandia D)," *Combustion and Flame*, vol. 145, no. 1-2, pp. 88–104, 2006.

[80] W. Jones, S. Navarro-Martinez, and O. Röhl, "Large eddy simulation of hydrogen auto-ignition with a probability density function method," *Proceedings of the Combustion Institute*, vol. 31, no. 2, pp. 1765–1771, 2007.

[81] W. P. Jones and S. Navarro-Martinez, "Large eddy simulation of autoignition with a subgrid probability density function method," *Combustion and Flame*, vol. 150, no. 3, pp. 170–187, 2007.

[82] W. P. Jones and S. Navarro-Martinez, "Numerical Study of n-Heptane Auto-ignition using LES-PDF Methods," *Flow, Turbulence and Combustion*, vol. 83, pp. 407–423, 2009.

[83] W. P. Jones and V. N. Prasad, "Large Eddy Simulation of the Sandia Flame Series (D-F) using the Eulerian stochastic field method," *Combustion and Flame*, vol. 157, no. 9, pp. 1621–1636, 2010.

[84] W. P. Jones and V. N. Prasad, "LES-pdf simulation of a spark ignited turbulent methane jet," *Proceedings of the Combustion Institute*, vol. 33, no. 1, pp. 1355–1363, 2011.

[85] N.-M. S. and D. I., "Large Eddy Simulation of Premixed Turbulent Flames Using the Probability Density Function Approach," *Flow, Turbulence and Combustion*, vol. 60, pp. 645–678, 2013.

[86] W. P. Jones, A. J. Marquis, and F. Wang, "Large eddy simulation of a premixed propane turbulent bluff body flame using the Eulerian stochastic field method," *Fuel*, vol. 140, pp. 514–525, 2015.

[87] E. Hodzic, J. M., R.-Z. Szasz, and X.-S. Bai, "Large eddy simulation of bluff body flames close to blow-off using an Eulerian stochastic field method," *Combustion and Flame*, vol. 181, pp. 1 – 15, 2017.

[88] T. Brauner, W. P. Jones, and A. J. Marquis, "Les of the cambridge stratified swirl burner using a sub-grid pdf approach," *Flow Turbulence and Combustion*, no. 96, p. 965, 2016.

[89] A. Advić, G. Kuenne, F. di Mare, and J. Janicka, "Les combustion modeling using the eulerian stocahstic field method coupled with tabulated chemistry," *Combustion and Flame*, no. 175, pp. 201–219, 2017.

[90] P. Anselmo-Filho, S. Hochgreb, R. S. Barlow, and C. R., "Experimental measurements of geometric properties of turbulent stratified flames," *Proceedings of the Combustion Institute*, no. 32, pp. 1763–1770, 2009.

[91] E. S. Richardson and J. H. Chen, "Application of PDF mixing models to premixed flames with differential diffusion," *Combustion and Flame*, vol. 159, no. 7, pp. 2398–2414, 2012.

[92] Y. C. Chen, N. Peters, G. a. Schneemann, N. Wruck, U. Renz, and M. S. Mansour, "The detailed flame structure of highly stretched turbulent premixed methane-air flames," *Combustion and Flame*, vol. 107, no. 3, pp. 223–244, 1996.

[93] W. Jones, F. di Mare, and A. J. Marquis, *LES BOFFIN: Users guide.* Imperial College London, 2002.

[94] P. Kloeden and E. Platen, *Numerical Solution of Stochastic Differential Equations.* Springer, 1992.

[95] B. Vreman, B. Geurts, and H. Kuerten, "Comparison of numerical schemes in large-eddy simulations of the temporal mixing layer," *International Journal for Numerical Methods in Fluids*, vol. 22, pp. 297–311, 1996.

[96] R. O. S. Prasad and J. P. Gore, "An evaluation of flame surface density models for turbulent premixed jet flames," *Combustion and Flame*, vol. 116, pp. 1–14, Jan. 1999.

[97] H. Pitsch and L. de Lageneste, "Large-eddy simulation of premixed turbulent combustion using a level-set approach," *Proceedings of the Combustion Institute*, vol. 29, no. 2, pp. 2001–2008, 2002.

[98] P. E. Dimotakis, "Turbulent free shear layer mixing and combustion," *AIAA Conference on High-Speed Flight Propulsion Systems*, 01 1991.

[99] M. Klein, A. Sadiki, and J. Janicka, "A digital filter based generation of inflow data for spatially developing direct numerical or large eddy simulations," *Journal of Computational Physics*, vol. 186, no. 2, pp. 652–665, 2003.

[100] A. J. Aspden, M. S. Day, and J. B. Bell, "Turbulence–flame interactions in lean premixed hydrogen: transition to the distributed burning regime," *Journal of Fluid Mechanics*, vol. 680, pp. 287–320, 2011.

[101] D. Linse, C. Hasse, and B. Durst, "An experimental and numerical investigation of turbulent flame propagation and flame structure in a turbo-charged direct injection gasoline engine," *Combustion Theory and Modelling*, vol. 13, no. March 2015, pp. 167–188, 2009.

[102] M. Matalon, "Intrinsic flame instabilities in premixed and nonpremixed combustion," *Annual Review of Fluid Mechanics*, vol. 39, no. 1, pp. 163–191, 2007.

[103] H. Boughanem and A. Trouvé, "The domain of influence of flame instabilities in turbulent premixed combustion," *Symposium (International) on Combustion*, vol. 27, no. 1, pp. 971 – 978, 1998. Twenty-Seventh Sysposium (International) on Combustion Volume One.

[104] J. H. Chen, A. Choudhary, B. de Supinski, M. DeVries, E. R. Hawkes, S. Klasky, W. K. Liao, K. L. Ma, J. Mellor-Crummey, N. Podhorszki, R. Sankaran, S. Shende, and C. Yoo, "Terascale direct numerical simulations of turbulent combustion using S3D," *Computational Science and Discovery*, vol. 2, Jan. 2009.

[105] T. Passot and A. Pouquet, "Numerical simulation of compressible homogeneous flows in the turbulent regime.," *Journal of Fluid Mechanics*, pp. 441–466, 1987.

[106] S. Yu and S. Navarro-Martinez, "Modelling of deflagration to detonation transition using flame thickening," *Proceedings of the Combustion Institute*, vol. 35, no. 2, pp. 1955 – 1961, 2015.

[107] W. Han, H. Wang, G. Kuenne, E. Hawkes, J. Chen, J. Janicka, and C. Hasse, "Large eddy simulation/dynamic thickened flame modeling of a high karlovitz number turbulent premixed jet flame," *Proceedings of the Combustion Institute*, pp. 1 – 9, 2018.

[108] R. Knikker, D. Veynante, and C. Meneveau, "A dynamic flame surface density model for large eddy simulation of turbulent premixed combustion," *Physics of Fluids*, vol. 16, no. 11, pp. 94–91, 2004.

[109] C. Fureby, "A fractal flame wrinkling large eddy simulation model for premixed turbulent combustion," *Proceedings of the Combustion Institute*, vol. 30, pp. 593–601, 2005.

[110] N. Chakraborty and M. Klein, "A priori direct numerical simulation assessment of algebraic flame surface density models for turbulent premixed flames in the context of large eddy simulation," *Physics of Fluids*, vol. 20, 2008.

[111] L. Durand and W. Polifke, "Implementation of the thickened flame model for large eddy simulation of turbulent premixed combustion in a commercial solver," *ASME Turbo Expo 2007: Power for Land, Sea, and Air*, 2007.

[112] H. Kobayashi, T. Tamura, K. Maruta, T. Niioka, and F. A. Williams, "Burning velocity of turbulent premixed flames in a high-pressure environment," *Symposium (International) on Combustion*, vol. 26, no. 1, pp. 389 – 396, 1996.

[113] R. Keppeler, E. Tangermann, U. Allaudin, and M. Pfitzner, "LES of Low to High Turbulent Combustion in an Elevated Pressure Environment," *Flow, Turbulence and Combustion*, vol. 92, pp. 767–802, Mar 2014.

[114] S. B. Pope, "A Monte Carlo Method for the PDF Equations of Turbulent Reactive Flow," *Combustion Science and Technology*, vol. 25, no. 5-6, pp. 159–174, 1981.

Appendix A

Adaptive Statistical Resolution

This Appendix provides a conceptual overview of a potential approach for controlling the statistical uncertainty of stochastic field simulations and reducing the computational cost by varying the number of fields though the solution domain. The number of samples in a Monte-Carlo PDF simulation should always be sufficient to give a converged and unbiased estimate of the statistics of the PDF at all points in the flow. However, the number of samples required to give a converged estimate is likely to depend on the local (sub-filter) PDF, but the local (sub-filter) PDF may vary throughout the flow domain. For example, in the previous chapters it was shown that the analysed Bunsen flame [92] had a varying combustion regime along its length due to the decay of velocity RMS; close to the jet inlet, the flame was best described by the thickened flame regime which may exhibit lower local (sub-filter) variance than farther downstream where the flow was characterised to be more flamelet-like.

The variation of composition variables such as mass fraction depends on the local flow, mixing, and combustion characteristics and, in the case of LES, the filter size. The sub-filter variance of the composition variable is expected to vary based on the combustion regime; as the Damköhler number increases and the combustion regime moves towards the flamelet regime, the sub-filter variance tends towards a maximum of the order $c(1-c)$. As the Damköhler number decreases, the sub-grid variance is expected to tend towards a minimum. The minimum number of stochastic fields required in a simulation should be sufficient to statistically resolve the highest Damköhler regime (or largest (sub-filter) variance) experienced in the flow as generally, a larger sample size would be required to estimate statistics of a PDF with a larger sub-filter variance. Currently, the constant number of fields would be used throughout the simulation domain, meaning that, in regions with lower sub-filter variances, the number of fields is greater than necessary.

A.1 General Approach

The general approach of the Adaptive Statistical Resolution method is to locally estimate the minimum number of samples required to obtain an adequate statistical prediction by stochastic fields to a specified uncertainty level in both space and time. With this estimate, the number of stochastic fields (or samples) can be modified to provide a pre-determined, user-defined uncertainty level. This modulation of the number of fields reduces the computational cost of a simulation with respect to an equivalent, statistically resolved, constant field number simulation.

The metric used to estimate the statistical uncertainty of the stochastic fields predictions should also provide a sample number required to obtain the target uncertainty. To avoid simply replacing the computational saving from a reduction of stochastic field number with other forms of complex and demanding computations, the metric used to determine this uncertainty should be available from the stochastic fields themselves. During simulation, active control of the statistical resolution is achieved by comparing the required number of fields to the current number of fields being solved at a particular spatial location.

An example of the resultant process is shown schematically in Figure A.1 where the number of fields available for use in a simulation are indicated by a dashed black line. In this figure, the current active number of fields being solved is indicated by the green dashed line at 8 fields. If at a given spatial position (or time), the number of required fields is determined to be below the current active number (8), but above the level below (4), no adaptation is required as the target minimum statistical resolution is surpassed. If the number of required fields is greater than that of the current number (> 8) or less than number of the level below (< 4), then a "zone" is formed, here defined as a *transition region*, where active control of the statistical resolution occurs.

The transition regions should be constructed in such a way that the termination of the transition zone occurs at the spatial location where the increased/decreased field number is required and should always stretch into the direction of statistical over-resolution. Active control of the statistical resolution within the transition regions occurs through smooth (de)merging of fields. Therefore, the transition regions defines the boundaries where spatial (de)merging of fields initialises and terminates. In Figure A.1, line N_1 illustrates a merging process, and N_2 a field demerging process; the shaded regions indicate where the transition regions would likely be required. The general effect of the spatial adaptation of field number ensures the statistical uncertainty of the stochastic field simulation meets a minimum requirement over the entire simulation domain.

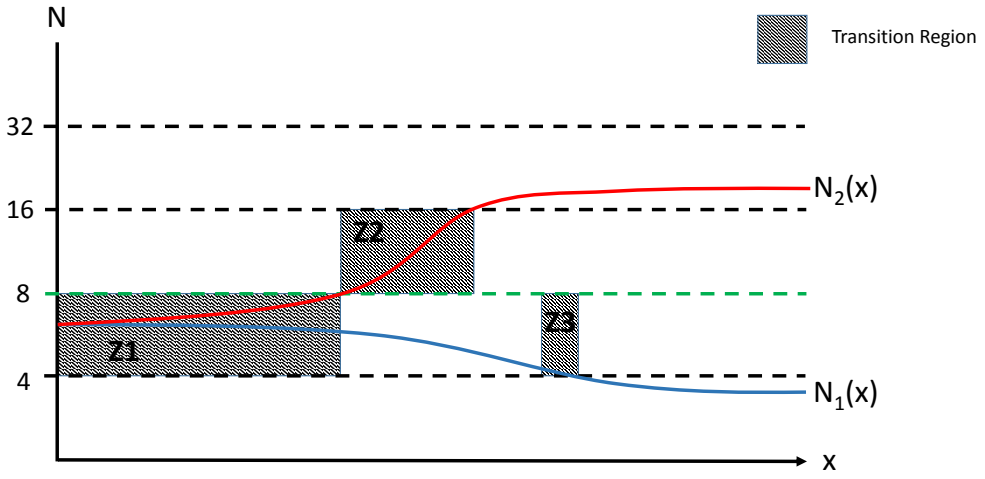

FIGURE A.1: Schematic evolution of field number through transition regions.

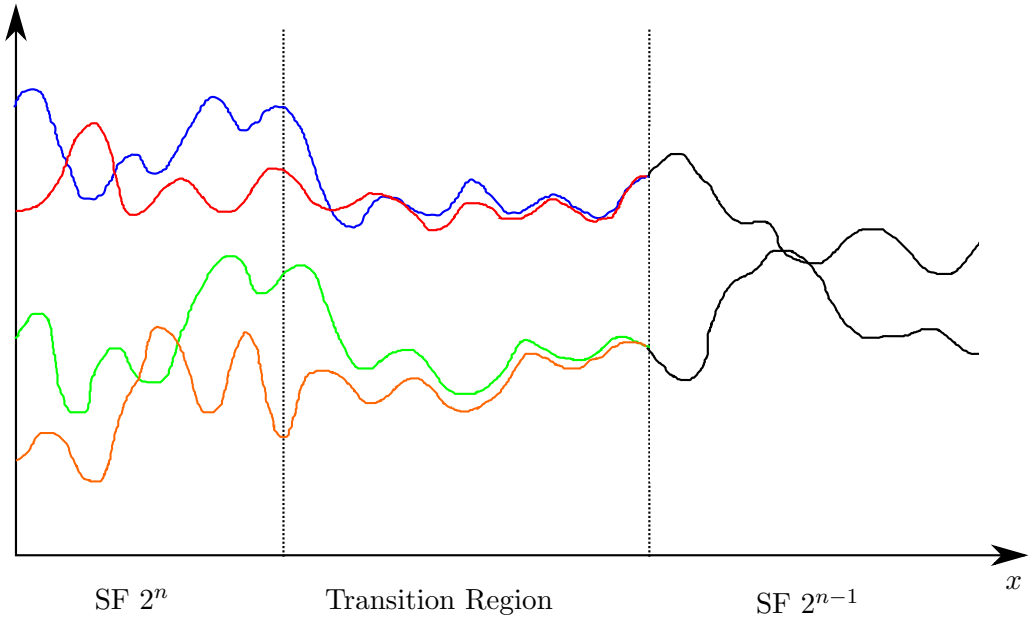

FIGURE A.2: Schematic of merging of fields though the transition zone

Within these transition regions, pairs of fields that are selected to merge are gradually relaxed towards their pairwise mean on a predetermined merging timescale. The magnitude of the timescale can be arbitrary but should be related to the width of the transition region required. Therefore, in Figure A.1, $Z1$ will likely have a larger merging timescale than $Z2$ and $Z3$.

A one-dimensional schematic representation of the merging process within a transition region is shown in Figure A.2. The merging of the fields is formulated in such a way that

arbitrarily-selected pairs of fields are smoothly brought together through the transition zone, gradually increasing their correlation until they become identical, and can be solved by a single field.

Merging of fields reduces the overall scalar variance, and it is therefore analogous to the micromixing term in the stochastic fields equation. In order to avoid excessive variance dissipation during the merging and demerging processes, it is proposed that the mixing rate applied in the micromixing model should be reduced in order to give the overall scalar dissipation rate intended.

A.2 Preliminary Framework and Implementation

A.2.1 Structure of Merging Tree

The current proposed methodology for field adaptation enables only 2^n fields to be solved at a particular spatial location at a given time. The maximum number of "levels" of merging is determined from the maximum number of fields (N_{max}) and by the power of two exponent n_{max} to obtain it. As such any level can be described by this procedure. For example, in Figure A.3, level 3 corresponds to 8 fields and level 2, 4 fields, etc. The choice of maximum number of fields is currently arbitrary and may be determined automatically and/or adapted temporally, or may be imposed by the user based on the computational resource available.

The various levels are sorted in ascending order such that the during initial stages of the simulation, a specified level is chosen as the starting level (n_{start}) corresponding to $2^{n_{start}}$ active fields. Relative to the current level, a field one level above corresponds to a parent field, and fields below correspond to the child fields. For example, SF 1.1 is the parent of SF 2.1, and SF 3.1 and 3.2 are the children of SF 2.1. The fields are distributed in such a way that every field has one parent and every parent has 2 children.

At every iteration, every field on all the levels are assigned their own dichotomic random variate (+1 or -1) for use in evaluation of the Wiener increment even if that level is not active at that particular point in space (dashed circles in Figure A.3).

On every level of the tree at every time step, dichotomic random variates for the Wiener terms are drawn without replacement from a set of numbers containing n/2 occurrences of -1 and n/2 occurrences of +1, such that the zero mean and unity variance conditions is enforced at every level of the tree.

In the example case of Figure A.3, it can be seen that every individual level (and thus all levels cumulatively) possess zero mean and unity variance. It should also be mentioned

that structure of the merge tree is fixed throughout the simulation domain. This avoids difficulties in the situation where separate regions with the same number of fields come together during the simulation.

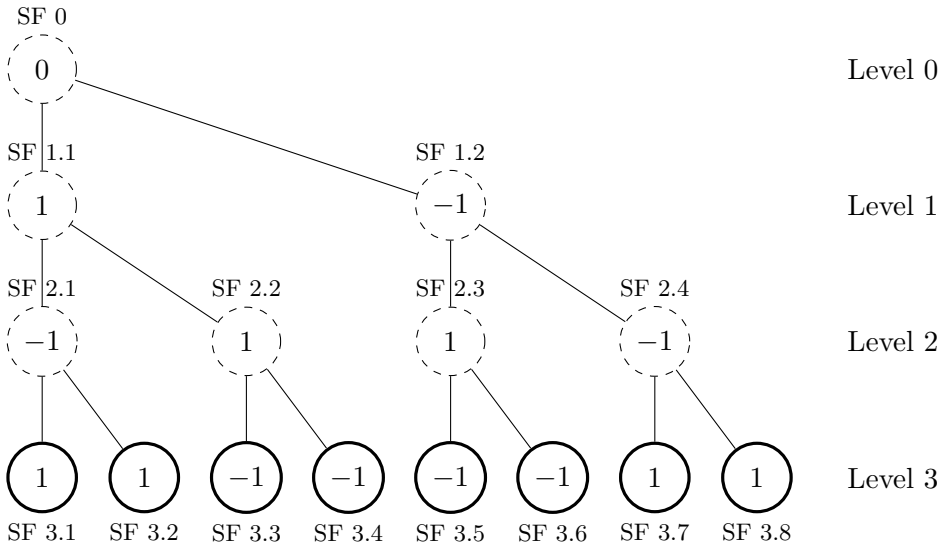

FIGURE A.3: Wiener term distributions of all fields at every level

A.2.2 Merging of Fields

For simplicity in the initial formulation, when it is determined that fields should be merged, an entire level is merged. Although this removes the ability for finer control of statistical uncertainty, it greatly simplifies the merging process and the numerical implementation.

Prior to merging, the two sibling fields have independent random variates and, after merging, they must have the same random variate (i.e. that of their parent). It is then necessary to devise a scheme for setting the Wiener increment for the two sibling fields during a merge or demerge process such that the overall requirement of zero mean and unity variance is enforced throughout the transition process. Additionally, it is preferable that the cumulative contribution of the random variates approximates the normal distribution of the Wiener process implied in the derivation of the stochastic fields equation.

The idea behind merging siblings is that throughout the merging process, the siblings will gradually inherit the Wiener term increment value of their parent. The result is a gradual blending of Wiener term increments from one level to the other while keeping the zero mean/unity variance satisfied.

A.3 Preliminary Formulation

A.3.1 Merging Progress - α

Within the transition regions the random variates applied to the the merging fields, $\xi_n^{i\prime}$ are taken as a weighted sum of the random variates of the child, ξ_n^i, and of its parent, $\xi^{p(i)}$ (where superscript i is the index of the child and p(i) is the index of the parent of field i). Thus, the merging of the random variates is specified by parameter α, so that the both children adopt the variate of their parent when $\alpha = 1$, as given by

$$\xi_n^{i\prime} = \left[(1-\alpha)\xi_n^i + \alpha\xi^{p(i)}\right]. \tag{A.1}$$

Since the random variates at each level of the tree have zero mean, the weighted sum of variates between levels is also guaranteed to have zero mean, however the variance is no longer necessarily equal to unity. A factor f is introduced in Equation A.1 in order to ensure unity variance. This yields

$$\xi_n^{i\prime} = \left[(1-\alpha)\xi_n^i + \alpha\xi^{p(i)}\right] f. \tag{A.2}$$

The expression for f can be obtained by taking the expectation of the variance of Equation A.2 and yields results in an expression

$$\frac{1}{f^2} = \frac{1}{2^n}\sum_{i=1}^{2^n}(\xi^{i\prime})^2 = (1-\alpha)^2 + \alpha^2 + \frac{1}{2^n}\alpha(1-\alpha)\sum_{i=1}^{2^n}\xi^i\xi^{p(i)}. \tag{A.3}$$

together, the two equations yield

$$\xi_n^{i\,\prime} = \frac{\left[(1-\alpha)\,\xi_n^i + \alpha\xi^{p(i)}\right]}{\sqrt{(1-\alpha)^2 + \alpha^2 + \alpha\,(1-\alpha)\,\frac{1}{2^n}\sum_{i=1}^{2^n}\xi_n^i\xi^{p(i)}} + \epsilon}, \tag{A.4}$$

In the rare case that $\alpha = 0.5$ and every child has an equal but opposite random variate to its parent, $f = 1/0$. Strictly, Equation A.3 remains defined and takes a value of zero in this limit, however a small parameter ϵ may be added in order to avoid computational difficulties due to rounding errors.

A.3.2 Merging Function

The evolution of a scalar composition for pairwise mixing models can be defined in terms of an interaction matrix (M_{ij}) by

$$\frac{d\phi_\alpha^i}{dt} = -\frac{1}{w_i}\sum_{j=1}^{N} M_{i,j}\phi_{\alpha,j} \tag{A.5}$$

where N is the number of the particles or fields and w_i their weight. For the IEM model used in this work, the interaction matrix coefficients are

$$M_{i,i}^{IEM} = \frac{C_\phi}{2\tau_{IEM}}\left(1 - w_i\right)w_i,$$
$$M_{i,j}^{IEM} = -\frac{C_\phi}{2\tau_{IEM}}w_j w_i, i \neq j,$$

where it can be readily shown that this interaction matrix satisfies all the criteria of pairwise-exchange models given in Section 3.2.2. For this adaptive field method, in the transition regions, the process of merging fields is achieved through a similar pairwise exchange between selected fields.

The pairwise exchange between fields leading to merging can be described through an interaction matrix, M^n, that describes the merging of fields at an arbitrary level n. The coefficients in this new matrix include the effects of both micromixing (M^M) and merging. The coefficients are

$$M_{i,j}^n = \left[M_{i,j}^M + \frac{1}{2\tau_{merge}}\left(1 - 2^{n-1}w_i\right)w_i\right]\delta_j^n, \qquad i = j$$
$$M_{i,j}^n = -\left[M_{i,j}^M + \frac{2^{n-1}w_j w_i}{2\tau_{merge}}\max\left(\delta_{i-2^{n_{max}-n},j}, \delta_{i,j-2^{n_{max}-n}}\right)\right]\delta_j^n \quad i \neq j \tag{A.6}$$

where the field weighting at level n is given by

$$w_i = \frac{1}{2^n}, \tag{A.7}$$

and δ_j^n represents a "switch" on level n which takes on a value of unity when the value of index j is that of an active field. It ensures that only active fields have coefficients within in the interaction matrix at the corresponding level. This switch is given by

$$\delta_j^n = \sum_{\alpha=1}^{2^n}\delta_{1+\alpha 2^{n_{max}-n}-j,1}. \tag{A.8}$$

The *max* of Kronecker deltas in Equation A.6 ensure that the correct pairs of fields are interacting (merging) with each other equally at level n. It also ensures that the

interaction matrix remains symmetric satisfying the conservation of means, variance decay, and boundness criteria.

The micromixing contribution can be descried by any pairwise exchange micromixing model. Since the IEM is used in this thesis, it is used to complete the formulation. The interaction matrix in the transition zones with IEM micromixing model then becomes

$$M^n_{i,j} = \left[\frac{C_\phi}{2\tau_{IEM}}\left(1-w_i\right)w_i + \frac{1}{2\tau_{merge}}\left(1-2^{n-1}w_i\right)w_i\right]\delta^n_j, \qquad i=j$$
$$M^n_{i,j} = -\left[\frac{C_\phi}{2\tau_{IEM}}w_j w_i + \frac{2^{n-1}w_j w_i}{2\tau_{merge}}\max\left(\delta_{i-2^{n_{max}-n},j},\delta_{i,j-2^{n_{max}-n}}\right)\right]\delta^n_j. \quad i\neq j \quad \text{(A.9)}$$

Through Equation A.5, evolution equation of for the $i-th$ scalar α at level n can be determined. The evolution equation becomes

$$\frac{\partial\phi^n_{\alpha,i}}{\partial t} = \left[-\frac{C_\phi}{2\tau_{IEM}}\left(\phi^n_{\alpha,i}-\langle\phi^n_\alpha\rangle\right) - \frac{1}{2\tau_{merge}}\left(\phi^n_{\alpha,i}-\langle\phi^n_\alpha\rangle_{i,i_p}\right)\right]\delta^n_i. \quad \text{(A.10)}$$

This equation implies that within the transition zone, if the field is active, it will be merging and (micro) mixing. This is consistent with the current merging strategy and can be seen from Figure A.3. In Equation A.10, $\langle\phi_\alpha\rangle$ is the mean of all active fields and $\langle\phi_\alpha\rangle_{i,i_p}$ is the pairwise mean of merging fields i and its pair $i_p = i + 2^{n_{max}-n}$

$$\langle\phi_\alpha\rangle_{ij} = \frac{\phi_{\alpha,i}+\phi_{\alpha,i+2^{n_{max}-n}}}{2}. \quad \text{(A.11)}$$

A.3.3 Merging Timescale

Note: The formulation in this sub-section has been provided as a contribution from Dr. Richardson and does not reflect work completed by the author.

The effect of the (de)merging of fields is to modify the total scalar dissipation rate. Therefore, within the transition regions the total scalar dissipation rate needs to be at the correct value to that which would occur in the absence of any (de)merging. Given a model for the scalar dissipation rate (ω_χ), and a specified the merging frequency (ω_T) scale, the required micromixing timescale can be determined. For a single scalar (Y), the turbulent mixing frequency for the IEM (for example) is given as

$$\omega_M = \frac{-1}{2\Delta t}\ln\left[\frac{\left(\overline{\phi^2_{i_o}}-\overline{\phi_{i_o}\phi_{i,i_p}}\right)+\left(\overline{\phi^2_{i,i_p}}-\overline{\phi}^2\right)-\overline{\phi''^2_o}\left(1+\exp\left(-2\omega_\chi\Delta t\right)\right)}{\left(\overline{\phi^2_{i_o}}-\overline{\phi_{i_o}\phi_{i,i_p}}\right)\exp\left(-2\omega_T\Delta t\right)+\left(\overline{\phi^2_{i,i_p}}-\overline{\phi}^2\right)}\right], \quad \text{(A.12)}$$

where

$$\phi_{i,i_p} = \frac{\left(\phi_i+\phi_{i_p}\right)}{2}. \quad \text{(A.13)}$$

The maximum allowable value of ω_T corresponds to the case $\omega_M \to 0$, yielding a maximum transition frequency of

$$\omega_{T_{max}} = \frac{-1}{2\Delta t} \ln \left[\frac{\left(\overline{\phi_{i_o}^2} - \overline{\phi_{i_o} \phi_{i,i_p}} \right) - \overline{\phi_o''^2} \left(1 + \exp\left(-2\omega_\phi \Delta t \right) \right)}{\left(\overline{\phi_{i_o}^2} - \overline{\phi_{i_o} \phi_{i,i_p}} \right)} \right]. \tag{A.14}$$

A.4 Outstanding Work

This Appendix presented an conceptual framework for the spatial adaption of statistical resolution. Additional work is required to develop a full mathematical description of the proposed method. The outstanding work is primarily in two areas:

1. **The establishment of a criterion that determines the required field number:** The premise of this function is to establish (and be able to quantify) an acceptable numerical uncertainty that allows the flow physics of interest to be captured accurately. This particular item will likely be derived as some function of the standard error of the instantaneous statistics of the stochastic fields or possibly as a ratio between the instantaneous variance and the maximum expected.

2. **The establishment of the transition regions:** Establishing the transition regions in the domain will require knowledge of how the imposed field number is required to change throughout the computational domain. Based on the spatial (or temporal) gradients of statistical uncertainty, the transition regions will need to be constructed accordingly. The size of the transition zone will directly influence the merging timescales imposed on the merging fields.

Appendix B

Statistical Convergence of Stochastic Fields

In this Appendix the influence of the sample number on the stochastic field solution is investigated. This is in order to quantify the level of uncertainty associated with a given stochastic field number across a range of different premixed combustion configurations. To achieve this, two different cases are analysed: a one-dimensional statistically stationary case and a 3D non-statistically stationary case.

In statistically stationary flows, sampling errors associated with lower sample number are not expected to be influential to the predictions of expectations as long as the method can be proven to be truly unbiased. In the stochastic field framework, confidence in the statistical predictions with a low field number can be obtained through increasing the sampling time. In non-statistically stationary cases such as in an internal combustion engine cycle, sampling errors may lead to errors in instantaneous turbulent flame speed predictions which affect the time-evolving properties of the flame.

B.1 One-dimensional Simulation

In order to investigate the effect of sample size on the stochastic field solution, one-dimensional simulations are conducted for a range of premixed combustion regimes. Contrary to the one-dimensional study conducted in Chapter 4, here, the grid spacing is held constant, and the number of stochastic field are varied. In order to maintain consistency with the findings of the previous chapters and to isolate the influence of sample size, the one-dimensional simulations conducted are sufficiently well resolved and numerically accurate with approximately 16 grid points resolving the average stochastic

field reaction-front. The conditions simulated in the one-dimensional configuration are shown in Table B.1.

TABLE B.1: Simulation Configuration

Ka	0.5, 5, 50, 500
L^*/δ_{th}	1, 10
Number of stochastic fields	4, 8, 16, 32, 64, 128, 256, 512

The turbulent (sub-filter) flame speed is of primary importance in premixed combustion modelling. As such the statistical convergence of the simulations was analysed though comparison of the expectation of this parameter. The time-averaged flame speed was calculated as in Equation 4.10 in Chapter 4. The results presented are normalised by the flame speed obtained with 512 fields for the corresponding case. This was done to be able to better visualise and compare convergence, and because 512 fields was deemed to be an unrealistic maximum number of fields to be used in practical 3D simulations; it is currently computationally infeasible to use more. Results of the simulations are shown in Figure B.1.

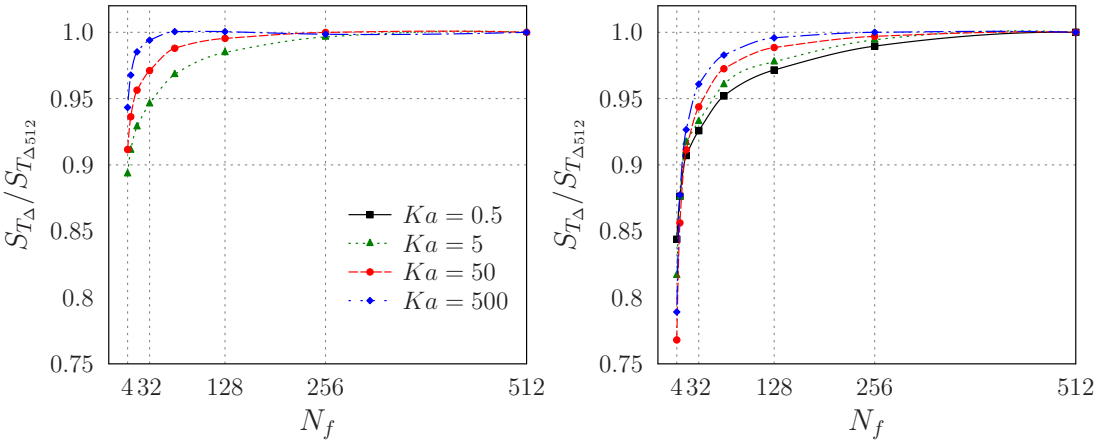

FIGURE B.1: Statistical convergence represented through normalised sub-filter flame speed at various Karlovitz numbers for: $\Delta/\delta_L = 1$ (left) and $\Delta/\delta_L = 10$ (right)

From this figure, it can be seen that the predictions of sub-filter flame speed are very much dependant on the field number. Nevertheless, the general trends observed are in line with the expected behaviour outlined at the beginning of Appendix A, namely: the number of required fields increases for decreasing Karlovitz number at a fixed filter width, and increases with filter size at a fixed Karlovitz number.

From the one-dimensional simulations it can be seen that the field number introduces bias to the stochastic field solution. This behaviour was not observed in the introductory

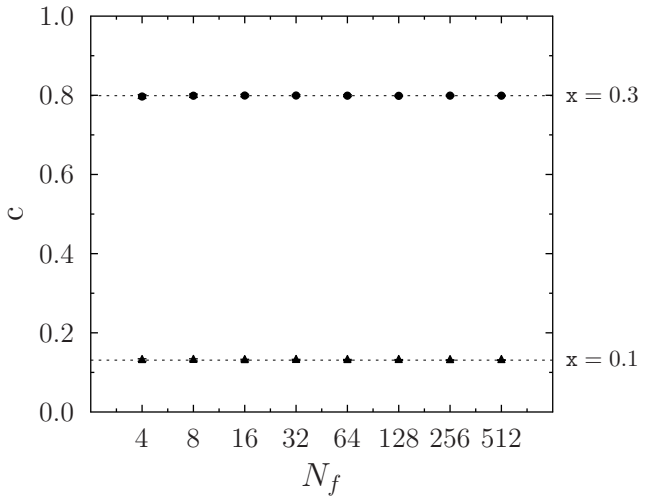

FIGURE B.2: Expectation of the mean scalar magnitude at two different spatial locations as a function of stochastic field number for the plug-flow reactor case [114]

work of [23] and [25] that presented the stochastic field variant of the plug-flow reactor test case used in [114] for the Lagrangian PDF framework. It is expected that this bias in the one-dimensional simulations presented here is a consequence of the coupling between the scalar (stochastic) fields and the momentum fields which is not present in the test case of [114]; a constant density and velocity were assumed.

To show this effect, the non-linear source term plug-flow reactor case from [114] was simulated with a numerically accurate grid spacing ($\Delta_x = 0.012$). The expectations were obtained by repeated simulation of the case and sampling at 1.5s until the smallest change in successive scalar expectations was below 0.5%. The results for the expectation of the mean scalar magnitude at two different spatial locations is presented in Figure B.2.

From this figure, it can be seen that the expectation of the scalar magnitude is independent of field number. It can therefore be expected that similar constant density conditions applied to the one-dimensional premixed flame calculations will yield similar statistical convergence behaviour.

Indeed, as seen from Figure B.3 the constant density premixed flame calculation compared to an equivalent variable density simulation shows vastly different behaviour. For the constant density case, all the stochastic fields predict a flame speed within 0.5% of the flame speed predicted by 512 fields.

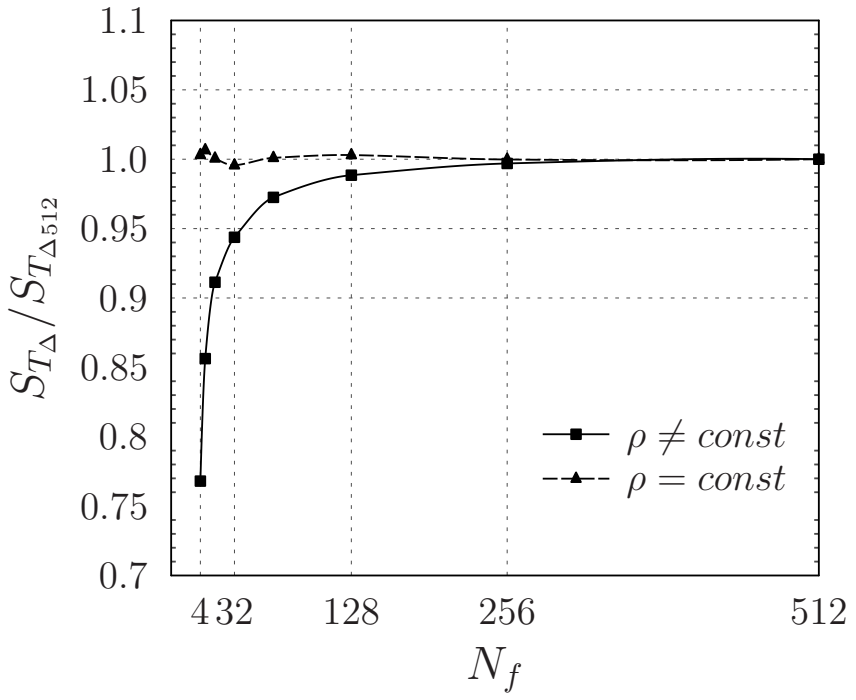

FIGURE B.3: Comparison of statistical convergence for $\Delta/\delta_L = 10$ at Ka=5 for constant and variable density

B.2 3D LES Statistical Convergence

One of the few investigations on the effect of field number in 3D LES-stochastic field simulations was conducted by Dodoulas [74] for the Bunsen flames of Chen et al. [92]. It is therefore not repeated in this work. From that statistical convergence study, although the differences were not substantial, it was shown that there was a difference in statistical moment predictions by stochastic fields between using 4 and 16 fields. In this section a statistical convergence analysis is conducted on the statistically-planar flame in isotropic decaying turbulence outlined in Section 4.3.

The results for case B_f are shown in Figure B.4 and case C_f in Figure B.5. In the results for the case B_f, the differences between the solutions of the different number of stochastic fields is almost negligible although an effect is seen by having a field number greater than unity. Thus, for this particular configuration, 8 fields can be considered and acceptable number of fields. Case C_f in Figure B.5 on the other hand shows different behaviour. By simply doubling the filter width, statistical independence is not observed between the different simulations and more fields may be required in excess of 64.

The results for the simulations with $\Delta = \Delta_x$ are shown in Figure B.6 for case B_c and Figure B.7 for C_c. The results for this set of simulations is more interesting. In case

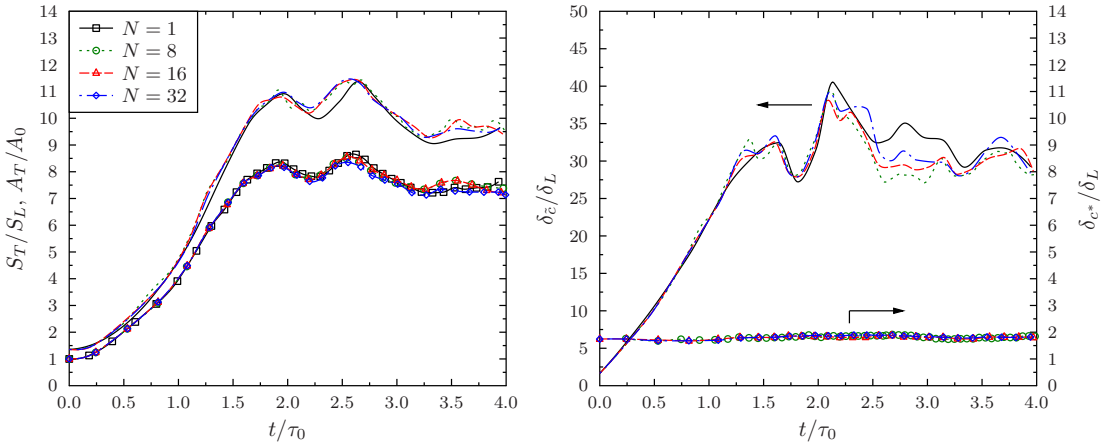

FIGURE B.4: Statistical convergence study of case B_f. Left: Temporal evolution of normalised turbulent flame speed (lines) and turbulent surface area (symbols). Right: non-dimensional mean flame brush thickness (lines) and mean stochastic field thickness (symbols)

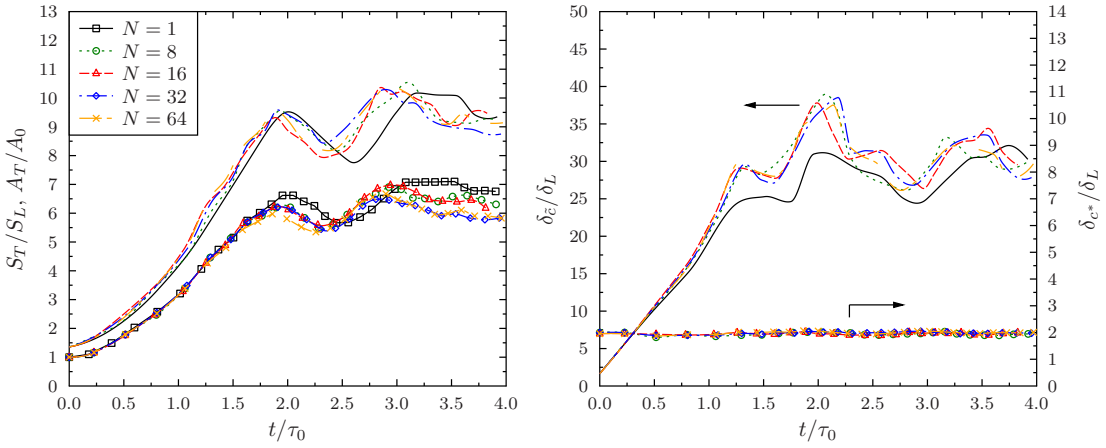

FIGURE B.5: Statistical convergence study of case C_f. Left: Temporal evolution of normalised turbulent flame speed (lines) and turbulent surface area (symbols). Right: non-dimensional mean flame brush thickness (lines) and mean stochastic field thickness (symbols)

B_c the simulations show very compelling convergence between using 8 and 16 fields, with a marginal difference in results obtained by using 1 field. For the larger filter width of case C_c, there appears to be almost no influence of stochastic fields on the evolution of flame speed. In this particular case, the conclusion would be that 1 field would be sufficient.

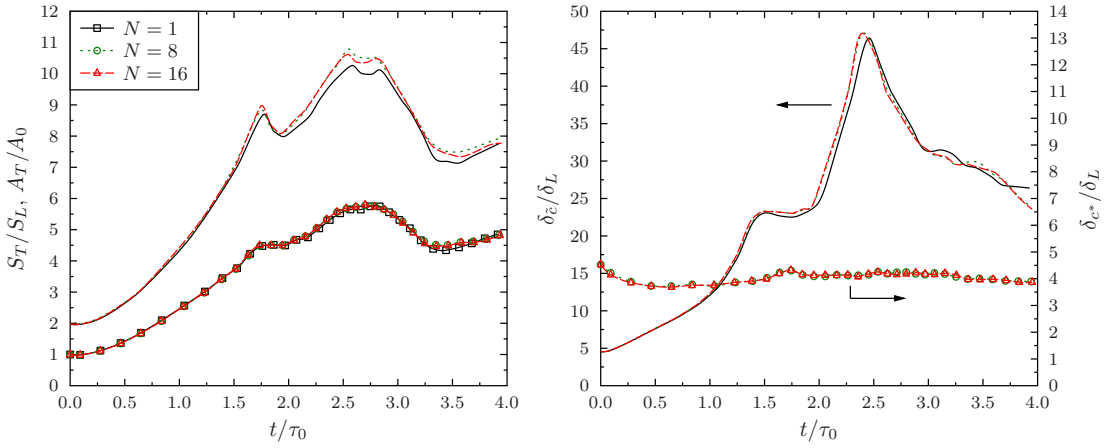

FIGURE B.6: Statistical convergence study of case B_c. Left: Temporal evolution of normalised turbulent flame speed (lines) and turbulent surface area (symbols). Right: non-dimensional mean flame brush thickness (lines) and mean stochastic field thickness (symbols)

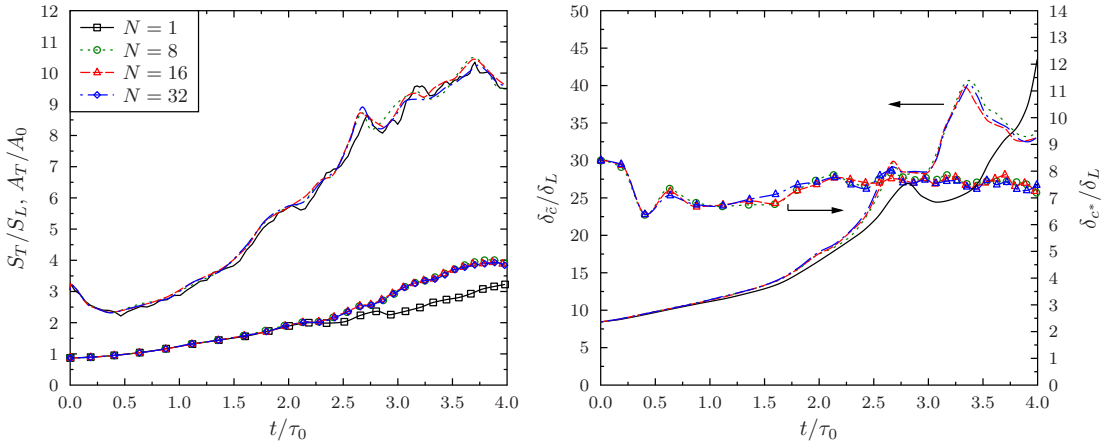

FIGURE B.7: Statistical convergence study of case C_c. Left: Temporal evolution of normalised turbulent flame speed (lines) and turbulent surface area (symbols). Right: non-dimensional mean flame brush thickness (lines) and mean stochastic field thickness (symbols)

B.3 Conclusion

From this brief investigation into statistical convergence of stochastic fields it can be seen that when setting the filter width equal to the grid spacing, numerical dissipation contributes to the scalar dissipation rate, un-naturally reducing the sub-filter variance and thus, field requirements.

However, from the numerically accurate simulations, this is not seen to be the case. It was shown that the number of stochastic fields required in a simulation to give a statistically converged solution will vary depending on the sub-filter combustion regime. The number of fields required will depend on what is deemed to be "converged" but for

increasingly flamelet sub-filter combustion regimes, the field requirement may be on the order of 256 fields.